ISSN 2074-272X

науково-практичний
журнал

2023/5

Електротехніка і Електромеханіка

Electrical Engineering & Electromechanics

Електричні машини та апарати
Промислова електроніка
Теоретична електротехніка
Інженерна електрофізика.
Техніка сильних електричних та магнітних полів
Електричні станції, мережі і системи

Журнал включено до найвищої категорії «А»
Переліку фахових видань України

З 2019 р. журнал індексується у Scopus

З 2015 р. журнал індексується
у Web of Science Core Collection:
Emerging Sources Citation Index

Electrical Engineering & Electromechanics

Scientific Journal was founded in 2002
Founder – National Technical University «Kharkiv Polytechnic Institute» (Kharkiv, Ukraine)

EDITORIAL BOARD

Sokol Ye.I.	**Editor-in-Chief**, Professor, Corresponding member of NAS of Ukraine, Rector of National Technical University «Kharkiv Polytechnic Institute» (NTU «KhPI»), Ukraine
Korytchenko K.V.	**Deputy Editor,** Professor, NTU «KhPI», Ukraine
Rozov V.Yu.	**Deputy Editor,** Professor, Corresponding member of NAS of Ukraine, Anatolii Pidhornyi Institute of Mechanical Engineering Problems of NAS of Ukraine, Kharkiv, Ukraine
Bolyukh V.F.	**Deputy Editor,** Professor, NTU «KhPI», Ukraine
Abu-Siada A.	Professor, Curtin University, Perth, Australia
Aman M.M.	Professor, NED University of Engineering & Technology, Karachi, Pakistan
Babak V.P.	Professor, Corresponding member of NAS of Ukraine, General Energy Institute of NAS of Ukraine, Kyiv, Ukraine
Baltag O.	Professor, Grigore T. Popa University Medicine and Pharmacy, Romania
Baranov M.I.	Professor, Research and Design Institute «Molniya» of NTU «KhPI», Ukraine
Batygin Yu.V.	Professor, Kharkiv National Automobile and Highway University, Ukraine
Bíró O.	Professor, Institute for Fundamentals and Theory in Electrical Engineering, Graz, Austria
Bouktir T.	Professor, Ferhat Abbas University, Setif 1, Algeria
Buriakovskyi S.G.	Professor, NTU «KhPI», Ukraine
Butkevych O.F.	Professor, Institute of Electrodynamics of NAS of Ukraine (IED of NASU), Kyiv, Ukraine
Colak I.	Professor, Nisantasi University, Istanbul, Turkey
Cruz S.	Professor, University of Coimbra, Portugal
Doležel I.	Professor, University of West Bohemia, Pilsen, Czech Republic
Féliachi M.	Professor, Technological Institute of Saint-Nazaire, University of Nantes, France
Guerrero J.M.	Professor, Aalborg University, Denmark
Gurevich V.I.	PhD, Honorable Professor, Central Electrical Laboratory of Israel Electric Corporation, Haifa, Israel
Hajjar A.A.	Professor, Tishreen University, Latakia, Syrian Arab Republic
Ida N.	Professor, The University of Akron, Ohio, USA
Izykowski J.	Professor, Wroclaw University of Science and Technology, Poland
Kildishev A.V.	Associate Research Professor, Purdue University, USA
Klepikov V.B.	Professor, NTU «KhPI», Ukraine
Korzeniewska E.	Professor, Lodz University of Technology, Poland
Ktena A.	Professor, National and Kapodistrian University of Athens, Greece
Kuznetsov B.I.	Professor, Anatolii Pidhornyi Institute of Mechanical Engineering Problems of NAS of Ukraine, Kharkiv, Ukraine
Kyrylenko O.V.	Professor, Academician of NAS of Ukraine, IED of NASU, Kyiv, Ukraine
Levin B.M.	Professor, Holon Institute of Technology, Tel Aviv-Yafo, Israel
Malik O.P.	Professor, University Of Calgary, Canada
Maslov V.I.	Professor, National Science Center «Kharkiv Institute of Physics and Technology», Ukraine
Mi Zou	PhD, Chongqing University of Posts and Telecommunications, China
Mikhaylov V.M.	Professor, NTU «KhPI», Ukraine
Miljavec D.	Professor, University of Ljubljana, Slovenia
Milykh V.I.	Professor, NTU «KhPI», Ukraine
Nacke B.	Professor, Gottfried Wilhelm Leibniz Universitat, Institute of Electrotechnology, Hannover, Germany
Petrushin V.S.	Professor, Odessa National Polytechnic University, Ukraine
Podoltsev A.D.	Professor, IED of NASU, Kyiv, Ukraine
Reutskiy S.Yu.	PhD, Anatolii Pidhornyi Institute of Mechanical Engineering Problems of NAS of Ukraine, Kharkiv, Ukraine
Rezinkin O.L.	Professor, NTU «KhPI», Ukraine
Rezinkina M.M.	Professor, NTU «KhPI», Ukraine
Shcherbak Ya.V.	Professor, NTU «KhPI», Ukraine
Sikorski W.	Professor, Poznan University of Technology, Poland
Suemitsu W.	Professor, Universidade Federal Do Rio de Janeiro, Brazil
Trichet D.	Professor, Institut de Recherche en Energie Electrique de Nantes Atlantique, France
Vaskovskyi Yu.M.	Professor, National Technical University of Ukraine «Igor Sikorsky Kyiv Polytechnic Institute», Kyiv, Ukraine
Vazquez N.	Professor, Tecnológico Nacional de México en Celaya, Mexico
Vinnikov D.	Professor, Tallinn University of Technology, Estonia
Yagup V.G.	Professor, O.M. Beketov National University of Urban Economy in Kharkiv, Ukraine
Yatchev I.	Professor, Technical University of Sofia, Bulgaria
Zagirnyak M.V.	Professor, Member of NAES of Ukraine, Kremenchuk M.Ostrohradskyi National University, Ukraine
Zgraja J.	Professor, Lodz University of Technology, Poland
Grechko O.M.	**Executive Managing Editor,** PhD, NTU «KhPI», Ukraine

From no. 1 2019 Journal «Electrical Engineering & Electromechanics» is indexing in **Scopus**
and from no. 1 2015 Journal is indexing in **Web of Science Core Collection: Emerging Sources Citation Index (ESCI)**.

Also included in DOAJ (Directory of Open Access Journals), in EBSCO's database, in ProQuest's databases – Advanced Technologies & Aerospace Database and Materials Science & Engineering Database, in Gale/Cengage Learning databases.

Editorial office address:
National Technical University «Kharkiv Polytechnic Institute», Kyrpychova Str., 2, Kharkiv, 61002, Ukraine
phones: +380 57 7076281, +380 67 3594696, **e-mail:** a.m.grechko@gmail.com (**Grechko O.M.)**

ISSN (print) 2074-272X
ISSN (online) 2309-3404

© National Technical University «Kharkiv Polytechnic Institute», 2023

Printed 28 August 2023. Format 60 × 90 ⅛. Paper – offset. Laser printing. Edition 200 copies.
Printed by Printing house «Madrid Ltd» (18, Gudanova Str., Kharkiv, 61024, Ukraine)

Electrical Engineering & Electromechanics
Scientific Journal

no. 5, 2023

Table of Contents

Electrical Machines and Apparatus

Industrial Electronics

Theoretical Electrical Engineering

Engineering Electrophysics. High Electric and Magnetic Fields Engineering

Power Stations, Grids and Systems

UDC 621.311: 621.311.6 https://doi.org/10.20998/2074-272X.2023.5.01

E.I. Bardyk, N.P. Bolotnyi

Development of fuzzy classifier for technical condition ranking of power transformer

*The work **aim** is to develop a fuzzy classifier for technical condition ranking of power transformer under condition of vagueness and ambiguity diagnostic information. **Methodology**. The fuzzy classifier developing for technical condition ranking of power transformer was based on approach of using fuzzy set theory and optimization methods. The proposed approach for power transformer rank assessment by using a classifier was developed on the basis of Takagi-Sugeno fuzzy inference system. The input indicators choice is justified and their efficiency for classifier is evaluated by expert evaluation method. This makes it possible to formalize expert assessments regarding the development of power transformer defects. **Results**. The formalization of technical condition assessment of power transformer in knowledge base form, which implemented in expert system prototype for technical condition assessment, was carried out. The complex technical condition assessment for each functional unit of power transformer was determined based on expert evaluations with using the test and measurement parameters results. **Originality**. The considered approach to formalization of uncertainty regarding technical condition of power transformer allows building a deterministic decision-making scheme for further maintenance strategy, in which the ranking and decommissioning procedures for specific objects are implemented on the basis of objective criteria. **Practical value.** The proposed fuzzy classifier allows determination with a high probability degree of technical condition assessment of power transformer based on the test and measurement parameters results. Thus, an applied aspect of using the obtained scientific result is the possibility to objectively rank of power transformers park based on the identified possible defects and their development degree. This constitutes the prerequisites for determining the failure probability evaluation of power transformer at nearest observation period and emergency risk assessment in integrated electric power systems under power transformer failures.* References 36, tables 8, figures 12.

Key words: **fuzzy classifier, electrical equipment, technical condition assessment, defect, power transformer.**

Розглянуто питання обґрунтування і розробки інтелектуальної системи для підтримки прийняття рішень щодо визначення рангу технічного стану силового трансформатора. Запропоновано підхід для встановлення рангу силового трансформатора шляхом застосування класифікатора, розробленого на базі системи нечіткого виведення Такагі – Сугено. Побудовано ієрархічні структурні схеми визначення рівнів факторів технічного стану окремих функціональних вузлів та силового трансформатора в цілому. Розроблено нечіткий класифікатор для ранжування технічного стану силового трансформатора за результатами окремих випробувань і вимірювань. Виконана адаптація нечітких моделей оцінки технічного стану шляхом навчання нечіткого класифікатора на вибірках з протоколів обстеження парку силових трансформаторів різних типів і класу напруг. Виконано комплексну оцінку технічного стану та класифікацію рангу за сукупністю контрольованих параметрів силових трансформаторів енергокомпанії. Бібл. 36, табл. 8, рис. 12.

Ключові слова: **нечіткий класифікатор, електрообладнання, оцінка технічного стану, дефект, силовий трансформатор.**

Introduction. The current state of the electric power industry in the industrialized countries of the world is characterized by a significant degree of wear of power transformers (PTs) as the most common element of the electric power system. Accelerated renewal of the PT park requires colossal investments in the electric power industry and determines the need for a comprehensive approach to solving these problems, not limited to equipment replacement [1-3]. Table 1 presents statistical data on the distribution of characteristic damage of PTs 110-500 kV by functional nodes [4, 5].

Table 1

Statistical data on the distribution of PT damage by functional nodes according to the duration of operation

PT functional node	Number of damages according to the duration of operation of the ST					Total
	10 years	10-20 years	20-30 years	30-40 years	>40 years	
Magnetic core	0	0	1	0	0	1
Cooling system	2	14	13	1	0	30
Windings	23	25	23	28	12	111
On-load tap-changer	12	28	21	10	0	71
High-voltage bushings	15	37	38	31	9	130
Oil leak	12	16	19	11	3	61
Vandalism	3	6	10	1	1	21
Oil drain	12	22	22	14	5	75
Total	79	148	147	96	30	500

Figure 1 shows the statistics of the main reasons for PTs failures according to SIGRE data as of 2015 for the period from 1950 to 2009 [6].

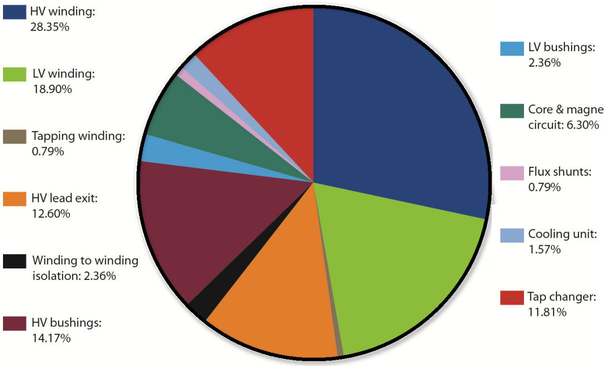

Fig. 1. The main causes of PT failures statistics for voltage more than 110 kV

In addition, most of the PT parks retain their operational capacity beyond the design life. It is urgent to improve the methods of diagnosing the technical condition of the equipment to determine the possibilities of its operation for 2-fold and more than the normative terms of operation [7-9].

Incorrect determination of the rank of the technical condition of the PT can lead to an erroneous calculation of the composition of the necessary volumes of diagnostic tests and measures for further operation [10].

Thus, the economic impracticality of prior equipment replacement is obvious, as well as the importance of timely detection of threatening defects, their further control with increasing reliability of determining the rank of the technical condition of the PT.

Analysis of literary sources and problem definition. Modern software and algorithms allow to significantly increase the reliability of solving such problems in conditions of uncertainty of diagnostic information. More reliable decisions regarding the ranking of the technical condition of PTs can be obtained when using intelligent decision support systems [11].

Currently, chromatographic analysis of dissolved gases (DGA) in PT oil is widely used to diagnose PT. Under the conditions of the occurrence and development of a defect inside the transformer, the composition and concentration of gases dissolved in the transformer oil intensively change both quantitatively and qualitatively [12].

Practically all available methods for evaluating the results of the DGA do not allow to clearly classify the technical condition of the PT based on the change in gas concentrations and, accordingly, cannot be used to assess the technical condition of the transformer at the observation time interval [13].

Table 2 presents certain results of some systems developed for diagnosing transformers based on DGA [14-16].

Table 2

Obtained results for some PT defect diagnosis systems

Number of PT	Diagnostic accuracy of the developed systems, %
711	90,3 – educational sample 93,81 – test sample
210	95,72 – educational sample 95,34 – test sample
711	96,2
33	90,91 – Dornenburg method 87,88 – modified Rogers method 90,91 – Rogers method 93,94 – IEC/IEEE method
820	90,49 – educational sample 93,54 – test sample

Quantitative indicators of diagnostic accuracy of the presented systems reflect the need to use methods that allow minimizing the error in assessing the technical condition of the PT.

The complexity of solving this problem is determined by the presence of a number of factors that simultaneously affect the concentration of gases in the oil: deterministic factors determined by the design of the PT, as well as stochastic factors that depend on the operating conditions of the PT.

A generalization of the results of basic and promising scientific works was carried out for the selection of software and algorithms for intelligent systems that allows obtaining reliable forecasting results in conditions of uncertainty [8-12].

Based on the results of the generalization, a technical and economic evaluation of production models (PM), semantic networks (SN), logical models (LM), artificial neural networks (ANN), fuzzy logic (FL), fuzzy neural networks (FNN), etc. was carried out [13-20].

Table 3 shows the characteristics of knowledge representation models for intelligent decision support systems.

It is obvious that among the listed models of the problem to be solved, models based on fuzzy neural networks are best suited [21]. They combine the advantages of such models of knowledge presentation as FL and ANN, which allows to compensate for the shortcomings inherent in each individual model.

Table 3

Technical and economic assessment of knowledge representation models

Name of the criterion	Knowledge representation model					
	LM	PM	SN	ANN	FL	FNN
1. Ability to operate with fuzzy data	-	+	-	+	+	+
2. Universality	-	-	-	+	-	+
3. Clarity of knowledge presentation	-	+	+	-	+	+
4. Modularity	+	+	-	+	-	+
5. Allowable time spent on building the model	+	+	-	+	+	+
6. Acceptable value	+	+	-	+	+	+
7. Ability to self-study	-	-	-	+	-	+
8. Efficiency coefficient	0,5	0,7	0,1	0,9	0,6	1

Based on the results of the analysis, it was decided to use FNN to build a fuzzy classifier based on the application of the Takagi-Sugeno fuzzy system model [22].

Therefore, **the goal of the article** is to improve the efficiency of the assessment of the technical condition of the power transformer by developing a fuzzy classifier to ensure the reliability of determining the rank of the technical condition of the power transformer.

To achieve the goal, the following tasks were solved:

- to develop a hierarchy of fuzzy assessment of the technical condition of the PT based on the aggregation of the most significant levels of factors affecting the technical condition;
- to develop an algorithm for conducting a fuzzy assessment of the technical condition of the PT based on a set of controlled parameters;
- to develop a fuzzy classifier for ranking the technical state of PT;
- to carry out a comprehensive fuzzy assessment of the technical condition of the PT in the conditions of information uncertainty in order to make effective preventive decisions regarding the strategy of further operation.

The concept of selecting parameters affecting the determination of the rank of the technical state of the PT. There are a number of diagnostic methods for determining the state of PT, but it is not easy to integrate their results into a single comprehensive assessment. The method based on fuzzy logic for calculating the health index proposed in [23] allows determining only the performance indicator of the insulation system. Over the past decades, various algorithms for diagnosing the state of PT have been proposed using intelligent information processing technology, such as the Bayes method [24], the method of evidentiary argumentation [25], the method of support vector machines [26], the method of artificial neural network [27]. When a PT defect occurs, it is often accompanied by a change in some parameters of the technical condition [28]. These algorithms have achieved good results in engineering practice, but there is a lack of analysis of the correlation of each parameter and the class of technical state of PT. In [29], when assessing the state of the transformer, each of the test indices and state rank corresponds to a separate pair of data sets. But the internal relationships between each test index were not considered in these works, so the types of PT damage cannot be diagnosed. On the other hand, the methods of assessing the condition of transformers based on the method of analysis of pairs of sets are the basis for the complex scoring method of assessing the technical condition by experts. This makes it possible to construct fuzzy matrices of expert evaluations using an analytical hierarchical process to determine weighting factors. However, the use of a complex scoring method for assessing the technical condition and analytical hierarchical process do not allow to completely avoid subjective disagreements of experts regarding the presence of a defect in the PT [30].

For the above reasons, this article makes an attempt to overcome the shortcomings of the considered approaches and methods of determining the comprehensive assessment of the technical condition of the PT.

The development of a fuzzy classifier involves the implementation of several main stages. At the initial stage of creating a classifier, it is necessary to select the factors that are most significant in determining the rank. Selection of the main parameters is also important, since the assessment of the technical condition rank of PT is characterized by a large number of factors that have certain differences for different classes of technical condition. The solution to this problem is possible using the method of expert evaluations for ranking the compared objects.

The proposed method of expert evaluations is based on the use of a fuzzy comprehensive evaluation of the object, the functioning of which is influenced by numerous factors.

The practice of conducting diagnostic tests on PT shows that when making a diagnostic hypothesis regarding the presence of a defect, there should be several factors that are considered and determined in the evaluation process. Since it is usually very difficult to make a decision using a classical mathematical method, fuzzy complex estimation is able to solve the multi-factor assessment decision-making problem. This assessment method is based on existing evaluation standards and fuzzy conversion of actually measured data or data with significant uncertainty, incomplete information. Compared to other methods, it is a comprehensive, objective and integrated method of evaluating results.

The algorithm for conducting a fuzzy assessment of the technical condition of the PT is as follows.

1. Determination of the set of X levels of factors influencing the technical condition of the PT, which requires assessment:

$$X = \{x_1, x_2, \dots, x_n\}; \tag{1}$$

where x_i is the i-th factor that can affect the technical condition of the PT and has a certain degree of ambiguity; n is the total number of factors that can affect the technical condition of the PT.

2. Formation of the set V of expert evaluations:

$$V = \{v_1, v_2, \dots, v_n\}; \tag{2}$$

where v_i is the i-th comprehensive result of the expert's comprehensive assessment; n is the total number of expert assessments regarding the technical condition of the PT.

3. Formation of the complex matrix of fuzzy relations of expert evaluations R:

$$R = \begin{vmatrix} r_{11} & \cdots & r_{1j} \\ \vdots & \ddots & \vdots \\ r_{j1} & \cdots & r_{ij} \end{vmatrix}, \tag{3}$$

where $r_{ij} \in [0, 1]$ is the element of the matrix of fuzzy relations between damage to functional nodes and the consequences of these damages.

4) Definition of the system of weighting coefficients W:

$$W = (w_1, w_2, \dots, w_n), \quad \sum_{i=1}^{n} w_i = 1, \tag{4}$$

where w_i is the i-th weighting coefficient reflecting the significance of each assessment factor x_i; n is the total number of weighting coefficients for assessing the significance of factors with regard to the impact on the assessment of the technical condition of the PT.

5) Definition of the set B of the fuzzy comprehensive assessment of the technical state of the PT. The equation of the fuzzy comprehensive assessment of experts regarding the technical condition of the PT

$$B = \max\{b_1, b_2, \dots, b_n\}, \tag{5}$$

where $b_j = \sum_{i=1}^{m} w_j \cdot r_{ij}$, j = 1, 2, ..., n is the j-th fuzzy comprehensive assessment of the technical condition of the PT; n is the total number of fuzzy comprehensive assessments of the technical condition of the PT.

An expert group consisting of n highly qualified specialists in the operation and repair of PTs is formed to carry out the work on the fuzzy comprehensive evaluation of technical state using the method of expert evaluations. The formation of the group began with the selection of candidates and their further evaluation using the Delphi method [31].

To determine the technical condition of the olive PT, based on the results of individual tests and measurements, a linguistic mathematical model was developed, which includes the rules of fuzzy logical inference, the term-set and the function of the input parameters belonging to one or another linguistic quantity. Figure 2 presents a fragment of a hierarchical structural diagram of a fuzzy logical inference about the technical condition of an oil transformer on the basis of defined separate levels of technical condition factors [32].

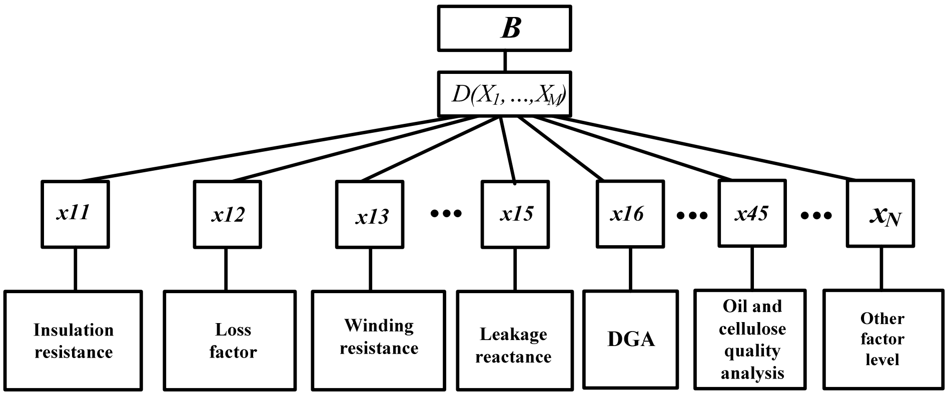

Fig. 2. The hierarchical structural scheme of fuzzy logical conclusion for PT technical condition

The model contains the rules of Takagi-Sugeno fuzzy logical inference, terms and functions of belonging of the input parameters to one or another linguistic quantity. The knowledge base of the prototype of the expert system for diagnosing the technical condition of the PT is based on a hierarchical representation and consists of a system of built-in knowledge bases. An integral assessment of the technical condition is carried out by aggregating inferences regarding the type of the PT defect based on individual test results, using relevant knowledge bases.

Fuzzy logic analysis includes three sequential processes, namely: fuzzification, fuzzy inference, and defuzzification. Fuzzification transforms, for example, a clear gas ratio into a fuzzy input set. The selected fuzzy logic inference system is responsible for obtaining inferencees from fuzzy rules based on the knowledge of «if-then» linguistic statements. Each rule consists of two components, in which there is the preceding part («if») and the following part («then»). With the help of a fuzzy approach, partial belonging to a certain class of technical condition (determined by the value of the belonging function) can increase the number of relevant inferences compared to the traditional criteria for assessing the technical condition of the PT, which are regulated by regulatory and technical documentation [6, 32].

For example, the linguistic rule for determining the assessment of technical condition indicators based on the results of the DGA has the following form: if «C2H2/C2H4 is 0, CH4/H2 is 2, and C2H4/C2H6 is also 0, then the type of defect that corresponds to this combination of ratios is D7», that is, a low-temperature defect (overheating) T<300 °C.

The defuzzification function then transforms the original values back into crisp values.

All inputs of the fuzzy logical inference system have membership functions, the basic forms and parameters of which are presented in detail in [32]. To take into account the objectively existing tolerance of the recognized defect to the change of parameters in a certain range, the trapezoidal membership functions are used.

At the initial stage, each expert was offered 7 indicators according to their significance for ranking the technical state of the PT:

- x1 – the level of the technical condition factor of the PT windings (Fig. 3);
- x2 – the level of the factor of the technical condition of the magnetic core of the PT (Fig. 4);
- x3 – the level of the factor of the technical condition of high-voltage bushings of the PT (Fig. 5);
- x4 – the level of the factor of the insulation characteristics of the transformer oil of the PT (Fig. 6);
- x5 – the level of the factor of the on-load tap-changer switch (Fig. 7);
- x6 – the level of the factor of the technical condition of other PT nodes (Fig. 8);
- x7 – the level of the factor of other PT operation indicators (Fig. 9).

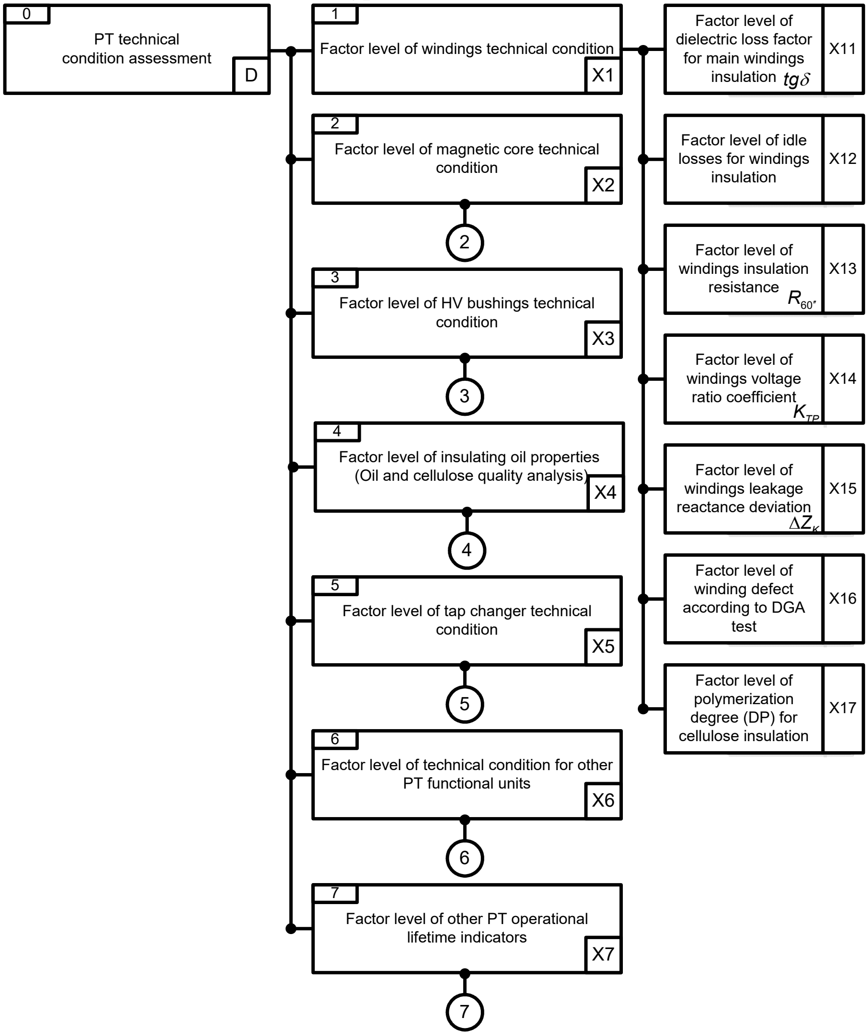

Fig. 3. The hierarchical structural scheme of PT technical condition assessment

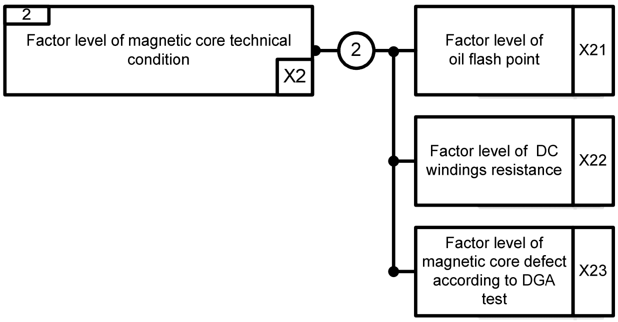

Fig. 4. The hierarchical structural scheme of factor level assessment for PT magnetic core

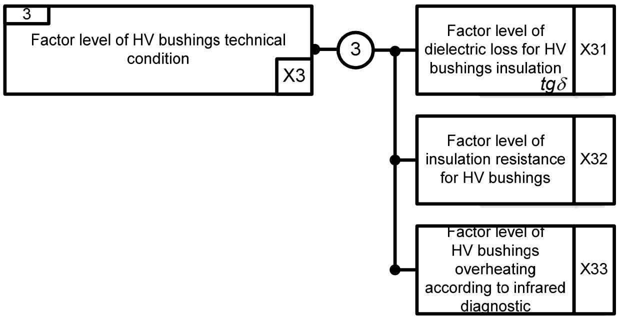

Fig. 5. The hierarchical structural scheme of factor level assessment for PT HV bushings

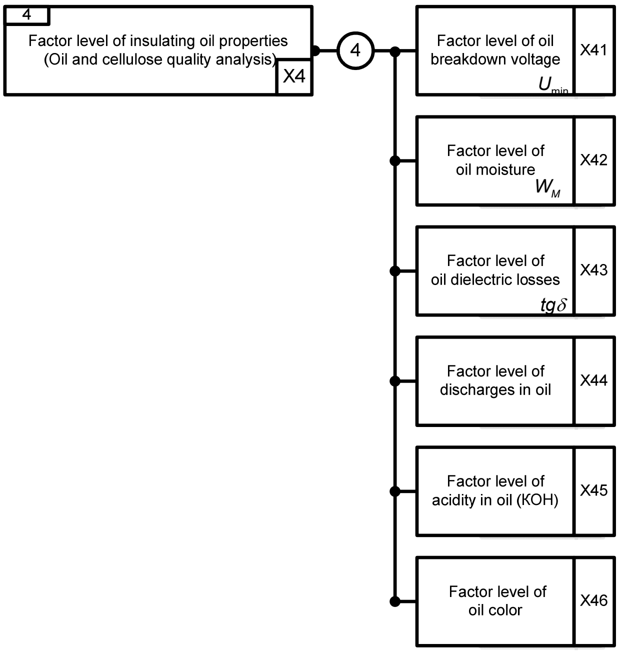

Fig. 6. The hierarchical structural scheme of factor level assessment for insulating oil properties (oil and cellulose quality analysis)

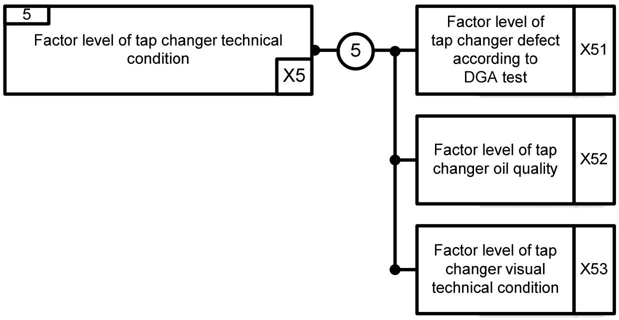

Fig. 7. The hierarchical structural scheme of factor level assessment for tap changer technical condition

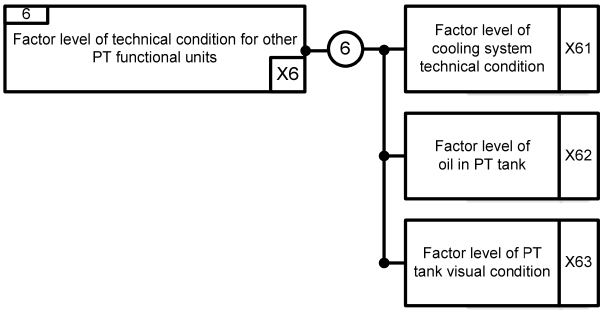

Fig. 8. The hierarchical structural scheme of factor level assessment for technical condition for other PT functional units

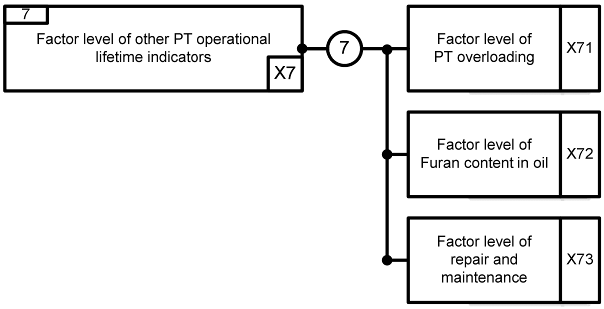

Fig. 9. The hierarchical structural scheme of factor level assessment for other PT operational lifetime indicators

Assessment of the technical condition of the PT by experts depends on overcoming the uncertainty of information:

- it is impossible to determine the state by one measurement, based on one method;
- reliable diagnosis is based on: several types of diagnosis; dynamics of changes in characteristics;
- impossibility of applying the same diagnosis criteria for different constructions and voltage classes;
- the reliability of the diagnosis results should be achieved with minimum costs for obtaining them.

Construction of a fuzzy classifier for ranking the technical condition of the PT. After determining the levels of factors of the technical state of the PT, the operating conditions of the PT are classified in order to establish the assessment of each factor for a comprehensive fuzzy assessment [33]. The operating conditions of the PT are classified as good, acceptable, requiring caution and risky in this article expressed as a set of expert assessments $V = \{v_1, v_2, v_3, v_4\}$ = {good, acceptable, requiring caution, risky}.

The operating condition «good» means that the test sample of transformer operation data is normal, and each technical condition parameter deviates slightly from the monitored values. The probability of a defect occurring is low and long-term operation within the limits of permissible deviations of the monitored parameters is available.

«Acceptable» operating conditions mean that the PT has been operated for a certain period of time, and satisfactory test data or reliability of a certain individual monitored parameter of the technical condition is slightly less than the limit of acceptable deviations. Since the data is reliable, the operation of the PT can be continued, and the probability of failure is low.

The operating condition «Requires caution» means that the test data deviates from the normal state during the test period. Some parameters of the technical condition indicate that a defect may exist, thus the probability of damage is increased, and although the transformer may continue to operate, the operating interval must be shortened.

The operating condition «risky» means that the overall operational properties of the PT are below average. Most of the obtained monitored parameters exceed the values regulated by the Standards, and the probability of failure is high.

Table 4 presents the semantic definition of the ratio of the rank of the technical condition and operating conditions of the PT.

Table 4

Semantic definition of the range of changes in the rank of the technical state of the PT

Range of change of value *B*	Semantic definition of assessment of the technical condition of the PT
0…0,25	Good technical condition of the PT. Continuation of operation without restrictions. Very low failure rate (VL)
0,25…0,5	A low degree of deterioration of the technical condition of the PT. Continuation of operation without restrictions. Low failure rate (L)
0,5…0,75	The average degree of deterioration of the technical condition of the PT. A slight degree of development of the defect. More frequent monitoring of parameters of technical state of the PT. Medium failure rate (M)
0,75…1,0	The technical condition shifted from a state of deterioration to a state of failure. A significant degree of defect development. High failure rate (H)

Linguistic variable *B* «fuzzy comprehensive assessment of the technical state of the PT», presented in Table 4 is represented by the basic term-set $T = \{T_{VL}, T_L, T_M, T_H\}$, where T_{VL}, T_L, T_M, T_H are the terms corresponding to very low, low, medium and high levels of deterioration of the technical condition of the PT. Graphs of membership functions of the term-set of the linguistic variable *B* are shown in Fig. 10.

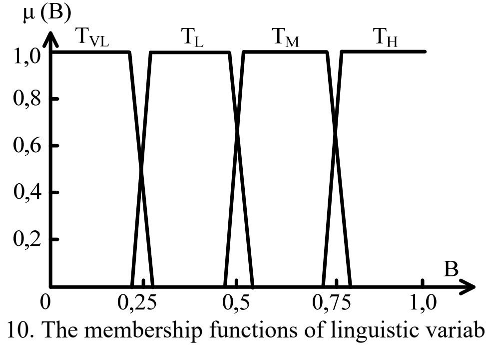

Fig. 10. The membership functions of linguistic variable B

Thus, the results of each type of diagnosis are classified independently, and then the final inference is made taking into account all expert assessments.

To determine the rank of the technical state of the olive PT, a linguistic model of the classifier based on the use of the fuzzy logic apparatus was developed [32, 34, 35].

The fuzzy model of the classifier of the comprehensive assessment of the PT state is built on the basis of the adaptive neuro-fuzzy network ANFIS (Adaptive Network-based Fuzzy Inference System), which is a hybrid multilayer artificial neural network of a special structure without feedback and allows implementing system models in the form of fuzzy production rules.

The fuzzy classifier for ranking the technical condition of the PT is presented in the form

$$B = F(X, V, C, W), \tag{6}$$

where $X = \{x_1, x_2, \dots, x_n\}$ is the input vector of rank estimates of indicators of factor levels of the fuzzy model of the classifier; $V = \{v_1, v_2, \dots, v_q\}$ is the vector of parameters of the membership functions of a comprehensive assessment by an expert of indicators of the levels of factors of the fuzzy model of the classifier; $C = \{c_1, c_2, \dots, c_q\}$ is the vector of parameters of fuzzy terms from the knowledge base of the fuzzy classifier model; $W = \{w_1, w_2, \dots, w_n\}$ is the vector of weight coefficients of fuzzy rules of the fuzzy classifier model; n is the total number of fuzzy rules in the knowledge base of the fuzzy classifier model; q is the total number of terms of the fuzzy model of the classifier; F is the «input-output» communication operator of the fuzzy classifier model.

The values of inputs, outputs and synaptic weights of the hybrid neural network are in the range [0, 1].

Figure 11 shows an example of a neural network representation of the rules of a fuzzy classifier for 2 levels of influencing factors on the technical condition of the PT.

The ANFIS network uses a hybrid learning algorithm. Neurons in the ANFIS network have a different structure and purpose, which correspond to the fuzzy inference system and implement the main subsequent stages of its operation.

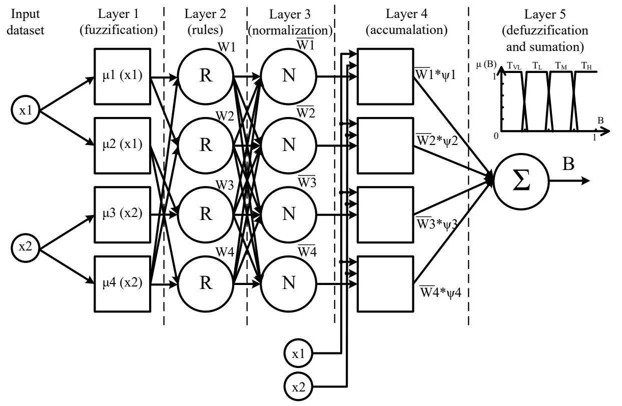

Fig. 11. The neural network representation of fuzzy classifier rules for two factors levels affecting PT technical condition

Layer 1. Fuzzification using membership functions of input variables. The first adaptive layer of the ANFIS network contains neurons that calculate the values of the membership functions of the input variables $\mu_i(x_1)$ and $\mu_j(x_2)$, where x_1 and x_2 are the input variables, i=1, 2 and j=3, 4. The adaptability of the layer is achieved by selecting the type of membership functions of the input variables.

Layer 2. Aggregation (determining the degree of truth of conditions) by processing the basis of fuzzy linguistic rules. The second fixed layer of the ANFIS network contains neurons that calculate the products of the values of the membership functions obtained on the first layer:

$$W_i = \mu_i(x_1) \cdot \mu_j(x_2), \tag{7}$$

where W_i are the synaptic weights of the network.

Layer 3. Activation (determining the degrees of truth of statements) by normalizing the activation levels of fuzzy rules. The third fixed layer of the ANFIS network contains neurons that calculate the normalized activation levels of the fuzzy rules:

$$\overline{W}_i = W_i / \left(W_1 + W_2 + W_3 + W_4\right). \tag{8}$$

Layer 4. Accumulation (combination of degrees of truth) using membership functions of the output variables. The fourth adaptive layer of the ANFIS network contains neurons that calculate the values of the membership functions of the output variables, as well as the product of the values of the synaptic weights and the membership functions:

$$\overline{W}_i \cdot \psi_i = \overline{W}_i \cdot \psi_i\left(x_1, x_2, c_i\right), \tag{9}$$

where ψ_i are the values of the membership functions of the output variables; c_i are the parameters of fuzzy terms of membership functions from the knowledge base.

Layer 5. Defuzzification (transition to clarity) with obtaining a clear value of the original variable. The fifth fixed layer of the ANFIS network contains a neuron that calculates the sum of the product of the values of the membership functions of the output variables and synaptic weights

$$\sum_{i=1}^{M} \overline{W}_i \cdot \psi_i \,. \tag{10}$$

Layer 6 consists of elements that determine the maximum value of belonging among all the rules that specify the rank label of the technical condition of the PT.

Layer 7 consists of one element containing the rank index of the technical condition of the PT with the maximum value of belonging.

Figure 12 presents the general structure of the neural network built for the fuzzy classifier for assessing the technical condition of the PT. Neurons corresponding to the rules, which set labels of a specific rank, are placed in separate groups.

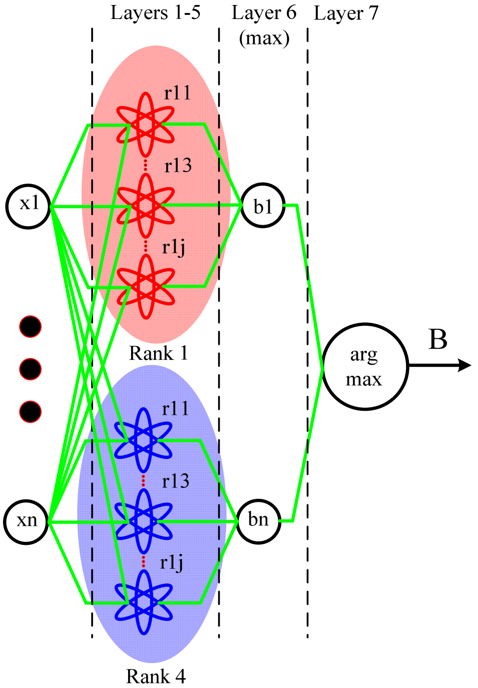

Fig.12. The fuzzy classifier architecture for identification of PT technical condition rank

Criterion values of the parameters used in the fuzzy model are statistically averaged over a large set of operating PTs. The actual modes of operation of each specific PT may differ. This requires adapting fuzzy models to real operating conditions by adjusting parameters.

In full, the input arguments are unknown, that is, there is uncertainty in the assessment of the technical condition of the PT. In this case, it is recommended to use machine learning algorithms in which there are no obvious logical relationships between parameters, but it is necessary to have a training sample. The study was conducted using statistical information on PT failures and the results of diagnostic procedures from functioning PTs that were registered in the energy system of Ukraine.

Tuning a fuzzy model consists in finding such parameters that minimize the deviation between the desired and actual behavior of the model. The algorithm for setting up the adaptive neuro-fuzzy network ANFIS consists of two stages [32, 35].

Stage 1 (direct flow of the algorithm). We set the initial values of the parameters of the first adaptive layer, make calculations on the second and third layers, determine the parameters of the fourth adaptive layer and calculate the value of the identification error function. If the value of the identification error function is within the acceptable limits, then the training of the adaptive neuro-fuzzy ANFIS network is finished, otherwise we proceed to the second stage.

Stage 2 (reversal of the algorithm). Using the method of backpropagation of the identification error, we refine the parameters of the first adaptive layer.

It is assumed that the parameters of the membership functions should be selected in such a way as to preserve the linear ordering of the terms.

It is planned to improve the developed system by adjusting the weighting coefficients for assessing the significance of factors regarding the impact on the assessment of the technical condition of the PT. The adjusting here means the solution of the problem of optimizing the weighting coefficients for assessing the significance of factors with regard to the impact on the assessment of the technical condition of the PT.

The task of adjusting a fuzzy classifier model is performed in [32]:

$$RMSE = \sqrt{\frac{1}{M} \cdot \sum_{r=\overline{1,M}} \left[B^r - F\left(X^r, V, C, W\right)\right]^2} \to \min \,.$$

where X^r is the input vector in the r-th row of the fuzzy sample; B^r is the output vector in the r-th row of the fuzzy sample in the form of a fuzzy number; r is the row number in the fuzzy sample used in the process of optimizing the parameters of the fuzzy classifier model, and $r = \overline{1, M}$; where M is the number of data pairs representing the fuzzy sample.

For this, the fmincon function of the Optimization Toolbox package of the MATLAB system is used [32]. That is, a sample is taken from the protocols of diagnostic measurements and tests of the investigated PT of electricity supplier companies with a clear conclusion.

After training a fuzzy classifier model, its performance is analyzed using a test sample. Comparison of the results of the fuzzy classifier model with the actual defect justifies the high efficiency and accuracy of identification of the proposed model.

The training of the fuzzy classifier was carried out on a test sample of 250 PTs examination protocols, which included 100 protocols with no defects and 150 protocols with signs of defects of various types. The results of testing the reliability of the fuzzy classifier on training samples showed that the classifier correctly identified 241 out of 250 technical states of the PTs. The error of classification of the technical state of the PTs RMSE was 1.6 %, which is an acceptable result.

Table 5 presents a fragment of the results of determining the assessment of the technical condition of the PTs according to the results of the DGA on the control sample. The developed fuzzy classifier system showed a fairly high accuracy during testing. The classification error did not exceed 5 %.

Table 5

The results of the assessment of the technical condition of the oil PT according to the results of the DGA on a control sample by a group of experts

No.	Transformer type	Identification of the state of the PT according to the results of the measurement of DGA	
		SOU-N EE 46.501-2006	A classifier based on the theory of fuzzy sets
1	TDCG-400000/330	Thermal defect $T > 700$ °C	Thermal defect $T > 700$ °C. $\mu^H(B)$=1,00
2	TDCG-10000/110	Not specified	Low power discharges. $\mu^M(B)$=0,6
3	TDTG-10000/110	Not specified	High power discharge. $\mu^H(B)$=1,00
4	TDC-400000/330	Not specified	Thermal defect $T > 700$ °C. $\mu^H(B)$=1,00
5	TRDCN-63000/110	Thermal defect T = 300-700 °C	Thermal defect T =150-300 °C. $\mu^L(B)$=0,24; Thermal defect T = 300-700 °C. $\mu^H(B)$=0,76
6	ATDCTG-240000/220	Thermal defect $T > 700$ °C	Thermal defect $T > 700$ °C. $\mu^H(B)$=1,00
7	TDTN-63000/110	Not specified	High power discharge. $\mu^H(B)$=1,00
8	ATDCTN-250000/500	Thermal defect $T > 700$ °C	Thermal defect $T > 700$ °C. $\mu^H(B)$=1,00
9	TDCG-315000/110	High power discharge	Low power discharges. $\mu^L(B)$=0,30; High power discharge. $\mu^M(B)$=0,7
10	TDTN-40000/110	Thermal defect $T > 700$ °C	Thermal defect $T > 700$ °C. $\mu^H(B)$=1,00
11	ODTGA-80000/220	High power discharge	High power discharge. $\mu^H(B)$=1,00

Modelling of a comprehensive fuzzy assessment of the technical condition of the PT under conditions of information uncertainty. During the next test and measurement of the parameters of the technical condition of the PT TDC-400000/330 according to the results of the DGA, the concentrations of gases dissolved in the transformer oil were registered. Exceeding the limit values of concentrations and relative growth rates of dissolved gases by more than 10 % per month recorded in several recent measurements indicates the presence of a progressive defect in the transformer.

To carry out work using the method of expert evaluations based on a fuzzy comprehensive evaluation, an expert group of 5 highly qualified specialists in the operation and repair of PTs was created, each of whom was assigned his/her own number (E1,...,E5). The formation of the group began with the selection of candidates and their further evaluation. Based on a subjective assessment, the expert chose a set of parameters of each functional node of the PT.

At the initial stage, each expert was offered 33 indicators according to their importance to determine the assessment of the technical condition of the PT. The method presented in [34, 35] was used to evaluate experts.

At the next stage, the experts assessed the technical condition of functional nodes and operating conditions with the corresponding determination of the weighting coefficients of indicators of the technical condition of the PT.

According to the developed algorithm for conducting a fuzzy assessment of the technical condition of the PT, the results of determining the set B of the fuzzy comprehensive assessment of the technical condition of the PT are summarized in Table 6-8.

Table 6

The results of determining the technical condition indicators of the oil PT based on the results of a comprehensive examination by a group of competent experts

Expert code	Rank assessments of indicators of the technical condition of the PT X										
	X1	X11	X111	X12	X121	X13	X131	X16	X17	X2	X3
E1	1	2	3	1	2	1	1	1	1	1	2
E2	1	1	2	1	3	1	1	1	2	1	2
E3	1	2	2	1	2	1	1	2	1	1	1
E4	1	3	5	1	3	1	1	1	2	1	2
E5	1	1	3	1	2	1	1	2	1	1	1
Expert code	Rank assessments of indicators of the technical condition of the PT CT X										
	X4	X41	X42	X43	X5	X6	X61	X7	X71	X73	X731
E1	1	1	3	2	3	3	1	1/3	1	2	1
E2	1	1	3	3	1	5	1	1/4	1	2	1
E3	1	1	3	3	2	4	2	1/3	1	2	1
E4	1	1	3	2	3	5	1	1/3	1	2	1
E5	2	1	3	3	2	4	1	1/4	1	1	1
Expert code	Rank assessments of indicators of the technical condition of the PT CT X										
	X7311	X7312	X7313	X7314	X732	X7321	X7322	X7323	X7324	X733	X734
E1	1	1	5	1/2	3	4	1/4	3	2	1	2
E2	1	2	4	1	3	1	1/4	2	2	1	1
E3	1	1	4	1/3	3	3	1/4	2	1	1	2
E4	1	1	5	1	3	3	1/5	3	2	1	1
E5	1	2	3	1/2	2	5	1/3	3	3	1	1

Table 7

The results of determining the weighting coefficients of indicators of the technical condition of the oil PT based on the results of a comprehensive examination by a group of competent experts

Weight coefficients of indicators of factor levels of the technical condition of the PT W										
X1	X11	X111	X12	X121	X13	X131	X16	X17	X2	X3
0,2658	0,6167	0,3790	0,3833	0,3105	0,1337	0,5	0,35	0,1768	0,5	0,3233
X4	X41	X42	X43	X5	X6	X61	X7	X71	X73	X731
0,3039	0,1524	0,4571	0,3905	0,43	0,4285	0,2467	0,0803	0,1171	0,1822	0,1036
X7311	X7312	X7313	X7314	X732	X7321	X7322	X7323	X7324	X733	X734
0,1390	0,1948	0,5770	0,0892	0,2858	0,3391	0,0295	0,2916	0,2227	0,4333	0,5667

Table 8

The results of determining the rank of the technical condition of the oil PT based on the results of a comprehensive examination by a group of competent experts

Indicator name	Indicator designation	Term-sets of a linguistic variable B			
		Very low	Low	Medium	High
		$\mu^{VL}(B)$	$\mu^{L}(B)$	$\mu^{M}(B)$	$\mu^{H}(B)$
Electrical tests	B_{X1}	0,082422	0,405655	0,511922	0
Insulating properties	X11	0,133658	0,39363	0,472712	0
tg δ of insulation	X111	0	0,258	0,742	0
Electrical strength	X12	0	0,425	0,575	0
Leakage current	X121	0	0,725	0,275	0
Insulation resistance level	X13	1	0	0	0
Direct current resistance	X131	0	0,025	0,975	0
DGA	X16	0,195	0,495	0,31	0
Degree of polymerization of paper insulation DP	X17	0	0,4	0,6	0
Condition of the magnetic core	B_{X2}	0	0,825	0,175	0
High-voltage bushings	B_{X3}	0,1	0,65	0,25	0
Condition of transformer oil	B_{X4}	0,030476	0,487505	0,482019	0
Oil breakdown voltage	X41	0,2	0,8	0	0
Oil moisture	X42	0	0,4	0,6	0
tg δ of oil	X43	0	0,468	0,532	0
On-load tap-changer	B_{X5}	0,2	0,8	0	0
Other nodes	B_{X6}	0,167667	0,726833	0,1055	0
Cooling system	B_{X61}	0,2	0,7	0,1	0
Other factors	B_{X7}	0,151045	0,651077	0,197878	0
Overload	B_{X71}	0,2	0,6	0,2	0
Repairs and technical inspection of the PT	B_{X73}	0,086667	0,556667	0,356667	0
Environmental factors	B_{X731}	0,249115	0,600815	0,15007	0
Ambient temperature	X7311	0,15	0,6	0,25	0
Air humidity	X7312	0,1	0,65	0,25	0
Aggressive gases	X7313	0,3	0,6	0,1	0
Wind speed	X7314	0,4	0,5	0,1	0
History of operation	B_{X732}	0,131613	0,61589	0,252497	0
Oil temperature	X7321	0,15	0,7	0,15	0
Extraneous noises	X7322	0,2	0,6	0,2	0
Number of short circuits	X7323	0,1	0,5	0,4	0
The number of relay protection trips	X7324	0,1	0,65	0,25	0
The records of the PTs similar in power and construction	X733	0,2	0,5	0,3	0
Inspection and repair protocols	X734	0	0,6	0,4	0
General evaluation of the technical condition of the PT	Qualitative assessment of B	0,1115	0,4815	0,4069	0
	Quantitative assessment of B	0,279			

According to the results of the calculations for determining the assessment of the technical condition of the PT, the rank is characterized as «Low degree of deterioration of the technical condition of the PT. Continuation of exploitation without restrictions» with a degree of 0.279.

Based on the results of the inspection, a technical report was sent to the power company, which includes an expert opinion on the technical condition of the PT, recommendations on the scope of necessary diagnostic, preventive, and repair measures, protocols based on the control results, as well as maps and diagrams that clearly illustrate the current technical condition.

Conclusions.

1. The task of assessing and ranking the technical condition of power transformers by using a classifier developed on the basis of fuzzy set theory is formulated. Hierarchical structural schemes for determining the levels of factors of the technical condition of individual functional nodes and the power transformer as a whole have been developed.

2. An algorithm and a fuzzy classifier of the results of the assessment of the technical condition of the power transformer have been developed, which are based on multi-parameter aggregation of the states of individual

functional units, which allows to increase the efficiency of the assessment of the technical condition of the power transformer. This, in turn, makes it possible to plan financial costs for the performance of a certain amount of repair work and minimize the risk of failures at the stage of the life cycle of power transformer operation in conditions of uncertainty of diagnostic information.

3. In order to increase the efficiency of recognizing classes of the technical condition of power transformers, the fuzzy classifier developed on the basis of the ANFIS adaptive neural network and the Takagi-Sugeno fuzzy inference system was adapted to real operating conditions by adjusting the model parameters using statistical information about the failures of power transformers and the results of diagnostic procedures of functioning power transformers, which were registered in the energy system of Ukraine. The relative error of identifying the technical state RMSE is 1.6 %, which is no more than 5 % and can serve as an acceptable result of increasing the reliability of determining the rank of the technical state. Avoiding the subjective disagreements of experts regarding the presence of a defect in a power transformer is achieved by harmonizing expert assessments using the Delphi method.

4. A comprehensive fuzzy assessment of the technical condition of the power company's actually functioning power transformers in conditions of information uncertainty was carried out, and a list of recommendations regarding the strategy for their further operation was formed [36].

Conflict of interest. The authors of the article declare that there is no conflict of interest.

REFERENCES

1. Silva J., Sumaili J., Bessa R.J., Seca L., Matos M., Miranda V. The challenges of estimating the impact of distributed energy resources flexibility on the TSO/DSO boundary node operating points. *Computers & Operations Research*, 2018, vol. 96, pp. 294-304. doi: https://doi.org/10.1016/j.cor.2017.06.004.

2. Shiwen Y., Hui H., Chengzhi W., Hao G., Hao F. Review on Risk Assessment of Power System. *Procedia Computer Science*, 2017, vol. 109, pp. 1200-1205. doi: https://doi.org/10.1016/j.procs.2017.05.399.

3. Haes Alhelou H., Hamedani-Golshan M., Njenda T., Siano P. A Survey on Power System Blackout and Cascading Events: Research Motivations and Challenges. *Energies*, 2019, vol. 12, no. 4, art. no. 682. doi: https://doi.org/10.3390/en12040682.

4. Bubenchikov A.A., Nurakhmet Y.Y., Molodikh V.O., Rudenok A.I. Are most characteristic faults in the power equipment. *International Research Journal*, 2016, vol. 5, pp. 56-58. doi: https://doi.org/10.18454/IRJ.2016.47.290.

5. Alekseev BA *Condition monitoring (diagnostics) of large power transformers*. Moscow, Publishing House of the NTs ENAS, 2002. 261 p. (Rus).

6. *CIGRE WGA2.37, Transformer Reliability Survey*, CIGRE Technical Brochure 642, December 2015.

7. Pirotti O.Y., Balenko O.I., Brechko V.O., Huzin M.Y., Gontar J.G. Analysis of construction principles and functionality of high-voltage power transformer condition monitoring systems. *Bulletin of the National Technical University "KhPI". Series: Energy: Reliability and Energy Efficiency*, 2020, no. 1, pp. 61-70. (Ukr). doi: https://doi.org/10.20998/2224-0349.2020.01.09.

8. Shutenko O. V., Baklay, D. N. Analysis of the functionality of expert systems used to diagnose the condition. *Bulletin of the National Technical University "KhPI". Series: Energy: Reliability and Energy Efficiency*, 2011, no. 3, pp. 179-193. (Rus).

9. Shutenko O. Method for Detection of Developing Defects in High-Voltage Power Transformers by Results of the Analysis of Dissolved Oil Gases. *Acta Electrotechnica et Informatica*, 2018, vol. 18, no. 1, pp. 11-18. doi: https://doi.org/10.15546/aeei-2018-0002.

10. Shutenko O., Kulyk O. Comparative Analysis of the Defect Type Recognition Reliability in High-Voltage Power Transformers Using Different Methods of DGA Results Interpretation. *2020 IEEE Problems of Automated Electrodrive. Theory and Practice (PAEP)*, 2020, pp. 1-6. doi: https://doi.org/10.1109/PAEP49887.2020.9240911.

11. Velásquez R.M.A., Lara J.V.M. Principal Components Analysis and Adaptive Decision System Based on Fuzzy Logic for Power Transformer. *Fuzzy Information and Engineering*, 2017, vol. 9, no. 4, pp. 493-514. doi: https://doi.org/10.1016/j.fiae.2017.12.005.

12. Gouda O.E., Saleh S.M., Hamdy EL-Hoshy S. Power Transformer Incipient Faults Diagnosis Based on Dissolved Gas Analysis. *TELKOMNIKA Indonesian Journal of Electrical Engineering*, 2015, vol. 16, no. 3, pp. 409-416. doi: https://doi.org/10.11591/tijee.v16i3.1630.

13. Faiz J., Soleimani M. Dissolved gas analysis evaluation in electric power transformers using conventional methods a review. *IEEE Transactions on Dielectrics and Electrical Insulation*, 2017, vol. 24, no. 2, pp. 1239-1248. doi: https://doi.org/10.1109/TDEI.2017.005959.

14. Castro A.R.G., Miranda V. An interpretation of neural networks as inference engines with application to transformer failure diagnosis. *International Journal of Electrical Power & Energy Systems*, 2005, vol. 27, no. 9–10, pp. 620-626. doi: https://doi.org/10.1016/j.ijepes.2005.08.002.

15. Taha I.B.M., Ghoneim S.S.M., Duaywah A.S.A. Refining DGA methods of IEC Code and Rogers four ratios for transformer fault diagnosis. *2016 IEEE Power and Energy Society General Meeting (PESGM)*, 2016, pp. 1-5. doi: https://doi.org/10.1109/PESGM.2016.7741157.

16. Li Z., Jiao Z., He A. Knowledge-based artificial neural network for power transformer protection. *IET Generation, Transmission & Distribution*, 2020, vol. 14, no. 24, pp. 5782-5791. doi: https://doi.org/10.1049/iet-gtd.2020.0542.

17. Bondarenko V.E., Shutenko O.V. Development of fuzzy neural network for the interpretation of the results of dissolved in oil gases analysis. *Electrical Engineering & Electromechanics*, 2017, no. 2, pp. 49-56. doi: https://doi.org/10.20998/2074-272X.2017.2.08.

18. Yang H., Zhang Z., Yin X. A novel method of decision-making for power transformer maintenance based on failure-probability-analysis. *IEEJ Transactions on Electrical and Electronic Engineering*, 2018, vol. 13, no. 5, pp. 689-695. doi: https://doi.org/10.1002/tee.22618.

19. Faiz J., Soleimani M. Assessment of computational intelligence and conventional dissolved gas analysis methods for transformer fault diagnosis. *IEEE Transactions on Dielectrics and Electrical Insulation*, 2018, vol. 25, no. 5, pp. 1798-1806. doi: https://doi.org/10.1109/TDEI.2018.007191.

20. Wang B., Li Y., Watada J. A New MOPSO to Solve a Multi-Objective Portfolio Selection Model with Fuzzy Value-at-Risk. *Lecture Notes in Computer Science*, 2011, vol. 6883, pp. 217-226. doi: https://doi.org/10.1007/978-3-642-23854-3_23.

21. Tran Q.T., Davies K., Roose L., Wiriyakitikun P., Janjampop J., Riva Sanseverino E., Zizzo G. A Review of Health Assessment Techniques for Distribution Transformers in Smart Distribution Grids. *Applied Sciences*, 2020, vol. 10, no. 22, atr. no. 8115. doi: https://doi.org/10.3390/app10228115.

22. Das S., Guha D. A Centroid-based Ranking Method of Trapezoidal Intuitionistic Fuzzy Numbers and Its Application to MCDM Problems. *Fuzzy Information and Engineering*, 2016, vol. 8, no. 1, pp. 41-74. doi: https://doi.org/10.1016/j.fiae.2016.03.004.

23. Abu-Elanien A.E.B., Salama M.M.A., Ibrahim M. Calculation of a Health Index for Oil-Immersed Transformers Rated Under 69 kV Using Fuzzy Logic. *IEEE Transactions on Power Delivery*, 2012, vol. 27, no. 4, pp. 2029-2036. doi: https://doi.org/10.1109/TPWRD.2012.2205165.

24. Javier Quispe Carita A., Cambraia Leite L., Pedro Pires Medeiros A., Barros R., Sauer L. Bayesian Networks applied to Failure Diagnosis in Power Transformer. *IEEE Latin America Transactions*, 2013, vol. 11, no. 4, pp. 1075-1082. doi: https://doi.org/10.1109/TLA.2013.6601752.

25. Tang W.H., Spurgeon K., Wu Q.H., Richardson Z.J. An evidential reasoning approach to transformer condition assessments. *IEEE Transactions on Power Delivery*, 2004, vol. 19, no. 4, pp. 1696-1703. doi: https://doi.org/10.1109/TPWRD.2003.822542.

26. Ma H., Ekanayake C., Saha T.K. Power transformer fault diagnosis under measurement originated uncertainties. *IEEE Transactions on Dielectrics and Electrical Insulation*, 2012, vol. 19, no. 6, pp. 1982-1990. doi: https://doi.org/10.1109/TDEI.2012.6396956.

27. Miranda V., Castro A.R.G., Lima S. Diagnosing Faults in Power Transformers With Autoassociative Neural Networks and Mean Shift. *IEEE Transactions on Power Delivery*, 2012, vol. 27, no. 3, pp. 1350-1357. doi: https://doi.org/10.1109/TPWRD.2012.2188143.

28. Shirai Y., Noda S., Yamabe K., Hattori K., Baba J., Nishihara T., Nitta T., Kobayashi S., Sato K. Current Limiting Performance of Three-Phase Concentric Transformer Type SFCL at Unbalanced Fault Conditions. *IEEE Transactions on Applied Superconductivity*, 2013, vol. 23, no. 3, pp. 5601905-5601905. doi: https://doi.org/10.1109/TASC.2012.2233533.

29. Li Lixiang. Research and application on Set Pair Analysis for E-government comprehensive evaluation model. *2010 3rd International Conference on Advanced Computer Theory and Engineering (ICACTE)*, 2010, pp. V1-70-V1-74. doi: https://doi.org/10.1109/ICACTE.2010.5579062.

30. Gao H., Sun Y., Li K., Zhou Q., Liu G., Ge H. An insulation condition assessment method of transformer based on set pair analysis and similarity clustering. *2016 IEEE 11th Conference on Industrial Electronics and Applications (ICIEA)*, 2016, pp. 43-48. doi: https://doi.org/10.1109/ICIEA.2016.7603549.

31. Niederberger M., Spranger J. Delphi Technique in Health Sciences: A Map. *Frontiers in Public Health*, 2020, vol. 8, pp. 457-467. doi: https://doi.org/10.3389/fpubh.2020.00457.

32. Bardyk E., Bolotnyi N. Parametric identification of fuzzy model for power transformer based on real operation data. *Eastern-European Journal of Enterprise Technologies*, 2017, vol. 6, no. 8(90), pp. 4-10. doi: https://doi.org/10.15587/1729-4061.2017.118632.

33. Bardyk Ye.I. Modelling and assessment of chances of failure of power systems electrical equipment taking into account the after repair resource restoration level. *Naukovyi Visnyk Natsionalnoho Hirnychoho Universytetu*, 2014, no. 3, pp. 82-90.

34. Bardyk E.I., Bolotnyi N. An Analysis of Uncertainty for Failure Risk Assessment of Power Transformer. *2022 IEEE 8th International Conference on Energy Smart Systems (ESS)*, 2022, pp. 31-35. doi: https://doi.org/10.1109/ESS57819.2022.9969341.

35. Bardyk E.I., Bolotnyi N. Improved Power Transformer Condition Assessment under Uncertainty using Fuzzy Logic. *2022 IEEE 8th International Conference on Energy Smart Systems (ESS)*, 2022, pp. 53-58. doi: https://doi.org/10.1109/ESS57819.2022.9969327.

36. Bardyk E., Bolotnyi N. Development of a mathematical model for cost distribution of maintenance and repair of electrical equipment. *Eastern-European Journal of Enterprise Technologies*, 2018, vol. 6, no. 8(96), pp. 6-16. doi: https://doi.org/10.15587/1729-4061.2018.147622.

Received 28.10.2022
Accepted 24.01.2023
Published 01.09.2023

E.I. Bardyk[1]*, PhD, Assistant Professor,*
N.P. Bolotnyi[1]*, PhD, Senior Lecturer,*
[1] National Technical University of Ukraine
«Igor Sikorsky Kyiv Polytechnic Institute»,
37, Prospect Beresteiskyi, Kyiv-56, 03056, Ukraine,
e-mail: bardik1953@gmail.com;
nickolai2007@ukr.net (Corresponding Author)

How to cite this article:
Bardyk E.I., Bolotnyi N.P. Development of fuzzy classifier for technical condition ranking of power transformer. *Electrical Engineering & Electromechanics*, 2023, no. 5, pp. 3-13. doi: https://doi.org/10.20998/2074-272X.2023.5.01

UDC 621.314 https://doi.org/10.20998/2074-272X.2023.5.02

S. Bechekir, A. Zeghoudi, D. Ould-Abdeslam, M. Brahami, H. Slimani, A. Bendaoud

Development of a boost-inverter converter under electromagnetic compatibility stress equipping a photovoltaic generator

Introduction. *Static converters are among the most widely used equipment in several applications, for example, electric power transmission, motor speed variation, photovoltaic panels, which constitute the electronic components. The design of a power electronics device is done without any real means of predicting electromagnetic disturbances during the product development phase. This case-by-case development process is repeated until a solution is found that best respects all the electromagnetic compatibility constraints. The* ***purpose*** *is the development of a boost-inverter converter under electromagnetic compatibility constraints. The improvements made to the inverter are mainly in the control, the choice of power switches and the electromagnetic compatibility solutions brought to the device. The quality of the wave is improved by acting on the type of control and the choice of switches.* ***Methods.*** *In the first time, we have highlighted a comparison between two most frequently used power components (MOSFET and IGBT) in the inverter and the boost by simulation using ISIS and LT-spice softwares. The sinusoidal voltage with modulation circuit is greatly simplified by the use of the PIC16F876A microcontroller. In a second step, we validate the obtained results with experimental measurements. We start with the boost, then the inverter. In addition, the circuits made are housed in boxes to avoid accidental contact for people. The equipment is designed to isolate the load from the power supply in case of: over voltages, under voltages, high and low battery level and short circuits.* ***Results.*** *All the simulations were performed using the ISIS and LT-spice softwares. The obtained results are validated by experimental measurements performed in the ICEPS Laboratory at the University of Sidi Bel-Abbes in Algeria. The realization of a single-phase inverter with a pulse width modulation control, associated with a boost chopper and the waveforms of the current and voltage across each static converter its opening are presented. The sources of disturbances in power devices are at the origin of the temporal and frequency characteristics of the signals coming from the hot spots of the power switches and the resonances created during the switching of these elements.* References 27, figures 23.

Key words: **inverter, converter, microcontroller, electromagnetic compatibility, MOSFET, IGBT.**

Вступ*. Статичні перетворювачі відносяться до обладнання, що найбільш широко використовується в декількох застосуваннях, наприклад, для передачі електроенергії, зміни швидкості двигуна, у фотогальванічних панелях, які складають електронні компоненти. Проєкт устрою силової електроніки виконується без будь-яких реальних засобів прогнозування електромагнітних перешкод на етапі розробки продукту. Цей процес індивідуальної розробки повторюється доти, доки знайдено рішення, яке найкраще враховує всі обмеження електромагнітної сумісності.* ***Метою*** *є розробка підвищувально-інверторного перетворювача при обмеженнях за електромагнітною сумісністю. Удосконалення, внесені в інвертор, в основному стосуються управління, вибору силових вимикачів та рішень щодо електромагнітної сумісності, реалізованих у пристрої. Якість хвилі покращується за рахунок впливу на тип керування та вибір перемикачів.* ***Методи****. Вперше ми підкреслили порівняння між двома найбільш часто використовуваними силовими компонентами (MOSFET та IGBT) в інверторі та підвищенням шляхом моделювання з використанням програмного забезпечення ISIS та LT-spice. Синусоїдальна напруга зі схемою модуляції значно спрощується за рахунок використання мікроконтролера PIC16F876A. На другому етапі ми підтверджуємо отримані результати експериментальними вимірами. Починаємо з Boost, потім з інвертора. Крім того, виготовлені схеми розміщені в коробках, щоб уникнути випадкового дотику людей. Устаткування призначене для відключення навантаження від джерела живлення у разі: перенапруги, зниженої напруги, високого та низького рівня заряду батареї та короткого замикання.* ***Результати.*** *Усі розрахунки проводилися з використанням програм ISIS та LT-spice. Отримані результати підтверджені експериментальними вимірами, проведеними в лабораторії ICEPS Університету Сіді-Бель-Аббес в Алжирі. Представлено реалізацію однофазного інвертора з керуванням на базі широтно-імпульсної модуляції, пов'язаного з підвищуючим переривником, а також осцилограми струму та напруги на кожному відкритті його статичного перетворювача. Джерелами збурень у силових пристроях є часові та частотні характеристики сигналів, що надходять від гарячих точок силових ключів, та резонанси, що створюються при комутації цих елементів.* Бібл. 27, рис. 23.

Ключові слова: **інвертор, перетворювач, мікроконтролер, електромагнітна сумісність, MOSFET, IGBT.**

Introduction. Electromagnetic compatibility (EMC) is the field of the interactions study that can take place between different devices. It imposes, through standards, constraints in terms of electromagnetic pollution generated by electrical devices (emission standards) and the ability of these same devices to operate in a polluted environment (susceptibility standards) [1].

The integration of EMC issues in the design of converters is quite recent. However, the severity of the standards is such that the measures required to comply with them have a strong impact in terms of cost and size. For example, the traditional interference filtering solution used in inverters and choppers can represent up to a third of their material cost. It is therefore particularly important to take into account the EMC aspect from the product design stage and to look for conversion solutions adapted to this constraint [2].

Inverters are made up of sophisticated, high-performance active and passive components which, however, have a number of limitations that have an impact on the synthesis of control loops [3-8].

Different inverter topologies have been studied with respect to the feasibility of adapting low power ranges at low input voltage to the grid. They can be divided into five categories:

1. Inverter concept with DC voltage link [9, 10]: In order to adapt the photovoltaic (PV) panel voltage to the public grid, DC/DC converters are used. These converters are connected via a DC voltage link to a high-frequency switching converter.
2. Inverter concept with pulsed DC voltage link [11]: these concepts use the same inverters as described in point 1, but their control unit generates the absolute value of a 50 Hz sine wave instead of a DC voltage. This pulsed DC link voltage is inverted by a 50 Hz switching inverter.
3. Inverter concept with AC voltage link [12] DC/DC converters with high frequency transformer, which need a diode rectifier to obtain a DC output voltage; otherwise the output voltage is a bidirectional square wave voltage with the switching frequency as the value. An inverter concept with AC voltage link makes it possible to supply the grid

with this voltage form. Therefore, the inverter needs bidirectional voltage switches.

4. Direct inverter concept: one of these concepts includes a high frequency switched inverter connected to a 50 Hz transformer. The other concept is a transformer less topology that includes 2 bidirectional inverters in parallel series connection [13, 14].

5. Pulsed DC link using a resonant converter: this is the same inverter concept as described in 2. However, instead of a series of parallel DC/DC converters or resonant converters, the converters are connected to the link [15, 16].

Switching is provided by power switches based on semiconductors. There are 2 types of switches with controlled switching (MOSFET, IGBT, thyristor and so on) with rapid variation the voltage or current as function of time, and others with uncontrolled switching (diodes), which generate harmonic distortion and low power factor [17-20].

Goal. In this paper, we characterize by simulation the different switches and we observe their impacts on the chopper and the inverter. We will choose the least disturbing switch. Moreover, we use 2 control techniques of the inverter in order to compare the spectrum of the output voltage. The objective is to be able to evaluate the EMC impact of the inverter during the design phase.

Structure of the proposed PV inverter. Figure 1 shows the general structure of the proposed PV system, which is presented in the form of 2 blocks: the boost part and the inverter part.

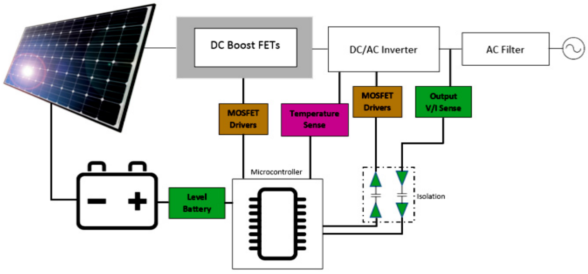

Fig. 1. Functional diagram of the inverter

The block diagram of the PV converter developed with the ISIS software consists inverter control part (Fig. 2), power part (Fig. 3) DC boost (Fig. 4). The inverter features input voltage protection, output voltage and current regulation, and switch overheating protection.

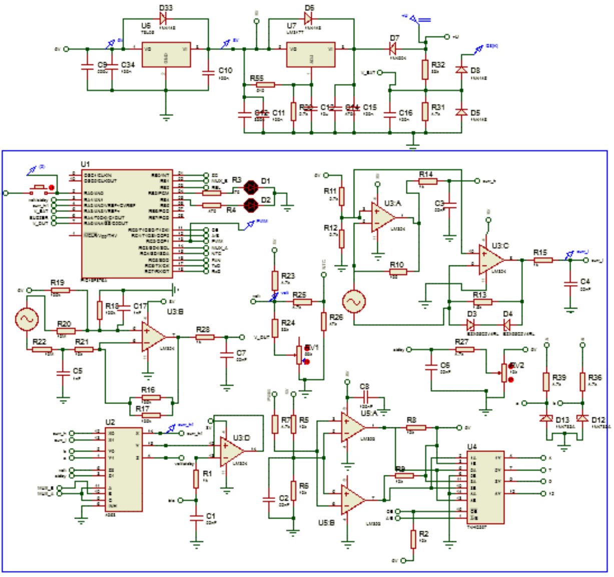

Fig. 2. Inverter control part in the developed PV converter circuit

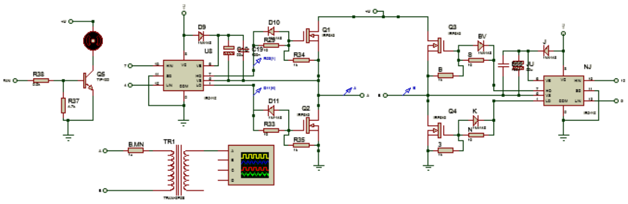

Fig. 3. Power part in the developed PV converter circuit

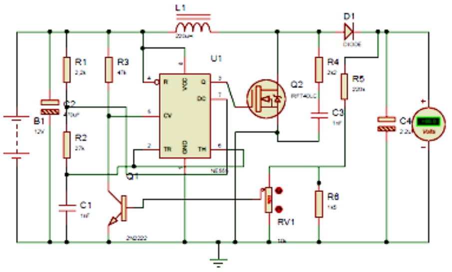

Fig. 4. DC boost in the developed PV converter circuit

Choice of switches. For the design of the boost and the inverter, there are 2 main types of switches used in power electronics: the power MOSFET, which looks very similar to a standard MOSFET, but it is designed to handle relatively large voltages and currents. The other component is the IGBT [14]. The specifications of the 2 switches overlap to a large extent.

Power MOSFETs have a much higher switching frequency capability than IGBTs and can be switched at frequencies above 200 kHz. They don't have the same capability for high-voltage, high-current applications, and tend to be used at voltages below 250 V and powers below 500 W. Both of MOSFETs and IGBTs have power losses due to the rise and fall of the voltage on and off (dV/dt losses). Unlike IGBTs, MOSFETs have a body diode.

As a general rule, IGBTs are the ideal solution for high-voltage, low-frequency applications (> 1000 V and < 20 kHz) and MOSFETs are ideal for low-voltage, high-frequency applications (< 250 V and > 200 kHz) [21]. Between these 2 extremes, there is a large gray area. In this area, other considerations such as power, duty cycle percentage, availability and cost tend to be the deciding factors.

To highlight the effects of the switches, the boost setup was analyzed by simulation with the LT-spice software. Three different IGBT switches (IRGBC20U, IRGBC30U and IRGBC40U) and 3 different MOSFET switches (IPB65R110CFD, R6020ANX and STW11NM80) were used in this work. The 3 selected IGBTs and 3 MOSFETs were tested by simulation during their operation in the boost and inverter, to compare the EMC disturbances generated by the different types of switches. The obtained results for the boost are shown in Fig. 5, 6, and for inverter parts – in Fig. 7, 8.

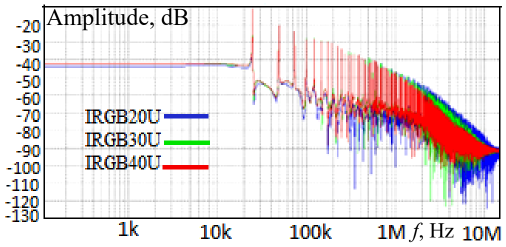

Fig. 5. Comparison of the boost voltages between the 3 IGBTs in frequency domain

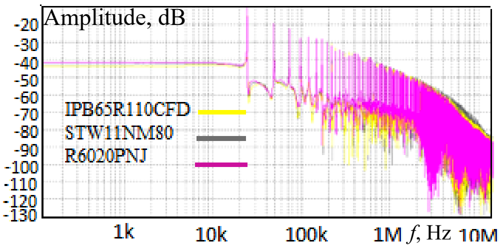

Fig. 6. Comparison of the boost voltages between the 3 MOSFETs in frequency domain

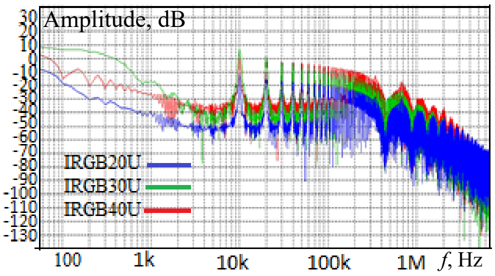

Fig. 7. Comparison of the inverter voltages between the 3 IGBTs in frequency domain

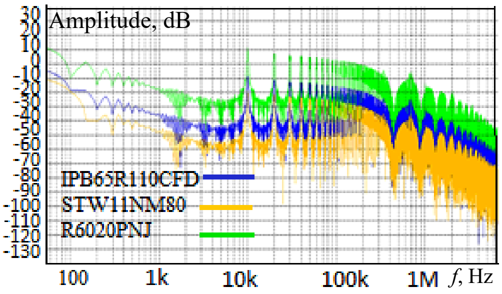

Fig. 8. Comparison of the inverter voltages between the 3 IGBTs in frequency domain

Figures 5, 6 present the spectra of the frequency variation of boost for 3 types of switches IGBT and MOSFET respectively. We can see that the spectrum of the IGBT IRGBC40U tends to decrease regularly and more quickly from 1 MHz. For the 3 MOSFETs the spectrum of R6020ANX tends to decrease compared to the others from 3MHz.

Figures 7, 8 present the spectra of the frequency variation of the inverter for 3 types of switches IGBT and MOSFET respectively. We can see that the spectrum of the IGBT IRGBC20U decreases regularly and in a less important way from 2 MHz. For the 3 MOSFETs the spectrum of STW11NM80 is lower than the others.

An analysis was performed to compare between the IGBT and the MOSFET with the least disturbance determined below. The results of the comparative analysis between the 2 types of switches are shown in Fig. 9, 10 for the boost and inverter respectively.

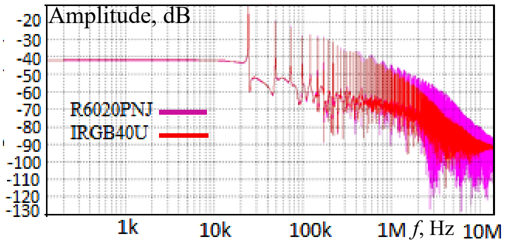

Fig. 9. Comparison of frequency analysis between IGBT and MOSFET in the case of boost

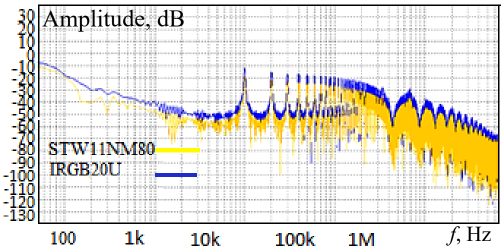

Fig. 10. Comparison of frequency analysis between IGBT and MOSFET in the case of inverter

Figures 9, 10 present a comparison of the frequency analysis between the IGBT and the MOSFET at the boost level and the inverter respectively. We can see that the spectrum of the IGBT IRGBC40U tends to decrease regularly and more quickly from 1 MHz. So, at the boost level the IGBT is the least disturbing. At the inverter level, the MOSFET STW11NM80 is the least disturbing switch with a difference of 8 dB compared to the IGBT.

Choice of the control type. A pulse width modulation (PWM) law results from the comparison of 2 modulators with a carrier. The implementation of this principle is shown in Fig. 11 [22-25].

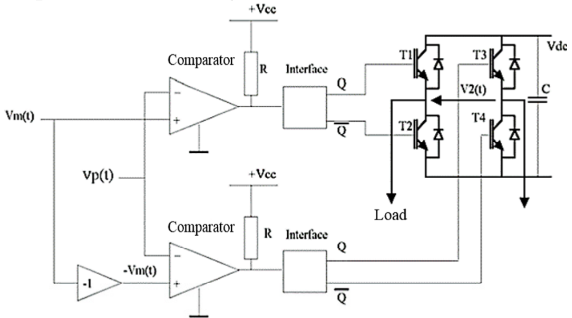

Fig. 11. Principle of generation of a unipolar PWM law with frequency doubling

The second law of PWM results from the comparison of 2 carriers with a modulator. The implementation of this principle is shown in Fig. 12 [13].

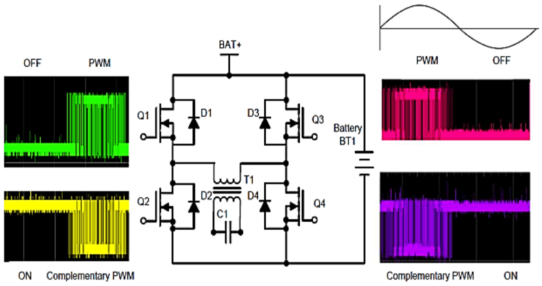

Fig. 12. Principle of PWM generation

For the positive half of the sine wave generation, Q2 is always on, Q1 is always off, Q3 is applied with 20 kHz PWM corresponding to positive half cycle 50 Hz sine wave and Q4 is applied with corresponding complementary (to Q3) PWM. For the negative half 50 Hz sine wave generation, Q4 is always high, Q3 is always off, Q1 is applied with 20 kHz PWM corresponding to positive half cycle 50 Hz sine wave and Q2 is applied with Q1 complementary PWM.

We apply these 2 commands to the inverter. The frequency analysis of the inverter is given in Fig. 13.

Figure 13 presents the frequency analysis of the inverter with the 2 commands. It can be seen that the control spectrum with the two-carrier impulse modulation law is the least disturbing. The spectrum decreases regularly and more rapidly from 20 kHz with a difference of 5 dB compared to that of 2 modulators with one carrier.

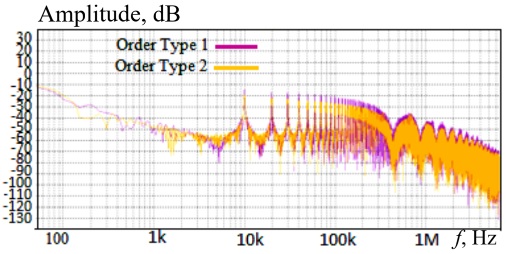

Fig. 13. Frequency analysis of the inverter with the 2 commands

Protection of the inverter. There are many feedback signals at the input of the microcontroller necessary for the proper operation of the inverter, we cite:

- input voltage sensor (battery);
- temperature sensor (R_t, negative temperature coefficient (NTC) –47 K) of electronic switches;
- AC output current and voltage sensor (230 V).

The current, which is the main source of heating, considerably reduces the efficiency of the inverter and can damage it. For this reason, a forced cooling is implemented to obtain a better efficiency. The control block diagram used is shown in Fig. 14.

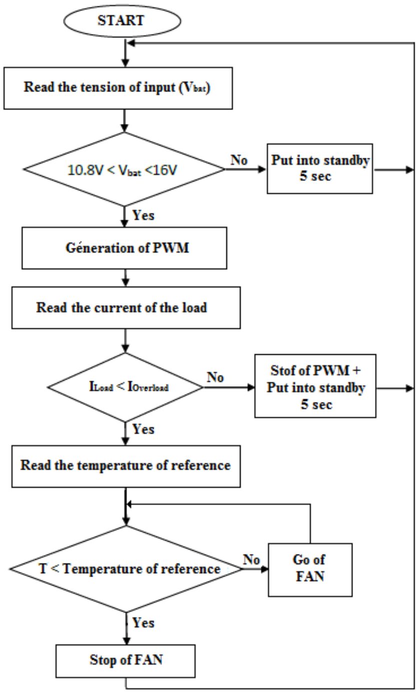

Fig. 14. Algorithm of control

MOSFET driver. It is advantageous to use N-channel MOSFETs as switches because they have a low on-resistance [26]. This results in low power losses. However, to do this, the drain of the high-side switch is connected to a 340 V DC supply converted to 240 V AC. The voltage at the gate terminal must be 10 V higher than that at the drain terminal [10, 14]. Therefore, to drive the H-bridge MOSFETs, a bootstrap capacitor designed specifically to drive a half-bridge is used. After considering different integrated circuit options, our choice was the IR2113. It is supplied by a 600 V rating, 2 A drive current, and a 10-20 V drive voltage. The activation and deactivation times are respectively 120 ns and 94 ns [23, 24].

We implemented the control routine in a programmable interface controllers (PIC) PIC16F876A microcontroller and configured the analog/digital conversion module integrated in this circuit, to automatically start the conversion.

The MOSFET driver is actuated by a signal delivered by the microcontroller. It is supplied by the battery. The driver is able to control the switches. The upper high side switch requires an additional voltage of 10 V. This is achieved by an external bootstrap capacitor charged by a diode from the 12 V supply when the device is off [27].

Obtained results. No-load test. Figures 15, 16 show the generation of the PWM. Figure 17 shows the output voltage signals from the inverter.

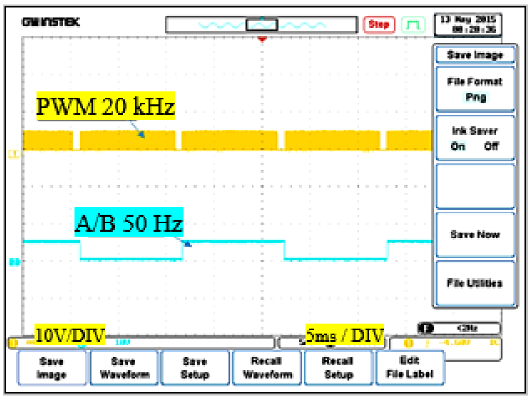

Fig. 15. PWM and A/B peak output

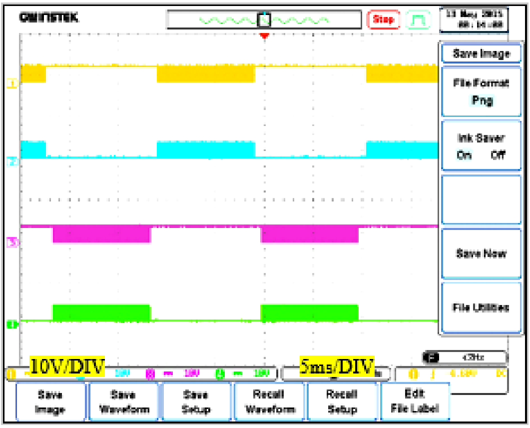

Fig. 16. 74HC257 output signal

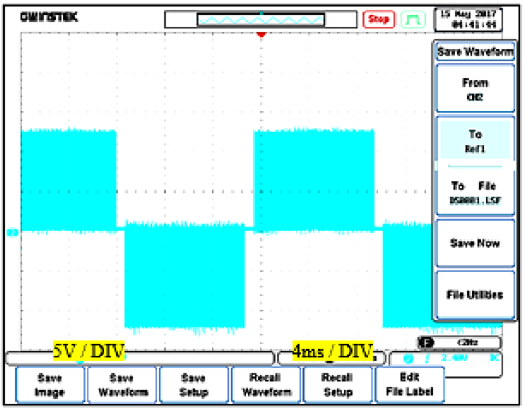

Fig. 17. Voltage at the output of the inverter (no-load test)

At a high temperature of the switches (MOSFET), the NTC heats up and gives the order to the PIN FAN to generate the signal to start the fan. At a very high temperature the microcontroller blocks the generation of the PWM. This stops the inverter. The fan runs until the switches cool down.

Boost mounting tests. Boost chopper is supplied by a 12 V voltage. The output voltage is adjustable by a potentiometer up to 340 V. Figure 18 shows the curve of the boost voltage.

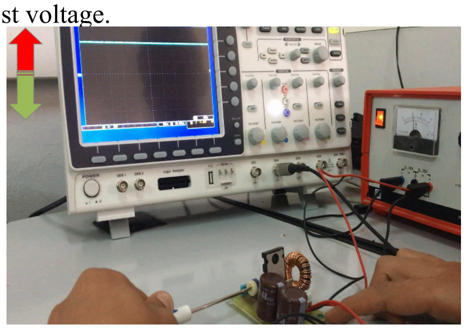

Fig. 18. Boost test at 12 V input voltage

The inverter test is shown in Fig. 19. Figure 20 shows the voltage delivered by the inverter.

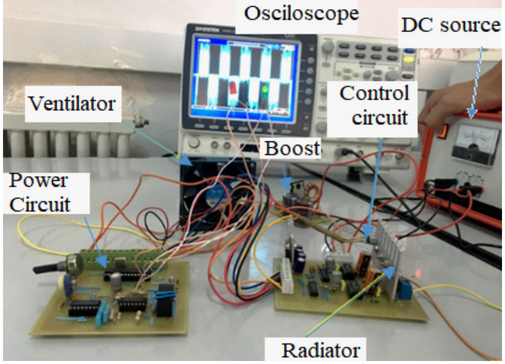

Fig. 19. Complete circuit (power part and inverter and boost control)

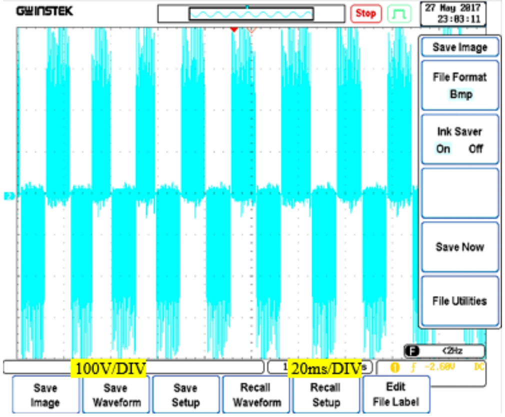

Fig. 20. Voltage at the output of the inverter (boost mounting tests)

Load test. The inverter feeds an inductive load consisting of a 100 Ω resistor and a 1 H coil (internal resistance of about 12 Ω). The voltage and current are shown in Fig. 21, 22.

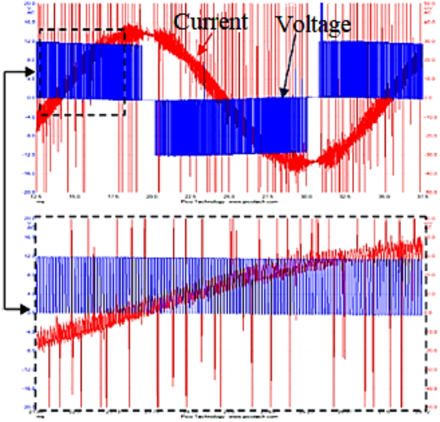

Fig. 21. Inverter output current and voltage signal

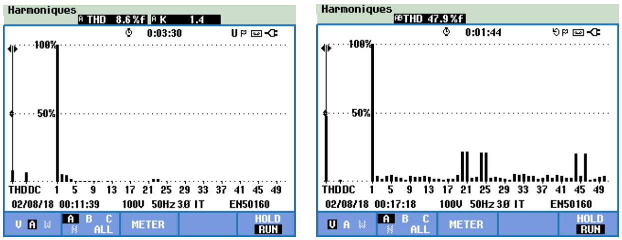

Fig. 22. Voltage/current spectrum for a modulation index $m = 0.9$

Enclosure and circuit location. The inverter boards are placed in suitable positions. A shielding technique is used. The separation of the power and control circuits is made by grids as shown in Fig. 23 in order to reduce the coupling between the circuits by electromagnetic radiation.

The LEDs L1, L2, signal the status of the inverter:

- L1 (green) → power on;
- L2 (red) → battery low (< 10 V);
- L1 (green) flashing → standby mode;
- L2 (red) flashing → high temperature of power transistors.

Voltage spikes. When the driver is used to drive an inverter with inductive load impedance, it can develop voltage spikes due to reverse voltages. These spikes can damage the MOSFETs and their control circuits. For this reason, integrated diode transistors have been used to conduct strongly as soon as the voltage increases excessively, thus protecting the MOSFETs.

Capacitive load. Since this inverter is a quasi-sine wave type, high frequency harmonics have been completely eliminated. When used with a capacitive load, the impedance is exactly as calculated. The problem with other types of inverters is that, due to high frequency harmonics, the capacitive impedance decreases, which implies an increase of the current beyond the nominal value.

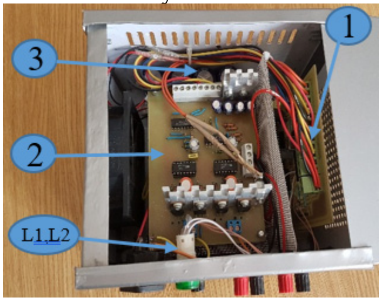

Fig. 23. Internal views of the realized inverter box:

1 – control circuit;
2 – power circuit;
3 – boost

Conclusions.

1. The rise and fall time as well as the switching frequency are very important factors to characterize a useful signal in the field of power electronics. We have highlighted a comparison between two most frequently used power components (MOSFET and IGBT) in the inverter and the boost.

2. We have studied the behavior of semiconductor components in the frequency domain generating a high harmonic number located in the high frequency region. The spectra have different amplitudes due to the difference between the intrinsic characteristics of each switch. Therefore, each power switch has its own electromagnetic compatibility signature.

3. The sinusoidal voltage with modulation circuit is greatly simplified by using the PIC16F876A microcontroller. In addition to the high programming flexibility, the switching pulse design can be changed without further hardware modification. The inverter is shielded against radiated electromagnetic interference. This increases its efficiency.

4. The realization of a single-phase inverter with PWM control, associated with a boost chopper; and this circuit are

housed in enclosures to avoid accidental contact with people. The equipment is designed to isolate the load from the power supply in case of: overvoltages, undervoltages, high and low battery levels and short circuits.

Acknowledgement. The authors of this article would like to thank the General Directorate of Scientific Research and Technological Development (DGRSDT) in Algeria for their technical support and the specific research budget allocated to this program.

Conflict of interest. The authors declare that they have no conflicts of interest.

REFERENCES

1. Kimmel W.D., Gerke D. *Electromagnetic compatibility in medical equipment: a guide for designers and installers*. CRC Press, 2019. 302 p.

2. Lee F.C., Daan Van Wyk J., Boroyevich D., Barbosa P. An integrated approach to power electronics systems. *Proceedings of the Power Conversion Conference-Osaka 2002 (Cat. No.02TH8579)*, Osaka, Japan, 2002, vol. 1, pp. 7-12. doi: https://doi.org/10.1109/PCC.2002.998503.

3. Song Y., Wang B. Survey on Reliability of Power Electronic Systems. *IEEE Transactions on Power Electronics*, 2013, vol. 28, no. 1, pp. 591-604. doi: https://doi.org/10.1109/TPEL.2012.2192503.

4. Rahim N.A., Selvaraj J. Multistring Five-Level Inverter With Novel PWM Control Scheme for PV Application. *IEEE Transactions on Industrial Electronics*, 2010, vol. 57, no. 6, pp. 2111-2123. doi: https://doi.org/10.1109/TIE.2009.2034683.

5. Barrade P. *Power Electronics: Converters Methodology and Elementals*. Lausanne Polytechnic and University Presses Romandes, First Edition, 2006.

6. Buttay C. *Contribution to Conception by Simulation in Power Electronics. Application to the inverter Low Voltage*. National Institute of Applied Sciences, Lyon, November 2004.

7. Hasan M., Maqsood J., Baig M.Q., Bukhari S.M.A.S., Ahmed S. Design and Implementation of Single Phase Pure Sine Wave Inverter Using Multivibrator IC. *2015 17th UKSim-AMSS International Conference on Modelling and Simulation (UKSim)*, 2015, pp. 451-455. doi: https://doi.org/10.1109/UKSim.2015.58.

8. Haeberlin H. Evolution of Inverters for Grid connected PV-Systems from 1989 to 2000. *17th European Photovoltaic Solar Energy Conference*, Munich, Germany, 2001, 5 p.

9. Koutroulis E., Chatzakis J., Kalaitzakis K., Voulgaris N.C. A bidirectional, sinusoidal, high-frequency inverter design. *IEE Proceedings - Electric Power Applications*, 2001, vol. 148, no. 4, pp. 315-321. doi: https://doi.org/10.1049/ip-epa:20010351.

10. Thukral R., Kumar G., Gupta A., Kumar Verma N., Asthana S. Microcontroller Based Solar Power Inverter. *International Journal of Electrical Engineering & Technology (IJEET)*, 2016, vol. 7, no. 5, pp. 70-78.

11. Bechekir S., Bousmaha I.S., Brahami M., Abdeslam D.O. Realization of an inverter with PWM command for photovoltaic system. *2017 5th International Conference on Electrical Engineering - Boumerdes (ICEE-B)*, 2017, pp. 1-6. doi: https://doi.org/10.1109/ICEE-B.2017.8192003.

12. Aganza T.A., Pérez R.J., Beristain J.J.A. Inversor trifásico SPWM para el control de velocidad de un motor de inducción implementado en el microcontrolador PIC18F2431. *Revista de Ingeniería Eléctrica, Electrónica y Computación*, 2006, vol. 2, no. 1, pp. 7-16. (Esp).

13. Dixit S., Tripathi A., Chola V., Verma A. *800VA Pure Sine Wave Inverter's Reference Design*. Texas Instruments. Application Report SLAA602A, June 2013 (Revised August 2017).

14. Mamun A.A., Elahi M.F., Quamruzzaman M., Tomal M.U. Design and implementation of single phase inverter. *International Journal of Science and Research (IJSR)*, 2013, vol. 2. no. 2, pp. 163-167.

15. Chuang Y.-C., Ke Y.-L., Chuang H.-S., Chen J.-T. A Novel Loaded-Resonant Converter for the Application of DC-to-DC Energy Conversions. *IEEE Transactions on Industry Applications*, 2012, vol. 48, no. 2, pp. 742-749. doi: https://doi.org/10.1109/TIA.2011.2180875.

16. Tseng S.-Y., Wang H.-Y. A Photovoltaic Power System Using a High Step-up Converter for DC Load Applications. *Energies*, 2013, vol. 6, no. 2, pp. 1068-1100. doi: https://doi.org/10.3390/en6021068.

17. Zeghoudi A., Slimani H., Bendaoud A., Benazza B., Bechekir S., Miloudi H. Measurement and analysis of common and differential modes conducted emissions generated by an AC/DC converter. *Electrical Engineering & Electromechanics*, 2022, no. 4, pp. 63-67. doi: https://doi.org/10.20998/2074-272X.2022.4.09.

18. Muttaqi K.M. Electromagnetic Interference Generated from Fast Switching Power Electronic Devices. *International Journal of Innovations in Energy Systems and Power*, 2008, vol. 3, no. 1, pp. 19-26.

19. Slimani H., Zeghoudi A., Bendaoud A., Reguig A., Benazza B., Benhadda N. Experimental Measurement of Conducted Emissions Generated by Static Converters in Common and Differential Modes. *European Journal of Electrical Engineering*, 2021, vol. 23, no. 3, pp. 273-279. doi: https://doi.org/10.18280/ejee.230312.

20. Zeghoudi A., Bendaoud A., Slimani H., Benazza B., Bennouna D. Determination of electromagnetic disturbances in a buck chopper. *Australian Journal of Electrical and Electronics Engineering*, 2022, vol. 19, no. 2, pp. 149-157. doi: https://doi.org/10.1080/1448837X.2021.2023073.

21. Bechekir S., Brahami M., Ould Abdeslam D., Nemmich S., Nassour K., Tilmatine A. Development of a Low-Cost Ozone Generator Supply-Optimization Using Response Surface Modeling. *International Journal of Plasma Environmental Science and Technology*, 2019, vol. 13, no. 1, pp. 7-13. doi: https://doi.org/10.34343/ijpest.2019.13.01.007.

22. Leung H.F., Crowley I.F. *PWM Techniques: A Pure Sine Wave Inverter*. Worcester Polytechnic Institute, Major Qualifying Project, 2011.

23. *IR2110/IR2113. Data Sheet No. PD60147-L*. IOR International Rectifier, 2003.

24. *HV Floating MOS-Gate Driver ICs. Application Note AN-978*. IOR International Rectifier, 2003.

25. Baazouzi K., Bensalah A.D., Drid S., Chrifi-Alaoui L. Passivity voltage based control of the boost power converter used in photovoltaic system. *Electrical Engineering & Electromechanics*, 2022, no. 2, pp. 11-17. doi: https://doi.org/10.20998/2074-272X.2022.2.02.

26. Janardhan G., Surendra Babu N.N.V., Srinivas G.N. Single phase transformerless inverter for grid connected photovoltaic system with reduced leakage current. *Electrical Engineering & Electromechanics*, 2022, no. 5, pp. 36-40. doi: https://doi.org/10.20998/2074-272X.2022.5.06.

27. Parimalasundar E., Kumar N.M.G., Geetha P., Suresh K. Performance investigation of modular multilevel inverter topologies for photovoltaic applications with minimal switches. *Electrical Engineering & Electromechanics*, 2022, no. 6, pp. 28-34. doi: https://doi.org/10.20998/2074-272X.2022.6.05.

Received 04.09.2022
Accepted 18.01.2023
Published 01.09.2023

Seyf Eddine Bechekir[1]*, Lecturer,*
Abdelhakim Zeghoudi[2]*, PhD,*
Djaffar Ould-Abdeslam[3]*, Professor,*
Mostefa Brahami[1]*, Professor,*
Helima Slimani[4]*, Lecturer,*
Abdelber Bendaoud[2]*, Professor,*
[1] Intelligent Control and Electrical Power Systems (ICEPS),
Djillali Liabes University of Sidi Bel-Abbes, Algeria,
e-mail: seyfeddine.electrotechnique@gmail.com;
mbrahami@yahoo.com
[2] Laboratory of Applications of Plasma, Electrostatics and Electromagnetic Compatibility (APELEC),
Djillali Liabes University of Sidi Bel-Abbes, Algeria,
e-mail: hakooumzeghoudi@gmail.com;
babdelber@gmail.com (Corresponding Author)
[3] MIPS Laboratory,
Universite de Haute Alsace, Mulhouse, France,
e-mail: djaffar.ould-abdeslam@uha.fr
[4] University of Tiaret, Algeria,
e-mail: halima.slimani@univ-tiaret.dz

How to cite this article:
Bechekir S., Zeghoudi A., Ould-Abdeslam D., Brahami M., Slimani H., Bendaoud A. Development of a boost-inverter converter under electromagnetic compatibility stress equipping a photovoltaic generator. *Electrical Engineering & Electromechanics*, 2023, no. 5, pp. 14-19. doi: https://doi.org/10.20998/2074-272X.2023.5.02

UDC 621.314 https://doi.org/10.20998/2074-272X.2023.5.03

K. Djazia, M. Sarra

Improving the quality of energy using an active power filter with zero direct power command control related to a photovoltaic system connected to a network

Introduction. *This article's subject is a dual function energy system that improves the quality of the electric energy with help of an active power filter and uses a new technique of command named ZDPC (Zero Direct Power Command) on one hand, and on the other hand it injects the photovoltaic (PV) renewable energy to the electrical networks in the presence of non-linear charges. The* ***novelty*** *of the work consists in the subtraction of disturbances resulting from the non-linear charges is provided by an active power filter based on a new ZDPC method.* ***Methods.*** *This strategy combines a classic PI controller for DC bus voltage regulation with a smart method to maximum power point tracking (MPPT) of power based on fuzzy logic.* ***Purpose.*** *The elimination of the undesirable harmonics from the source currents makes the current almost sinusoidal with a harmonic distortion rate close to 1 %. The injection of PV energy into the electrical grid is provided by a PV panel in series with a chopper through a two-state inverter.* ***Results.*** *This system is simulated using MATLAB/Simulink software. The results prove the robustness and feasibility of the ZDPC control which simultaneously guarantees the compensation of harmonic currents, the correction of the power factor and the injection of the solar power into the electrical grid.* References 16, table 3, figures 20.

Key words: **active power filter, zero direct power command, photovoltaic array, fuzzy logic maximum power point tracking controller.**

Вступ*. Предметом цієї статті є енергосистема подвійного призначення, що покращує якість електроенергії за допомогою фільтра активної потужності та використовує, з одного боку, нову техніку управління під назвою ZDPC (Zero Direct Power Command), а з іншого боку, фотоелектричні відновлювані джерела енергії в електричні мережі за наявності нелінійних зарядів.* ***Новизна*** *роботи полягає в тому, що віднімання перешкод, що виникають від нелінійних зарядів, забезпечується фільтром активної потужності на основі нового методу ZDPC.* ***Методи****. Ця стратегія поєднує класичний ПІ-регулятор для регулювання напруги на шині постійного струму з інтелектуальним методом відстеження точки максимальної потужності (MPPT) на основі нечіткої логіки.* ***Мета****. Усунення небажаних гармонік із струмів джерела робить струм майже синусоїдальним з коефіцієнтом гармонічних спотворень, близьким до 1 %. Подача фотоелектричної енергії в електричну мережу забезпечується фотоелектричною панеллю, послідовно з'єднаної з переривником через інвертор з двома станами.* ***Результати****. Ця система моделюється за допомогою програмного забезпечення MATLAB/Simulink. Результати доводять надійність та здійсненність управління ZDPC, яке одночасно гарантує компенсацію гармонічних струмів, корекцію коефіцієнта потужності та подачу сонячної енергії в електричну мережу.* Бібл. 16, табл. 3, рис. 20.

Ключові слова: **фільтр активної потужності, команда прямої нульової потужності, фотогальванічна батарея, контролер відстеження точки максимальної потужності з нечіткою логікою.**

Introduction. Harmonic pollution affects all domestic and industrial networks. No modern environment can escape this pollution from equipment, such as computers, servers, air conditioners, variable speed drives, etc... all these charges are called «non-linear». These equipments generate harmonic currents, which cause reactive power consumption and a degradation of the power factor of the electrical network [1, 2]. The quality of the current and the voltage of the network are seriously degraded [3-5].

The combination of a shunt active power filter (SAPF) and a photovoltaic (PV) source, which is not only a renewable source, but also clean, unlimited and at a very low level of risk; the purpose of the photovoltaic generator (GPV) is to inject the active power into the electrical grid. This combination gives us a clean source of energy and efficiently enhances the quality of energy [2, 6]. SAPF injects a current that opposes the harmonic current emitted by the non-linear charge to mitigate the effect of the harmonic currents and the reactive power. Thus, the current delivery by the power source remains sinusoidal.

Researchers have suggested new methods, such as direct power control (DPC) introduced by Noguchi [8], which was developed from direct torque control (DTC) intended for electric machine drives [3, 7].

DPC was essentially to remove both the pulse width modulation modulator and the internal regulation loops by through replacing them by a predetermined switching table [3]. This switching table, based on the correction of the active and reactive power and on the sector indicating the position angle of the source voltage vector, is intended to select the switching states of the converter [8].

The standard DPC requires a zero reactive power reference, whereas the active power reference is calculated from the DC bus controller output [3, 9]. This article proposes a DPC technique, which as opposed to the standard implementation, requires zero active and reactive power disturbance references to reject all disturbances due to harmonics. This is why we call it zero DPC or ZDPC (Zero Direct Power Command).

Given that the solar insulation is variable, several maximum power point tracking (MPPT) algorithms, such as incremental conductance, perturb and observe, and escalation have been proposed [2]. The tracking algorithm based on fuzzy logic, is considered to be on of the most efficient algorithms [10]. In our research the maximum power point (MMP) is reached smartly regardless of the degree of variation of the solar radiation due to the fuzzy MPPT technique [2].

Description of the studied model. The model studied in Fig. 1 consists of a solar GPV connected to the DC bus of a three-phase voltage inverter through a chopper circuit, coupled in parallel to the network through an inductance. This electrical network supplies a non-linear receiver constituted by a rectifier PD3 whose charge is a resistor in series with an inductance. The synoptic of Fig. 1 illustrates this configuration with ideal flow of powers. The analysis of these flows is therefore examined in various regimes imposed by the fluctuation of the level of irradiation during the day and the alternation with the night part where only the functions of the active filter are activated. During the day, depending on the levels of irradiation and the consumption of the charge, it is possible to distinguish several regimes (P_{pv} is the PV active power; P_{charge} is the load active power):

- $P_{pv} < P_{charge}$, the network power remains positive;
- $P_{pv} > P_{charge}$, the network receives an active power, it becomes a receiver.

These power flow management phases are coupled with the active filter functionalities. The voltage inverter control algorithm is adapted to simultaneously ensure the compensation of the harmonic pollution and of the reactive power, and also the injection of the power supplied by the PV panels into the electrical network.

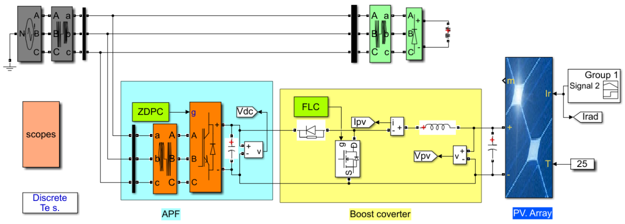

Fig. 1. Synoptic studied model

The proposed ZDPC principle. Figure 2 shows the structure of the proposed ZDPC. In this control strategy, the active and reactive power disturbance references are set to zero. We note that in this structure the phase locked loop is not necessary [3]. The high selective filter (HSF) is used to separate the fundamental and harmonic components of the line currents and voltages in order to perform power compensation [3].

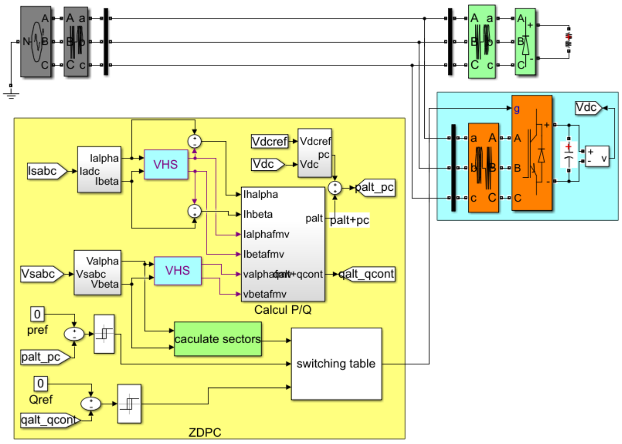

Fig. 2. Synoptic of the ZDPC

Choice of sector. The signal d_{ps}, d_{pq} and the position (θ) of the source voltage vector (1), from a digital word, allowing access to the address of the switch table to select the appropriate voltage vector:

$$\theta = \operatorname{arctg}\left(v_\alpha / v_\beta\right). \quad (1)$$

For this reason, the stationary coordinates are divided into 12 sectors (Fig. 3), and the sectors can be expressed numerically as [3]:

$$(n-2)\frac{\pi}{6} \le \theta_n \le (n-1)\frac{\pi}{6} \qquad n = 1,2,....,12\,. \quad (2)$$

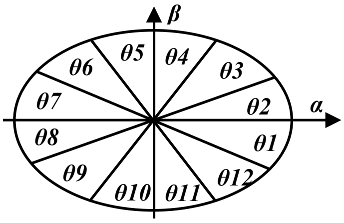

Fig. 3. (α, β) sectors

The signals d_{ps}, d_{qs} and the sector n of the source voltage are the inputs of the commutation table (Table 1), whereas the output represents the switching state of the inverter (S_a, S_b, S_c). By using this switching table, the optimal state of the inverter can be uniquely selected during each time interval depending on the combination of the table entries. The selection of the optimal switching state is made so that power errors can be reduced in the hysteresis bands.

Table 1

ZDPC switching table

d_p	d_q	θ_1	θ_2	θ_3	θ_4	θ_5	θ_6	θ_7	θ_8	θ_9	θ_{10}	θ_{11}	θ_{12}
1	0	v_6	v_7	v_1	v_0	v_2	v_7	v_3	v_0	v_4	v_7	v_5	v_0
	1	v_7	v_7	v_0	v_0	v_7	v_7	v_0	v_0	v_7	v_7	v_0	v_0
0	0	v_6	v_1	v_1	v_2	v_2	v_3	v_3	v_4	v_4	v_5	v_5	v_6
	1	v_1	v_2	v_2	v_3	v_3	v_4	v_4	v_5	v_5	v_6	v_6	v_1
v_1(100), v_2(110), v_3(010), v_4(011), v_5(001), v_6(101), v_0(000), v_7(111)													

Hysteresis controller. The main idea of the ZDPC method is to keep the instantaneous active and reactive power within a desired band. This command is based on two comparators with hysteresis whose input is the error between the reference values and the estimate of the active and reactive power [11], given respectively as:

$$\Delta p_s = p_{ref} - p_s\,; \quad (3)$$

$$\Delta q_s = q_{ref} - q_s\,. \quad (4)$$

where p_{ref}, q_{ref} are the instantaneous active and reactive power reference; p_s, q_s are the instantaneous active and reactive power source.

The hysteresis comparators are used to provide 2 logic outputs d_{ps} and d_{qs}. State «1» corresponds to an increase in the controlled variable (ps and qs), whereas «0» corresponds to a decrease according to (5), (6)

$$\text{if } \Delta p_s \ge h_p \;\; d_{ps} = 1; \text{ if } \Delta p_s \le -h_p \;\; d_{ps} = 0\,; \quad (5)$$

$$\text{if } \Delta q_s \ge h_q \;\; d_{qs} = 1; \text{ if } \Delta q_s \le -h_q \;\; d_{qs} = 0\,. \quad (6)$$

PI controller. The ZDPC method must ensure DC bus regulation to maintain the capacitor voltage, around the voltage reference (V_{dcref}). For this purpose, a PI controller is usually used [11]. Figure 4 shows the controller simulation model.

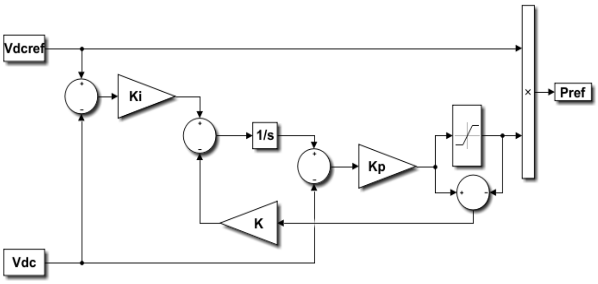

Fig. 4. Simulation model of PI controller

The values of proportional and integral gain (K_p and K_i) are given respectively as:

$$K_i = \frac{\omega_n}{2\zeta};\tag{7}$$

$$K_p = 2C\zeta\omega_n,\tag{8}$$

where ξ is the damping coefficient ($\xi = 0.707$); ω_n is the nominal pulse.

High selective filter. To improve the performance of the classical instantaneous power method, HSF has been implemented, to extract the fundamental component of current and voltage in the synchronous frame without any phase shift or amplitude errors. The functional diagram of HSF is shown in Fig. 5. The transfer function can be expressed as [11]:

$$H(s) = \frac{\hat{x}_{\alpha\beta}(s)}{x_{\alpha\beta}} = k\frac{(s+k) + j\omega_c}{(s+k)^2 + \omega_c^2}.\tag{9}$$

From (9), we obtain:

$$\hat{x}_\alpha(s) = \frac{k}{s}\left[x_\alpha(s) - \hat{x}_\alpha(s)\right] - \frac{\omega_c}{s}\hat{x}_\beta(s);\tag{10}$$

$$\hat{x}_\beta(s) = \frac{k}{s}\left[x_\beta(s) - \hat{x}_\beta(s)\right] - \frac{\omega_c}{s}\hat{x}_\alpha(s),\tag{11}$$

where $\hat{x}_{\beta\alpha}$, $x_{\alpha\beta}$ are respectively the output and the input of the filter, which can be $V_{\alpha\beta}$ or $I_{\alpha\beta}$. We note that for the pulsation $\omega = \omega_c$, the phase shift introduced by the filter is zero and the gain is equal to 1. We also observe that the decrease in the value K improves the selectivity of the HSF.

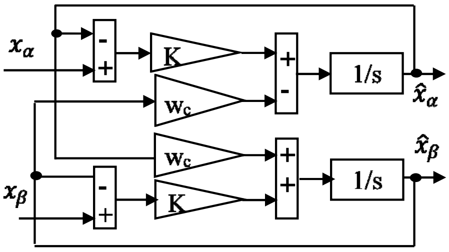

Fig. 5. Block diagram of HSF

From the HSF output, the AC component of the instantaneous active power can be obtained by (12) [3]:

$$\tilde{p} = \hat{v}_\alpha i_{h\alpha} + \hat{v}_\beta i_{h\beta},\tag{12}$$

where $i_{h\alpha}$, $i_{h\beta}$ given respectively by (13) and (14):

$$i_{h\alpha} = \left(i_{\alpha d} - \hat{i}_{\alpha d}\right) + \left(i_{\alpha inv} - \hat{i}_{\alpha inv}\right);\tag{13}$$

$$i_{h\beta} = \left(i_{\beta d} - \hat{i}_{\beta d}\right) + \left(i_{\beta inv} - \hat{i}_{\beta inv}\right),\tag{14}$$

where $i_{h\alpha}$, $i_{h\beta}$ are the harmonic components in the axis $\alpha\beta$, whereas the instantaneous reactive power is defined as:

$$q_s = \hat{v}_\beta \hat{i}_\alpha - \hat{v}_\alpha \hat{i}_\beta.\tag{15}$$

Figure 6 shows the calculation of the disturbing powers $\tilde{p}$ and q_s.

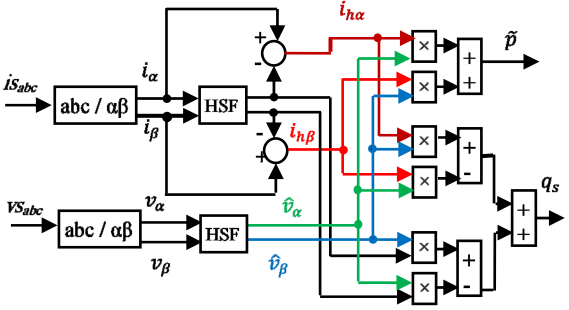

Fig. 6. Computation of v_α, v_β, $\tilde{p}$ and q_s with HSF

Generation of control vector. By adding the alternating component ($\tilde{p}$) of the instantaneous active power which is linked to both current and voltage disturbances, to the active power p_c necessary for the regulation of the DC bus, we obtain the disturbing active power p_p:

$$p_p = \tilde{p} + p_c.\tag{16}$$

To compensate for active and reactive power disturbances (p_p and q_s), a comparison with their zero reference is carried out. The results of the comparison pass through a hysteresis block which generates output hysteresis controller (dps and dqs). Depending on the sector selected (θ_n) and (d_{ps}, d_{qs}), the appropriate command vector (S_a, S_b, S_c) is produced using the commutation table (Table 1).

Advanced MPPT controller. The extraction of the maximum power is an essential step in the field of energy conversion of the PV solar system. To increase the efficiency of the GPV, a MPPT search algorithm is applied to the DC/DC converter (local MPPT) in the case of a double power stage. In this article the algorithm based on fuzzy logic is studied. This method is used here for finding the MPPT of a PV module under all weather conditions, because it does not require knowledge of mathematical models of linear and nonlinear controlled systems [12, 13].

Generally, the fuzzy logic controller comprises 3 essential blocks: fuzzification, inference rules and defuzzification [14]. The fuzzification stage is the process of transforming numerical input variables into linguistic variables using membership functions. The inference rules step gives the output of the fuzzy logic controller by the Mamdani method with a max-min technique depending on the set belonging to the rule base. The defuzzification step converts the linguistic variables into a net value, which determines the duty cycle increment ΔD. The fuzzy MPPT values are represented by an E error and an ΔE error variation as inputs. The error and its variation are given by the following equations [13]:

$$E(K) = \frac{P(K) - P(K-1)}{V(K) - V(K-1)};\tag{17}$$

$$\Delta E = E(K) - E(K-1),\tag{18}$$

where $P(k)$, $P(k–1)$, $V(k)$ and $V(k–1)$ are the power and the voltage of the GPV for 2 sampling times k and $(k–1)$ respectively. The proposed algorithm has 2 input variables: $\Delta P(k)$ and $\Delta V(k)$. The output variable is the duty cycle $\Delta D(k)$. The variables $\Delta P(k)$ and $\Delta V(k)$ are given as [13, 14]:

$$\Delta P(K) = P(K) - P(K-1);\tag{19}$$

$$\Delta V(K) = V(K) - V(K-1).\tag{20}$$

where $\Delta P(k)$ and $\Delta V(k)$ are zero at the MPP of the GPV.

The basic rules of the fuzzy MPPT algorithm are based on the 2 input variables ($\Delta P(k)$, $\Delta V(k)$) and on the output variable (ΔD). $\Delta P(k)$ and $\Delta V(k)$ are divided into 5 denoted fuzzy sets: Negative Big (*NB*), Negative Small (*NS*), Zero (*Z*), Positive Small (*PS*) and Positive Big (*PB*). The rule base relates the fuzzy inputs to the fuzzy output by the master syntax rule: «If: *A* is... and *B* is..., Then: *C* is...». According to Table 2 [13, 14], that groups together all the possible connections between the inputs and the output of the developed controller, the following example can be given: If: ΔP is *PB* and ΔV is *NB* Then: ΔD is *NS*. The choice of the shape of the membership functions of the proposed controller is of a triangular type. The center of gravity method for the defuzzification step is used to calculate the incremental duty cycle ΔD [10, 14-16]:

$$\Delta D = \frac{\sum_{j=0}^{n} \omega_j \Delta D_j}{\sum_{j=0}^{n} \omega_j}, \tag{21}$$

where *n* is the maximum number of effective rules, *w* is the weighting factor, ΔD_j is the value corresponding to ΔD.

Table 2

Decision table

$\Delta P \backslash \Delta V$	NB	NS	Z	PS	PB
NB	PS	PB	PB	NB	NS
NS	Z	PS	PS	NS	Z
Z	Z	Z	Z	Z	Z
PS	Z	NS	NS	PS	Z
PB	NS	NB	NB	PB	PS

Finally, the duty cycle is obtained by adding this change to the previous value of the control duty cycle as mentioned in (22) [10, 14, 15]:

$$D(K+1) = D(K) + \Delta D(K). \tag{22}$$

Discussion of the simulation results. Various simulations were performed using MATLAB/Simulink model (Fig. 1) to evaluate the proposed approaches. The parameters used for these tests are represented in Table 3.

Table 3

Simulation parameters

Parameters	Value	Parameters	Value
V_s, V	80	C_{dc}, μF	2200
f_s, Hz	50	*L*, mH	10
f switching (DC/AC APF converter), kHz	20	*R*, Ω	40
f switching (DC/DC boost converter), kHz	5	C_{pv}, μF	20
L_s, mH	0.1	L_{pv}, mH	3
R_s, Ω	0.1	V_{cref}, V	235
L_l, mH	0.566	*N*	2
R_l, Ω	0.01	ω_b, rad/s	0,01
L_f, mH	2.5	ω_h, rad/s	100
R_f, Ω	0.01		

SAPF simulation results controlled by the ZDPC, equipped with conventional PI and fuzzy MPPT, operating under a balanced network, are shown in the following figures. Figure 7 shows all simulated cases together during time (0 – 1.4) s. Figure 8 zooms the signals in the time interval (0 – 0.2) s, where the filter is not activated and in the absence of irradiation (absence of the injection of energy to the network), in this case we notice the load current and the source current are identical as shown in Fig. 9.

The charge current and the source current are superimposed and have a total harmonic distortion (THD) 27.87 % (Fig. 10).

Figure 11 shows the signals after the activation of the APF and in the absence of irradiation during the time interval (0.2-0.5) s.

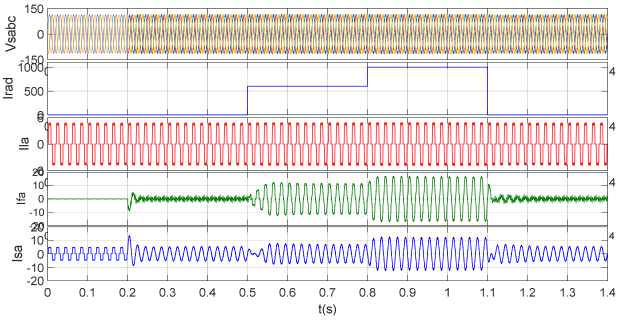

Fig. 7. Simulation signals in the different cases

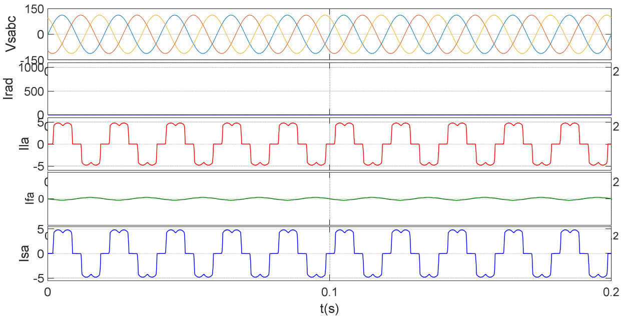

Fig. 8. Simulation signals in the absence of the filter and of irradiation

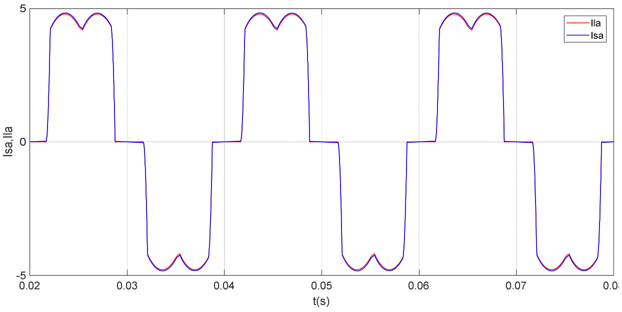

Fig. 9. The charge current and the source current are superimposed

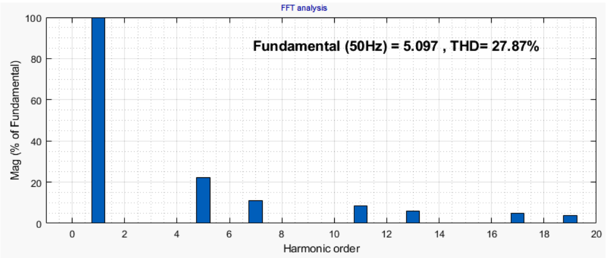

Fig. 10. THD of source current

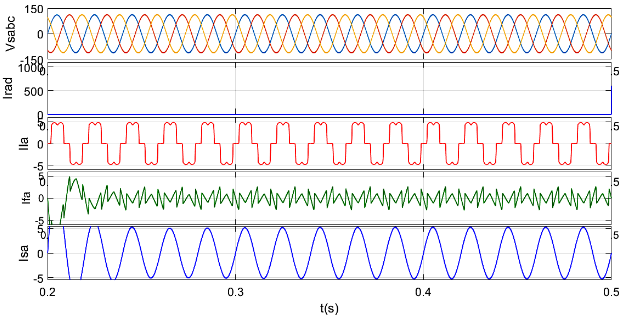

Fig. 11. Simulation signals after the activation of the APF and in absence of irradiation

It is noted in Fig. 12 that the source current resumes its sinusoidal form in phase with the charge current and with a THD = 1.14 % as shown in Fig. 13.

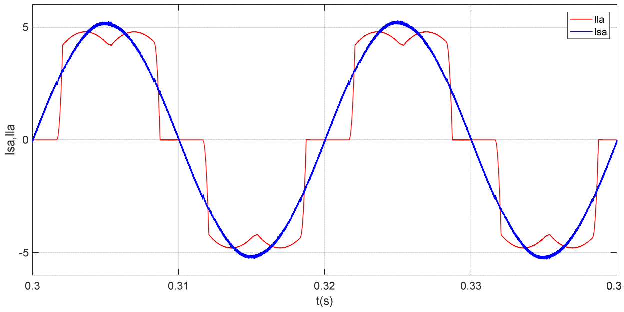

Fig. 12. The source current is in phase with the charge current

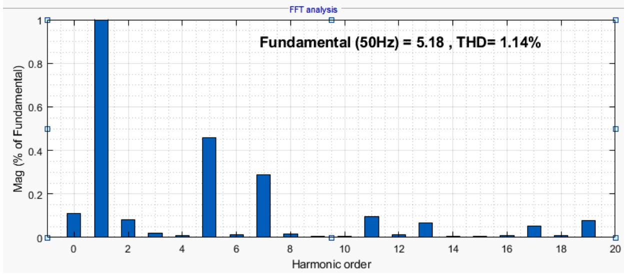

Fig. 13. THD of source current

Figure 14 represents the simulation signals during the activation of the APF and the injection of energy to the network, this is in the time interval (0.5-0.8) s, in this case the source current changes direction towards the network and becomes in phase opposition with the charge current, which means that the network becomes a receiver. The source current has a THD = 1.09 %

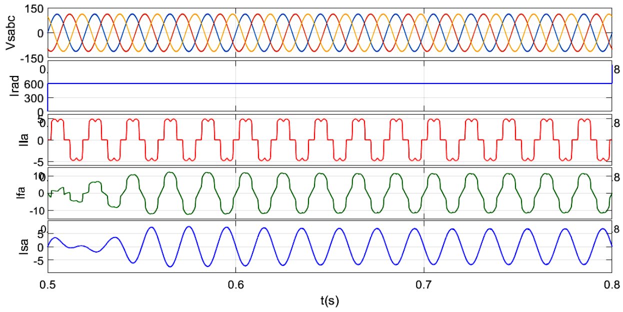

Fig. 14. Simulation signals after the activation of the APF and with the presence of irradiation

Figure 15 shows the transition from the network to a receiver. The source current retains its sinusoidal shape with a THD = 1.09 % (Fig. 16).

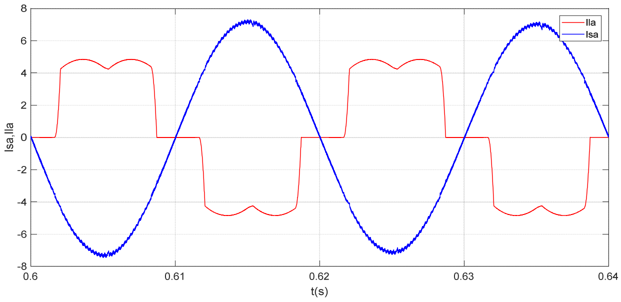

Fig. 15. The source current is in phase opposition with the charge current

Figures 17, 18 show the crossing of the source current with that of the irradiation while keeping the sinusoidal form of the source current with a THD = 1.29 % (Fig. 19).

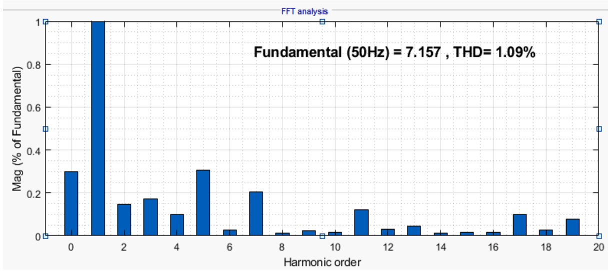

Fig. 16. THD of source current

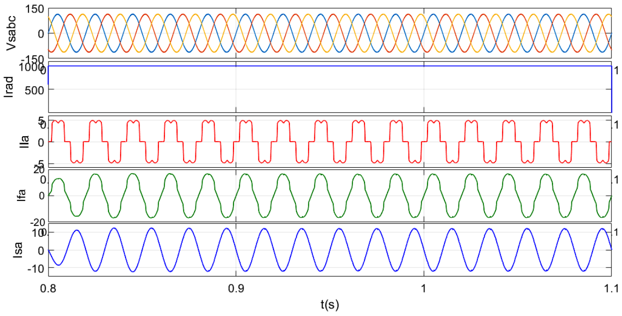

Fig. 17. Simulation during the increase in irradiation

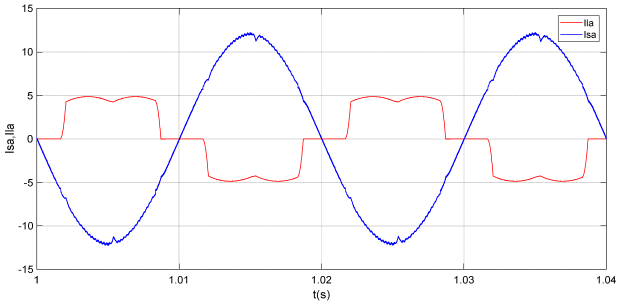

Fig. 18. Crossing of the source current with the irradiation current

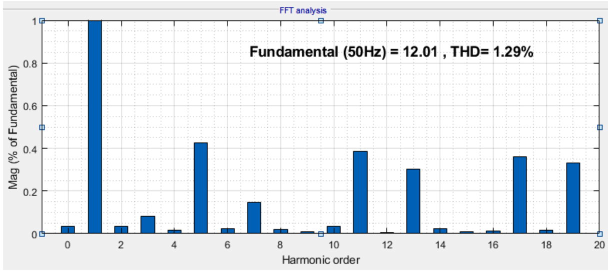

Fig. 19. THD of source current

Figure 20 shows the evolution of the energy of the network in the various cases discussed:

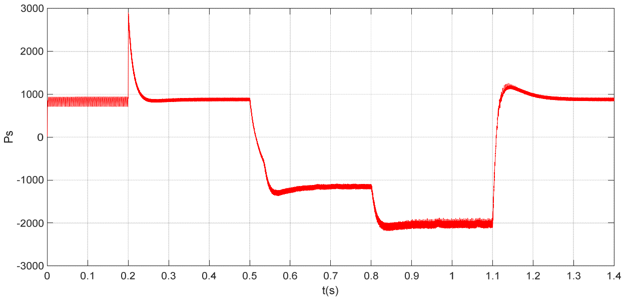

Fig. 20. Energy of the network in the different discussed cases

- Case 1: before activation of the APF and in the absence of irradiation.

- Case 2: after activation of the APF and in the absence of irradiation.
- Case 3: after the activation of the APF and in the presence of the irradiation.
- Case 4: during the change of irradiation.

Conclusions. In this article, a new direct power control technique called zero direct power control, suitable for harmonic and reactive power compensation, has been proposed; high selectivity filters are used to separate harmonic currents and voltages causing a degradation in the quality of power on the network. The shunt active power filter based on the zero direct power control command assembled with a photovoltaic system driven by a fuzzy command to inject energy into the network and improve the quality of energy. The simulation shows the good performance of the proposed approach.

Conflict of interest. The authors declare that they have no conflicts of interest.

REFERENCES

1. Mohamed Rida B., Rahli M., Slami S., Hassaine L. PSO based Direct Power Control for a Multifunctional Grid Connected Photovoltaic System. *International Journal of Power Electronics and Drive Systems (IJPEDS)*, 2018, vol. 9, no. 2, pp. 610-621. doi: https://doi.org/10.11591/ijpeds.v9.i2.pp610-621.

2. Boudechiche G., Sarra M., Aissa O., Gaubert J.-P. An investigation of solar active power filter based on direct power control for voltage quality and energy transfer in grid-tied photovoltaic system under unbalanced and distorted conditions. *Journal of Engineering Research*, 2021, vol. 9, no. 3B, pp. 168-188. doi: https://doi.org/10.36909/jer.v9i3B.9061.

3. Djazia K., Krim F., Chaoui A., Sarra M. Active Power Filtering Using the ZDPC Method under Unbalanced and Distorted Grid Voltage Conditions. *Energies*, 2015, vol. 8, no. 3, pp. 1584-1605. doi: https://doi.org/10.3390/en8031584.

4. Baazouzi K., Bensalah A.D., Drid S., Chrifi-Alaoui L. Passivity voltage based control of the boost power converter used in photovoltaic system. *Electrical Engineering & Electromechanics*, 2022, no. 2, pp. 11-17. doi: https://doi.org/10.20998/2074-272X.2022.2.02.

5. Sai Thrinath B.V., Prabhu S., Meghya Nayak B. Power quality improvement by using photovoltaic based shunt active harmonic filter with Z-source inverter converter. *Electrical Engineering & Electromechanics*, 2022, no. 6, pp. 35-41. doi: https://doi.org/10.20998/2074-272X.2022.6.06.

6. Tareen W.U., Mekhilef S., Seyedmahmoudian M., Horan B. Active power filter (APF) for mitigation of power quality issues in grid integration of wind and photovoltaic energy conversion system. *Renewable and Sustainable Energy Reviews*, 2017, vol. 70, pp. 635-655. doi: https://doi.org/10.1016/j.rser.2016.11.091.

7. Aissa O., Moulahoum S., Colak I., Kabache N., Babes B. Improved Performance and Power Quality of Direct Torque Control of Asynchronous Motor by Using Intelligent Controllers. *Electric Power Components and Systems*, 2016, vol. 44, no. 4, pp. 343-358. doi: https://doi.org/10.1080/15325008.2015.1117541.

8. Noguchi T., Tomiki H., Kondo S., Takahashi I. Direct power control of PWM converter without power-source voltage sensors. *IEEE Transactions on Industry Applications*, 1998, vol. 34, no. 3, pp. 473-479. doi: https://doi.org/10.1109/28.673716.

9. Mesbahi N., Ouari A., Ould Abdeslam D., Djamah T., Omeiri A. Direct power control of shunt active filter using high selectivity filter (HSF) under distorted or unbalanced conditions. *Electric Power Systems Research*, 2014, vol. 108, pp. 113-123. doi: https://doi.org/10.1016/j.epsr.2013.11.006.

10. Benlahbib B., Bouarroudj N., Mekhilef S., Abdelkrim T., Lakhdari A., Bouchafaa F. A Fuzzy Logic Controller Based on Maximum Power Point Tracking Algorithm for Partially Shaded PV Array-Experimental Validation. *Elektronika Ir Elektrotechnika*, 2018, vol. 24, no. 4, pp. 38-44. doi: https://doi.org/10.5755/j01.eie.24.4.21476.

11. Sujith M., Padma S. Optimization of harmonics with active power filter based on ADALINE neural network. *Microprocessors and Microsystems*, 2020, vol. 73, art. no. 102976. doi: https://doi.org/10.1016/j.micpro.2019.102976.

12. Chavan U.M., Thorat A.R., Bhosale S.S. Shunt Active Filter for Harmonic Compensation Using Fuzzy Logic Technique. *2018 International Conference on Current Trends towards Converging Technologies (ICCTCT)*, 2018, pp. 1-6. doi: https://doi.org/10.1109/ICCTCT.2018.8550962.

13. Boukezata B., Chaoui A., Gaubert J.-P., Hachemi M. An improved fuzzy logic control MPPT based P&O method to solve fast irradiation change problem. *Journal of Renewable and Sustainable Energy*, 2016, vol. 8, no. 4, art. no. 043505. doi: https://doi.org/10.1063/1.4960409.

14. Manoharan P., Subramaniam U., Babu T.S., Padmanaban S., Holm-Nielsen J.B., Mitolo M., Ravichandran S. Improved Perturb and Observation Maximum Power Point Tracking Technique for Solar Photovoltaic Power Generation Systems. *IEEE Systems Journal*, 2021, vol. 15, no. 2, pp. 3024-3035. doi: https://doi.org/10.1109/JSYST.2020.3003255.

15. Kumar A., Kumar P. Power Quality Improvement for Grid-connected PV System Based on Distribution Static Compensator with Fuzzy Logic Controller and UVT/ADALINE-based Least Mean Square Controller. *Journal of Modern Power Systems and Clean Energy*, 2021, vol. 9, no. 6, pp. 1289-1299. doi: https://doi.org/10.35833/MPCE.2021.000285.

16. Verma N., Jain A., Nishi, Ahuja H., Singh G. Maximum Power Point Tracking MPPT Methods for Photovoltaic Modules. *2021 International Conference on Advance Computing and Innovative Technologies in Engineering (ICACITE)*, 2021, pp. 223-227. doi: https://doi.org/10.1109/ICACITE51222.2021.9404571.

Received 17.12.2022
Accepted 10.02.2023
Published 01.09.2023

Kamel Djazia[1]*, Doctor of Electronics,*
Mustapha Sarra[2]*, Doctor of Electronics, Professor,*
[1] Department of Electronics, University of Msila, Algeria,
e-mail: kamel.djazia@univ-msila.dz (Corresponding Author);
[2] Department of Electronics,
University of Bordj Bou Arreridj, Algeria,
e-mail: mustapha.sarra@univ-bba.dz

How to cite this article:
Djazia K., Sarra M. Improving the quality of energy using an active power filter with zero direct power command control related to a photovoltaic system connected to a network. *Electrical Engineering & Electromechanics*, 2023, no. 5, pp. 20-25. doi: https://doi.org/10.20998/2074-272X.2023.5.03

UDC 621.314 https://doi.org/10.20998/2074-272X.2023.5.04

H. Slimani, A. Zeghoudi, A. Bendaoud, S. Bechekir

Experimental evaluation of conducted disturbances induced during high frequency switching of active components

Introduction. *Power electronics devices are among the most widely used equipment in all fields. The increasing performance of these devices makes their electromagnetic interference factor very important. On the other hand, electromagnetic compatibility research is more and more interested in studies on the sources of electromagnetic disturbances, their propagation paths and the methods of reducing these electromagnetic disturbances. The* ***purpose*** *is to study the behavior of the various active power components at high frequency as well as the evaluation of their electromagnetic noise by using simulation and experimental measurement.* ***Methods.*** *In first time, the simulation was realized with the Lt-spice software which presents many advantages in its use and we validate in the second time the results obtained with experimental measurements. We start by study of the behavior of the diode, then the behavior of MOSFET transistor and finally the study of the behavior of the IGBT transistor.* ***Results.*** *All the simulations were performed using the Lt-spice software and the results obtained are validated by experimental measurements performed in the APELEC Laboratory at the University of Sidi Bel-Abbes in Algeria. The waveforms of the current and voltage across each component during its opening are presented. The results of the simulations are compared and validated with the realized measurements in order to better present the influence of the fast switching of semiconductors on the electrical quantities, which causes electromagnetic disturbances in the interconnected electrical system.* References 19, figures 19.

Key words: **electromagnetic compatibility, electromagnetic disturbances, high frequency switching of active components, experimental measurement.**

Вступ. *Пристрої силової електроніки знаходяться серед обладнання, що найбільш широко використовується у всіх областях. Підвищення продуктивності цих пристроїв робить фактор їх електромагнітних перешкод дуже важливим. З іншого боку, при дослідженні електромагнітної сумісності дедалі більше цікавляться джерелами електромагнітних перешкод, шляхів їх поширення та методами зменшення цих електромагнітних перешкод.* ***Мета*** *роботи полягає в тому, щоб вивчити поведінку різних компонентів активної потужності на високих частотах, а також оцінити їхній електромагнітний шум за допомогою моделювання та експериментальних вимірювань.* ***Методи***. *Уперше моделювання було реалізовано за допомогою програмного забезпечення Lt-spice, яке дає багато переваг при його використанні, і вдруге ми підтверджуємо результати, отримані за допомогою експериментальних вимірів. Ми починаємо з вивчення поведінки діода, потім поведінки MOSFET транзистора і, нарешті, вивчення поведінки IGBT транзистора.* ***Результати***. *Усі моделювання були виконані з використанням програмного забезпечення Lt-spice, а отримані результати підтверджені експериментальними вимірами, проведеними в лабораторії APELEC в Університеті Сіді-Бель-Аббес в Алжирі. Представлені осцилограми струму та напруги на кожному компоненті під час його відкриття. Результати моделювання порівнюються та підтверджуються реалізованими вимірами, щоб краще уявити вплив швидкого перемикання напівпровідників на електричні величини, що викликає електромагнітні перешкоди у взаємозалежній електричній системі.* Бібл. 19, рис. 19.

Ключові слова: **електромагнітна сумісність, електромагнітні перешкоди, високочастотне перемикання активних елементів, експериментальне вимірювання.**

Introduction. With the development of new sources of renewable energy, more static converters are connected to the power network. They supply of the network with electric power produced by generators; but in contrast to conventional systems, they usually introduce low frequency and high frequency (HF) switching harmonics [1-5]. These power converters use fast switching power semiconductor switches, such as MOSFET and IGBT transistors as the preferred switching devices because of their various properties, such as higher efficiency, smaller size, and lower overall cost, low losses associated with switching device. However, the fast switching speed of new converter technologies has the potential to cause electromagnetic disturbances and high dV/dt [6-9].

The orders of magnitude of the commutation gradients can vary between 100 to 1000 A/μs for the dI/dt and from 5 to 50 kV/μs for the dV/dt. Moreover, very high commutation frequency is another factor that increases the electromagnetic pollution, as it can vary from 100 Hz to 1 MHz. This condition presents a serious problem in regards to the Electromagnetic Compatibility (EMC) [10, 11].

The brutal variations of the voltage associated with parasitic elements between the system and the ground plane induce disturbing currents in the ground circuits.

To show the role that a switch can play in the plan [voltage $V(t)$ across the switch – current $i(t)$ through the switch] Fig. 1 shows:

- the feature branches where the switch can operate;
- the branch changes it can provide [10-12].

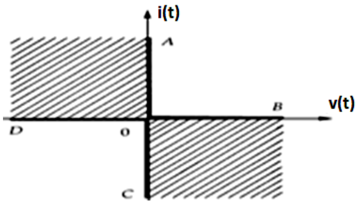

Fig. 1. Quadrants of the plan [$V(t)$, $i(t)$] [13]

The first step of evaluating the conducted emission interferences consist of determining the sources of theses interferences. For this reason in this work we have made an evaluation of the conducted disturbances emitted during the HF switching of active components such as the diode, MOSFET, IGBT the study is made by simulation using the Lt-spice software and the experimental measurements by measurement benches carried out at the APELEC Laboratory at the University of Sidi Bel-Abbes.

The **purpose** of this article is to study the behavior of the various active power components at high frequency as well as the evaluation of their electromagnetic noise by using simulation and experimental measurement.

Study of the real behavior of active components. In this part of the work, the dynamic characteristics and the equivalent models of the real behavior for each component studied were presented. These components are: the diode, the MOSFET and IGBT transistors. Our objective is to know the influence of these elements on some electrical quantities at well determined switching times and the disturbances generated in the interconnected electrical system [13-15]. To do this, we will first study the switching cells (Fig. 2), which allows us to describe the operation of power electronics structures and also gives us a more detailed analysis of switching phenomena [16, 17]. The benches used have been developed for many years for the characterization of power components in switching whose operation has been largely validated by experimental measurements. In order to represent the switching characteristics of the components mentioned above, we have carried out simulations under Lt-spice software, where the results are validated by experimental measurements.

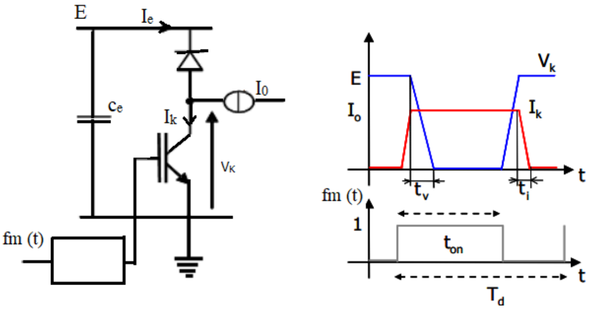

Fig. 2. Switching cell and associated waveforms

The main switch is controlled by a periodic modulation function $f_m(t)$ with T_d as the binary period value and $\alpha = t_{on}/T_d$ as a variable duty cycle. This duty cycle modulates the power transfer. For simplification, the external switching cell values (E, I_0) are considered constant while internal ones (I_e, V_k) are taken as variables modulated by the $f_m(t)$ function [3, 4]

Study of the behavior of the diode. For the identification of the dynamic characteristics of the diodes, we used the circuit presented in Fig. 3.

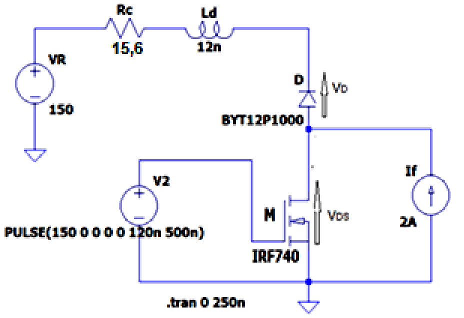

Fig. 3. Simulation diagram for the switching of a power diode, (M: IRF740, D: BYT12P1000)

This circuit presents the switching of a MOSFET/diode cell, in which the switch is a MOSFET transistor of type IRF740 connected with a diode of type BYT12P1000. For this simulation, we used directly the component models provided by the Lt-spice library. The inductance L_d represents the global parasitic inductances in the circuit [18, 19]. It is a series inductance introduced in particular by the legs of the diode in order to simulate the dynamic behavior of the diode. Figure 4 represents a photo of the measurement bench to compare the simulation results of the voltage across the diode and the current through it with the measurements.

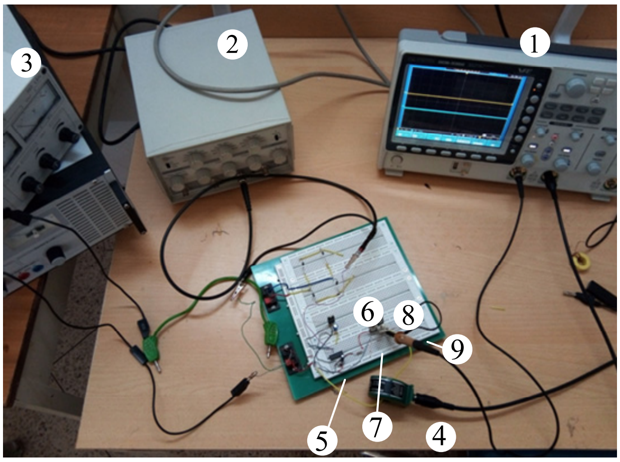

Fig. 4. Photo of the measurement bench [14]:
1 – oscilloscope; 2 – pulse generator; 3 – stabilized power supply; 4 – amperometric probe; 5 – driver IR2110;
6 – 12 V regulator; 7 – MOSFET IRF740;
8 – diode BYT12P1000; 9 – resistance 15,6 Ω

Figure 5 shows the descriptive diagram of the main elements used to switch a BYT12P1000 type power diode.

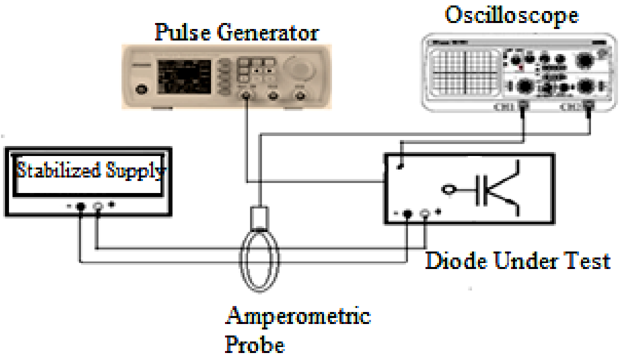

Fig. 5. Descriptive diagram of the test bench
for switching a power diode

According to the diagram (Fig. 3), we can establish the equation that describes the mesh of this circuit [15]:

$$V_R = L_d \frac{\mathrm{d}i(t)}{\mathrm{d}t} - V_D + V_{DS}\,, \tag{1}$$

where V_R is the source voltage; V_D is the voltage at the diode terminal; V_{DS} is the voltage between drain source of MOSFET; L_d represents the global parasitic inductances in the circuit.

If the MOSFET does not intervene during switching ($V_{DS} << V_R$), then we have:

$$V_R = L_d \frac{\mathrm{d}i(t)}{\mathrm{d}t} - V_D\,. \tag{2}$$

The simulation diagram has the following characteristics: the current I_f generates by the current source $I_f = 2$ A, $V_R = 150$ V, $R_c = 15.6$ Ω; $L_D = 12$ nH.

Results and analysis. Figures 6, 8 show the temporal variations in the blocking of the diode tested according to the simulation and measurements, they also illustrate the phenomenon of reverse overlap on the current and voltage when the diode is blocked. For the frequency response, the results are shown in Fig. 7, 9, where we note respectively a decrease of amplitude from 20 dB to –80 dB for the current and a decrease of amplitude from 30 dB to –70 dB for the voltage.

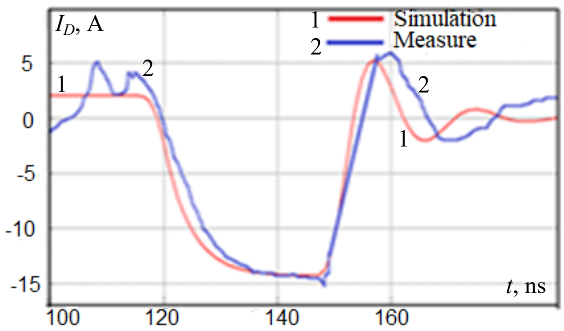

Fig. 6. Temporal characteristics of the I_D current at the opening of the diode

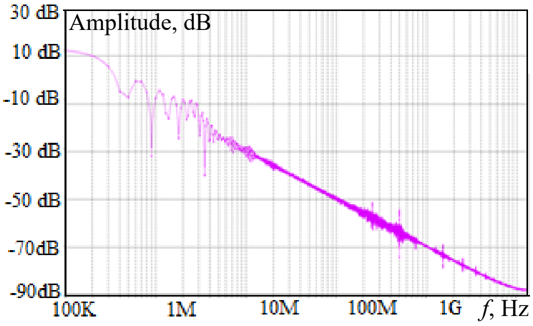

Fig. 7. Frequency characteristics of the I_D current at the opening of the diode

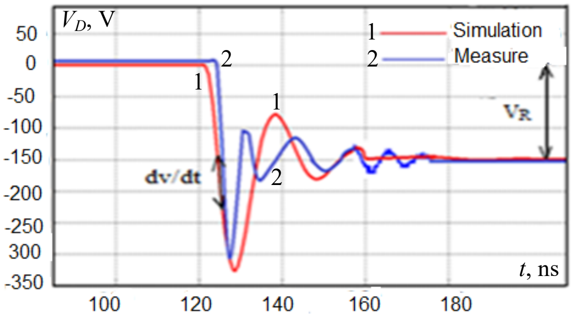

Fig. 8. Temporal characteristics of the voltage V_D at the opening of the diode

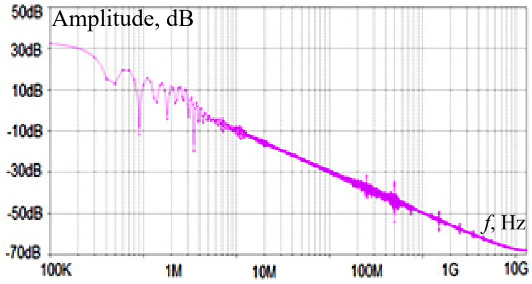

Fig. 9. Frequency characteristics of the voltage V_D at the opening of the diode

From Fig. 6, 8, we notice a good agreement between the simulation results and the experimental measurements. We can extract the transient parameters of the studied diode such as: V_{RM} – maximum reverse voltage; I_{RM} – maximum reverse recovery current of the diode; t_{RR} – reverse recovery time. At the beginning, a current I_f flows in the power diode. From the conduction of the MOSFET (M: closed switch, $V_{DS} = 0$), the current in the diode starts to decrease from the value $I_f = I_D$ with a slope:

$$\frac{\mathrm{d}i(t)}{\mathrm{d}t} = -\frac{V_R}{L_D}. \qquad (3)$$

The slope is imposed by the inductance L_D (V_D is negligible compared to V_R). We obtain the following results: I_{RM} = 14,5 A; t_{RR} = 38 ns; V_{RM} = 340 V.

At the end of recovery, the diode then behaves as a nonlinear capacitor in series with the inductance and resistance of the circuit, resulting in a damped oscillatory response of the system with a rapid decay of the current.

We have therefore defined with these results the transient parameters describing the switching at the opening of the diode. It appears clearly the transient oscillatory phenomenon whose period is of the order of the hundred of nanoseconds.

For the frequency responses shown in Fig. 7, 9, we notice from the conduction of the MOSFET of frequency 300 kHz, an electromagnetic disturbance created between –20 dB and 20 dB due to the variation of current and voltage.

Study of the behavior of MOSFET transistor. Figure 10 shows the electrical circuit used to record the dynamic characteristics of the MOSFET. In this simulation circuit, the inductance L_d represents the overall parasitic inductances in the circuit that causes the oscillation when the MOSFET opens [15-19]. The simulation results will be validated by experimental measurements carried out on the experimental bench shown in Fig. 4.

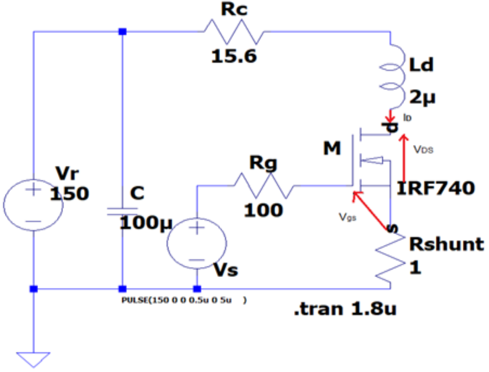

Fig. 10. Simulation scheme used to identify the dynamic parameters of the IRF740 MOSFET

According to the diagram presented in Fig. 10, we can establish the equations that describe the mesh of this circuit. The opening of the MOSFET starts with a decrease of the control voltage to zero. Consequently, the voltage across this component increases from 0 V to V_R. In this phase, the current growth rate can be expressed by (4) linking the voltage V_{DS}, V_R, and the resistances R_c and R_{shunt}

$$\frac{\mathrm{d}i(t)}{\mathrm{d}t} = \frac{V_R - V_{RC} - V_{Rshunt} - V_{DS}}{L_D}. \qquad (4)$$

Results and analysis. The waveforms of the current and voltage across the MOSFETs during their opening are presented in Fig. 11, 13. The results of the simulations are validated with the realized measurements. For the frequency response, the results are shown in Fig. 12, 14. The simulated scheme has the following characteristics: R_g = 100 Ω, R_c = 15.6 Ω, L_D = 2 µH, V_R = 150 V, R_{shunt} = 1 Ω.

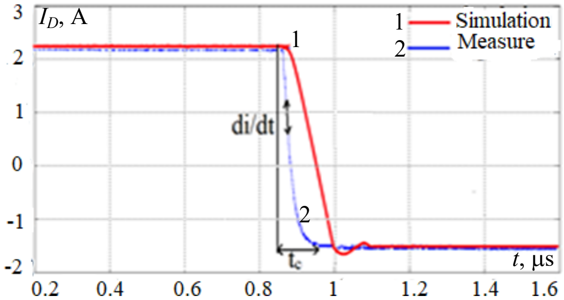

Fig. 11. Temporal characteristics of the I_D current at the opening of the MOSFET

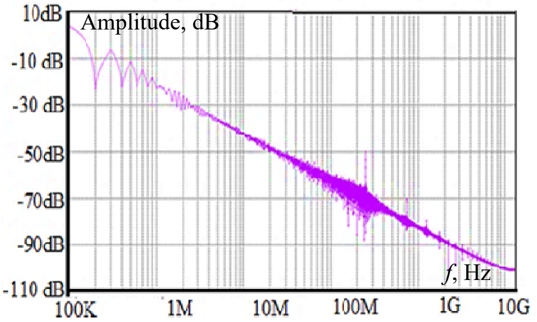

Fig. 12. Frequency characteristics of the I_D current at the opening of the MOSFET

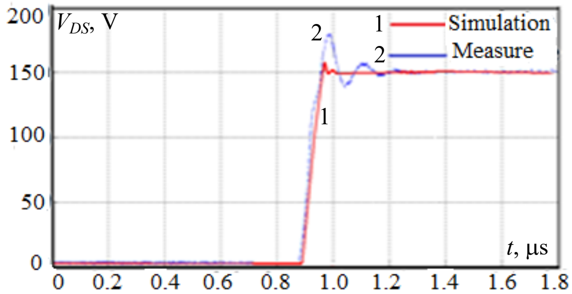

Fig. 13. Temporal characteristics of the V_{DS} voltage at the opening of the MOSFET

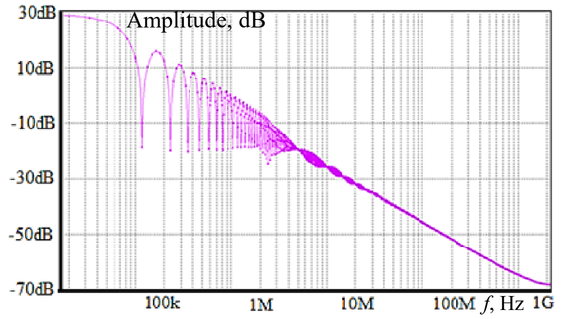

Fig. 14. Frequency characteristics of the V_{DS} voltage at the opening of the MOSFET

From the results illustrated in Fig. 11, 13, we notice that the switching of the MOSFET causes an overvoltage with an overshoot $V_{\max}$ = 170 V and a switching time t_c very reduced, of the order of ns which implies very important dv/dt and di/dt. In addition, an oscillatory phenomenon appears after the opening of the MOSFET. This phenomenon is explained by the effect of the connection inductance in the circuit. It can be said that the oscillatory and steep-edge phenomena of current and voltage are the cause of electromagnetic disturbances in electronic devices. For EMC problems, it is therefore essential to define the dv/dt and di/dt and the evolution of the current I_D and the voltage V_{DS} during the switching of the active components.

From the frequency results illustrated in Fig. 12, 14, we notice respectively a decrease of amplitude from 10 dB to –100 dB for the current and for the voltage a decrease of amplitude from 30 dB to –70 dB. We see in Fig. 14 that from 30 dB to –30 dB, there is a slight disturbance for the voltage V_{DS}.

Study of the behavior of the IGBT transistor. Figure 15 shows the electrical circuit used to identify the dynamic characteristics of the IGBT under Lt-spice software.

The experimental bench used for the switching of the IGBT remains the same used in Fig. 4, except that the MOSFET must be replaced by the IGBT transistor of type APT 25GF100BN, in order to visualize the voltage across the IGBT transistor and the current flowing through.

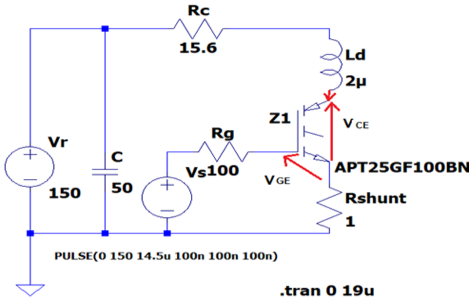

Fig. 15. Simulation diagram used to identify the dynamic parameters of the IGBT transistor

The study of dynamic behavior of the power IGBT transistor in a switching cell allowed us to define the transient and frequency parameters of the latter to represent the switching phase. The IGBT transistor used in this study is type of APT25GF100BN. Figures 16, 18 show the current and voltage time characteristics obtained from respectively simulation and measurements. Figures 17, 19 show the frequency characteristics of respectively the current and voltage at the opening of the APT25GF100BN IGBT.

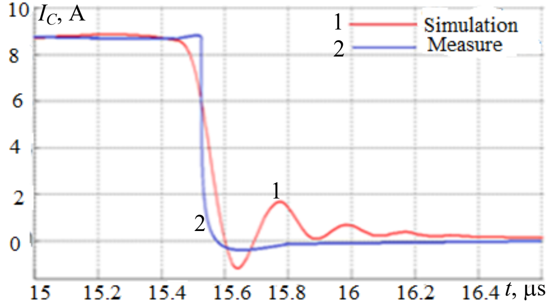

Fig. 16. Transient characteristics of the I_C current when the IGBT transistor is open

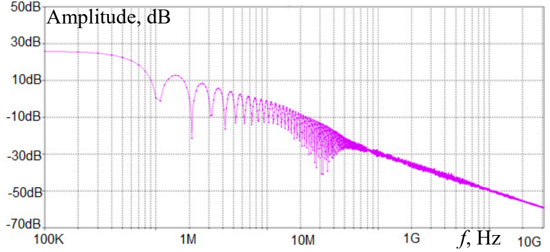

Fig. 17. Frequency characteristics of the I_C current at the opening of the IGBT transistor

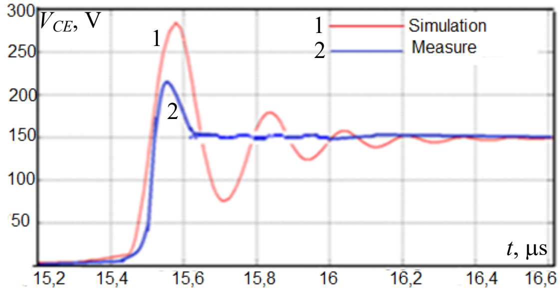

Fig. 18. Temporal characteristics of the voltage V_{CE} at the opening of the IGBT transistor

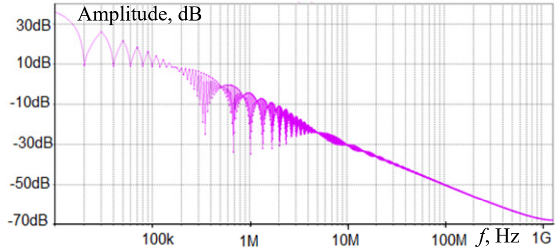

Fig. 19. Frequency characteristics of the V_{CE} voltage at the opening of the IGBT transistor

In the simulations carried out, we considered the values of the following parameters: $R_g = 100\ \Omega$, $R_c = 15.6\ \Omega$, $L_D = 2\ \mu\text{H}$, $V_R = 150$ V, $R_{shunt} = 1\ \Omega$.

In this study, we used the same switching cell of the MOSFET, so the waveform of the current and the voltage at the terminals of the IGBT transistor remains similar to those of the MOSFET (temporal and frequency), what changes are the amplitudes and the frequency of these waves. The aspects of the dynamic behavior of an IGBT are similar to those of a MOSFET.

Conclusions.

1. Numerous electromagnetic disturbances mainly due to fast switching of the semiconductors. The disturbances propagate towards the power source of the converter and towards the load that it feeds and a part of this energy is radiated.
2. An experimental evaluation was presented in this work compared by simulation results in order to better present the influence of the fast switching of semiconductors on the electrical quantities, which causes electromagnetic disturbances in the interconnected electrical system.
3. These disturbances can be minimized by using an optimized EMC filter according to the international standards of our future work.

Acknowledgement. The authors of this article would like to thank the General Directorate of Scientific Research and Technological Development (DGRSDT) in Algeria for their technical support and the specific research budget allocated to this program.

Conflict of interest. The authors declare that they have no conflicts of interest.

REFERENCES

1. Santos V.D. *Modélisation des émissions conduites de mode commun d'une chaîne électromécanique: Optimisation paramétrique de l'ensemble convertisseur filtres sous contraintes CEM*. These de Institut National Polytechnique de Toulouse, Spécialité génie Electrique, 2019. (Fra).

2. Benhadda N., Bendaoud A., Chikhi N. A conducted EMI noise prediction in DC/DC converter using a frequency-domain approach. *Elektrotehniski Vestnik/Electrotechnical Review*, 2018, vol. 85, no. 3, pp. 103-108.

3. Chikhi N., Bendaoud A. Evaluation of Conducted Disturbances Generated by the Chopper-rectifier Association Propagating to the Electrical Network. *European Journal of Electrical Engineering*, 2019, vol. 21, no. 1, pp. 1-6. doi: https://doi.org/10.18280/ejee.210101.

4. Moreau M. *Modélisation haute fréquence des convertisseurs d'énergie. Application à l'étude des émissions conduites vers le réseau.* PHD Thesis, Electrical Engineering, Central School of Lille-France, 2009. (Fra).

5. Fakhfakh L., Ammous A. New simplified model for predicting conducted EMI in DC/DC converters. *Electrical Engineering*, 2017, vol. 99, no. 3, pp. 1087-1097. doi: https://doi.org/10.1007/s00202-016-0474-2.

6. Fakhfakh L., Alahdal A., Ammous A. Fast modeling of conducted EMI phenomena using improved classical models. *2016 Asia-Pacific International Symposium on Electromagnetic Compatibility (APEMC)*, 2016, pp. 549-552. doi: https://doi.org/10.1109/APEMC.2016.7522795.

7. Haque M.E., Bokhari A.A., Alolah A.I. Simulink modeling of the problem associated with fast switching PWM IGBT-inverter fed AC motor drive with long cable and its remedies. *IEEE International Conference on Systems, Signals & Devices*, 2005.

8. Boroyevich D., Zhang X., Bishinoi H., Burgos R., Mattavelli P., Wang F. Conducted EMI and systems integration. *CIPS 2014 8th International Conference*, Nurenberg, 2014.

9. Ales A., Gouichiche Z., Schanen J.-L., Roudet J., Boudaren M.E.Y., Karouche B., Moussaoui D. The accurate input impedances of a DC-DC converters connected to the network. *2015 IEEE 15th International Conference on Environment and Electrical Engineering (EEEIC)*, 2015, pp. 331-336. doi: https://doi.org/10.1109/EEEIC.2015.7165183.

10. Slimani H., Zeghoudi A., Bendaoud A., Reguig A., Benazza B., Benhadda N. Experimental Measurement of Conducted Emissions Generated by Static Converters in Common and Differential Modes. *European Journal of Electrical Engineering*, 2021, vol. 23, no. 3, pp. 273-279. doi: https://doi.org/10.18280/ejee.230312.

11. Zeghoudi A., Bendaoud A., Slimani H., Benazza B., Bennouna D. Determination of electromagnetic disturbances in a buck chopper. *Australian Journal of Electrical and Electronics Engineering*, 2022, vol. 19, no. 2, pp. 149-157. doi: https://doi.org/10.1080/1448837X.2021.2023073.

12. Mahesh G., Subbarao B., Karunakaran S. Effect of power frequency harmonics in conducted emission measurement. *Proceedings of the International Conference on Electromagnetic Interference and Compatibility*, 2008, pp. 273-277.

13. Seguier G., Labrique F., Delarue P. *Electronique de puissance. Structures, commandes, applications*, 10e edition, Dunod, Paris, 2015. 425 p. (Fra).

14. Duan Z., Fan T., Zhang D., Wen X. Differential Mode Conducted EMI Prediction in Three Phase SiC Inverters. *IOP Conference Series: Materials Science and Engineering*, 2017, vol. 199, art. no. 012126. doi: https://doi.org/10.1088/1757-899X/199/1/012126.

15. Mrad R., Morel F., Pillonnet G., Vollaire C., Lombard P., Nagari A. N-Conductor Passive Circuit Modeling for Power Converter Current Prediction and EMI Aspect. *IEEE Transactions on Electromagnetic Compatibility*, 2013, vol. 55, no. 6, pp. 1169-1177. doi: https://doi.org/10.1109/TEMC.2013.2265048.

16. Fedyczak Z., Kempski A., Smoleński R. Conducted high frequency disturbances observed in electrical power systems with switch mode converters. *Przeglad Elektrotechniczny*, 2013, vol. 89, no. 6, pp. 41-50.

17. Zeghoudi A., Slimani H., Bendaoud A., Benazza B., Bechekir S., Miloudi H. Measurement and analysis of common and differential modes conducted emissions generated by an AC/DC converter. *Electrical Engineering & Electromechanics*, 2022, no. 4, pp. 63-67. doi: https://doi.org/10.20998/2074-272X.2022.4.09.

18. Lounis Zohra. *Apports des techniques de cablages laminaires dans un onduleur a IGBT de moyenne puissance*. These de doctorat, Institut National Polytechnique de Loraine, 2000. (Fra).

19. Marlier C. *Modélisation des perturbations électromagnétiques dans les convertisseurs statiques pour des applications aéronautiques*. These de doctorat, en Génie électrique Université Lille Nord-de-France, 2013. (Fra).

Received 09.08.2022
Accepted 12.12.2022
Published 01.09.2023

Helima Slimani, [1,2]*, Lecturer,*
Abdelhakim Zeghoudi[1]*, PhD,*
Abdelber Bendaoud[1]*, Professor,*
Seyf Eddine Bechekir[1]*, Lecturer,*
[1] Laboratory of Applications of Plasma, Electrostatics and Electromagnetic Compatibility (APELEC),
Djillali Liabes University of Sidi Bel-Abbes, Algeria,
e-mail: hakooumzeghoudi@gmail.com;
babdelber@gmail.com (Corresponding Author);
seyfeddine.electrotechnique@gmail.com
[2] University of Tiaret, Algeria,
e-mail: halima.slimani@univ-tiaret.dz

How to cite this article:
Slimani H., Zeghoudi A., Bendaoud A., Bechekir S. Experimental evaluation of conducted disturbances induced during high frequency switching of active components. *Electrical Engineering & Electromechanics*, 2023, no. 5, pp. 26-30. doi: https://doi.org/10.20998/2074-272X.2023.5.04

UDC 621.314.26 https://doi.org/10.20998/2074-272X.2023.5.05

E.M. Vereshchago, V.I. Kostiuchenko, S.M. Novogretskyi

Analysis of a DC converter working on a plasma arc

Introduction. *The article is devoted to the analysis of a stabilized direct current converter operating on a plasma arc. Electroplasma technologies of the new generation cause the need to design workable systems that provide control of technological processes and their dynamic optimization in real time. The improvement of any electroplasma technology begins with the improvement of the operating parameters of the main element of plasma installations - the power source.* ***Goal*** *is to build and study a continuous model of a pulsed source of secondary power supply, which works on an electric welding and plasma arc.* ***Methodology.*** *In the work, a mathematical description of the converter was performed. The continuous model of the system is substantiated, taking into account its features, namely, the load (gas-discharge gap) is a source of voltage and dynamic resistance. The parameters of the constant part during circuit synthesis are determined: the components of the gain of the constant part, the relative signal coefficient of the current sensor and the PWM gain. Studies of the open system «power source - arc» have been carried out.* ***Results.*** *MATLAB objects were created - continuous mathematical models of the object in the form of transfer functions. The obtained transient characteristics for different options: «arc current - control signal» and « inductor current - control signal» showed that open systems are unstable. It was found that in the case of instability, the filling frequency of self-oscillations occurring in the linear mode is close to the frequency of natural oscillations of the circuit. The dependence of the module and the argument of the input resistance of the power part of the pulsed power supply with parallel capacitance to the electric arc and without it, which have matching frequency characteristics, is established. The circuit considered with the initial data adopted in this article has a frequency transfer coefficient of the same type as the first-order non-minimum-phase (phase-shifting) link. Frequency response graphs for the output impedance of the power unit show that this power unit is a broadband frequency-selective system with a bandwidth of* $B_{0.707}$ *= 100 kHz.* ***Originality.*** *Expressions for the frequency transfer function, input and output resistance of the pulse voltage converter operating on an arc load were obtained by the method of averaging and linearization. The frequency amplitude and phase characteristics for the pulse voltage converter with an LC filter and the output according to the arc current and the choke current were studied. The transfer functions of the continuous model in terms of arc current and choke current at the specified parameters are the same, which must be taken into account when designing regulators.* ***Practical significance.*** *The frequency characteristics of the input and output resistances and transfer functions can be used when forming a technical task for designing a power source to assess the stability of the «pulse converter - arc» system and rational calculation of input filters.* References 22, tables 1, figures 7.

Key words: **input and output resistance, filter, impedance, stabilization system, stability, complex load.**

В роботі проведено аналіз стабілізованого перетворювача постійного струму, що працює на плазмову дугу. Обґрунтовано безперервну модель системи з урахуванням її особливостей. Визначені параметри незмінної частини під час аналізу схеми заміщення замкнутої структури системи електроживлення для дугового навантаження із від'ємним диференціальним опором. Проведені дослідження розімкнутої системи «джерело живлення - дуга». Встановлено, що розглянута схема з вихідними даними, прийнятими в даній статті, має частотний коефіцієнт передачі такого ж виду, що і немінімально-фазова ланка першого порядку. Отримано частотні характеристики вхідного та вихідного опорів перетворювача, навантаженого на дугу. Бібл. 22, табл. 1, рис. 7.

Ключові слова: **вхідний та вихідний опір, фільтр, імпеданс, система стабілізації, стійкість, комплексне навантаження.**

Introduction. In today's advanced fields of science, technology and industry, electroplasma and welding technologies are widely used, which use low-temperature plasma (devices with negative differential resistance). A large class of such devices is DC plasmatrons. Plasmatrons are most often used for cutting materials, heating gas, as plasma ignition systems in the combustion chambers of gas turbine engines for various purposes, etc. [1-3]. Here we should also mention plasma melting, strengthening of metals, plasma chemistry, special metallurgy, solving environmental problems, obtaining new clean materials, applying films and coatings by the vacuum-plasma method, etc.

The improvement of any electroplasma technology must begin with the improvement of the operating parameters of the main element of plasma installations – the power source, which is achieved by designing and constructing its main nodes. Thus, the study of a DC converter operating on a plasma arc is not only of practical, but also theoretical interest, as well as an important and relevant scientific and applied problem.

Two classes of models are used for the analysis of processes in pulse power converters – key (simulation) and continuous [4-7]. Continuous (averaged) ones became the most widespread during the analysis of the stability of closed stabilization systems taking into account pulse energy converters and the synthesis of regulators of these systems [4-7].

Note that the differential resistance of the arc R_{diff0} depending on the location of the operating point on one or another section of the arc volt-ampere characteristic can take on zero, positive, and negative values. It is in the case of finding the operating point on the falling section of the arc volt-ampere characteristic that the converter, taking into account the behavior of the object, forms a system with negative resistance. The behavior of such systems is significantly different from the systems described in the literature under constant load. Instabilities and self-oscillating modes may occur in a system with negative resistance [8]. Self-oscillations, as a rule, have negative consequences: deterioration of the quality of the technological process, reduction of productivity, etc.

The study of systems with negative R_{diff0} is of not only practical, but also theoretical interest [8]. It is appropriate to study the peculiarities of the dynamics of open systems. This makes sense not only because of their wide application in practice, but also because, on simple examples, we can learn the used analysis method and show the influence of certain external feedbacks on the dynamic properties of a closed system compared to an open one.

The complexity of the nonlinear discrete model of the pulse converter (its exact mathematical model), which works on a non-linear load, makes the analysis of the latter in an automatic current stabilization system (closed control system) extremely difficult [5]. At the same time, works [1, 5, 6] show that when the commutation period T (T→0) decreases, nonlinear pulse systems approach linear continuous systems in terms of properties [1, 5]. Considering the high switching frequency of modern converters for electrical technologies, the task of building their limit continuous models turns out to be very promising. Averaged models are the most convenient for practice, as they allow applying well-developed methods of analysis and synthesis of linear continuous systems to nonlinear discrete systems.

When designing key power sources, continuous linear models of pulse converters are widely used [1, 5]. Their averaged models are substantiated and widely used in various works.

In [9], for example, continuous linearized models of basic converters are given. The method of their construction is based on the assumption that the choke has no active resistance. In addition, the used approach does not allow taking into account the output resistance of the power source, the filter at the input of the converter, etc.

In works [4, 5], the need to take into account the active resistance of the choke circuit during the analysis and synthesis of pulse converter control systems is indicated.

Structural dynamic models of DC pulse converters operating on a complex load with and without taking into account the choke resistance are substantiated, for example, in works [4-7].

In [8], the general issues of power supply and interaction of an electric arc from a current-controlled voltage source and a voltage-controlled current source are considered.

In [10], a power source with a current characteristic, which is made according to the following block diagram, was investigated: an AC source – a transformer – a rectifier – an inductance connected in series with an arc resistance.

Since the pulse converter working on an arc load is not sufficiently studied in the literature, the task of this article is to build a continuous model of the converter and to study the peculiarities of its operation.

Next, an attempt is made to perform an analysis using a simple continuous model of the converter, which takes into account the active resistance of the keys, the choke and the output resistance of the power source and operating on an arc load. It is assumed that the adjustment of the output parameter is carried out using PWM-2.

The goal of the article is to build and study a continuous model of a pulse source of secondary power supply, which works on an electric welding and plasma arc.

Mathematical description of the converter. Replacing circuit of the power supply system for an electric arc load, which includes a loaded LC filter, a correction device (CD), a modulator (M) implementing PWM-2, a pulse converter (PC), which forms pulses with the amplitude of the supply voltage nU_{in} at the input of the filter and duration, which is determined by the switching function k_F of the modulator, and sensors of voltage VS and current CS with k_V and R_{CS} coefficients, respectively, is shown in Fig. 1, where, for commonality, the resistance R connected in parallel with the capacitor C of the output filter is shown.

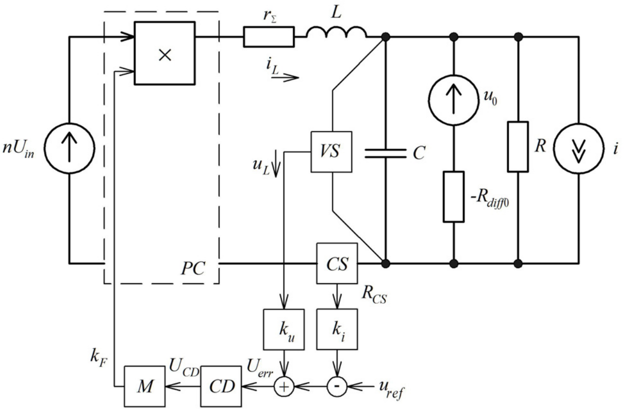

Fig. 1. Replacing circuit of the closed structure of the power supply system for arc load with negative differential resistance

In Fig. 1: i is the current source considered as a disturbance (change) in the load current. The resistance r_Σ includes both the output resistances of the converter and the rectifier, as well as the ohmic losses of the filter choke. Here, the losses resistance may depend on the frequency [11-15]. The load (gas discharge gap) is the series-connected voltage source U_0 and dynamic resistance R_{diff0}.

The converter on the circuit is presented in the form of a power four-pole with an information controlled input (Fig. 1) [5, 16], where $n = w_{21} / w_1 = w_{22} / w_1$. The transmission coefficient of the modulator PC, which in our case is defined as $k_F(t)$, if the error signal does not depend on time, is determined by the relationship:

$$k_{PWM} = T / U_m ,$$

where U_m is the amplitude (range) of the fractional function (sawtooth voltage), T is the sweep period.

Usually $R >> r_\Sigma$ (in particular R is missing, i.e. $R\to\infty$).

Denoting by $Z_n(s)$ the operator resistance of the parallel connection of C and R_{diff0}:

$$Z_n(s) = -R_{diff\,0} \big/ \left(1 - sR_{diff\,0}C\right) = -R_{diff\,0} \big/ \left(-\tau s + 1\right),\ \tau > 0 ,$$

we obtain the following expression of the transfer function (TF) of the output LC filter in terms of voltage:

$$K(s) = \frac{Z_n(s)}{Z_{in}(s)} = \frac{Z_n(s)}{r_\Sigma + sL + Z_n(s)} =$$

$$= k_f (s^2 k_f LC + s(L/(r_\Sigma - R_{diff\,0}) + R_{eq}C) + 1)^{-1} =$$

$$= \frac{k_f}{T_f{}^2 s^2 + 2\xi_f T_f s + 1} = \frac{k_f}{T_f{}^2[(s+\alpha_f)^2 + \omega_f{}^2]},$$

where $\tau = R_{diff0}C > 0$ is the time constant of the circuit of the output capacitor; $R_{eq} = r_\Sigma \parallel (-R_{diff0})$; $k_f = -R_{diff0}/(-R_{diff0} + r_\Sigma) > 0$ is the transmission coefficient of the DC filter; $Z_{in}(s)$ is the input operator resistance of the regulator at $R = \infty$ in the continuous current mode; T_f and ξ_f are the time constant and damping coefficient of the filter, defined as

$$T_f = \sqrt{k_f LC}\ ;\ \xi_f = \frac{1}{2}\sqrt{k_f}\left(r_\Sigma \sqrt{C/L} + \frac{1}{R_{diff0}}\sqrt{L/C} \right) =$$

$$= \frac{1}{2}\sqrt{k_f}\left(1/Q + d_s\right) = \frac{1}{2}\sqrt{k_f}(d_r + d_s)\ ;\quad \alpha_f = \xi_f / T_f\ ;$$

$$\omega_f = \sqrt{1/T_f^2 - \alpha_f^2} = \sqrt{\omega_0^2 - \alpha_f^2}\ ;\quad \omega_0^2 = 1/(k_f LC)\ ,$$

where $Q = \frac{1}{r_\Sigma}\sqrt{L/C} = \rho / r_\Sigma$ is the Q factor of the LC filter without taking into account the attenuation introduced by the resistance R and regeneration; $d_s = -S_{diff}\sqrt{L/C}$ is the regeneration introduced into the circuit by a load (electric arc); $d_r = r_\Sigma \sqrt{C/L}$ is the damping introduced into the circuit by resistance; $\rho = \sqrt{L/C}$ is the characteristics of the circuit forming the filter; $d = d_r + d_s$ is the complete fading (regeneration) of the circuit; $S_{diff} = 1 / R_{diff0}$ is the differential steepness of the arc volt-ampere characteristic.

For the circuit in Fig. 1 equation that determines the current in the filter choke $\tilde{i}_L$ will be as follows:

$$Z(s)\tilde{i}_L = nD\tilde{u}_{in} + nU_{in}\tilde{d} + Z_n(s)\tilde{i} - (Z_n(s)/R_{diff0})\tilde{u}_0\ ,$$

where

$$Z(s) = \frac{Z_n(s)}{K(s)} = \frac{R_{diff0}[s^2 k_f LC + s\left(\frac{L}{r_\Sigma - R_{diff0}} + R_{eq}C\right) + 1]}{k_f(-\tau s + 1)}\ ;$$

the symbol «~» shows an infinitesimally small change of the variable with respect to the value in the periodic mode; $d = 2t_p / T$ is the filling factor; D is the value of the filling factor in the steady state (periodic) mode [17-20].

At $C = 0$, the last equation will take the form

$$\tilde{i}_L = k_f \frac{\tilde{i} - \tilde{u}_0 / R_{diff0} + (nD/R_{diff0})\tilde{u}_{in} + (nU_{in}/R_{diff0})\tilde{d}}{s[L/(r_\Sigma - R_{diff0})] + 1}\ .$$

Having chosen as the output variable the arc current $i_{arc} = i_n$, which does not coincide with the state variable, we obtain the transfer functions for the control influence «arc current – control signal»:

$$\frac{\tilde{I}_{arc}(s)}{\tilde{d}(s)} = nU_{in}\frac{Z_n(s)}{Z_1(s) + Z_n(s)}S_{diff} = nU_{in}K(s)S_{diff}\ ,$$

and by disturbing influences – the sensitivity of the arc current to a change in the input voltage u_{in} and to the disturbing current i and voltage u_0:

$$\frac{\tilde{I}_{arc}(s)}{\tilde{U}_{in}(s)} = nDK(s)S_{diff}\ ;\quad \frac{\tilde{I}_{arc}(s)}{\tilde{I}(s)} = -Z_1(s)K(s)S_{diff}\ ;$$

$$\frac{\tilde{I}_{arc}(s)}{\tilde{U}_0(s)} = -(s^2 LC + sr_\Sigma C + 1)K(s)S_{diff}\ ,$$

where $Z_1(s) = Ls + r_\Sigma$ is the operator resistance of the choke circuit.

Determination of the parameters of the constant part of the circuit. Let's find the components of the gain factor of the constant part. Having chosen the steepness of the current sensor R_{CS} = 0.75 mΩ, we determine the CS relative signal coefficient k_i = 82 and the PWM gain

$$k_{PWM} / T = F(T/U_m)(1/T) = F/U_m = 1/2{,}5 = 0{,}4\ \text{В}^{-1}\ ,$$

where the ripple factor F is taken equal to 1; U_m = 2.5 V is the amplitude (span) of sawtooth voltage.

The amplification factor of the constant part at k_f = 1 and F = 1

$$k_0 = k_i k_{PWM} nU_{in}(R_{CS} / -R_{diff0}) / T =$$

$$= -82 \cdot 250 \cdot 0{,}4 \cdot 75 \cdot 10^{-5} / 0{,}49 = -12{,}55.$$

The switching frequency is taken as 26 kHz, the choke inductance of the output LC filter is L = 300 μH, and the capacity of the output capacitor, which depends on the requirements, is C = 3 μF, r_Σ = 0.01 Ω, R_{diff0} = –0.49 Ω [21].

Study of the open system «power source – arc». Let's create MATLAB objects – continuous mathematical models of our object in the form of transfer functions (*transfer function form*). The answer will be the following result in the command window (Table 1).

Table 1

Transfer functions of the object

No.	Transfer function*
1	$\frac{416.4}{9 \cdot 10^{-10} \cdot s^2 - 0.000612 \cdot s + 1}$
2	$\frac{208.2}{9 \cdot 10^{-10} \cdot s^2 - 0.000612 \cdot s + 1}$
3	$\frac{-0.000612 \cdot s + 416.4}{9 \cdot 10^{-10} \cdot s^2 - 0.000612 \cdot s + 1}$
4	$\frac{-0.000306 \cdot s + 208.2}{9 \cdot 10^{-10} \cdot s^2 - 0.000612 \cdot s + 1}$

*options 1, 2 – TF «arc current – control signal» with k_{CR} = 33.18 and k_{CR} = 16.59; options 3, 4 – TF «choke current – control signal» with k_{CR} = 33.18 and k_{CR} = 16.59.

For the TF of object 3-4, the indicators are equal: the order and the instability index are equal to two $n = s_n = 2$, the degree $r_C = n - m = 2 - 1 = 1$, the indexes of aperiodic and oscillatory neutrality are equal to zero $s_a = s_v = 0$, the index of non-minimum phase $s_{nf} = 1$, the amplification factor $k = k_0 k_{CR}$. The assignment of these indicators and the amplification factor k reflects the essential features of the TF $W(s)$ and they can be used to characterize certain properties of the system determined by this TF [22].

Transient characteristics (TC) for options 1, 3 are shown in Fig. 2. Open systems are unstable s_n = 2>0. Nyquist diagrams for the considered options are shown in Fig. 3. As shown in Fig. 3, the frequency response never covers the point –1, j0, so closed systems are also unstable.

The input resistance of the power part (PP) according to the diagram in Fig. 1 in operator form

$$Z_{i0}(s) = -(R_{diff0} - r_\Sigma)\frac{s^2 k_f LC + s\left(-L/(R_{diff0} - r_\Sigma) - R_{eq}C\right) + 1}{-\tau_C s + 1}\ ,$$

where $\tau_C = R_{diff0}C > 0$ is the time constant of the circuit of the output capacitor; $R_{eq} = r_\Sigma \parallel (-R_{diff0})$; $k_f = R_{diff0} / (R_{diff0} - r_\Sigma)$ is the transmission coefficient of the DC filter.

It is easy to show that its output resistance is determined by the expression

$$Z_{00}(s) = k_f \frac{sL + r_\Sigma}{s^2 k_f LC + s\left(-L/(R_{diff0} - r_\Sigma) + R_{eq}C\right) + 1}\ .$$

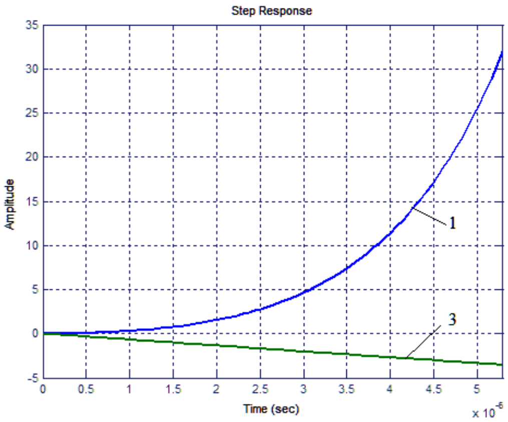

Fig. 2. TC graphs of unstable systems: option 1 (1), option 3 (3)

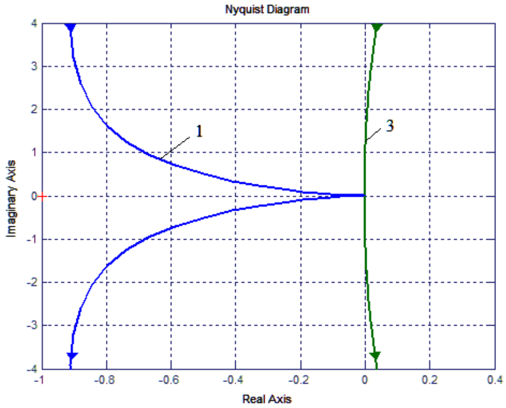

Fig. 3. Nyquist diagrams for unstable systems: option 1 (1), option 3 (3)

Since the losses resistance is quite small, then

$$Z_{00}(s)=\frac{s/C}{s^2-s/(R_{diff\,0}C)+1/(LC)}. \qquad (1)$$

Noting that, in the general case, $1/\sqrt{LC}=\omega_0$ is the frequency of natural oscillations of the circuit without losses and $\alpha=-0{,}5S_{diff}/C=-0{,}5\omega_0 Q$ is the damping coefficient of the circuit, we rewrite the expression as follows (here, the main conditions were chosen so that instabilities could occur)

$$Z_{00}(s)=\frac{s/C}{s^2-2\alpha s+\omega_0^2} \quad (\alpha>0).$$

In this case $\omega_0=1/\sqrt{LC}=$ $=(\sqrt{300\cdot 10^{-6}\cdot 3\cdot 10^{-6}})^{-1}$ $=33.33\cdot 10^3$ s^{-1} or f_0 = 5.307 kHz.

Therefore, in the case of instability, the filling frequency of self-oscillations occurring in the linear mode is close to the frequency of natural oscillations of the circuit f_0.

If C = 0, then

$$Z_{00}(s)=sL(-\tau_{load}s+1)^{-1}, \qquad (2)$$

where $\tau_{load}=L/R_{diff0}>0$ is the load circuit time constant.

Options (Fig. 4) of the dependencies of the module and the argument of the input resistance of the PP of the pulse power supply with and without parallel capacitance to the electric arc have frequency characteristics (FC) that coincide.

The closeness of FC indicates similarity and small differences in transient processes according to the main quality indicators. Thus, the circuit under consideration with the initial data adopted in this article has a frequency transfer coefficient of the same type as a first-order non-minimum phase (phase-shifting) link

$$Z(j\omega)=k(\tau j\omega-1),$$

where $k=R_{diff0}$, $\tau=L/R_{diff0}>0$.

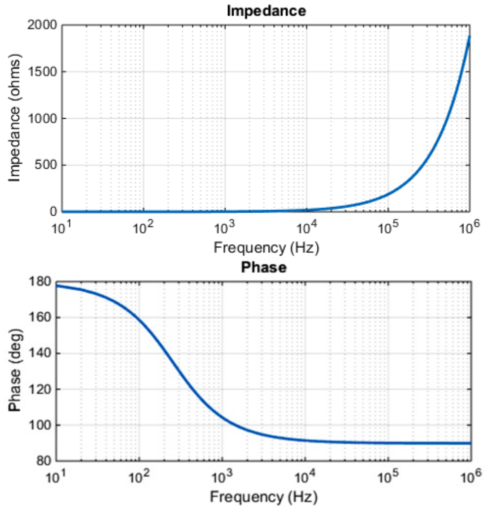

Fig. 4. Frequency characteristics of the input impedance of the PP of the power source loaded on an electric arc, for C = 0 and C = 3 μF

Frequency response graphs for the output impedance of the PP, constructed according to expressions (1), (2), are shown in Fig. 5. Note that for $C\neq 0$, this PP is a broadband frequency-selective system ($B_{0.707}/f_0 >> 1$) with bandwidth $B_{0.707}$ = 100 kHz.

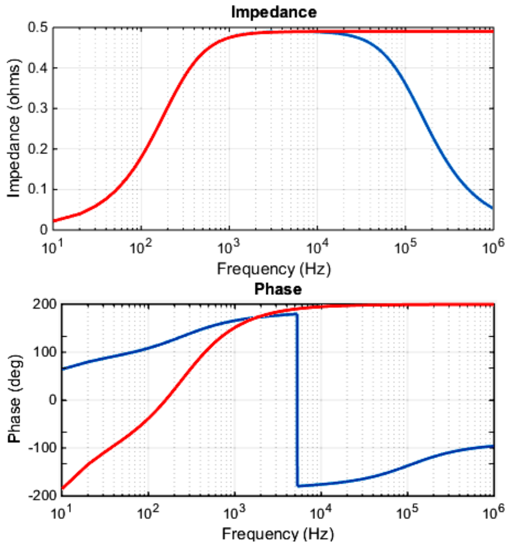

Fig. 5. Graphs of frequency response (above) and phase response (below) of the output circuit impedance

Logarithmic characteristics of the module and phase of the input conductance of the PP of the *PC* for the case of the absence of capacitance at the output of the pulse current stabilizer – unstable with negative self-alignment of the aperiodic link

$$Y_{i0}(s)=1/Z_{i0}(s)=k(-1+\tau s)^{-1} \qquad (3)$$

have been constructed in Fig. 6,*a*; the Nyquist diagram is shown in Fig. 6,*b*. According to (3), the asymptotic characteristic has a break at the point $\omega_1 = 1 / \tau$. Bandwidth is 0 – 465 Hz.

Figure 7 shows the frequency response and phase response of the «power source – arc» system in the open state.

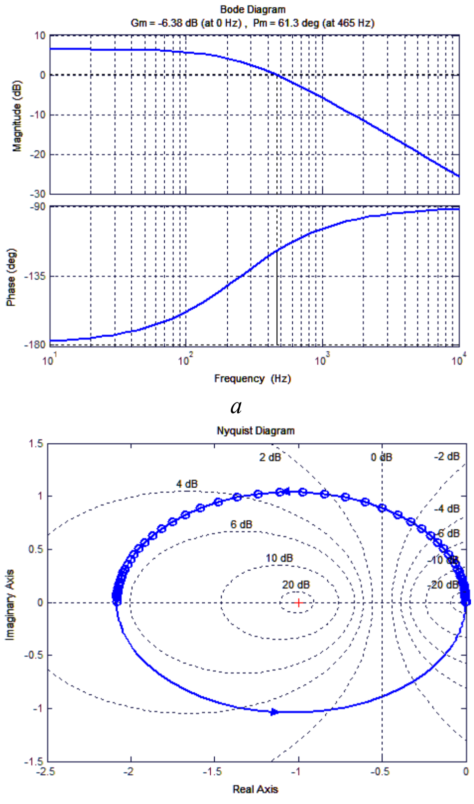

a

b

Fig. 6. Modulus and argument of the input admittance of the PP (*a*); Nyquist hodograph for this case (*b*)

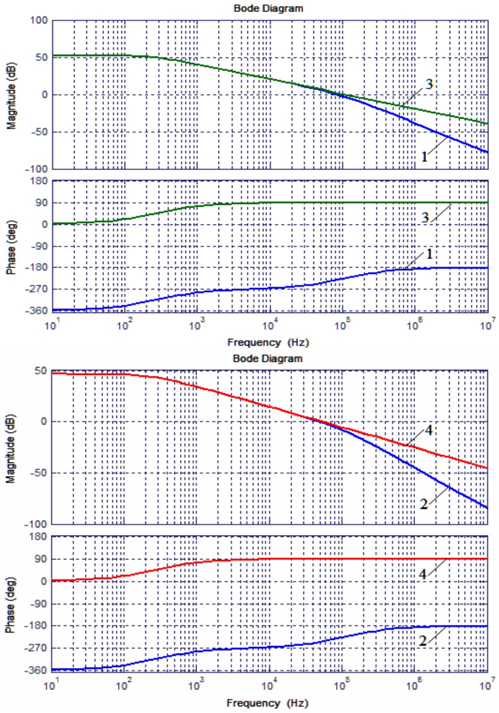

Fig. 7. Frequency response and phase response of the open circuit of the pulse current stabilizer when controlled by the output current i_{arc} (1-2) and the choke current i_L (3-4)

From graphs shown in Fig. 7 it can be seen that the closed system for the considered options will be unstable ($L(\omega) > 0$, $\varphi_{\text{margin}}(\omega) < 0$; $L \to \infty$, $\varphi_{\text{margin}} = -51.9^\circ \div 90.2^\circ$), which introduces additional complications in the construction of the converter control circuit [21].

From the nature of $\varphi(\omega)$ and $A(\omega)$ (Fig. 7), it follows that the construction of closed current stabilization systems of the considered converter causes difficulties, since it is very difficult to ensure a sufficient margin of stability at a high amplification factor in a closed circuit due to a very rapid increase in the phase shift (the angle $|\varphi|$ exceeds 180°) with an almost unchanged frequency response of the converter.

Thus, the considered continuous models can be used in the process of designing devices based on pulse voltage converters for loads with negative differential resistance: sources of secondary power supply, etc., to conduct research on the main properties of these converters.

Conclusions.

1. Expressions for the frequency transfer function, input and output resistances of a pulse voltage converter operating on an arc load with negative differential resistance were obtained by the method of averaging and linearization.

2. The transfer functions of the converter with output by arc current and choke current are not minimally in phase. This explains the nature of the phase characteristics of the converter and the complexity of the synthesis of current regulators for it.

3. The frequency response and phase response for the pulse voltage converter by arc current and choke current were studied.

4. The transfer functions of the continuous model by arc current and choke current at the given parameters are the same, which must be taken into account when designing regulators.

Conflict of interest. The authors of the article declare that there is no conflict of interest.

REFERENCES

1. Vereshchago E.N., Kostiuchenko V.I. *Modeling of power sources for electroplasma and welding technologies*. LAP Lambert Academic Publishing, 2022. 112 p. (Rus).

2. Paton B. E. Advanced studies and developments of the E.O. Paton Electric Welding Institute in the field of welding and related technologies. *Automatic Welding*, 2018, vol. 11-12, pp. 5-18. (Ukr). doi: https://doi.org/10.15407/as2018.12.01.

3. Vereshchago E.N., Kvasnitsky V.F., Miroshnichenko L.N., Pentegov I.V. *Circuitry of inverter power supplies for arc load*. Nikolaev, UGMTU Publ., 2000. 283 p. (Rus).

4. Denisyuk S.P., Derevyanko D.G. *Industrial electronics. Modeling of power electronics devices in MATLAB Simulink*. Kyiv, Igor Sikorskyi KPI Publ., 2019. 95 p. (Ukr).

5. Lazarev Yu.F. *Modeling of dynamic systems in MATLAB. Electronic study guide*. Kyiv, NTUU «KPI» Publ., 2011. 421 p. (Ukr).

6. Gaevskyi O.Yu., Ivanchuk V.Yu. *Basics of conversion technology*. Kyiv, KPI named after I. Sikorskyi Publ., 2023. 63 p. (Ukr).

7. Bondar R.P., Podoltsev O.D. *Modeling of electrical devices*. Kyiv, KNUBA Publ., 2012. 391 p. (Ukr).

8. Sidorets V.N., Pentegov I.V. *Deterministic chaos in non-linear circuits with an electric arc*. Kyiv, International Association «Welding», 2013. 272 p. (Rus).

9. Chetty P.R.K. *Switch-mode Power Supply Design*. Tab Professional and Reference Books, 1986. 179 p.

10. Volkov I.V., Gubarevich V.N., Spirin V.M. Stability of the system current source - an electric arc with a negative differential resistance. *Technical Electrodynamics*. 1998, no. 4, pp. 43-45. (Rus).

11. Vereshchago E., Kostiuchenko V., Hrieshnov A. Calculation and Analysis of Dynamic Properties of a Soft Switching Converter under Operation on the Arc Load. *2020 IEEE 40th International Conference on Electronics and Nanotechnology (ELNANO)*, 2020, pp. 820-825. doi: https://doi.org/10.1109/ELNANO50318.2020.9088776.

12. Chen G., Sun Q., Hu T., Guo Q. A Novel Digital Control Algorithm for a DC-DC Converter in Plasma Application. *2011 Asia-Pacific Power and Energy Engineering Conference*, 2011, pp. 1-4. doi: https://doi.org/10.1109/APPEEC.2011.5748827.

13. Pastor M., Dudrik J., Revak O. High-Frequency soft-switching DC-DC converter with full-bridge output rectifier. *2016 IEEE International Power Electronics and Motion Control Conference (PEMC)*, 2016, pp. 110-115. doi: https://doi.org/10.1109/EPEPEMC.2016.7751983.

14. Bordry F. Power converters: definitions, classification and converter topologies. *In Proc. CAS–CERN Accelerator School and CLRC Daresbury Laboratory: Specialized CAS Courseon Power Converters*, Warrington, UK, 2004, pp. 13-41.

15. Zulauf G., Tong Z., Plummer J.D., Rivas-Davila J.M. Active Power Device Selection in High- and Very-High-Frequency Power Converters. *IEEE Transactions on Power Electronics*, 2019, vol. 34, no. 7, pp. 6818-6833. doi: https://doi.org/10.1109/TPEL.2018.2874420.

16. Kwon M.-J., Kim T.-H., Lee W.-C. Analysis of the Gain Characteristic in LLCC Resonant Converter for Plasma Power Supply. *The Transactions of The Korean Institute of Electrical Engineers*, 2016, vol. 65, no. 12, pp. 1992-1999. doi: https://doi.org/10.5370/KIEE.2016.65.12.1992.

17. Suntio T., Hankaniemi M., Karppanen M. Analysing the dynamics of regulated converters. *IEE Proceedings - Electric Power Applications*, 2006, vol. 153, no. 6, pp. 905-910. doi: https://doi.org/10.1049/ip-epa:20050481.

18. Hankaniemi M., Suntio T., Sippola M., Oyj E. Load-Impedance Based Interactions in Regulated Converters. *INTELEC 05 - Twenty-Seventh International Telecommunications Conference*, 2005, pp. 569-573. doi: https://doi.org/10.1109/INTLEC.2005.335161.

19. Lee B.-H., Kim M.-Y., Kim C.-E., Park K.-B., Moon G.-W. Analysis of LLC Resonant Converter considering effects of parasitic components. *INTELEC 2009 - 31st International Telecommunications Energy Conference*, 2009, pp. 1-6. doi: https://doi.org/10.1109/INTLEC.2009.5351740.

20. Hankaniemi M., Suntio T. Dynamical Modeling and Control of Current-Output Converters. *International Journal on Energy Conversion (IRECON)*, 2019, vol. 7, no. 5, pp. 197-206. doi: https://doi.org/10.15866/irecon.v7i5.18544.

21. Vereschago E., Kostiuchenko V., Novogretskyi S. Analysis of dynamic characteristics of the inverter operating on a complex load. *Eastern-European Journal of Enterprise Technologies*, 2020, vol. 5, no. 5(107), pp. 23-31. doi: https://doi.org/10.15587/1729-4061.2020.215145.

22. Kuntsevich V.M., Chekhovoy Yu.N. *Nonlinear control systems with frequency and pulse width modulation*. Kyiv, Tekhnika Publ., 1970. 340 p. (Rus).

Received 08.11.2022
Accepted 07.02.2023
Published 01.09.2023

E.M. Vereshchago[1]*, PhD, Assistant Professor,*
V.I. Kostiuchenko[1]*, PhD, Assistant Professor,*
S.M. Novogretskyi[1]*, PhD, Assistant Professor,*
[1] Admiral Makarov National University of Shipbuilding,
9, Heroyiv Ukraine Ave, Mykolaiv, 54025, Ukraine,
e-mail: venmkua@gmail.com;
vitalii.kostiuchenko@nuos.edu.ua (Corresponding Author);
sergii.novogretskyi@nuos.edu.ua

How to cite this article:
Vereshchago E.M., Kostiuchenko V.I., Novogretskyi S.M. Analysis of a DC converter working on a plasma arc. *Electrical Engineering & Electromechanics*, 2023, no. 5, pp. 31-36. doi: https://doi.org/10.20998/2074-272X.2023.5.05

UDC 621.314 https://doi.org/10.20998/2074-272X.2023.5.06

N. Zerzouri, N. Ben Si Ali, N. Benalia

A maximum power point tracking of a photovoltaic system connected to a three-phase grid using a variable step size perturb and observe algorithm

Purpose. *The production of electricity from solar energy is necessary because of the global consumption of this energy. This article's study is based on increased energy extraction by improving maximum power point tracking (MPPT). From different MPPT techniques proposed, the perturb and observe (P&O) technique is developed because of its low implementation cost and ease of implementation.* ***Methods***. *A modified variable step-size P&O MPPT algorithm is investigated which uses fuzzy logic to automatically adjust step-size to better track maximum power point, compared with the conventional fixed step-size method. The variable step P&O improves the speed and the tracking accuracy. This controller is implemented on a boost DC-DC power converter to track the maximum power point. The suggested controlled solar energy system includes a boost converter, a voltage-source inverter, and a grid filter. The control scheme of a three-phase current-controlled pulse-width modulation inverter in rotating synchronous coordinate d-q with the proposed MPPT algorithm and feed-forward compensation is studied.* ***Results***. *The photovoltaic grid-connected system controller employs multi-loop control with the filter inductor current of the inverter in the inner loop to achieve a fast dynamic response and the outer loop to control bus voltage for MPPT, the modeling, and control of three phase grid connected to photovoltaic generator is implemented in the MATLAB/Simulink environment and validated by simulation results.* References 27, tables 5, figures 29.

Key words: **photovoltaic generator, perturb and observe maximum power point tracking, modified perturb and observe maximum power point tracking, fuzzy logic control, boost converter, pulse-width modulation inverter, three phase grid.**

Мета. *Виробництво електроенергії із сонячної енергії необхідне через глобальне споживання цієї енергії. Дослідження цієї статті ґрунтується на збільшенні вилучення енергії за рахунок покращення відстеження точки максимальної потужності (MPPT). З різних запропонованих методів MPPT був розроблений метод збурення та спостереження (P&O) через його низьку вартість реалізації та простоту реалізації.* ***Методи***. *Досліджується модифікований алгоритм P&O MPPT зі змінним розміром кроку, який використовує нечітку логіку для автоматичного налаштування розміру кроку для кращого відстеження точки максимальної потужності порівняно із звичайним методом фіксованого розміру кроку. Змінний крок P&O підвищує швидкість та точність відстеження. Цей контролер реалізований на перетворювачі, що підвищує потужності постійного струму для відстеження точки максимальної потужності. Пропонована керована сонячна енергетична система включає підвищуючий перетворювач, інвертор джерела напруги і мережевий фільтр. Досліджується схема управління трифазним струмокерованим інвертором з широтно-імпульсною модуляцією в синхронній координаті, що обертається, d-q із запропонованим алгоритмом MPPT і попереджувальною компенсацією.* ***Результати***. *Контролер фотоелектричної системи, підключеної до мережі, використовує багатоконтурне керування зі струмом індуктора фільтра інвертора у внутрішньому контурі для досягнення швидкого динамічного відгуку та зовнішнім контуром для керування напругою шини для MPPT, моделювання та керування трифазною мережею. підключений до фотогальванічного генератора, реалізований у середовищі MATLAB/Simulink та підтверджений результатами моделювання.* Бібл. 27, табл. 5, рис. 29.

Ключові слова: **фотоелектричний генератор, збурення та відстеження точки максимальної потужності, модифіковане збурення та відстеження точки максимальної потужності, нечітке логічне управління, підвищуючий перетворювач, інвертор з широтно-імпульсною модуляцією, трифазна мережа.**

Introduction. World energy consumption is mainly covered by fossil fuels (oil, coal, natural gas, and nuclear) which gives rise to greenhouse gas emissions and therefore an increase in pollution. The additional danger is that excessive consumption of the stock of natural resources reduces the reserves of this type of energy dangerously for future generations. In this sense, the world converges toward using renewable energies, which are available and inexhaustible and inhibit emitting CO_2 gas. The development and integration of renewable energies into electrical production and distribution networks pose major technical challenges today. These networks must support a high demand, react quickly and safely to expected and unanticipated variations, and adapt to the constraints of users and environmental constraints. However, the major problem of this electrical energy production technique lies in the design and the realization of the photovoltaic (PV) systems, making it possible to ensure the optimal operation of the PV modules in various conditions. Since PV cells have electrical characteristics (current-voltage) non-linear, which strongly depend on climatic conditions, such as solar radiation and temperature, these climatic variations lead to non-linear and fluctuating power output. For this and with the development of specific power electronics for PV applications, several innovative conversion systems have been designed, particularly inverters with input matching stages that provide maximum power point (MPP) tracking. Indeed, these devices make it possible to adapt and optimize the production of PV through DC-DC power converters inserted between PV modules and inverter input. Usually, this equipment has electrical management mechanisms that allow the maximum power to be extracted from the PV generator output and ensure perfect adaptation between the generator's voltage and inverter input voltage regardless of meteorological conditions. These mechanisms are usually called maximum power point tracking (MPPT). In recent years, many different techniques or algorithms for automatically identifying and producing operations at approximately the MPP have been presented with practical implementations in the literature. These methods vary in complexity, cost, range of effectiveness, hardware implementation, popularity, convergence speed, and other respects. MPPT methods can be classified as incremental conductance [1-5], fractional short-circuit current [2], fractional open-circuit voltage [3], load current voltage maximization, ripple correlation control, hill climbing or perturb and observe (P&O) [4], neural network [6], fuzzy logic control and other MPPT methods [7, 8]. So far, the P&O method is the most commonly used technique in practice, owing to its ease of implementation in a low-cost controller. It has relatively good MPPT performance compared to the other techniques. Nevertheless, the P&O method fails to track the MPP effectively when radiation and temperature conditions change rapidly.

The conventional P&O is usually implemented with a fixed step size by which the controlled parameter such as reference voltage or duty cycle is adjusted; large step-size values increase the losses in the steady state condition due to large oscillation around the MPP, while small step-size values slow down the tracking speed when the atmospheric conditions quickly change. A trade-off between steady-state accuracy and dynamic tracking should be performed to solve this problem. In the literature, many improvements of the P&O method have been proposed to reduce the oscillation around the MPP in steady-state conditions. However, they increase the complexity, slow the tracking speed when the atmospheric conditions rapidly change and, degrade the algorithm efficiency on cloudy days [9]. To solve this problem, many authors have used P&O MPPT with variable step sizes, each in her own way and they deduced results that prove an improvement in tracking of maximum power. We find in the reference [8] many MPPT methods are reviewed and have been made to improve the conventional MPPT methods. However, in [10–12] shows the performance with the modified P&O algorithm which gives a faster response than the traditional P&O algorithm under variable irradiance conditions during peak power generation the impacts of partial shading conditions and temperature led to a high convergence rate with less overshoot and oscillation. On the other hand, [11] proposes a modified hill-climbing algorithm the proposed algorithm has good steady-state and dynamic performances. In work [13] introduced MPPT with a P&O algorithm with variable step size based on modified shuffled frog leaping algorithm (MSFLA) and sliding mode control (SMC) for PV power systems. The operation of the system with various partial shading regimes was evaluated and it was demonstrated that the developed MSFLA-SMC combinatorial scheme gives good efficiency in output power with significantly better response time and dynamic behavior.

In this study, P&O MPPT with variable step size is proposed. The step size is automatically tuned according to the variation of the atmospheric conditions, using a fuzzy logic controller.

To control active and reactive power for grid-connected inverters, the most common method has been used voltage-oriented control (VOC) which depends on two cascaded loops. The outer loop or voltage loop is tied to the DC link capacitor voltage, where a PI controller is used to generate the reference current for the inner or current loop. Then, two PI controllers are used to control the currents, and hence active/reactive power control.

The goal of the paper is the extraction of the maximum powers provided by the photovoltaic generator using the perturb and observe algorithm with fixed step size and variable step size adjusted by a fuzzy logic controller, another objective is the control of this power to be injected into a three-phase distribution network via a two-stage conversion system. The schematic of the proposed system is shown in Fig. 1, which illustrates the three-phase grid-connected PV generation system. The proposed system consists of two main parts; the first part is a power scheme, which includes: a PV array supply, DC link capacitor, boost converter, three-phase inverter, RL filter, and the three-phase utility grid. The second is the control scheme MPPT by using different MPPT techniques and the inverter controller with a three-phase PV grid-connected system.

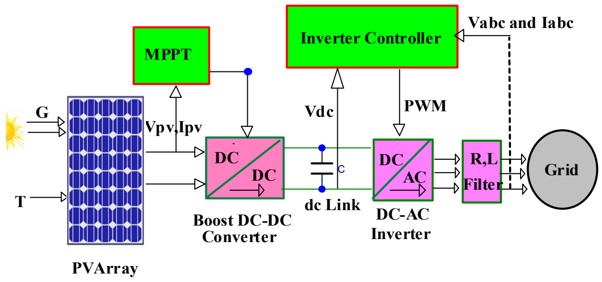

Fig. 1. Configuration of the proposed two-stage grid-connected PV system

PV cell model. Figure 2 shows the PV model based on a one-diode equivalent circuit. In the literature, an ideal *p-n* junction PV cell is often modeled as an electric current generator whose behavior is equivalent to an ideal current source which models the photoelectric current (I_{ph}) associated with a parallel diode which models the *p-n* junction. To take into account all the dissipative phenomena present during the conversion of light energy at the level of the cell, the circuit is completed by two resistors, one in series (R_s) and the other in parallel (R_{sh}). The series resistance characterizes the losses by the Joule effect and the parallel resistance characterizes the leakage current at the level of the *p-n* junction.

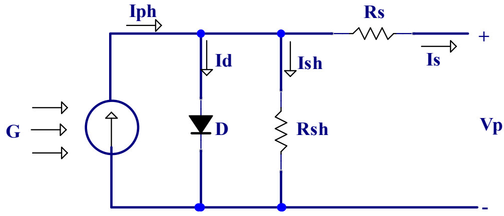

Fig. 2. The equivalent circuit of a solar cell

The PV cell output current I_{PV} (Fig. 2) is given as [14, 15]:

$$I = I_{ph} - I_s\left(\exp\left[\frac{q}{A\cdot K\cdot T_c}\cdot\left(V_{pv}+I_{pv}R_s\right)-1\right]\right) - \left(\frac{V_{pv}+I_{pv}R_s}{R_{sh}}\right), \tag{1}$$

where V_{pv} is the PV array output voltage; I_{pv} is the PV array output current; I_{ph} is the PV cell photocurrent; I_s is the PV cell saturation current; q is the electron charge (q = 1.602·10^{-19} C); A is the *p-n* junction ideality factor; K is the Boltzmann constant (K = 1.38·10^{-23} J/K); T_c is the absolute working temperature.

The photocurrent I_{ph} is related to the cell's operating temperature and solar intensity as:

$$I_{ph} = \left[I_{sc} + K_i\left(T_c - T_{ref}\right)\right]\frac{G}{1000}, \tag{2}$$

where I_{sc} is the short circuit current at standard temperature and irradiance condition (G = 1000 W/m^2 and T_{ref} = 25 °C); K_i is the short circuit current temperature coefficient; T_{ref} is the PV cell reference temperature.

PV cell reverse saturation current I_{rs} varies with the cell temperature [16, 17] as:

$$I_{rs}=\frac{I_{sc}+K_i\left(T_c-T_{ref}\right)}{\exp\left(\dfrac{V_{oc}+K_i\left(T_c-T_{ref}\right)}{V_t}\right)-1}; \tag{3}$$

$$V_t=\frac{N_s\cdot K\cdot T_c}{q}, \tag{4}$$

where V_{oc} is the open-circuit voltage at reference temperature T_{ref}; V_t is the junction thermal voltage; N_s is the number of solar cells connected in series (N_s = 1 for the solar cell).

The PV cell saturation current I_s varies with temperature [18] as:

$$I_s=I_{rs}\left(\frac{T_c}{T_{ref}}\right)^3\exp\left[\frac{q\cdot E_g}{A\cdot K}\left(\frac{1}{T_{ref}}-\frac{1}{T_c}\right)\right], \tag{5}$$

where E_g is the band energy of the semiconductor used in the cell.

In this work, the studied PV field is composed of two PV arrays, each comprising 2 series and 9 parallel connected modules of type Canadian Solar CS6X-305P. Each module contains a series of 72 polycrystalline silicon cells; resulting in total peak power of 305 W. Table 1 shows the specifications of the used PV modules in standard conditions.

Table 1

Parameters of Canadian Solar CS6X-305P PV module

Parameters	Value
Peak power, W	305.285
Peak power voltage, V	36.3
Peak power current, A	8.41
Short-circuit current, A	8.97
Open circuit voltage, V	44.8

The characteristics (I-V) and (P-V) of the studied PV field, under standard conditions of solar irradiation and temperature, is given in Fig. 3.

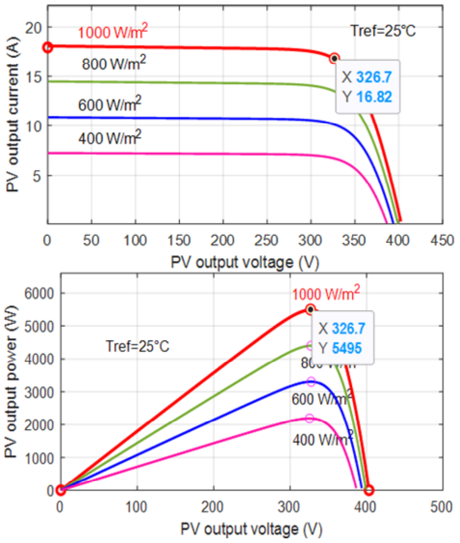

Fig. 3. (I-V) and (P-V) characteristic curves of a solar module at 25 °C temperature and 1000 W/m^2 irradiance level

Boost converter model. DC-DC converters have wide applications in PV systems. Whether it is a boost converter [15-19], buck-boost converter [20, 21], or buck converter [13]. DC-DC converters are considered the main element in the MPPT process; without them, the maximum power could not be achieved. In this study boost converter is used to change the terminal voltage of the PV array and from which MPPT can be obtained. The boost converter presented in Fig. 4 is composed of an inductance L_{pv}, a diode D, capacitors C_{pv}, C_{dc} and a switch S. The converter has two modes (states) of operation based on the switch action OFF and ON. The mathematic expression of the voltage and current on the input and output side of the DC-DC boost converter at duty cycle (D) can be described as:

$$V_{dc}=\frac{V_{pv}}{1-D}; \tag{6}$$

$$I_{dc}=I_{pv}(1-D). \tag{7}$$

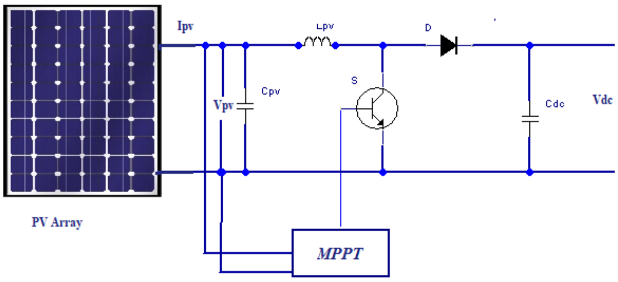

Fig. 4 Step-up boost converter

In the current source PV cell, the capacitor C_{pv} is evaluated by (8) and the standards of its elements:

$$C_{pv}=\frac{D\cdot V_{pv}}{4\cdot \varDelta V_{pv}\cdot f_s^2\cdot L_{pv}}; \tag{8}$$

$$D=1-\frac{V_{pv}}{V_{dc}}; \tag{9}$$

$$L_{pv}=\frac{V_{pv}\cdot\left(V_{dc}-V_{pv}\right)}{\varDelta I_{L_{pv}}\cdot f_s\cdot V_{dc}}; \tag{10}$$

$$\varDelta I_{L_{pv}}=0.13\cdot I_{pv}\cdot\frac{V_{dc}}{V_{pv}}; \tag{11}$$

$$C_{dc}\geq\frac{P_{pv}}{\varDelta V_o\cdot f_s\cdot V_{dc}}, \tag{12}$$

where V_{pv} is the converter input voltage; I_{pv} is the array maximum current; P_{PV} is the nominal power of PV; f_s is the converting frequency; C_{pv} is the link capacitance of PV; C_{dc} is the capacitance of DC-link; L_{pv} is the inductance of boost converter; V_{dc} is the boost converter output voltage; $\varDelta V_{pv}$ is the voltage variation; $\varDelta I_{Lpv}$ is the current ripple of boost inductance; $\varDelta V_o$ is the ripple of output voltage.

Modeling and control of DC/AC inverter. The main inverter function is to interface the PV generator with the network (Fig. 5). At the same time, the inverter is used to transform the DC voltage on the output side of the boost converter (the intermediate circuit of the inverter) into an AC voltage at its output. Voltage-source converter (VSC) is controlled in the rotating d-q frame to inject a controllable three-phase alternating current into the network. Current is injected in phase with the grid voltage to achieve unity power factor operation. The three-phase VSC is made up of three arms of two switches each reversible in current, they are made by controllable semiconductors on opening and closing (of the IGBT type in almost all cases). A recovery diode is mounted head to tail with the controllable semiconductor for each switch. A filter is placed between the network and the inverter, connecting them to the common point of interconnection.

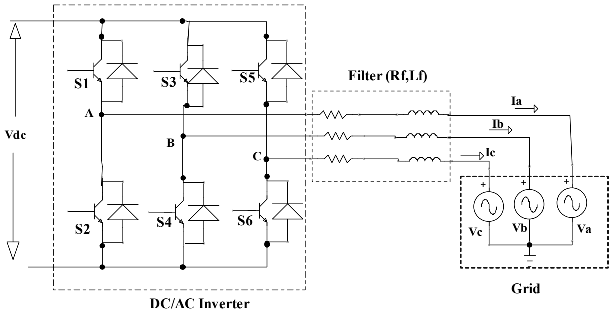

Fig. 5. Three-phase grid-connected inverter

The three-phase equations of the electrical network can be established as [22, 23]:

$$\begin{cases} u_a = R_f \cdot i_a + L_f \cdot \dfrac{\mathrm{d}i_a}{\mathrm{d}t} + v_a; \\ u_b = R_f \cdot i_b + L_f \cdot \dfrac{\mathrm{d}i_b}{\mathrm{d}t} + v_b; \\ u_c = R_f \cdot i_c + L_f \cdot \dfrac{\mathrm{d}i_c}{\mathrm{d}t} + v_c; \end{cases} , \tag{13}$$

where v_a, v_b, v_c are the grid voltages; i_a, i_b, i_c are the injected currents; u_a, u_b, u_c are the inverter side voltages.

This type of inverter is known as an on two levels because its output voltage has two voltage levels ($+V_{dc}$ and $-V_{dc}$). Using the a-b-c to d-q transformations, the converter 3-phase currents and voltages are expressed in a 2-axis d-q reference frame, synchronously rotating at a given AC frequency ω:

$$\begin{cases} u_d = R_f \cdot i_d + L_f \cdot \dfrac{\mathrm{d}i_d}{\mathrm{d}t} - \omega \cdot L_f \cdot i_q + v_d; \\ u_q = R_f \cdot i_q + L_f \cdot \dfrac{\mathrm{d}i_q}{\mathrm{d}t} - \omega \cdot L_f \cdot i_d + v_q. \end{cases} \tag{14}$$

The current controller and control equations of u_d and u_q can be rewritten as:

$$\begin{cases} u_d = P \cdot I \cdot \left(I_{dref} - I_d\right) - \omega \cdot L_f \cdot i_q + v_d; \\ u_q = P \cdot I \cdot \left(I_{qref} - Iq\right) + \omega \cdot L_f \cdot i_d + v_q. \end{cases} \tag{15}$$

The active and reactive power injected by the PV generator in the grid can be defined for a balanced three-phase system as follows [17]:

$$P = \frac{3}{2} \cdot \left(v_d \cdot i_d + v_q \cdot i_q\right); \quad Q = \frac{3}{2} \cdot \left(v_q \cdot i_d + v_d \cdot i_q\right). \tag{16}$$

Applying the voltage orientation technique to the d-axis, the active and reactive power (16) can be rewritten as:

$$P = \frac{3}{2} \cdot v_d \cdot i_d; \quad Q = -\frac{3}{2} \cdot v_d \cdot i_q . \tag{17}$$

According to (17), the active power can be controlled by the current i_d, and the reactive power can be controlled by the current i_q.

DC-link voltage control. The DC voltage controller is discussed as the outer controller. Dimensioning of the DC link voltage controller is determined by the function between the current reference value to be given and the DC link voltage [24]. The general model of the external controller can thus be given in Fig. 6. For the PI controller block of the function of $K(s)$, the outer voltage control can be implemented as:

$$i_{dref} = \left(U_{dcref} - U_{dc}\right) \cdot \left(K_{pu} + \frac{K_{iu}}{s}\right). \tag{18}$$

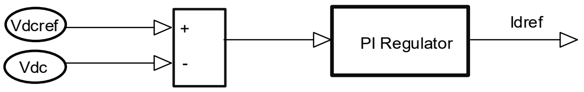

Fig. 6. Model of the DC-voltage controller

The phase-locked loop (PLL) technique [25] has been used to synthesize the electrical system's phase and frequency information, especially when interfacing with power electronic devices. PLL block [26] measures the system frequency and provides the phase synchronous angle θ (more precisely [sinθ, cosθ]) for the d-q transformations block. In the steady state, sinθ is in phase with the fundamental (positive sequence) of α component and phase A. In the three-phase system, the d-q transform of the three-phase variables has the same characteristics and the PLL system can be implemented using the d-q transform. The block diagram of the PLL system is described in Fig. 7.

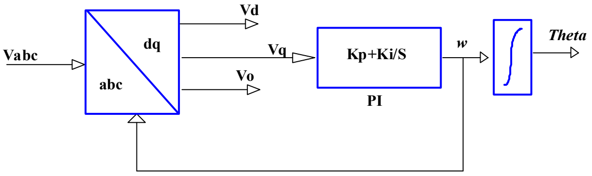

Fig. 7. Schematic diagram of the PLL

Fixed step size P&O algorithm. The P&O method compares the power of the previous step with the new step's power to increase or decrease the tension in search of the MPP. According to [6–10, 13–26], the MPP value is never definitively reached since the disturbances only leave the system oscillating close to the MPP in a steady state. The P&O method presents good results when the irradiance or temperature does not change rapidly with time. On the other hand, among the disadvantages of the method, in addition to the error in steady state, the dynamic response is considered slow when there are rapid temperature and solar radiation changes. The flowchart of this technique with the reference voltage variation is shown in Fig. 8.

Generally, the P&O MPPT algorithm run with a fixed step size. The P&O MPPT with fixed step size gives a good dynamic performance, he converges faster to a steady state but the oscillation is much higher. So, this hurts the MPPT efficiency. A solution that remedies this problem is the variable-step P&O algorithm which has been developed [11, 12]. The proposed MPPT algorithm is based on the conventional P&O algorithm; a fuzzy logic controller block is used to provide variable step size to overcome the limitation that exists in conventional P&O algorithm implementations. The flow chart of the proposed P&O algorithm with variable step size is illustrated in Fig. 9.

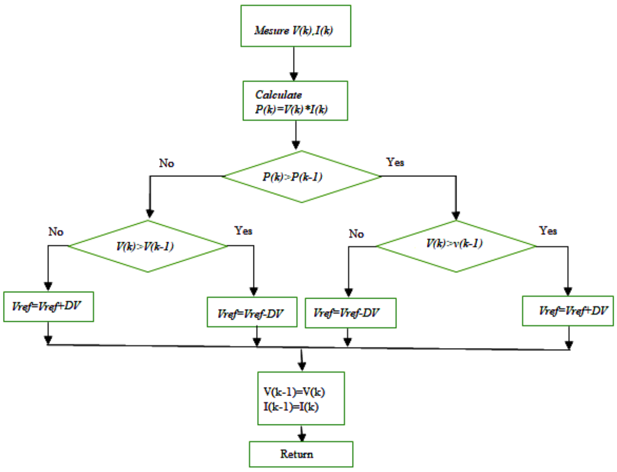

Fig. 8. Flowchart for MPPT for P&O algorithm

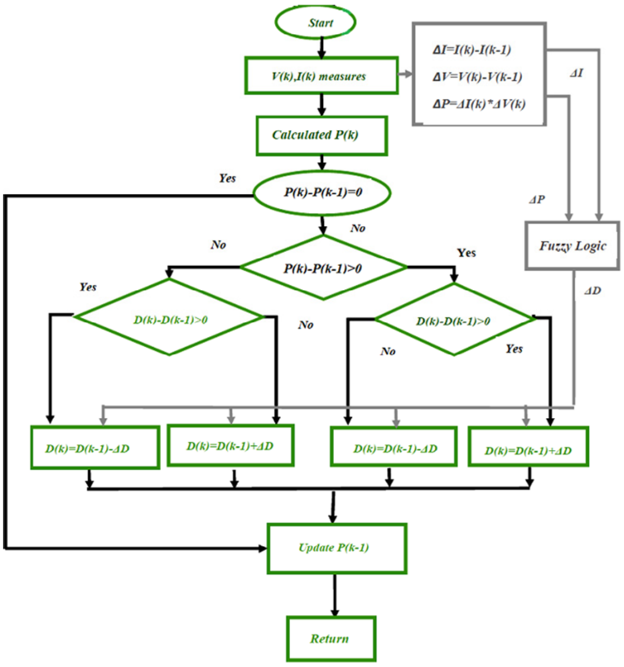

Fig .9. Block diagram of the proposed P&O with a variable step size

When the operating point is far from the MPP, the fuzzy logic control (FLC) adjusts the step size to a large value, and if the operating point is close to the MPP, the step size value is set to a small value.

FLC used as the variable step size. Control by FLC is a method that allows the construction of non-linear controllers from heuristic information from the specialist's knowledge FLC consists of the variation of voltage (or current) and power of the PV array, and according to these variations, the algorithm acts on the converter, through a pulse-width modulation, to correct the MPP voltage. Fuzzy MPPT is a well-established technique, generally acting on power variation (ΔP) and voltage variation (ΔV). In this work, the variable ΔV was replaced by the current variation (ΔI), because in this implemented arrangement the output variable of the FLC is the variation of the step-size ΔD, which is sent to the P&O algorithm. The input variables, ΔP_{pv} and ΔI_{pv}, of the proposed fuzzy logic variable step-size can be calculated by the following equations, where $P_{pv}(k)$ and $I_{pv}(k)$ are the PV array power and current respectively and $V_{pv}(k)$ is the PV array voltage:

$$\Delta V_{pv} = V_{pv}(k) - V_{pv}(k-1); \tag{19}$$

$$\Delta I_{pv} = I_{pv}(k) - I_{pv}(k-1); \tag{20}$$

$$\Delta P_{pv} = \Delta V_{pv} \cdot \Delta I_{pv}. \tag{21}$$

The MPPT fuzzy implemented consisted of input variables ΔP and ΔI, and output variable ΔD. The membership function of the input and the output variables used in this model has the same shape and is shown in Fig. 10–12. All the membership functions are expressed with a triangular function and they consist of 5 fuzzy subsets, which are denoted by NB (negative big), NS (negative small), ZZ (zero), PS (positive, small), and PB (positive big) curves.

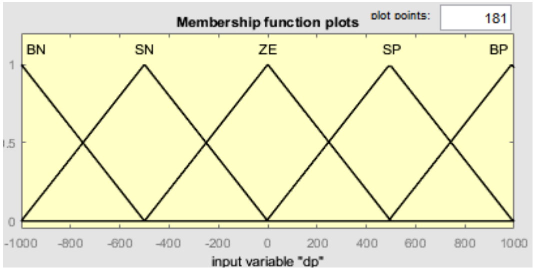

Fig. 10. Input variable ΔP

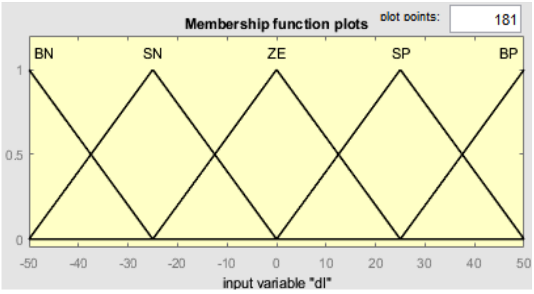

Fig. 11. Input variable ΔI

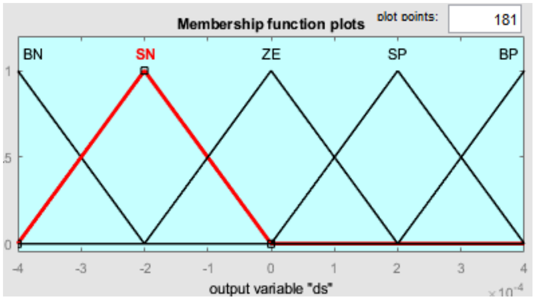

Fig. 12. Output variable ΔD

The fuzzy rule base is a collection of if-then rules which all the information is available for the controlled parameters. Since the number of membership function of each input is 5, then the fuzzy inference rules of the FLC consist of 25 rules as illustrated in Table 2. These rules are used to determine the output of the controller (the variable step-size for the P&O algorithm) to track the MPP and stop iterating once this point is reached.

Table 2

Membership function rules

ΔI_{pv}	ΔP_{pv}				
	NB	NS	ZZ	PS	PB
NB	NB	NS	NS	ZZ	ZZ
NS	NS	ZZ	ZZ	ZZ	PS
ZZ	ZZ	ZZ	ZZ	PS	PS
PS	ZZ	PS	PS	PS	PB
PB	PS	PS	PB	PB	PB

Mamdani's method is used as a fuzzy interface method with max-min operation combined with fuzzy law in this work. After the rules have been evaluated, the output of the fuzzy controller is still a fuzzy set. However, the actual system usually requires a non-fuzzy value of a control. Hence the process of defuzzification is required to as the last step to calculate the crisp output of the proposed fuzzy control. The output of the proposed FLC is defuzzified using the center of gravity method to calculate ΔD computed as:

$$\Delta D(k)=\frac{\sum_{i=1}^{25}\mu(\Delta D_i(k))\Delta D_i(k)}{\sum_{i=1}^{25}\mu(\Delta D_i(k))}, \qquad (22)$$

where ΔD_i is the center of max–min technique composition at the output membership function. The FLC output that is a variable step size $\Delta D(k)$ is used to compute the final duty cycle $D(k)$ as:

$$D(k)=D(k-1)+\Delta D(k). \qquad (23)$$

Results and discussion. In this section, the performances of the proposed system are analyzed by simulation in the MATLAB/SimPowerSys environment. Figure 13 shows the architecture of the three-phase two-stage grid-connected PV system, in which the control of injected current, DC link voltage, and MPPT is realized. Also, the influence of variation in climatic conditions on the output performance of the system is realized. After that, a simulation of the P&O and variable step-size P&O (VSP&O) MPPT algorithm with analysis covering stability, time response, oscillation, and overshoot is performed. The simulation parameters of the system are shown in Table 3.

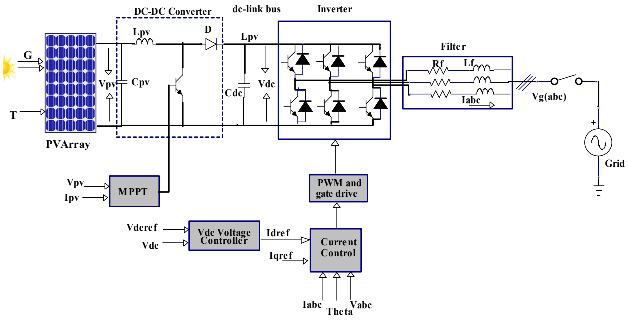

Fig. 13. Model of the three-phase two-stage grid-connected PV system

Table 3

Simulation parameters of the system

Parameters	Value
Input capacitor C_{pv}, F	$5\cdot10^{-6}$
Inductance L, H	$3\cdot10^{-2}$
DC link capacitor C_{dc}, F	$12\cdot10^{-3}$
Switching frequency f_{sw}, kHz	4
DC link voltage V_{dc}, V	700
Grid frequency f, Hz	50
Utility grid voltage V_g, V	220
Inductance filter L_f, H	$5\cdot10^{-3}$
Resistance filter R_f, Ω	0.1

The simulation was performed for variable irradiance, with a fixed ambient temperature (25 °C), to test the performance of the two proposed algorithms. The applied irradiance was with a range between 400 and 1000 W/m², at the time step was 0.5 s. The results shown in Fig. 14, 21 are limited to those for the PV array respectively show the irradiance profile applied to the PV array and the output power of the PV array with a comparison between P&O MPPT and VSP&O MPPT which clearly shows the stabilization of the power around its maximum for all the variations of the irradiation in the VSP&O, whereas it oscillates around the maximum power and moves away from the maximum for the weak irradiance in the P&O. In Fig. 15 we observe how the increase in incident solar radiation causes an increase in the current generated, at a constant temperature of 25 °C thus increasing the power produced by the photovoltaic generator as seen in Fig. 16. It is clear that the direct component of the current represented in Fig. 23, coincides perfectly with the reference direct component and that the overshoot with VSP&O is less than in the case of P&O.

Table 4 provides a summary of tracking performance for the VSP&O MPPT and P&O MPPT methods with different levels of illumination.

Table 4

Tracking performance comparison between P&O MPPT and VSP&O MPPT methods

Irradiance / MPPT	G, W/m^2	1000	800	600	400
	$P_{\max}$, W	5495	4402	3302	2189
Irradiance P&O with fixed step-size	P_{pv}, W	5413	4185	3178	2033
	Efficiency η, %	98.5	95.07	96.03	92.86
	Tracking time, s	0.153	0.101	0.046	0.0786
	Steady-state power oscillation	high	V-high	V-high	high
P&O with variable step-size	P_{pv}, W	5438	4365	3272	2175
	Efficiency η, %	98.95	99.04	99.1	99.34
	Tracking time, s	0.149	0.0479	0.0556	0.0151
	Steady-state power oscillation	none	none	none	none

From Fig. 17, 18 of PV current and voltage, it is clear that large oscillations appear around the maximum values when the irradiation is reduced, and they move away from the maximum point when the irradiation becomes very low, these problems disappear when using the VSP&O method, as shown in Fig. 19, 20, where the PV output voltage and current reach the maximum with a rapid time and almost without oscillations. For the three-phase grid-connected system, the phase current and voltage are shown in Fig. 24 which is obtained with a conventional PI controller for both algorithms, to indicate the impact of irradiation variation on the current and the voltage, we focus on the time range [0 – 0.04] s where the irradiation is at 1000 W/m^2. Only the peaks of the current for VSP&O are observed to be reduced concerning P&O and the currents decrease when the irradiation decreases while the amplitude of the voltage remains constant. From Fig. 27 it can be observed that the recorded overshoot of the DC bus voltage is 140 V with P&O, while with VSPO the overshoot is 110 V. From these parameters, the VSP&O performs very well in terms of stability.

To illustrate the impact of the MPPT method on the power quality, a spectral analysis of the current obtained with standard test conditions is performed and the spectrum of the harmonic is shown in Fig. 28, 29. We note that the total harmonic distortion (THD) obtained with P&O is 8.42 % while a THD of 6.17 % was obtained with VSP&O, which proves the effectiveness of the VSP&O algorithm compared to P&O.

It is noticed in the interval [0 – 0.06] s that the transient responses for VSP&O of the active and reactive powers are characterized by a very small overshoot compared to the P&O MPPT, while the steady-state error is close to zero as shown in Fig. 25, 26. According to the results obtained, the VOC strategy with classic PI in terms of speed, system stability, and precision has led to satisfactory results.

From the simulation results, the proposed VSP&O MPPT performs well compared to P&O MPPT.

Comparison with existing variable step size MPPT methods. Table 5 summarizes and compares the performances for each controller, the tracking error and the tracking efficiency reveal at any point the proposed controller is efficient and accurate with regards to harvesting the maximum power from the PV system. Also, Fig. 22 presents the average tracking efficiency of the conventional and proposed techniques [27]:

$$Eff = P_{pv}\cdot 100\%/P_{MPP}. \qquad (23)$$

The error is calculated as:

$$Err = (P_{MPP} - P_{pv})\cdot 100\%/P_{MPP}, \qquad (24)$$

where P_{pv} is the power generated by the controller; P_{MPP} is the PV MPP.

Table 5

Comparison between the conventional and VSP&O MPPT technique at 1000 W/m^2 and 25 °C

MPPT Algorithm	Settling time, s	Theoretical power P_{MPP}, W	Output power P_{pv}, W	Efficiency, %	Error, %
Fixed step P&O	0.078	5495	5413	93.04	6.95
Variable step P&O [24]	0.025	13183.3	12576.8	95.4	4.6
Variable step P&O [27]	0.0399	2563	2554	99.6	–
Variable step P&O proposed	0.068	5495	5438	98.95	1.02

Comparing our results with the two references [24] and [27], we notice that the proposed P&O method has also contributed to improving efficiency and reducing oscillations around the MPP.

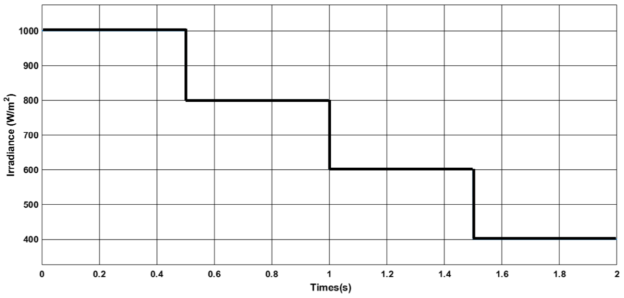

Fig. 14. Irradiance profile

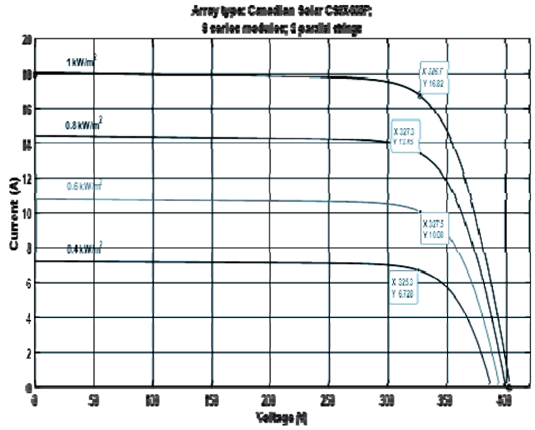

Fig. 15. PV current characteristics under fixed temperature and variable irradiance

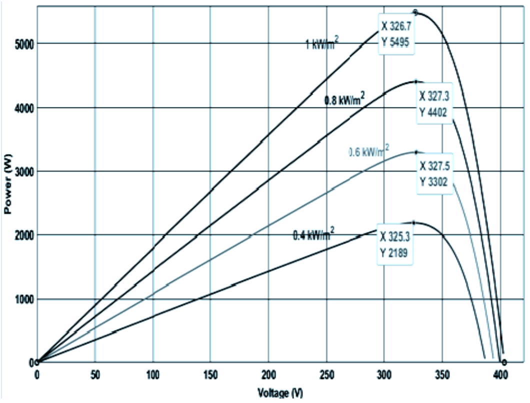

Fig. 16. PV power characteristics under fixed temperature and variable irradiance

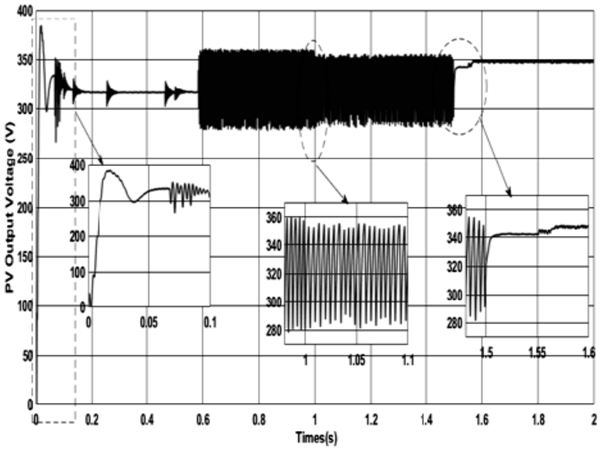

Fig. 17. PV output voltage with fixed step size P&O MPPT

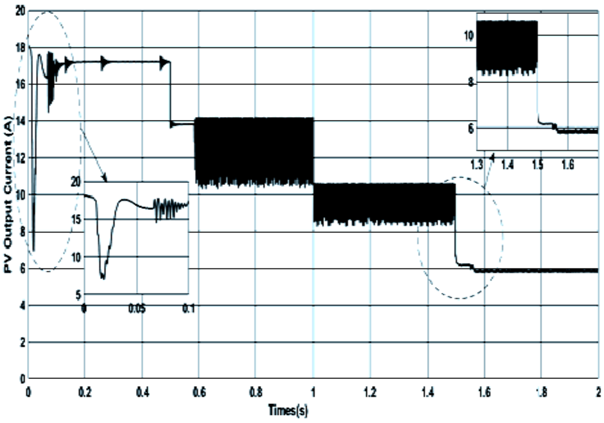

Fig. 18. PV output current with fixed step size P&O MPPT

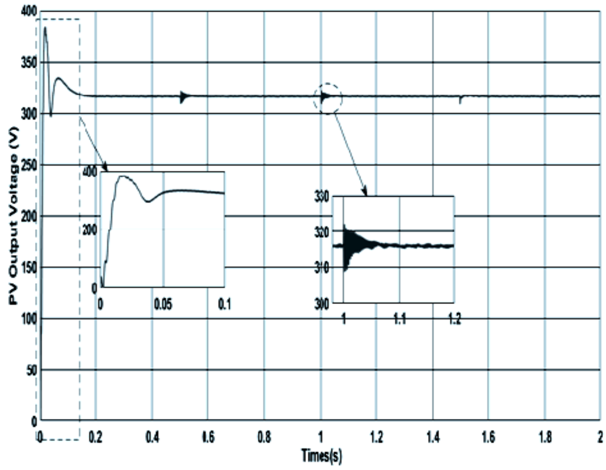

Fig. 19. PV output voltage with variable step size P&O MPPT

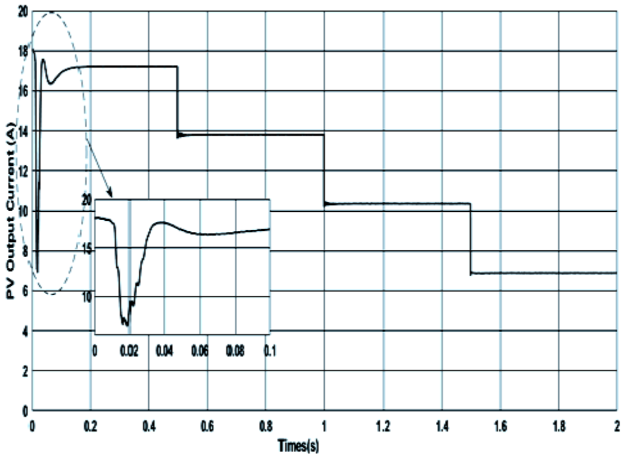

Fig. 20. PV output current with variable step size P&O MPPT

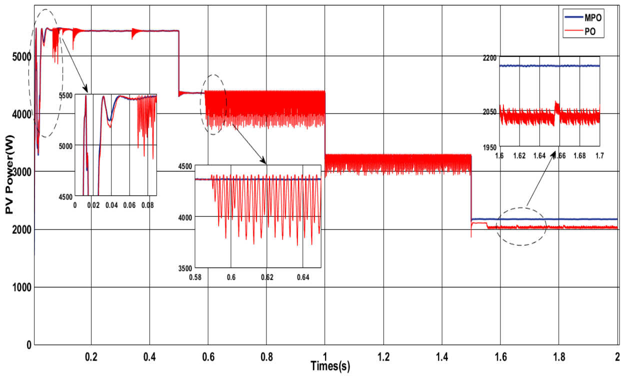

Fig. 21. Simulation result with comparison of fixed step size P&O MPPT and the proposed FLC-based variable step size P&O MPPT with change in irradiance: PV power

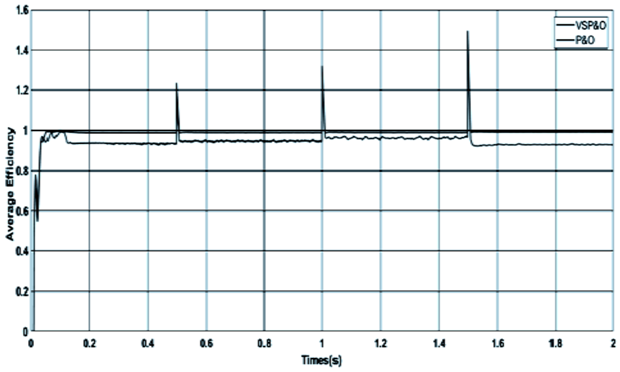

Fig. 22. Efficiency curves

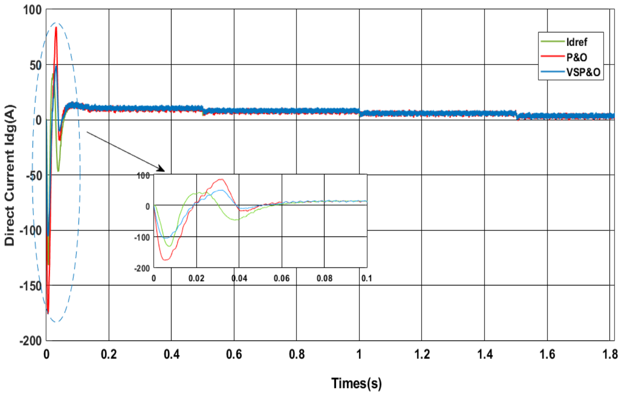

Fig. 23. Simulation result with comparison of fixed step size P&O MPPT and the proposed FLC-based variable step size P&O MPPT with change in irradiance: direct current grid

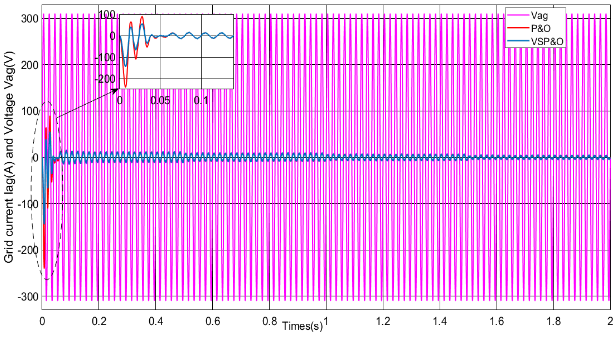

Fig. 24. Simulation result with comparison of fixed step size P&O MPPT and the proposed FLC-based variable step size P&O MPPT with change in irradiance: voltage and current grid

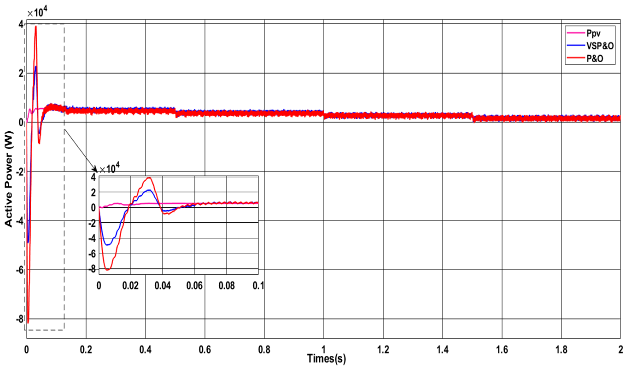

Fig. 25. Simulation result with comparison of fixed step size P&O MPPT and the proposed FLC-based variable step size P&O MPPT with change in irradiance: active power to grid

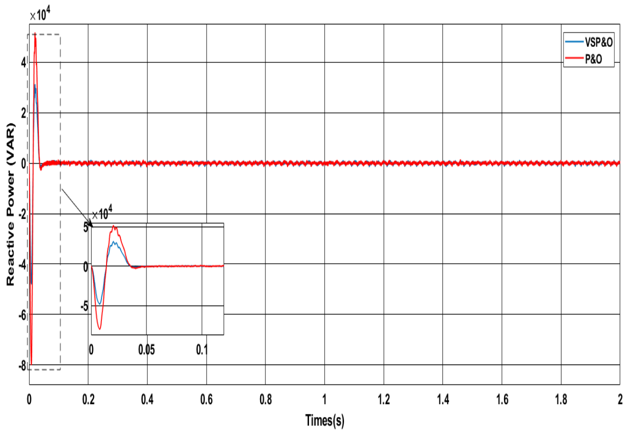

Fig. 26. Simulation result with comparison of fixed step size P&O MPPT and the proposed FLC-based variable step size P&O MPPT with change in irradiance: reactive power to grid

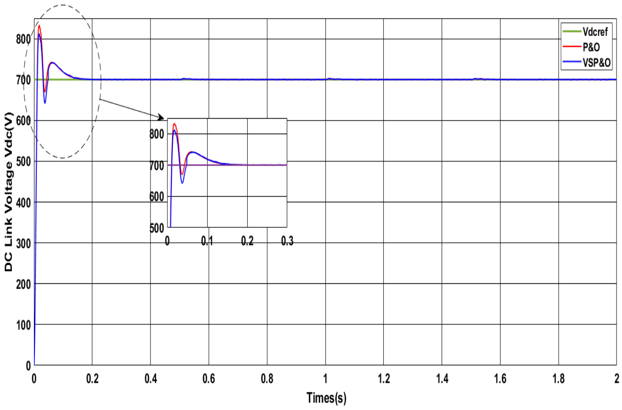

Fig. 27. Simulation result with comparison of fixed step size P&O MPPT and the proposed FLC-based variable step size P&O MPPT with change in irradiance: DC link voltage

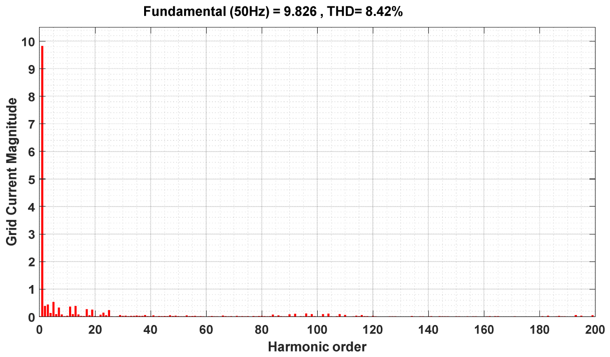

Fig. 28. THD of grid current with P&O MPPT

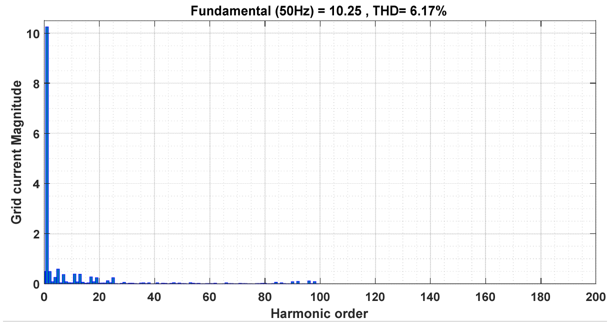

Fig. 29. THD of grid current with VSP&O MPPT

Conclusions. This work presented two photovoltaic generator power maximization algorithms applied to a two-stage three-phase network. A boost converter is used to increase the voltage at the output of the photovoltaic generator by using the two cases of maximum power point tracking, i.e. the perturb and observe method with fixed step and the variable step method calculated by a fuzzy logic block in such a way efficient and precise. The maximum power point tracking variable step size perturb and observe method was found to be more robust compared to the fixed step size perturb and observe method, due to an oscillation-free photovoltaic power response at the instant of irradiance variations. In a steady state, the performance of the maximum power point tracking fixed step size was inferior to the maximum power point tracking variable step size perturb and observe, as it had a larger error, due to the relevance curves and the level of oscillation, especially at the low irradiation.

Conflict of interest. The authors declare that they have no conflicts of interest.

REFERENCES

1. Hlaili M., Mechergui H. Comparison of Different MPPT Algorithms with a Proposed One Using a Power Estimator for Grid Connected PV Systems. *International Journal of Photoenergy*, 2016, pp. 1–10. doi: https://doi.org/10.1155/2016/1728398.

2. Nzoundja Fapi C.B., Wira P., Kamta M., Badji A., Tchakounte H. Real-Time Experimental Assessment of Hill Climbing MPPT Algorithm Enhanced by Estimating a Duty Cycle for PV System. *International Journal of Renewable Energy Research*, 2019, vol. 9, no. 3, pp. 1180-1189. doi: https://doi.org/10.20508/ijrer.v9i3.9432.g7705.

3. Shebani M.M., Iqbal T., Quaicoe J.E. Comparing bisection numerical algorithm with fractional short circuit current and open circuit voltage methods for MPPT photovoltaic systems. *2016 IEEE Electrical Power and Energy Conference (EPEC)*, 2016, pp. 1-5. doi: https://doi.org/10.1109/EPEC.2016.7771689.

4. Louarem S., Kebbab F.Z., Salhi H., Nouri H. A comparative study of maximum power point tracking techniques for a photovoltaic grid-connected system. *Electrical Engineering & Electromechanics*, 2022, no. 4, pp. 27-33. doi: https://doi.org/10.20998/2074-272X.2022.4.04.

5. Shang L., Guo H., Zhu W. An improved MPPT control strategy based on incremental conductance algorithm. *Protection and Control of Modern Power Systems*, 2020, vol. 5, no. 1, p. 14. doi: https://doi.org/10.1186/s41601-020-00161-z.

6. Elhor A., Soares O. Grid-connected PV System with a modified-Neural Network Control. *International Journal of Renewable Energy Research*, 2022, vol. 12, no. 2, pp. 1013-1022. doi: https://doi.org/10.20508/ijrer.v12i2.12754.g8485.

7. Xu S., Shao R., Cao B., Chang L. Single-phase grid-connected PV system with golden section search-based MPPT algorithm. *Chinese Journal of Electrical Engineering*, 2021, vol. 7, no. 4, pp. 25-36. doi: https://doi.org/10.23919/CJEE.2021.000035.

8. Li X., Wang Q., Wen H., Xiao W. Comprehensive Studies on Operational Principles for Maximum Power Point Tracking in Photovoltaic Systems. *IEEE Access*, 2019, vol. 7, pp. 121407-121420. doi: https://doi.org/10.1109/ACCESS.2019.2937100.

9. Manoharan P., Subramaniam U., Babu T.S., Padmanaban S., Holm-Nielsen J.B., Mitolo M., Ravichandran S. Improved Perturb and Observation Maximum Power Point Tracking Technique for Solar Photovoltaic Power Generation Systems. *IEEE Systems Journal*, 2021, vol. 15, no. 2, pp. 3024-3035. doi: https://doi.org/10.1109/JSYST.2020.3003255.

10. Kumar V., Singh M. Derated Mode of Power Generation in PV System Using Modified Perturb and Observe MPPT Algorithm. *Journal of Modern Power Systems and Clean Energy*, 2021, vol. 9, no. 5, pp. 1183-1192. doi: https://doi.org/10.35833/MPCE.2019.000258.

11. Zhu W., Shang L., Li P., Guo H. Modified hill climbing MPPT algorithm with reduced steady-state oscillation and improved tracking efficiency. *The Journal of Engineering*, 2018, vol. 2018, no. 17, pp. 1878-1883. doi: https://doi.org/10.1049/joe.2018.8337.

12. Ali Z.M., Vu Quynh N., Dadfar S., Nakamura H. Variable step size perturb and observe MPPT controller by applying θ-modified krill herd algorithm-sliding mode controller under partially shaded conditions. *Journal of Cleaner Production*, 2020, vol. 271, art. no. 122243. doi: https://doi.org/10.1016/j.jclepro.2020.122243.

13. Mohammadinodoushan M., Abbassi R., Jerbi H., Waly Ahmed F., Abdalqadir kh ahmed H., Rezvani A. A new MPPT design using variable step size perturb and observe method for PV system under partially shaded conditions by modified shuffled frog leaping algorithm- SMC controller. *Sustainable Energy Technologies and Assessments*, 2021, vol. 45, art. no. 101056. doi: https://doi.org/10.1016/j.seta.2021.101056.

14. Kumar N., Saha T.K., Dey J. Multilevel Inverter (MLI)-Based Stand-Alone Photovoltaic System: Modeling, Analysis, and Control. *IEEE Systems Journal*, 2020, vol. 14, no. 1, pp. 909-915. doi: https://doi.org/10.1109/JSYST.2019.2900485.

15. Delavari H., Zolfi M. Maximum power point tracking in photovoltaic systems using indirect adaptive fuzzy robust controller. *Soft Computing*, 2021, vol. 25, no. 16, pp. 10969-10985. doi: https://doi.org/10.1007/s00500-021-05823-0.

16. Yang B., Yu T., Shu H., Zhu D., An N., Sang Y., Jiang L. Perturbation observer based fractional-order sliding-mode controller for MPPT of grid-connected PV inverters: Design and real-time implementation. *Control Engineering Practice*, 2018, vol. 79, pp. 105-125. doi: https://doi.org/10.1016/j.conengprac.2018.07.007.

17. Ali A.I.M., Mohamed H.R.A. Improved P&O MPPT algorithm with efficient open-circuit voltage estimation for two-stage grid-integrated PV system under realistic solar radiation. International *Journal of Electrical Power & Energy Systems*, 2022, vol. 137, art. no. 107805. doi: https://doi.org/10.1016/j.ijepes.2021.107805.

18. Roselyn J.P., Chandran C.P., Nithya C., Devaraj D., Venkatesan R., Gopal V., Madhura S. Design and implementation of fuzzy logic based modified real-reactive power control of inverter for low voltage ride through enhancement in grid connected solar PV system. *Control Engineering Practice*, 2020, vol. 101, art. no. 104494. doi: https://doi.org/10.1016/j.conengprac.2020.104494.

19. Ahmed M., Abdelrahem M., Farhan A., Harbi I., Kennel R. DC-link sensorless control strategy for grid-connected PV systems. *Electrical Engineering*, 2021, vol. 103, no. 5, pp. 2345-2355. doi: https://doi.org/10.1007/s00202-021-01228-2.

20. López Seguel J., Seleme S.I., Moráis L.M.F. Comparison of the performance of MPPT methods applied in converters Buck and Buck-Boost for autonomous photovoltaic systems. *Ingeniare. Revista Chilena de Ingeniería*, 2021, vol. 29, no. 2, pp. 229-244. doi: https://doi.org/10.4067/S0718-33052021000200229.

21. Boumaaraf H., Talha A., Bouhali O. A three-phase NPC grid-connected inverter for photovoltaic applications using neural network MPPT. *Renewable and Sustainable Energy Reviews*, 2015, vol. 49, pp. 1171-1179. doi: https://doi.org/10.1016/j.rser.2015.04.066.

22. Hai T., Zhou J., Muranaka K. An efficient fuzzy-logic based MPPT controller for grid-connected PV systems by farmland fertility optimization algorithm. *Optik*, 2022, vol. 267, art. no. 169636. doi: https://doi.org/10.1016/j.ijleo.2022.169636.

23. Bhunia M., Subudhi B., Ray P.K. Design and Real-Time Implementation of Cascaded Model Reference Adaptive Controllers for a Three-Phase Grid-Connected PV System. *IEEE Journal of Photovoltaics*, 2021, vol. 11, no. 5, pp. 1319-1331. doi: https://doi.org/10.1109/JPHOTOV.2021.3093047.

24. Charaabi A., Zaidi A., Barambones O., Zanzouri N. Implementation of adjustable variable step based backstepping control for the PV power plant. *International Journal of Electrical Power & Energy Systems*, 2022, vol. 136, art. no. 107682. doi: https://doi.org/10.1016/j.ijepes.2021.107682.

25. Repak M., Otcenasova A., Altus J., Regula M. Grid-tie power converter for model of photovoltaic power plant. *Electrical Engineering*, 2017, vol. 99, no. 4, pp. 1377-1391. doi: https://doi.org/10.1007/s00202-017-0611-6.

26. Shayestegan M. Overview of grid-connected two-stage transformer-less inverter design. *Journal of Modern Power Systems and Clean Energy*, 2018, vol. 6, no. 4, pp. 642-655. doi: https://doi.org/10.1007/s40565-017-0367-z.

27. Ali A.I.M., Sayed M.A., Mohamed E.E.M. Modified efficient perturb and observe maximum power point tracking technique for grid-tied PV system. *International Journal of Electrical Power & Energy Systems*, 2018, vol. 99, pp. 192-202. doi: https://doi.org/10.1016/j.ijepes.2017.12.029.

Received 19.12.2022
Accepted 21.01.2023
Published 01.09.2023

Nora Zerzouri[1]*, Doctor of Technical Sciences,*
Nadia Ben Si Ali[1]*, Professor of Electrical Engineering,*
Nadia Benalia[1]*, Doctor of Technical Sciences,*
[1] Electrical Engineering Laboratory of Annaba,
Badji Mokhtar University Annaba, Algeria,
e-mail: nora.zerzouri@univ-annaba.dz (Corresponding Author);
bensialin@yahoo.fr; benalianadia13@yahoo.com

How to cite this article:
Zerzouri N., Ben Si Ali N., Benalia N. A maximum power point tracking of a photovoltaic system connected to a three-phase grid using a variable step size perturb and observe algorithm. *Electrical Engineering & Electromechanics*, 2023, no. 5, pp. 37-46. doi: https://doi.org/10.20998/2074-272X.2023.5.06

UDC 621.3.013 https://doi.org/10.20998/2074-272X.2023.5.07

B.I. Kuznetsov, T.B. Nikitina, I.V. Bovdui, K.V. Chunikhin, V.V. Kolomiets, B.B. Kobylianskyi

Method for control by orbital spacecraft magnetic cleanliness based on multiple magnetic dipole models with consideration of their uncertainty

***Aim**. Development of method for control by orbital spacecraft magnetic cleanliness based on multiple magnetic dipole models using compensation of the initial magnetic field with consideration of magnetic characteristics uncertainty. **Methodology.** Orbital spacecraft multiple magnetic dipole models calculated as solution of nonlinear minimax optimization problem based on near field measurements for prediction orbital spacecraft far magnetic field magnitude. Nonlinear objective function calculated as the weighted sum of squared residuals between the measured and predicted magnetic field. Weight matrix calculated as inverse covariance matrix of random errors vector. Values of magnetic moments and coordinates of placement of compensating magnetic dipoles for compensation of the orbital spacecraft initial magnetic field also calculated as solution of nonlinear minimax optimization problem. Both solutions of this nonlinear minimax optimization problems calculated based on particle swarm nonlinear optimization algorithms. **Results.** Results of prediction spacecraft far magnetic field magnitude based on orbital spacecraft multiple magnetic dipole models using near field measurements and compensation of the initial magnetic field with consideration of orbital spacecraft magnetic characteristics uncertainty for ensuring the orbital spacecraft magnetic cleanliness. **Originality.** The method for control by orbital spacecraft magnetic cleanliness based on multiple magnetic dipole models using compensation of the initial magnetic field with consideration of magnetic characteristics uncertainty is developed. **Practical value.** An important practical problem of ensuring orbital spacecraft magnetic cleanliness based on orbital spacecraft multiple magnetic dipole models using near field measurements and compensation of the initial magnetic field with consideration of orbital spacecraft magnetic characteristics uncertainty solved.* References 50, figures 2.

Key words: **orbital spacecraft, magnetic cleanliness, multiple magnetic dipole models, near magnetic field, far magnetic field, magnitude prediction, measurements, uncertainty.**

***Мета.** Розробка методу управління магнітною чистотою орбітального космічного апарату на основі багатодипольної моделі магнітного поля з використанням компенсації вихідного магнітного поля та з урахуванням невизначеності магнітних характеристик. **Методологія**. Багатодипольна модель магнітного поля орбітального космічного апарату розрахована як рішення задачі нелінійної мінімаксної оптимізації на основі вимірювань ближнього магнітного поля для прогнозування величини дальнього магнітного поля. Нелінійна цільова функція обчислена у вигляді зваженої суми квадратів залишків між виміряним і прогнозованим магнітним полем. Вагова матриця розрахована у вигляді оберненої коваріаційної матриці вектора випадкових помилок. Значення магнітних моментів і координати розміщення компенсуючих магнітних диполів для компенсації початкового магнітного поля орбітального космічного апарату також розраховані як рішення нелінійної задачі мінімаксної оптимізації. Рішення обох задач нелінійної мінімаксної оптимізації розраховані на основі алгоритмів нелінійної оптимізації роєм частинок. **Результати.** Результати прогнозування величини дальнього магнітного поля орбітального космічного апарату на основі багатодипольної моделі магнітного диполя з використанням вимірювань ближнього поля та компенсації вихідного магнітного поля з урахуванням невизначеності магнітних характеристик для забезпечення магнітної чистоти орбітального космічного апарату. **Оригінальність**. Розроблено метод управління магнітною чистотою орбітального космічного апарату на основі багатодипольної моделі магнітного поля з використанням компенсації вихідного магнітного поля та з урахуванням невизначеності магнітних характеристик. **Практична цінність.** Вирішено важливу практичну задачу забезпечення магнітної чистоти орбітального космічного апарату на основі багатодипольної моделі магнітного диполя з використанням вимірювань ближнього поля та компенсації вихідного магнітного поля з урахуванням невизначеності магнітних характеристик орбітального космічного апарату.* Бібл. 50, рис. 2.

Ключові слова: **орбітальний космічний апарат, магнітна чистота, багатодипольна модель магнітного поля, ближнє магнітне поле, дальнє магнітне поле, прогнозування, вимірювання, невизначеність.**

Introduction. The problem of creating technical objects with a given distribution of the generated magnetic field is an urgent problem for many branches of science and industry. The strictest requirements for the accuracy of the spatial distribution of the magnetic field imposed when ensuring the magnetic cleanliness of orbital spacecraft [1, 2], the development of anti-mine magnetic protection of ships [3], the creation of magnetometry devices, including for medical diagnostic devices. Modern trends in the reduction of spacecraft mass set strictest requirements for magnetic systems by control their orientation [4, 5]. The fulfillment of these requirements requires the maximum minimization of the spacecraft's magnetic moment, which is one of the main destabilizing factors during its movement in near-Earth orbit and requires high accuracy of its experimental measurements [6]. So the level of the magnetic moment of a spacecraft weighing up to 100 kg should be within 0.1 A·m^2, and its experimental determination should preferably be performed with a resolution of less than 0.02 A·m^2 [5]. The main result of the work on ensuring the magnetic purity of the spacecraft is the reduction to a predetermined level of the spacecraft magnetic moment and the magnetic field induction at the location of the onboard magnetometer [6].

NASA and ESA developed a regulatory framework that summarizes their rich experience on this issue [5, 6]. Thus for «Pioneer-6» spacecraft magnetic field level at the magnetometer installation point [4] did not exceed 0.3 nT. On the Danish satellite «Oersted» for the Earth magnetic field measuring a boom is 8 m. The modern level of ensuring magnetic cleanliness considered the «Swarm» spacecraft for researching the Earth magnetic field. Its magnetometric equipment measurements the Earth magnetic field with an error of ±0.1 nT [5].

According to the requirements [2] for the «MikroSAT» spacecraft the magnetic field level at the place of installation of the scientific apparatus was limited to 1 nT with a length of the extension boom of –2.5 m. During the development of the «Sich-2» spacecraft, a limitation was set on the characteristics of the magnetic field of its equipment – the magnetic field strength magnitude of each of the nodes and blocks should not exceed 20 A/m at 0.1 m distance from their surface. On a later «EqyptSAT» spacecraft - this limitation was already more «hard» – 10 A/m at 0.1 m distance from the surface of his equipment [2].

Currently, the experimental measurements of the magnetic characteristics of all Ukrainian spacecraft is carried out exclusively at the magnetic measuring stand of the Anatolii Pidhornyi Institute of Mechanical Engineering Problems of the National Academy of Sciences of Ukraine, which is a unique Magnetodynamic Complex in Ukraine and included in the list of scientific objects that constitute the national heritage of Ukraine.

Technologies for ensuring the magnetic cleanliness of spacecraft managed by NASA, ESA and CAST include interrelated works of an organizational, technical and metrological nature [6]. The foundation of this technology is the calculation models of the spacecraft, which allow analytical or numerical prediction of the magnetic characteristics of the spacecraft, based on the knowledge of the magnetic field of its constituent parts [7–10]. The angular displacement of the spacecraft occurs due to the interaction of the magnetic moment of the included electromagnet of magnetic spacecraft attitude control and stabilization systems with the Earth magnetic field. The accuracy of this movement determined by the reliability of current measurements of the on-board magnetometer and the error of calculating the magnetic moment of the spacecraft with its correspondingly activated electromagnets [11].

Analytical description of the distribution of the magnetic field of spacecraft traditionally carried out using the multipole model proposed by K. Gauss in the study of the Earth magnetism [12]. However to date the methods that would allow in practice to use the integral characteristics of the magnetic field – spatial harmonics, and associate them with the parameters of the spacecraft – remain insufficiently developed. The need to develop such methods confirmed by one of the latest standards of the European Space Agency ECSS-E-HB-20-07A [11], which recommends using its spherical harmonics as integral characteristics of the spatial distribution of the magnetic field to ensure the spacecraft magnetic cleanliness [12].

For most electrical equipment, the magnetic field at distances is greater than three of its maximum overall dimensions are determined mainly by members of the first degree series, i.e. the first three multipole coefficients [13–15]. Therefore, if the measurement of the magnetic field of the technical object performed at a distance greater than three of its maximum overall dimensions, then it can be limited to the construction of the mathematical model of the spacecraft in the form of a multidipole model [16, 17].

The magnetic test requirements in accordance to European cooperation for space standardization during space engineering testing it is necessary to take into account test conditions, input tolerances and measurement uncertainties [18–21]. The main uncertainties of the spacecraft magnetic cleanliness calculated are the changing values of the magnetic moments of the spacecraft elements when the spacecraft operating modes changing [6, 11]. In particular, the magnetic moments change most strongly when the polarization relays operate in the «on» and «off» positions, when the battery operates in the «charge» or «discharge» mode, during operation of high-frequency valves etc. The values of these uncertainties of the magnetic moments of the spacecraft elements during the operation of the spacecraft change within certain limits. In addition, strict restrictions are imposed on these changes in the values of the magnetic moments of the spacecraft elements to ensure the magnetic cleanliness of the entire spacecraft.

Therefore, an urgent problem is the develop of method for design of a model for predicting the far spacecraft magnetic field from measurements of the near magnetic field, which is robust to the spacecraft elements magnetic moments uncertainties and based on this model to calculate the parameters of compensating magnetic dipoles to improve the spacecraft magnetic cleanliness and its controllability in orbit.

The aim of the work is to develop the method for control by orbital spacecraft magnetic cleanliness based on multiple magnetic dipole models using compensation of the initial magnetic field with consideration of magnetic characteristics uncertainty to improve the spacecraft magnetic cleanliness and its controllability in orbit.

Statement of the problem. Consider as an example the general view of the «MicroSAT» spacecraft with the «Ionosat-Micro» instrumentation [2] shown in Fig. 1. On-board magnetometer FGM and three wave probes WP are fixed on the rods. Rod lengths are 2 m, the size of the spacecraft side is about 1 m. For this spacecraft the distance between the spacecraft and the installation point of the onboard magnetometer is more than three times greater than the size of the spacecraft, which makes it possible to adequately describe the spacecraft magnetic field using the multiple magnetic dipole models [11, 12].

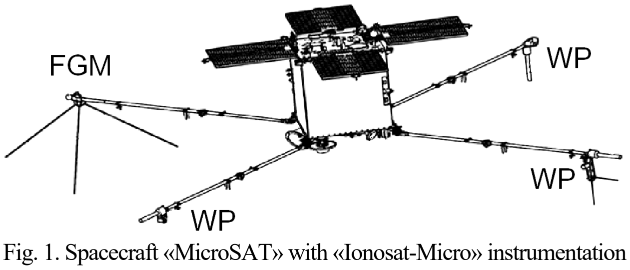

Fig. 1. Spacecraft «MicroSAT» with «Ionosat-Micro» instrumentation

The three-axis system of magnetic spacecraft attitude control and stabilization systems in the Earth orbit includes a three-component magnetic sensor (on-board magnetometer for the orientation of the spacecraft according to the Earth magnetic field and three special executive bodies – electromagnets for the formation of magnetic moments of the spacecraft of a certain magnitude and direction.

Magnetic orientation of spacecraft in the Earth orbit performed by the position control of the spacecraft only by the lines of force of the Earth magnetic field [1]

$$T = MB\,, \qquad (1)$$

where T is the mechanical torque; M is the magnetic moment of the spacecraft; B is the Earth magnetic field.

The spacecraft magnetic moment M include the magnetic moment M_C of the actuator (electromagnet) of the spacecraft and its own magnetic moment M_S of the spacecraft

$$M = M_C + M_S. \tag{2}$$

The characteristics of the accuracy of electromagnetic systems are negatively affected by orientation magnetic moment M_S of the spacecraft itself and the magnetic field generated by spacecraft at the on-board magnetometer location point.

All technical objects elements undergo strict control for magnetic cleanliness and, as a rule, their preliminary demagnetization is performed. The components M_{nx}, M_{ny}, M_{nz} of the magnetic moment of all technical objects elements are measured before installation and meet the stringent requirements of magnetic cleanliness.

Then, the components B_{KX}, B_{KY}, B_{KZ} of technical object magnetic field at any point P_k of space with coordinates x_k, y_k, z_k in the form of the multiple magnetic dipole models of the technical object with the magnetic moment M_{nx}, M_{ny}, M_{nz} of N dipole located at the points of the space of the technical object with coordinates (x_n, y_n, z_n), can be calculated [17]

$$\begin{bmatrix} B_{KX} \\ B_{KY} \\ B_{KZ} \end{bmatrix} = \mu_0 \sum_{n=1}^{N} \frac{1}{4\pi r'^5} \begin{bmatrix} 2x'^2 - y'^2 - z'^2 & \ldots \\ 3x'y' & \ldots \\ 3x'z' & \end{bmatrix}$$

$$\ldots \begin{matrix} 3x'y' & 3x'z' \\ 2y'^2 - x'^2 - z'^2 & 3y'z' \\ 3y'z' & 2z'^2 - y'^2 - x'^2 \end{matrix} \Bigg] \cdot \begin{bmatrix} M_{nx} \\ M_{ny} \\ M_{nz} \end{bmatrix}. \tag{3}$$

Here the designations are introduced

$$x^i = x_k - x_n\,,\ \ y^i = y_k - y_n\,,$$

$$z^i = z_k - z_n\,,$$

$$r' = ((x_k - x_n)^2 + (y_k - y_n)^2 + (z_k - z_n)^2)^{1/2}\,.$$

Then, for the known magnetic moments M_{nx}, M_{ny}, M_{nz} of the dipoles and the coordinates of their location (x_n, y_n, z_n) in the space of technical object, one can calculate magnetic moment of the spacecraft [1]

$$M_x = \sum_{I=1}^{N} M_{nx}\,,\ M_y = \sum_{I=1}^{N} M_{ny}\,,\ M_z = \sum_{I=1}^{N} M_{nz} \tag{4}$$

and the magnetic field B_{KX}, B_{KY}, B_{KZ} at any point of space with coordinates x_k, y_k, z_k including the installation point of the technical object onboard magnetometer.

All Ukrainian spacecraft after installing all the elements are examined for magnetic cleanliness at the magnetic measuring stand Anatolii Pidhornyi Institute of Mechanical Engineering Problems of the National Academy of Sciences of Ukraine. According to real measurements, the spacecraft magnetic moment and the magnetic field at the installation point of the onboard magnetometer are calculated. For this purpose, according to the data of measurements of the magnetic field in the near zone of the spacecraft, the real values of the moment vectors of the dipoles of the received M_n are restored. In this case, it is assumed that the coordinates of the location of the dipoles in the space of the spacecraft remain unchanged.

Let us introduce the vector X of the desired parameters, the components of which are the components M_{nx}, M_{ny}, M_{nz} – of the magnetic moment vectors M_n of dipoles located at the given points P_n of the technical object with coordinates (x_n, y_n, z_n).

For the given coordinates (x_n, y_n, z_n) of the location of the N dipoles based on (3), we calculate the vector of the Y_C prediction values of the magnetic field at the given measurement points with the coordinates x_k, y_k, z_k in the form of the following linear dependence

$$Y_C = AX\,, \tag{5}$$

where the elements of the matrix A are the elements of the matrix from expression (3) calculated for the given coordinates x_n, y_n, z_n of the location of the dipoles in the space of technical object and for the given coordinates x_k, y_k, z_k of the location of the measurement points.

Let us introduce the vector Y_M of measurements of the magnetic field, the components of which are measurements components B_{KX}, B_{KY}, B_{KZ} at the given points P_K of the space with coordinates (x_k, y_k, z_k).

The mathematical model (5) should predict the magnetic field at the measurement points

$$Y_M = AX\,. \tag{6}$$

The number of unknown components of the vector X in (6) is equal to three times the number of dipoles, and the number of equations (dimension of vector Y_M) is equal to three times the number of measurement points. Usually, the number of equations in (6) exceeds the number of unknowns. To calculate this over determined system of linear equations, we use the generalized least squares method. Let us introduce the E vector of the discrepancy between the vector Y_M of the measured magnetic field and the vector Y_C of the predicted by model (5) magnetic field

$$E = Y_M - Y_C = Y_M - AX\,. \tag{7}$$

We write the objective function as the weighted sum of squared residuals between the measured Y_M and predicted Y_C by the model (5) values of the magnetic field

$$\begin{aligned} f(X) = E(X)^T W E(X) = (Y_M - AX)^T \times \ldots \\ \ldots \times W(Y_M - AX). \end{aligned} \tag{8}$$

The minimum of this quadratic objective function (8), based on the necessary minimum condition

$$\partial f(X) / \partial X = 0 \tag{9}$$

calculated based on the expression

$$X = (A^T W A)^{-1} A^T W Y_M\,. \tag{10}$$

The weight matrix W takes into account the different importance of the error components between the measured Y_M and the predicted Y_C model (5) magnetic field values. If the inverse covariance matrix V of random errors vector E use as weight matrix W than generalized least squares method is the most effective in the class of linear unbiased estimates. If the components of the magnetic field measurement vector Y_M are not correlated with each other, then the weight matrix W diagonal. Then the generalized least squares method becomes the weighted least squares method.

If the technical object multiple magnetic dipole model (5) obtained on the basis of the vector Y_M of measured magnetic field is too rough, then on the basis of the vector Y_M of the measured magnetic field, not only the magnetic moments M_{nx}, M_{ny}, M_{nz} of the dipoles, but also their position in the space of the technical object with coordinates x_n, y_n, z_n can be calculated.

Let us consider the design of the technical object multiple magnetic dipole models only on the basis of the vector Y_M of the measured magnetic field. Let us introduce the vector of desired parameters X, the components of which are the desired values magnetic moments M_{nx}, M_{ny}, M_{nz} of the dipoles and coordinates x_n, y_n, z_n of their position in the space of the spacecraft.

We also introduce the vector G of uncertainty parameters of the magnetic moments of the technical object the components of which are the deviations during the operation of the technical object of the magnetic moments of the technical object elements from their central values, taken in the design of the control system for the magnetic field of the technical object. Then, based on (1), the initial nonlinear equation for the spacecraft multiple magnetic dipole model can be obtained.

$$Y_M = F(X,G) . \qquad (11).$$

Here, the vector nonlinear function $F(X, G)$ obtained on the basis of expression (3) with respect to the vector X of unknown variables, whose components are the desired values magnetic moments M_{nx}, M_{ny}, M_{nz} of the dipoles and coordinates x_n, y_n, z_n of their position in the space of the spacecraft and the vector G of the parameters of the uncertainties of the magnetic moments of the elements of the technical object.

In nonlinear equation (11) the number of unknown components of the vector X equal to six times the number N of dipoles, and the number of equations is equal to three times the number K of measurement points.

Let us introduce the E vector of the discrepancy between the vector Y_M of the measured magnetic field and the vector Y_C of the predicted by model (11) magnetic field

$$E(X,G) = Y_M - Y_C(X,G) = y_M - F(X,G) . \qquad (12)$$

We write the objective nonlinear function as the weighted sum of squared residuals between the measured and predicted by the model (12) values of the magnetic field

$$f(X,G) = (E(X,G))^T WE(X,G) . \qquad (13)$$

The nonlinear objective function (13) is obtained on the basis of expression (3) with respect to the vector X of unknown variables, whose components are the desired values magnetic moments M_{nx}, M_{ny}, M_{nz} of the dipoles and coordinates x_n, y_n, z_n of their position in the space of the spacecraft and the vector G of the parameters of the magnetic moments uncertainties of the spacecraft elements.

As a rule, when optimizing the nonlinear objective function (13),

$$X^{\bullet} = \arg\min f(X,G) ; \qquad (14)$$

$$G^{\bullet} = \arg\max f(X,G) , \qquad (15)$$

it is necessary to take into account restrictions on the values of magnetic moments M_{nx}, M_{ny}, M_{nz} of the dipoles and coordinates x_n, y_n, z_n of their position in the space of the spacecraft. These restrictions can usually be written as vector inequalities

$$G(X,G) \le G_{\max} . \qquad (16)$$

Let's consider another approach to the design of spacecraft multiple magnetic dipole models. Usually the designer of the spacecraft knows the N of the elements of the technical object, which are the main sources of the initial magnetic field of the technical object. These are polarization relays, batteries and high-frequency valves. The technical object designer knows the number N of these elements, the coordinates x_n, y_n, z_n of their location in the spacecraft space, as well as the nominal values M_{nx}, M_{ny}, M_{nz} of their magnetic moments. Then the vector Y_C of the magnetic field components B_{KX}, B_{KY}, B_{KZ} at the given points P_K of the space with coordinates x_k, y_k, z_k can be calculated based on spacecraft multiple magnetic dipole model (3).

Note that the values M_{nx}, M_{ny}, M_{nz} of the magnetic moments of these N main elements of the spacecraft can be refined on the basis of the vector Y_M of the measured magnetic field according to (2)–(6).

As a rule, the technical object multiple magnetic dipole models obtained in this way is a rather rough approximation to the actual magnetic range of the technical object. To refine this model, consider the following approach. Let's introduce more M dipoles wits magnetic moment M_{mx}, M_{my}, M_{mz} located at the points P_m of the technical object with coordinates x_m, y_m, z_m. Let us introduce the vector of desired parameters X, the components of which are the desired values magnetic moments M_{mx}, M_{my}, M_{mz} of the M dipoles and coordinates x_m, y_m, z_m of their position in the space of the technical object. We also introduce the vector G of uncertainty parameters of the magnetic moments of the technical object. Then, based on the spacecraft multiple magnetic dipole models (1) can be calculated the vector $Y_A(X, G)$ of additional magnetic field, generated by only M additional dipoles at the measurement points.

$$Y_A(X,G) = F_A(X,G) . \qquad (17).$$

We introduce the vector Y_I of the initial magnetic field of the technical object, the components of which are the components of the magnetic field of the technical object calculated in this way at the measurement points generated by the main N elements of the technical object with known values of the magnetic moments and the coordinates of their location in the space of the technical object.

Then one can calculate the vector Y_R of resulting magnetic field generated by N dipoles with known magnetic moments nominal values M_{nx}, M_{ny}, M_{nz} and coordinates x_n, y_n, z_n of their location in the technical object space and generated by M additional dipoles with unknown magnetic moments M_{mx}, M_{my}, M_{mz} and unknown coordinates x_m, y_m, z_m of their location in the technical object space

$$Y_R(X,G) = Y_I + Y_A(X,G) . \qquad (18)$$

Then the problem (18) of calculated the vectors of unknown parameters of additionally introduced M dipoles can be solved similarly to the problem (13) of calculated the vector of unknown parameters of N dipoles for design of the technical object multiple magnetic dipole model.

Usually, the technical object magnetic cleanliness requirements are presented in the form of restrictions on the total magnetic moment of the technical object and the magnitude of the magnetic field at the installation point of the onboard magnetometer [6, 11]. If the magnetic properties of the spacecraft do not satisfy the overall magnetic cleanliness requirements magnetic compensation tests shall be conducted. According to the technical object multiple magnetic dipole model obtained in the form (13), it is possible to calculate the spacecraft far magnetic field components B_{KX}, B_{KY}, B_{KZ}, and in particular, at the point of installation of the onboard magnetometer and technical object magnetic moments M_{nx}, M_{ny}, M_{nz}. Let us now consider the application of the developed technical object multiple magnetic dipole model to ensure the spacecraft magnetic cleanliness by introducing additional magnetic dipoles to compensate for the far magnetic field of the technical object, in particular, at the point of the onboard magnetometer installation [22–25].

To compensate for the initial magnetic field of the technical object, we introduce C magnetic dipoles with unknown magnetic moments M_{cx}, M_{cy}, M_{cz} located at C points P_c with unknown coordinates x_c, y_c, z_c.

Let us introduce the vector X of the desired parameters for solving the problem of compensating the initial magnetic field of the technical object, whose components are the oblique values of the magnetic moments M_{cx}, M_{cy}, M_{cz} and coordinates x_c, y_c, z_c of the location of the compensating magnetic dipoles in the technical object space. Then, for a given value of the vector X of the desired parameters of the compensating dipoles, based on (1), the vector $B_C(X)$ of the compensating magnetic field generated by all compensating dipoles at the installation point of the onboard magnetometer and the vector $M_C(X)$ of the compensating magnetic moment generated by all compensating dipoles can be calculated [26–30].

Then we calculated the vector $M_R(X, G)$ of resulting magnetic moment and vector $B_R(X, G)$ of resulting magnetic field generated at the installation point of the onboard magnetometer by the technical object elements and all compensating dipoles

$$M_R(X,G) = M(G) + M_C(X)\,; \tag{19}$$

$$B_R(X,G) = B(G) + B_C(X)\,. \tag{20}$$

Then the problem of calculated the coordinates x_c, y_c, z_c of spatial arrangement and magnetic moments M_{cx}, M_{cy}, M_{cz} of the compensating dipoles can be reduced to solving the problem of vector minimax optimization of resulting magnetic moment of the technical object and the resulting magnetic field at the installation point of the onboard magnetometer

$$X^{\bullet} = \arg\min M_R(X,G)\,; \tag{21}$$

$$X^{\bullet} = \arg\min B_R(X,G)\,; \tag{22}$$

$$G^{\bullet} = \arg\max M_R(X,G)\,; \tag{23}$$

$$G^{\bullet} = \arg\max B_R(X,G)\,. \tag{24}$$

This six-criteria minimax problem (21)–(24) can be reduced to a single-criteria problem by the following linear trade-off scheme

$$\begin{aligned} f(X,G) = (M_R(X,G))^T W_1 (M_R(X,G)) + \ldots \\ \ldots + (B_R(X,G))^T W_2 (B_R(X,G)), \end{aligned} \tag{25}$$

where W_1 and W_2 are weight matrices.

Note that this approach is standard when designing of robust control, when the coordinates of the spatial arrangement and the magnitudes of the magnetic moments of the compensating dipoles are found from the conditions for minimizing the modulus of technical object magnetic field at the magnetometer installation point for the «worst» values of the magnetic moments of the elements of the technical object.

The developed technical object multiple magnetic dipole model can be used to calculate the most magnetically clean point at a given distance from the technical object to onboard magnetometer point [31–37]. Let's consider this approach. Let us set a limit on the maximum distance of the technical object onboard magnetometer in the form of a sphere of radius R

$$X^2 + Y^2 + Z^2 \le R^2\,. \tag{26}$$

Let's solve the optimization problem

$$X^{\bullet}, Y^{\bullet}, Z^{\bullet} = \arg\min B(X,Y,Z)\,. \tag{27}$$

With constraint (26) on the required variables. In this case, the technical object multiple magnetic dipole model in the objective function (27) calculated according (10) or (14) – (15).

At present, in order to improve the magnetic cleanliness, the onboard magnetometer is mounted on a boom 1–10 m long. Naturally, the length of this rod must be taken as small as possible [38–40]. Let us consider the application of the developed spacecraft multiple magnetic dipole models to calculate the minimum length of a boom, at the end of which an onboard magnetometer installed.

Let us set the installation direction of the onboard magnetometer in the spherical coordinate system in the form of the length of the radius R and two angles φ and θ. Then the X, Y, Z coordinates of the onboard magnetometer location in the orthogonal coordinate system associated with the spacecraft are calculated

$$\begin{aligned} Z = R\cos(\theta), \quad X = R\cos(\varphi)\sin(\theta), \\ Y = R\sin(\theta)\sin(\varphi). \end{aligned} \tag{28}$$

Then, in order to calculate the minimum boom length R, at the end of which an on-board magnetometer is installed, it is necessary to solve a one-parameter optimization problem

$$R^{\bullet} = \arg\min B(R) R\cos(\varphi) \tag{29}$$

with restriction

$$B(R) \le B_{\max}\,, \tag{30}$$

where $B_{\max}$ is the maximum value of the magnetic field at the installation point of the on-board magnetometer.

The method for problem solving. The problem (10) is usually solved by finding the pseudo inverse matrix or LU decomposition of a matrix or the very effective Cholesky method [15]. If it is necessary to take into account the restrictions type (16) on the values of the magnetic moments of the dipoles, then this problem solved [41–44] as an optimization problem (14) – (15) with restrictions (16). A feature of this optimization problem is the quadratic objective function (8) and linear constraints. To solve such an optimization problem, an algorithm for sequential quadratic programming developed.

Let us represent (8) in the following form

$$f(x) = \frac{1}{2}\sum_{i=1}^{l} f_i(x)^2\,. \tag{31}$$

Gradient of this objective function represented as follows

$$\nabla f(x) = \nabla F(x) F(x)\,, \tag{32}$$

where the Jacobian $\nabla F(x) = (\nabla f_1(x), ..., \nabla f_l(x))$ of this function is indicated and it is assumed that the components of the objective function can be differentiated twice. Then the matrix of second derivatives of the objective function – the Hesse matrix can be written in the following form

$$\nabla^2 f(x) = \nabla F(x) \nabla F(x)^T + B(x), \tag{33}$$

where

$$B(x) = \sum_{i=1}^{l} f_i(x) \nabla^2 f_i(x) \nabla^2 f_i(x). \qquad (34).$$

Then the iterative procedure for choosing the direction $d_k \in R^n$ of motion using the Newton method reduced to solving the linear system

$$\nabla^2 f(x_k) d + \nabla f(x_k) = 0, \qquad (35).$$

or to the solution of an equivalent system in the following form

$$\nabla F(x_k) \nabla F(x_k)^T d + B(x_k) d + \nabla F(x_k) F(x_k) = 0. \qquad (36).$$

At the optimal solution point x^* the following condition is satisfied

$$F(x^*) = \left(f_1(x^*), \ldots, f_l(x^*)\right)^T = 0, \tag{37}$$

therefore, finding the motion step d can be reduced to solving the normal equation of the least squares problem

$$\min_{d \in R^n} \left\| \nabla F(x_k)^T d + F(x_k) \right\|, \qquad (38).$$

from which a recursive equation can be obtained for iteratively finding the vector of desired parameters,

$$x_{k+1} = x_k + \alpha_k d_k, \tag{39}$$

in which d_k is the solution of the optimization problem, and α_k is an experimentally determined parameter.

This algorithm uses the Gauss–Newton method, which is a traditional algorithm for solving the problem of the nonlinear least squares method, to calculate the direction of movement. In the general case, the Gauss–Newton method allows one to obtain a solution to the problem of sequential quadratic programming using only first-order derivatives, but in real situations it often cannot obtain a solution. Therefore, to improve convergence, second-order methods are used, in which the matrix of second derivatives of the objective function is used – the Hesse matrix when solving optimization problems without restrictions. Second-order algorithms, compared to first-order methods, make it possible to effectively obtain a solution in a region close to the optimal point, when the components of the gradient vector have sufficiently small values.

Recently, methods using Levenberg-Marquardt algorithms have become widespread in quasi-Newtonian methods. The idea of these methods is to replace the Hesse matrix with some matrix $\lambda_k I$ with a positive coefficient λ_k. Then we get the following linear equations system

$$\nabla F(x_k) \nabla F(x_k)^T d + \lambda_k d + \nabla F(x_k) F(x_k) = 0. \tag{40}$$

One of the most promising methods of solving problems of this class is the use of stochastic multi-agent algorithms, which do not require the calculation of derivatives of the objective function, and are also much more effective than the simple multi-start method, since they use special heuristic methods to search for the optimum [45, 46]. Genetic algorithms, which are a universal tool for finding an optimal solution close to the global one, deserve special attention, and they work equally well for both discrete and continuous parameter values. The particle swarm optimization method, which simulates the social behavior of individuals in a flock, has a higher speed of convergence to the optimum, but when the number of varied parameters increases, as practice shows, the probability of stopping the search near one of the local optima increases. To date, a large number of particle swarm optimization algorithms have been developed – PSO algorithms based on the basic ideas of the collective intelligence of particle swarms, such as the gbest PSO and lbest PSO algorithms. Practically all these algorithms described by the following expression for changing the position and speed of movement of that particle

$$\begin{aligned} v_{ij}(t+1) = v_{ij}(t) + c_1 r_{1j}(t)\left[y_{ij}(t) - x_{ij}(t)\right] + \ldots \\ \ldots + c_2 r_{2j}(t)\left[y_j^*(t) - x_{ij}(t)\right]; \end{aligned} \quad , \tag{41}$$

$$x_{ij}(t+1) = x_{ij}(t) + v_{ij}(t+1), \tag{42}$$

where $x_{ij}(t)$, $v_{ij}(t)$ are the position and speed of the particle i in the swarm j; c_1 and c_2 are positive constants that determine the weights of the cognitive and social components of the speed of particle movement; $r_{1j}(t)$ and $r_{2j}(t)$ are random numbers from the range [0, 1], which determine the stochastic component of the particle speed component.

Here $y_{ij}(t)$ and y_j^* the best local and global positions of that particle i are found, respectively, by only one particle and all swarm particles, which are analogs of the local optimum determined by that particle and the global optimum determined by all swarm particles.

In the standard particle swarm optimization algorithm [45, 46] particle velocities change according to linear laws [47, 48]. To increase the speed of finding a global solution, special nonlinear stochastic multi-agent optimization algorithms [49, 50], in which the movement of a particle i of a swarm j is described by the following expressions

$$\begin{aligned} & v_{ij}(t+1) = w_j v_{ij}(t) + \ldots \\ & \ldots + c_{1j} r_{1j}(t) H\left(p_{1j} - \varepsilon_{1j}(t)\right)\left[y_{ij}(t) - x_{ij}(t)\right] + \ldots \\ & \ldots + c_{2j} r_{2j}(t) H\left(p_{2j} - \varepsilon_{2j}(t)\right)\left[y_j^*(t) - x_{ij}(t)\right] \end{aligned} \tag{43}$$

Heaviside function H is used as an option for switching the particle motion according to the local $y_{ij}(t)$ and global $y_j^*(t)$ optimum.

Parameters of switching the cognitive p_{1j} and social p_{2j} components of the speed of particle movement in accordance with the local and global optimum; $\varepsilon_{1j}(t)$ and $\varepsilon_{2j}(t)$ random numbers and determine the parameters of switching the particle motion according to the local and global optimum. If $p_{1j} < \varepsilon_{1j}(t)$ and $p_{2j} < \varepsilon_{2j}(t)$ then the speed of movement of particle i of swarm j does not change at a step and the particle moves in the same direction as in the previous optimization step.

During their movement, the particles try to improve the solution they found earlier and exchange information with their neighbors, due to which they find the global optimum in a smaller number of iterations. The advantage of these methods over classical gradient optimization methods is also that they do not require the calculation of the derivatives of the objective function, they are practically insensitive to the proximity of the initial approximation to the desired solution, and allow for easier consideration of various restrictions when finding global optimum.

Note that the search algorithm for the vector G that maximizes the objective function (15) is described by the same expressions (42). However, in contrast to the search for the vector X, which minimizes the objective function (7), $y_{ij}(t)$ and y_j^* are the best local and global positions, which maximizes the objective function (15).

Optimization results. Let us consider the application of the developed method for solving the problem of ensuring the magnetic cleanliness of the «Sich-2-1» spacecraft. Based on the experimental measured magnetic field generated by «Sich-2-1» spacecraft, performed in 2021 by researchers Sergey Petrov and Anatoliy Erisov of the Department of Magnetism of Technical Objects, calculations of the characteristics of the spacecraft magnetic cleanliness carried out.

The experimentally measured value of the total magnetic moment of spacecraft is equal $M = [0.24, 0.5, 0.4]$. The dispersion of the magnetic field prediction error in this case is $D = 7560.6$. The value of the experimentally measured magnetic moment of the spacecraft implies the presence of several dipoles located in the space of the spacecraft. In the calculation it is assumed that the model of the magnetic field of the spacecraft represents one dipole located at the origin of the spacecraft.

Based on the experimental measured magnetic field at first the spacecraft magnetic field model was presented as a single dipole located in the center of the spacecraft. To calculate the vector of moments of this dipole on the basis of (6), the inverse matrix of 3×3 size was calculated. Based on the vector of the measured magnetic field of the spacecraft Y_M, the moments of this single dipole $M = [0.2400, 0.5000, 0.4000]$ were calculated. The dispersion of the magnetic field prediction error in this case is $D = 7272.7$.

Then the magnitude of the magnetic moment of this single dipole, located at the center of the spacecraft, calculated by solving the problem of unconstrained optimization (9) unlimited (12). The values of the magnetic moments of the spacecraft, calculated by the expression (6) using the inverse matrix, and those calculated in the course of solving the optimization problem (9) coincide.

Note that when calculating the magnetic moment of the spacecraft in the form of a solution to the optimization problem (9), one can also take into account the restrictions on the values of the components of the vector of the magnetic moments of the spacecraft.

Let us now consider the mathematical model of the magnetic field of the spacecraft in the form of a single dipole, the location coordinates of which in the space of the spacecraft also need to be calculated. For the calculated value of the moment $M = [0.2664, 0.1641, 0.1434]$ and coordinates $P = [0.2158, –0.4136, 0.0859]$ of the location of such a single dipole, the prediction error variance is $D = 3239.8$. Note that the location of the only dipole not at the origin of the coordinates, but at the point with the optimal coordinates made it possible to reduce the dispersion of the magnetic field prediction by a factor of 2.3337.

If, when solving the problem of optimizing the values of the magnetic moments and the coordinates of the location of one dipole, we introduce restrictions on the magnitude of the dipole moments in the form of restrictions $[–0.8, –0.8, –0.8] \le M \le [0.8, 0.8, 0.8]$, optimal values of the moments $M = [0.2388, 0.1921, 0.1258]$ and coordinates $P = [0.2056, –0.4146, 0]$ of the location of such a single dipole, the prediction error variance is $D = 3325.1$. Thus, under restrictions on the magnitude of the dipole moments, the optimum values of the magnetic moments are at the limits and, in this case, the dispersion increases by a factor of 2.2738.

Let us now consider the model of the spacecraft magnetic field in the form of two dipoles. If, when solving the problem of optimizing the values of the magnetic moments and the coordinates of the location of two dipoles, we introduce restrictions on the magnitude of the dipole moments in the form of restrictions $[–0.8, –0.8, –0.8] \le M \le [0.8, 0.8, 0.8]$, optimal values of the moments $M1 = [0.3538, –0.0326, –0.0345]$ and $M2 = [–0.6137, 0.6695, –0.2802]$ and the coordinates $P1 = [0.3090, –0.3080, 0.0867]$ and $P2 = [–0.0657, –0.0789, –0.3908]$ of the location of two dipoles, the dispersion the prediction error is $D = 1203.4$. Thus, under restrictions on the magnitude of the two dipoles moments, the optimum values of the magnetic moments are at the limits and, in this case, the dispersion increases by a factor of 6.2827.

Let us now consider the design of the spacecraft magnetic field model for the most common case, when the coordinates and magnetic moments of the magnetic field sources, which are the main sources of the initial spacecraft magnetic field, are preliminarily set. In particular, consider an example in the form of six dipoles,

$M1 = [–0.6119, 0.6682, –0.2796]$,
$M2 = [0.0787, –0.0356, –0.0337]$,
$M3 = [0.0915, –0.0015, –0.0137]$,
$M4 = [0.0893, –0.0322, –0.0104]$,
$M5 = [0.0314, 0.0137, –0.0076]$,
$M6 = [0.0621, 0.0233, 0.0312]$,
$P1 = [–0.0664, –0.0790, –0.3903]$,
$P2 = [0, 0, 0]$,
$P3 = [0, 0, 0]$,
$P4 = [0, 0, 0]$,
$P5 = [0, 0, 0]$,
$P6 = [0.3092, –0.3083, 0.0870]$.

For these six dipoles, the dispersion of the prediction error is $D = 1203.4$.

Figure 2 shows the spatial arrangement of the modules of the measured and predicted magnetic field and the deviation between the measured and predicted magnetic field for six dipoles.

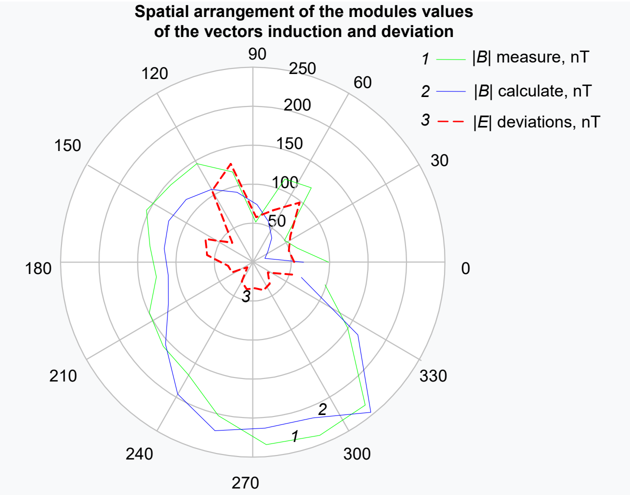

Fig. 2. The spatial arrangement of the modules of the measured, predicted and deviation magnetic field

Using the developed spacecraft magnetic field model, the spacecraft magnetic moment M = [–0.2619, 0.6356, –0.3112] was calculated and the magnetic field B = [5.0638, 13.7326, 2.5545] was predicted at the installation point of the onboard magnetometer. As a result of solving the problem of compensation for the initial magnetic field of the spacecraft, the magnetic moments $M1$ = = [0.6119, –0.6682, 0.2796] and $M2$ = [–0.0621, –0.0233, –0.0312] and coordinates $P1$ = [–0.0664, –0.0790, –0.3903] and $P2$ = [0.3092, –0.3083, 0.0870] of two compensation dipoles were calculated.

The calculated value of the resulting spacecraft magnetic moment M = [0.0246, –0.0566, 0.0363] and the predicted resulting magnetic field B = [1.3506, –3.702, 0.6872] at the installation point of the onboard magnetometer show that due to the introduction of two compensating dipoles, it was possible to reduce the magnitude of the resulting spacecraft magnetic moment by a factor of 6.21 and also to reduce the value of the predicted resulting magnetic field at the point of installation of the onboard magnetometer by a factor of 3.7.

Conclusions.

1. Method for control by orbital spacecraft magnetic cleanliness based on multiple magnetic dipole models using compensation of the initial magnetic field with consideration of magnetic characteristics uncertainty developed.

2. Magnetic moments and coordinates values of orbital spacecraft multiple magnetic dipole models calculated based the solution of nonlinear minimax optimization problem. Nonlinear objective function calculated as the weighted sum of squared residuals between the measured and predicted magnetic field. Values of magnetic moments and coordinates of placement of compensating magnetic dipoles for compensation of the orbital spacecraft initial magnetic field also calculated as solution of nonlinear minimax optimization problem. Solutions of this both nonlinear minimax optimization problems calculated based on particle swarm nonlinear optimization algorithms.

3. The developed method for control by orbital spacecraft magnetic cleanliness allows at the design stage to calculate the multiple magnetic dipole models and based on its to calculate the parameters of compensating magnetic dipoles to improve the spacecraft magnetic cleanliness and its controllability in orbit.

Acknowledgments. The authors express their gratitude to the researcher Anatoliy Erisov of the department of magnetism of technical object of Anatolii Pidhornyi Institute of Mechanical Engineering Problems of the National Academy of Sciences of Ukraine for the kindly provided materials on the results of experimental measured magnetic field generated by elements and «Sich-2-1» spacecraft and also for numerous discussions that allowed the authors to improve the article manuscript.

Conflict of interest. The authors declare that they have no conflicts of interest.

REFERENCES

1. Rozov V.Yu., Getman A.V., Petrov S.V. Spacecraft magnetism. *Technical Electrodynamics. Thematic issue «Problems of modern electrical engineering»*, 2010, part 2, pp. 144-147. (Rus).

2. Droughts S.A., Fedorov O.P. Space project Ionosat-Micro. Monograph. Kyiv, Akademperiodika Publ., 2013. 218 p. (Rus).

3. Birsan M., Holtham P., Carmen. Using global optimisation techniques to solve the inverse problem for the computation of the static magnetic signature of ships. *Defense Research Establishment Atlantic*, 9 Grove St., PO Box 1012, Dartmouth, Nova Scotia, B2Y 3Z7, Canada.

4. Acuña M.H. *The design, construction and test of magnetically clean spacecraft – a practical guide*. NASA/GSFC internal report. 2004.

5. Junge A., Marliani F. Prediction of DC magnetic fields for magnetic cleanliness on spacecraft. *2011 IEEE International Symposium on Electromagnetic Compatibility*, 2011, pp. 834-839. doi: https://doi.org/10.1109/ISEMC.2011.6038424.

6. *ECSS-E-HB-20-07A. Space engineering: Electromagnetic compatibility hand-book. ESA-ESTEC. Requirements & Standards Division*. Noordwijk, Netherlands, 2012. 228 p.

7. Lynn G.E., Hurt J.G., Harriger K.A. Magnetic control of satellite attitude. *IEEE Transactions on Communication and Electronics*, 1964, vol. 83, no. 74, pp. 570-575. doi: https://doi.org/10.1109/TCOME.1964.6539511.

8. Junge A., Trougnou L., Carrubba E. Measurement of Induced Equivalent Magnetic Dipole Moments for Spacecraft Units and Components. *Proceedings ESA Workshop Aerospace EMC 2009 ESA WPP-299*, 2009, vol. 4, no. 2, pp. 131-140.

9. Mehlem K., Wiegand A. Magnetostatic cleanliness of spacecraft. *2010 Asia-Pacific International Symposium on Electromagnetic Compatibility*, 2010, pp. 936-944. doi: https://doi.org/10.1109/APEMC.2010.5475692.

10. Messidoro P., Braghin M., Grande M. Magnetic cleanliness verification approach on tethered satellite. *16th Space Simulation Conference: Confirming Spaceworthiness into the Next Millennium*, 1991, pp. 415-434.

11. *ECSS-E-HB-20-07C. Space engineering: Electromagnetic compatibility hand-book. ESA-ESTEC. Requirements & Standards Division*. Noordwijk, Netherlands, 2012. 91 p.

12. Rozov V.Yu., Dobrodeev P.N., Volokhov S.A. Multipole model of a technical object and its magnetic center. *Technical Electrodynamics.* 2010, no 2, pp. 98-104.

13. Mehlem K., Narvaez P. Magnetostatic cleanliness of the radioisotope thermoelectric generators (RTGs) of Cassini. *1999 IEEE International Symposium on Electromagnetic Compatability*, 1999, vol. 2, pp. 899-904. doi: https://doi.org/10.1109/ISEMC.1999.810175.

14. Eichhorn W.L. *Magnetic dipole moment determination by near-field analysis*. Goddard Space Flight Center. Washington, D.C., National Aeronautics and Space Administration, 1972. NASA technical note, D 6685. 87 p.

15. Matsushima M., Tsunakawa H., Iijima Y., Nakazawa S., Matsuoka A., Ikegami S., Ishikawa T., Shibuya H., Shimizu H., Takahashi F. Magnetic Cleanliness Program Under Control of Electromagnetic Compatibility for the SELENE (Kaguya) Spacecraft. *Space Science Reviews*, 2010, vol. 154, no. 1-4, pp. 253-264. doi: https://doi.org/10.1007/s11214-010-9655-x.

16. Boghosian M., Narvaez P., Herman R. Magnetic testing, and modeling, simulation and analysis for space applications. *2013 IEEE International Symposium on Electromagnetic Compatibility*, 2013, pp. 265-270. doi: https://doi.org/10.1109/ISEMC.2013.6670421.

17. Mehlem K. Multiple magnetic dipole modeling and field prediction of satellites. *IEEE Transactions on Magnetics*, 1978, vol. 14, no. 5, pp. 1064-1071. doi: https://doi.org/10.1109/TMAG.1978.1059983.

18. Martynenko G. Analytical Method of the Analysis of Electromagnetic Circuits of Active Magnetic Bearings for Searching Energy and Forces Taking into Account Control Law. *2020 IEEE KhPI Week on Advanced Technology (KhPIWeek)*, 2020, pp. 86-91. doi: https://doi.org/10.1109/KhPIWeek51551.2020.9250138.

19. Martynenko G., Martynenko V. Rotor Dynamics Modeling for Compressor and Generator of the Energy Gas Turbine Unit with Active Magnetic Bearings in Operating Modes. *2020 IEEE Problems of Automated Electrodrive. Theory and Practice (PAEP)*, 2020, pp. 1-4. doi: https://doi.org/10.1109/PAEP49887.2020.9240781.

20. Ostroverkhov M., Trinchuk D. Increasing the Efficiency of Electric Vehicle Drives with Supercapacitors in Power Supply.

2020 IEEE 7th International Conference on Energy Smart Systems (ESS), 2020, pp. 258-261. doi: https://doi.org/10.1109/ESS50319.2020.9160291.

21. Ostroverkhov N., Buryk N. Control System with Field Weakening of Synchronous Motor Drive. *2020 IEEE Problems of Automated Electrodrive. Theory and Practice (PAEP)*, 2020, pp. 1-5. doi: https://doi.org/10.1109/PAEP49887.2020.9240903.

22. Chen C.S., Reutskiy S.Y., Rozov V.Y. The method of the fundamental solutions and its modifications for electromagnetic field problems. *Computer Assisted Mechanics and Engineering Sciences*, 2009, vol. 16, no. 1, pp. 21-33.

23. Rozov V.Y., Pelevin D.Y., Pielievina K.D. External magnetic field of urban transformer substations and methods of its normalization. *Electrical Engineering & Electromechanics*, 2017, no. 5, pp. 60-66. doi: https://doi.org/10.20998/2074-272X.2017.5.10.

24. Rozov V.Yu., Reutskyi S.Yu., Pelevin D.Ye., Kundius K.D. Approximate method for calculating the magnetic field of 330-750 kV high-voltage power line in maintenance area under voltage. *Electrical Engineering & Electromechanics*, 2022, no. 5, pp. 71-77. doi: https://doi.org/10.20998/2074-272X.2022.5.12.

25. Rozov V.Yu., Kundius K.D., Pelevin D.Ye. Active shielding of external magnetic field of built-in transformer substations. *Electrical Engineering & Electromechanics*, 2020, no. 3, pp. 24-30. doi: https://doi.org/10.20998/2074-272x.2020.3.04.

26. Tytiuk V., Chornyi O., Baranovskaya M., Serhiienko S., Zachepa I., Tsvirkun L., Kuznetsov V., Tryputen N. Synthesis of a fractional-order $PI^{\lambda}D^{\mu}$-controller for a closed system of switched reluctance motor control. *Eastern-European Journal of Enterprise Technologies*, 2019, no. 2 (98), pp. 35-42. doi: https://doi.org/10.15587/1729-4061.2019.160946.

27. Zagirnyak M., Serhiienko S., Chornyi O. Innovative technologies in laboratory workshop for students of technical specialties. *2017 IEEE First Ukraine Conference on Electrical and Computer Engineering (UKRCON)*, 2017, pp. 1216-1220. doi: https://doi.org/10.1109/UKRCON.2017.8100446.

28. Chornyi O., Serhiienko S. A virtual complex with the parametric adjustment to electromechanical system parameters. *Technical Electrodynamics*, 2019, pp. 38-41. doi: https://doi.org/10.15407/techned2019.01.038.

29. Shchur I., Kasha L., Bukavyn M. Efficiency Evaluation of Single and Modular Cascade Machines Operation in Electric Vehicle. *2020 IEEE 15th International Conference on Advanced Trends in Radioelectronics, Telecommunications and Computer Engineering (TCSET)*, Lviv-Slavske, Ukraine, 2020, pp. 156-161. doi: https://doi.org/10.1109/tcset49122.2020.235413.

30. Shchur I., Turkovskyi V. Comparative Study of Brushless DC Motor Drives with Different Configurations of Modular Multilevel Cascaded Converters. *2020 IEEE 15th International Conference on Advanced Trends in Radioelectronics, Telecommunications and Computer Engineering (TCSET)*, Lviv-Slavske, Ukraine, 2020, pp. 447-451. doi: https://doi.org/10.1109/tcset49122.2020.235473.

31. Solomentsev O., Zaliskyi M., Averyanova Y., Ostroumov I., Kuzmenko N., Sushchenko O., Kuznetsov B., Nikitina T., Tserne E., Pavlikov V., Zhyla S., Dergachov K., Havrylenko O., Popov A., Volosyuk V., Ruzhentsev N., Shmatko O. Method of Optimal Threshold Calculation in Case of Radio Equipment Maintenance. *Data Science and Security. Lecture Notes in Networks and Systems*, 2022, vol. 462, pp. 69-79. doi: https://doi.org/10.1007/978-981-19-2211-4_6.

32. Ruzhentsev N., Zhyla S., Pavlikov V., Volosyuk V., Tserne E., Popov A., Shmatko O., Ostroumov I., Kuzmenko N., Dergachov K., Sushchenko O., Averyanova Y., Zaliskyi M., Solomentsev O., Havrylenko O., Kuznetsov B., Nikitina T. Radio-Heat Contrasts of UAVs and Their Weather Variability at 12 GHz, 20 GHz, 34 GHz, and 94 GHz Frequencies. *ECTI Transactions on Electrical Engineering, Electronics, and Communications*, 2022, vol. 20, no. 2, pp. 163-173. doi: https://doi.org/10.37936/ecti-eec.2022202.246878.

33. Havrylenko O., Dergachov K., Pavlikov V., Zhyla S., Shmatko O., Ruzhentsev N., Popov A., Volosyuk V., Tserne E., Zaliskyi M., Solomentsev O., Ostroumov I., Sushchenko O., Averyanova Y., Kuzmenko N., Nikitina T., Kuznetsov B. Decision Support System Based on the ELECTRE Method. *Data Science and Security. Lecture Notes in Networks and Systems*, 2022, vol. 462, pp. 295-304. doi: https://doi.org/10.1007/978-981-19-2211-4_26.

34. Shmatko O., Volosyuk V., Zhyla S., Pavlikov V., Ruzhentsev N., Tserne E., Popov A., Ostroumov I., Kuzmenko N., Dergachov K., Sushchenko O., Averyanova Y., Zaliskyi M., Solomentsev O., Havrylenko O., Kuznetsov B., Nikitina T. Synthesis of the optimal algorithm and structure of contactless optical device for estimating the parameters of statistically uneven surfaces. *Radioelectronic and Computer Systems*, 2021, no. 4, pp. 199-213. doi: https://doi.org/10.32620/reks.2021.4.16.

35. Volosyuk V., Zhyla S., Pavlikov V., Ruzhentsev N., Tserne E., Popov A., Shmatko O., Dergachov K., Havrylenko O., Ostroumov I., Kuzmenko N., Sushchenko O., Averyanova Yu., Zaliskyi M., Solomentsev O., Kuznetsov B., Nikitina T. Optimal Method for Polarization Selection of Stationary Objects Against the Background of the Earth's Surface. *International Journal of Electronics and Telecommunications*, 2022, vol. 68, no. 1, pp. 83-89. doi: https://doi.org/10.24425/ijet.2022.139852.

36. Gal'chenko V.Y., Vorob'ev M.A. Structural synthesis of attachable eddy-current probes with a given distribution of the probing field in the test zone. *Russian Journal of Nondestructive Testing*, Jan. 2005, vol. 41, no. 1, pp. 29-33. doi: https://doi.org/10.1007/s11181-005-0124-7.

37. Halchenko V.Y., Ostapushchenko D.L., Vorobyov M.A. Mathematical simulation of magnetization processes of arbitrarily shaped ferromagnetic test objects in fields of given spatial configurations. *Russian Journal of Nondestructive Testing*, Sep. 2008, vol. 44, no. 9, pp. 589-600. doi: https://doi.org/10.1134/S1061830908090015.

38. Zhyla S., Volosyuk V., Pavlikov V., Ruzhentsev N., Tserne E., Popov A., Shmatko O., Havrylenko O., Kuzmenko N., Dergachov K., Averyanova Y., Sushchenko O., Zaliskyi M., Solomentsev O., Ostroumov I., Kuznetsov B., Nikitina T. Practical imaging algorithms in ultra-wideband radar systems using active aperture synthesis and stochastic probing signals. *Radioelectronic and Computer Systems*, 2023, no. 1, pp. 55-76. doi: https://doi.org/10.32620/reks.2023.1.05.

39. Chystiakov P., Chornyi O., Zhautikov B., Sivyakova G. Remote control of electromechanical systems based on computer simulators. *2017 International Conference on Modern Electrical and Energy Systems (MEES)*, Kremenchuk, Ukraine, 2017, pp. 364-367. doi: https://doi.org/10.1109/mees.2017.8248934.

40. Zagirnyak M., Bisikalo O., Chorna O., Chornyi O. A Model of the Assessment of an Induction Motor Condition and Operation Life, Based on the Measurement of the External Magnetic Field. *2018 IEEE 3rd International Conference on Intelligent Energy and Power Systems (IEPS)*, Kharkiv, 2018, pp. 316-321. doi: https://doi.org/10.1109/ieps.2018.8559564.

41. Maksymenko-Sheiko K.V., Sheiko T.I., Lisin D.O., Petrenko N.D. Mathematical and Computer Modeling of the Forms of Multi-Zone Fuel Elements with Plates. *Journal of Mechanical Engineering*, 2022, vol. 25, no. 4, pp. 32-38. doi: https://doi.org/10.15407/pmach2022.04.032.

42. Hontarovskyi P.P., Smetankina N.V., Ugrimov S.V., Garmash N.H., Melezhyk I.I. Computational Studies of the Thermal Stress State of Multilayer Glazing with Electric Heating. *Journal of Mechanical Engineering*, 2022, vol. 25, no. 1, pp. 14-21. doi: https://doi.org/10.15407/pmach2022.02.014.

43. Kostikov A.O., Zevin L.I., Krol H.H., Vorontsova A.L. The Optimal Correcting the Power Value of a Nuclear Power Plant Power Unit Reactor in the Event of Equipment Failures. *Journal of Mechanical Engineering*, 2022, vol. 25, no. 3, pp. 40-45. doi: https://doi.org/10.15407/pmach2022.03.040.

44. Rusanov A.V., Subotin V.H., Khoryev O.M., Bykov Y.A., Korotaiev P.O., Ahibalov Y.S. Effect of 3D Shape of Pump-Turbine Runner Blade on Flow Characteristics in Turbine Mode. *Journal of Mechanical Engineering*, 2022, vol. 25, no. 4, pp. 6-14. doi: https://doi.org/10.15407/pmach2022.04.006.

45. Ummels M. *Stochastic Multiplayer Games Theory and Algorithms*. Amsterdam University Press, 2010. 174 p.

46. Shoham Y., Leyton-Brown K. *Multiagent Systems: Algorithmic, Game-Theoretic, and Logical Foundations.* Cambridge University Press, 2009. 504 p.

47. Sushchenko O., Averyanova Y., Ostroumov I., Kuzmenko N., Zaliskyi M., Solomentsev O., Kuznetsov B., Nikitina T., Havrylenko O., Popov A., Volosyuk V., Shmatko O., Ruzhentsev N., Zhyla S., Pavlikov V., Dergachov K., Tserne E. Algorithms for Design of Robust Stabilization Systems. *Computational Science and Its Applications – ICCSA 2022. ICCSA 2022. Lecture Notes in Computer Science*, 2022, vol. 13375, pp. 198-213. doi: https://doi.org/10.1007/978-3-031-10522-7_15.

48. Zhyla S., Volosyuk V., Pavlikov V., Ruzhentsev N., Tserne E., Popov A., Shmatko O., Havrylenko O., Kuzmenko N., Dergachov K., Averyanova Y., Sushchenko O., Zaliskyi M., Solomentsev O., Ostroumov I., Kuznetsov B., Nikitina T. Statistical synthesis of aerospace radars structure with optimal spatio-temporal signal processing, extended observation area and high spatial resolution. *Radioelectronic and Computer Systems*, 2022, no. 1, pp. 178-194. doi: https://doi.org/10.32620/reks.2022.1.14.

49. Xin-She Yang, Zhihua Cui, Renbin Xiao, Amir Hossein Gandomi, Mehmet Karamanoglu. *Swarm Intelligence and Bio-Inspired Computation: Theory and Applications*, Elsevier Inc., 2013. 450 p.

50. Hashim F.A., Hussain K., Houssein E.H., Mabrouk M.S., Al-Atabany W. Archimedes optimization algorithm: a new metaheuristic algorithm for solving optimization problems. *Applied Intelligence*, 2021, vol. 51, no. 3, pp. 1531-1551. doi: https://doi.org/10.1007/s10489-020-01893-z.

Received 30.11.2022
Accepted 13.03.2023
Published 01.09.2023

B.I. Kuznetsov[1], *Doctor of Technical Science, Professor,*
T.B. Nikitina[2], *Doctor of Technical Science, Professor,*
I.V. Bovdui[1], *PhD, Senior Research Scientist,*
K.V. Chunikhin[1], *PhD, Research Scientist,*
V.V. Kolomiets[2], *PhD, Assistant Professor,*
B.B. Kobylianskyi[2], *PhD, Associate Professor,*
[1] Anatolii Pidhornyi Institute of Mechanical Engineering
Problems of the National Academy of Sciences of Ukraine,
2/10, Pozharskogo Str., Kharkiv, 61046, Ukraine,
e-mail: kuznetsov.boris.i@gmail.com (Corresponding Author)
[2] Educational scientific professional pedagogical Institute
of Ukrainian Engineering Pedagogical Academy,
9a, Nosakov Str., Bakhmut, Donetsk Region, 84511, Ukraine,
e-mail: nnppiuipa@ukr.net

How to cite this article:
Kuznetsov B.I., Nikitina T.B., Bovdui I.V., Chunikhin K.V., Kolomiets V.V., Kobylianskyi B.B. Method for control by orbital spacecraft magnetic cleanliness based on multiple magnetic dipole models with consideration of their uncertainty. *Electrical Engineering & Electromechanics*, 2023, no. 5, pp. 47-56. doi: https://doi.org/10.20998/2074-272X.2023.5.07

UDC 621.316.98 https://doi.org/10.20998/2074-272X.2023.5.08

V.V. Kniaziev

Determination of the probability of a lightning strike in the elements of the object taking into account the statistical distribution of the current value

Problem. *Modern international standards in the field of lightning protection, when assessing the probability of a lightning strike into an object, do not take into account the statistical distribution of the lightning current.* ***Goal.*** *Justification of the expediency of taking into account the statistical distribution of the lightning current with a determined probability of lightning striking the elements of the object, and the effectiveness of the application of the improved «rolling sphere» method.* ***Methodology.*** *Method of mathematical modeling, based on RSM with additional consideration of the probability distribution of lightning current.* ***Results.*** *The expediency of taking into account the statistical distribution of lightning current at the determined probability of lightning striking the elements of the object has been proven. The effectiveness of the improved «rolling sphere» method, implemented in the form of a computer program, which takes into account the given probability distribution of lightning current in the range from 2 kA to 200 kA, has been proved. The expediency of introducing the concept of «average value of the area of the collection area» is substantiated, taking into account the probability of lightning with a current in a given range. It has been established that the application of the standardized formula leads to a significant (many times) overestimation of the predicted number of lightning strikes to the object, if the height of the object exceeds 20 m. The reasons for the difference, according to the author, are due to the following properties of the standardized methodology: usually, the real shape of the object is not taken into account; statistical distribution of lightning current is not taken into account; it is based on the results of experimental studies obtained mainly for mast or rod-type objects in laboratory conditions with a limited discharge interval.* ***Practical value.*** *This approach will provide an opportunity to optimize the layout of lightning arresters during the restoration of objects, taking into account green reconstruction. The obtained results are proposed for consideration by the Technical Committee TC 81 IEC for inclusion in the next editions of the standards.* References 21, table 2, figure 1.

Key words: **lightning protection, risk assessment, RSM - Rolling Sphere Method, object of arbitrary shape, probability distribution of lightning current, collection area.**

В роботі розглянуто застосування методу «сфери що котиться» до об'єктів інфраструктури у вигляді території, яка включає будівлі та споруди довільної форми. Запропоновано алгоритм урахування статистичного розподілу ймовірності сили струму блискавки для визначення ймовірності влучення блискавки у елементи об'єкту. Визначено, що не урахування цього аспекту у сучасних нормативних документах, призводить до суттєвих помилок. Такий підхід наддасть можливість оптимізувати схему розміщення блискавкоприймачів під час відновлення об'єктів з урахуванням зеленої реконструкції. Бібл. 21, табл. 2, рис. 1.

Ключові слова: **блискавкозахист, оцінка ризику, RSM – метод сфери що котиться, об'єкт довільної форми, розподіл ймовірності сили струму блискавки, площа стягування.**

Problem definition. The widespread use in production and everyday life of various technical means equipped with electronic elements of control, decision-making and control requires a more careful approach to determining the need to equip objects with protection systems (Lightning Protection System – LPS) against the negative consequences of lightning strikes. Such systems must provide a given probability of lightning interception and reduction of voltage and current levels arising in the object's galvanic connections as a result of a lightning strike. International standards IEC series 62305 [1-3] require the implementation of such an assessment, but the methods proposed in them, based on the definition of protection zones, do not allow to solve the problem in full. These standards provide zones only for a limited group of lightning arresters, and do not take into account the probability distribution of lightning current, the presence of other buildings and structures that are nearby. The regulated Rolling Sphere Method (RSM) can potentially be used to refine the calculated estimate of the probability of lightning striking the elements of the object.

Analysis of the latest research and publications. The modern approach to determining requirements for LPS of buildings and structures is regulated by international standards [1-3]. The standard [2] defines the algorithm for assessing the value of the risk due to a possible lightning strike to a building or structure, etc. (hereinafter referred to as the object). The risk R, defined as the probable average annual loss at the facility due to lightning flashes, depends on [2]:

- the annual number of lightning flashes affecting the object;
- the probability of damage from the action of one of these lightning strikes;
- the average number of indirect losses.

Based on the results of the risk assessment, a decision is made about the necessity of setting up the LPS system and the requirements for its level of protection. Ground-level flashes of lightning acting on an object can be divided into:

- flashes that hit the object;
- flashes that hit near the object, directly on the power line, telecommunication line, or near the lines.

The number of lightning strikes affecting an object depends on the density of ground-level lightning flashes in the region where the object is located. In item 4.1.1 [2] it is determined that the return current of lightning is the primary source of damage. Among the factors that affect the risk components is the number of dangerous events [2]. The average annual number of dangerous events N that affect an object due to lightning flashes depends on the thunderstorm activity in the region where the object is located and on its geometric and physical characteristics. To calculate the value of N, the density of ground-level lightning flashes N_G is usually multiplied by the equivalent area of the assembly of the building (structure), taking into account the correcting coefficients.

The density of ground-level lightning flashes N_G is the number of lightning flashes per 1 km^2 during the year. This value is usually available from lightning location networks and is adjusted annually. In the absence of data on N_G values, for the middle latitudes of the northern hemisphere of the Earth, this indicator can be estimated as [2]:

$$N_G \approx 0{,}1\ T_D, \qquad (1)$$

where T_D is the number of thunderstorm days during the year (which can be obtained from isokeraunic maps).

It should be noted that nowadays there are more accurate methods for determining N_G, so the use of thunderstorm days is proposed [4] to be changed to:

$$N_G = 0{,}25 \cdot N_t,$$

where N_t is the total density of optically detected flashes per km^2 during the year, obtained from [5].

The standard [3] regulates the possibility of using the RSM method for the construction of LPS protection zones. The radius of the sphere depends on the class of the building. It is clear that class I requires the highest level of protection, so the radius of the sphere is defined as the smallest (equal to 20 m). Examples of the application of this approach are presented in [6-11]. It is noted that the calculated zones differ from the zones determined by the protective angle method. This contradiction requires an assessment of which method is more correct. As a result of many years of discussion, the possibility of using both methods has been determined, and the choice is made by the designer. This happened because none of these methods has evidence of unconditional reliability. Protection zones based on the protective angle method cannot be substantiated by laboratory experiments, the results of which are ambiguous. It was established that the results of model tests strongly depend on the length of the spark discharge used, on the polarity of the pulse voltage and its time parameters. In addition, the protective properties of the zone are not confirmed by the experience of operating lightning arresters of different heights.

The RSM method has significant advantages because it allows to calculate zones for objects of arbitrary shape, to take into account the collective action of lightning arresters, including natural ones. Calculations confirm the higher efficiency of the system of lightning arresters compared to a single one, due to the reduction of the collection area. However, the method in its standardized form does not take into account the presence of opposing leaders from the object elements. Which definitely affect the location of the lightning strike, but also have a stochastic nature. Attempts to take into account opposing leaders are presented in [12, 13]. The obtained results have a certain value for the development of methods, but have not yet been reflected in standards. Therefore, the influence of opposing leaders cannot be taken into account by LPS designers.

It should be additionally noted that the RSM method allows taking into account any radius of the sphere, which is determined by the lightning return current. It is this nuance that is used in the work, which is described below. For a clear understanding of the content of the work, let's discuss a number of important points.

Up to the orientation height H_{at}, lightning trajectories are not deterministic and their heads fill the orientation plane with a uniform density. Then everything depends on the state of the earth's surface. Lightning is most likely to go further down the shortest distance, but even at laboratory intervals, the spread of long spark trajectories and the spread of breakdown voltage are clearly recorded. The lightning channels going to the lightning arrester and to the undisturbed surface of the earth are, as a rule, distant by a distance of tens of meters or more. Therefore, the mutual influence of their electric fields on each other is insignificant, and the development of each of the channels should be considered independent of the others. Probability theory is well developed for such processes. According to its laws, the probability of breakdown of one of the two discharge gaps – to the lightning arrester and to the surface of the earth, in addition to geometric dimensions, is determined by a single parameter – the breakdown voltage standard σ, which is an orientation standard, it changes little with the length of the multi-meter gap and therefore can be borrowed from laboratory measurements, where its relative value is close to 0.1. It is clear that the presence of an orientation standard determines the well-known fact of lightning striking the side surfaces of buildings and structures. This aspect is not taken into account by the standardized RSM method. However, this probability should not be taken into account for structures with a height of less than 60 m [3].

To design a lightning protection system, among other characteristics, it is important to estimate the expected number of strikes N_s for a certain period (usually 1 year) to the territory of the object and to determine the probabilistic statistical distributions of lightning strikes to its elements. It is clear that the number of hits depends on N_G and the collection area S_{at}. For isolated buildings (structures) on flat terrain, S_{at} is the area defined by the intersection between the ground surface and a straight line with an inclination of 1/3, which is tangent to the highest points of the building (structure) and which revolves around them [2]. Determining the size of S_{at} can be done graphically or mathematically. For the mathematical definition of S_{at}, the empirical formula (2) is given in the standard [2, formula A.2] for an isolated rectangular structure with length L, width W, and height H, located on a flat terrain:

$$S_{at} = L \cdot W + 6 \cdot H \cdot (L + W) + 9 \cdot \pi \cdot H^2 . \qquad (2)$$

The use of (2) for real objects of critical infrastructure is difficult and not sufficiently reliable. The RSM method is based on the application of the lightning strike distance (R) to the structure or to the ground, which are related to the maximum value of the return current (I). The dependence of the R value on the current is determined by a number of formulas obtained by different authors for different variants of the current polarity and the shape of the structure based on experimental observations. A comparison of such formulas is given in

[14]. At this time, it is appropriate to apply formula (3) given in the standard [1]:

$$R = 10 \cdot I^{0.65}, \qquad (3)$$

where R is the lightning strike distance, m; I is the maximum value of the lightning current, kA.

An important factor influencing the results of the assessments is the probability distribution of the maximum lightning current in the area where the object is located. Variants of statistical current distributions are differentiated depending on the height of structures, for positive or negative lightning polarity, obtained on supports and power lines or by remote methods in lightning detection networks. This should be taken into account when using statistical distributions. At this time, it is appropriate to use the dependencies that are summarized in the standard [1] and the CIGRE technical report [15]. It should be understood that research on the clarification of dependence continues [16]. However, changing the dependency will not affect the applicability of the proposed approach. The application of the concept of the RSM method allows to estimate the probability of lightning striking the elements of the object for any given lightning current. In [14], the calculation results for 5 shapes of buildings (cylinder, parallelepiped, hangar in the form of part of a cylindrical surface, round and rectangular houses with internal deflection) and three levels of probability of current (0.5 %, 50 % and 95 %) are given. The results show that the number of lightnings calculated by the RSM method is significantly different from the estimation by the standard approach [2], due to the use of the collection area.

Taking into account the probability distribution of lightning current in a given range of currents, with an arbitrary number of intervals, is proposed in [17-19].

The goal of the work is to substantiate the expediency of taking into account the statistical distribution of lightning current when determining the probability of lightning striking the elements of the object, and the effectiveness of using the improved «rolling sphere» method.

Research methods: the method of mathematical modeling, based on RSM with additional consideration of the probability distribution of lightning current.

Mathematical model of the process. The research object is the territory where the elements of the object (buildings and structures) are arbitrarily placed. With a certain step, a mesh is set on the surface of the earth. If mesh nodes are indexed by the value i on the X axis, and by the value j on the Y axis, then an arbitrary mesh node is denoted as (i, j). In fact, the mesh nodes determine the coordinates of the projection of the point from which the lightning strikes the object onto the horizontal plane. The density of mesh nodes should be set taking into account the size of the object's elements. For each mesh node, the maximum height at which the «rolling sphere» touches the surface of any structure is determined. It is clear that for the surface of the earth the height is zero. If there are several such points (let's denote their number as k), then, assuming that they will be struck with the same probability from the given center of the «rolling sphere», it is concluded that the number of lightning strikes of any of these points will be k times less.

The lightning orientation process is considered started when the radius R (discharge distance) reaches the surface of the object's element. Thus, the orientation distance of each lightning depends on the lightning current. This aspect significantly affects the determination of the probable collection area, and as a result, the probable number of lightning strikes to the object during the year. The proposed process model leads to important conclusions:

- the collection area is determined by the maximum current from the range taken into account;
- the lightnings with minimum current have probability of bypassing the system of lightning arresters.

It is obvious that such properties are not taken into account when using (2), and defined protection zones by the angle method. It is advisable to specify the geometric parameters of the object's elements directly in a specialized PC code without using additional elements of CAD software. Using the general plan of the object, the optimal mesh step is determined. Research experience [17-19] shows that arbitrary structures can be adequately specified using a combination of vertical wires and cables (horizontal or inclined). The distance between such structural elements must be consistent with the mesh step and be less than the minimum radius R of the current range under consideration.

Object points – points of fragments of structures and nodal points of the ground on the territory of the object for which the statistical characteristics of their strike by lightning with a given level of reverse current are determined in the course of the software operation. The discharge distance is determined by the given value of the lightning current by (3). The implementation of the calculation algorithm in the form of two specialized codes [20, 21] for a personal computer was performed by Docent of NTU «KhPI» V.M. Dronov. Codes [20, 21] assume that the law of lightning current distribution is described by the dependence under which the probability P that the peak value of the lightning current will exceed the value I is determined according to (4) [1]:

$$P(I) = \frac{1}{1 + (I/a)^b}, \qquad (4)$$

where P is the probability ($0 \le P \le 1$); I is the limit value of lightning current, kA; a and b are the non-negative parameters that, according to [1], have the following values: $a = 31$ kA, $b = 2.6$.

The values of parameters a and b can have the above default values, as well as other values at the request of the software user.

The results of the calculation estimation. As an example, consider the results of the application of the code [20] to estimate the predicted number of lightning strikes in the structure of the New Safe Confinement (NSC) of the 4th power unit of the Chornobyl NPP. The NSC has the shape of part of a cylindrical surface. In order to estimate the number of expected lightning discharges in the construction of the NSC, the following dimensions of the NSC should be adopted: width 256 m, length 163 m, height 110 m. The density of lightning discharges in the Chernobyl NPP area is taken as $N_G = 4.69$ discharges per 1 km^2 per year. The construction of the NSC is modeled by 75 horizontal cables located along the length with vertical descents, including:

- medium (along the crest);
- right and left on the ground;
- intermediate with a step of 3.4 m along the width.

The range of lightning current (2–200) kA is considered. According to [1, Table A.3] the probability that the lightning current will exceed the specified range is no more than 2 %. The results of the calculations are presented in the Table 1.

Table 1

The results of the calculation estimation

Current range, kA	Probability of a strike in the NSC	Number of hits per year	Mesh step, m
2 – 200	0.2478	1.162	2.5
2 – 200	0.2481	1.164	0.31

Note: The calculations were made for two versions of the calculation mesh step, which differ from each other by 8 times. The results of both cases differ by less than 0.2 %.

The code [20], in addition to the integral value, allows to determine the distribution of the probability of lightning strikes by individual elements. As an example Fig. 1 shows a screenshot of the probability distribution over the ground around the NSC. Such information is also useful for rational placement of additional NPP equipment.

It should be noted that the determination of the relative probability of the strike is carried out for each object separately (in this case, it is the NSC and the ground). Therefore, the maximum values (marked in red – 1) are found both on the shelter and on the ground far from the shelter. As you approach the NSC, the probability decreases, because part of the lightning with a large current is oriented to the NSC.

According to the results of the calculation estimation, it was determined that the predicted number of lightning discharges in the NSC structure is 1.16 per year. Therefore, for 100 years of operation, the number of lightning strikes in the NSC will be 116. The error of the estimation is within 3 %.

We compare with the results of the calculation according to the standardized method [2]. The collection area is determined by (2). After substituting the NSC parameters, the obtained value of S_{at} = 0.66 km^2 per year. Taking into account the average density of N_G = 4.69 discharges/(year·km^2), the number of lightning strikes in the NSC is estimated at 3.095 per year. Therefore, 310 lightning strikes may occur within 100 years, which is 2.67 times more than the number of strikes calculated according to the refined methodology.

The reasons for the difference are determined by the following circumstances:

- the standardized method does not take into account the real shape of the NSC, different from a parallelepiped;
- the standardized method does not take into account the statistical distribution of the lightning current;
- the standardized method is based on the results of experimental studies obtained mainly for mast or rod type objects.

It should be noted that the presence of a significant difference between the results of estimating the number of lightning strikes in the NSC using a standardized method and a method that takes into account statistical distribution is also indicated in [14].

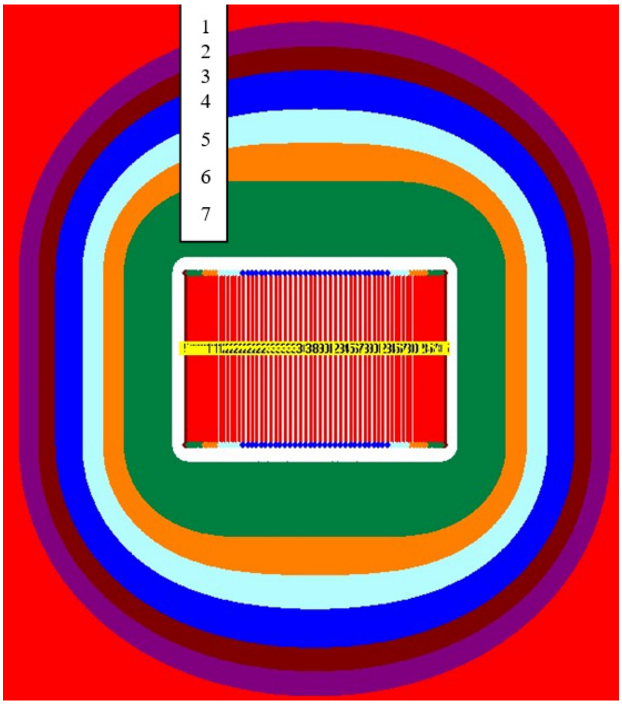

Color correspondence of the probability range P relative to the maximum level:

🟥 1 – max
🟪 2 – [90% – 100%)
🟫 3 – [80% – 90%)
🟦 4 – [60% – 80%)
⬜ 5 – [40% – 60%)
🟧 6 – [20% – 40%)
🟩 7 – [5% – 20%)
⬜ 8 – < 5%

Fig. 1. Distribution of the probability of a lightning strike on the ground around the NSC

Let's consider the features of the calculation model of the code [21] for determining the collection area. For the purpose of simplification and clarity, as a model we will consider the most common variant of a lightning arrester – a mast with a height of h. The code takes into account that for the mast h and the lightning current, which corresponds to the lightning breakdown radius r, the radius of the collection area R_{at} is determined as:

$$\begin{array}{l} R_{at} = r, \;\; r \le h, \\ R_{at} = \sqrt{h \cdot (2r - h)}, \;\; r > h. \end{array}, \tag{5}$$

It follows from (5), if $r \ge 5h$, R_{at} is proportional to $h^{0.5}$. Thus, the collection area is proportional to h, not h^2, as defined in (2), in which $H \equiv h$. For the option when $r \le h$, the collection area approaches the proportionality to r^2, and does not depend on the height h, that also differs from the empirical formula (2). It is known that (2) is based on the results of experimental studies under most laboratory conditions, in which the height of the rod was proportional to the length of the breakdown gap ($R_{at} \approx h$). The author assumes that this very fact caused the appearance of formula (2).

Appropriate formulas for cables, both horizontal and inclined, parallelepipeds, cylinders, etc., were defined [19]. For a rectangular structure, the collection area is calculated as:

$$S_{at} = \pi \cdot R^2 + L \cdot W + 2R(L + W), \qquad (6)$$

where R is the radius of the collection area of the mast of the same height as the height of the building H. The value of R is determined by (5); other notations are the same as (2).

Another aspect, from the point of view of the developed approach, is that the values of the lightning currents are stochastic in nature. Each of these random values corresponds to its lightning breakdown radius value and defines the collection area. Thus, it is necessary to talk about the value of the area S_{at} as a random value, and therefore it is advisable to calculate the average value of the collection area for a specific composition of buildings. Then, knowing the dependence of the values of S_{at} for a specific structure with the specified parameters of its geometry on the radius of the lightning breakdown, and therefore, according to (3), on the value of the lightning current, it is possible to determine the average value of the collection area S_m:

$$S_m = \int_2^{200} S(I) F(I) \mathrm{d}I, \qquad (7)$$

where the lower and upper values determine the current range under consideration; $S(I)$ is the object's collection area for a given value of the lightning current; $F(I)$ is the function of the density of lightning current values, which is defined as:

$$F(I) = \frac{b \cdot a^b \cdot I^b}{I \cdot \left(a^b + I^b\right)^2}, \qquad (8)$$

where a and b are defined in (4).

The code uses a simplified formula:

$$S_m = \sum_{i=1}^{n} \left(S_i F_i\right), \qquad (9)$$

where n is the number of numerical integration intervals; S_i is the value of the desired characteristic when the lightning current is equal to the average value of the current within the i-th integration interval; F_i is the probability that the value of the lightning current will be within the i-th integration interval.

The results of the comparison of two methods of estimating the collection area for masts of different heights are given in Table 2. Calculations of S_m are made for the range of current from 2 kA to 200 kA. Calculation according to (2) does not take this range into account.

Table 2

Comparison of the results of the collection area calculation by RSM and standard [2]

Height h, m	Current range, kA	Area S_m, km^2	S_{at}, km^2	S_{at} / S_m
20	2-100	0.012	0.011	0.92
40	2-100	0.020	0.045	2.25
60	2-100	0.027	0.102	3.78
80	2-200	0.031	0.181	5.86

Note: S_{at} is calculated by (2) for a mast of height h.

The results given in Table 2 unequivocally indicate a significant overestimation of the value of the collection area of lightning, as a result of which the result of estimating the number of hits to the object has overestimated values. From the point of view of risk assessment, this fact is unacceptable.

Conclusions.

1. The expediency of taking into account the statistical distribution of the lightning current at the determination of probability of lightning striking the elements of the object, which is determined by the dependence of the breakdown distance of the air gap between lightning and the object on the potential of the head of the lightning leader, which is related to the lightning current, has been proven. Increasing the reliability of estimating the number of strikes on an object affects the quality of decision-making regarding the risks associated with the consequences of a lightning strike.
2. The effectiveness of the improved «rolling sphere» method, implemented in the form of a computer code, which takes into account the given probability distribution of lightning current in the range from 2 kA to 200 kA, has been proven. Setting the real configuration of the object elements is provided by a combination of vertical wires and cables.
3. The expediency of introducing the concept of «average value of the collection area» is substantiated taking into account the probability of lightning with current in a given range, for example 2 – 200 kA. Examples of the difference of the obtained results from the evaluation according to standardized formulas in the direction of decreasing probability are given. For a hangar-type object with dimensions: width 256 m, length 163 m, height 110 m, the probability of lightning strikes is 2.67 times lower.
4. It has been established that the application of the standardized formula leads to a significant (many times) overestimation of the predicted number of lightning strikes to the object, if the height of the object exceeds 20 m. The reasons for the difference, according to the author, are due to the following properties of the standardized methodology:

- usually, the real shape of the object is not taken into account;
- statistical distribution of lightning current is not taken into account;
- it is based on the results of experimental studies obtained mainly for objects of the mast or rod type in laboratory conditions with a limited discharge gap.

Acknowledgements. The author expresses his sincere gratitude to Volodymyr Dronov, Docent of NTU «KhPI» for many years of fruitful cooperation. Without the use of computer codes developed by him, it was impossible to carry out the analysis and draw the above conclusions.

Conflict of interest. The author declares no conflict of interest.

REFERENCES

1. *Standard IEC 62305-1:2010 (Ed.2) Protection against Lightning – Part 1: General principles.* IEC, Geneva, Switzerland, 2010. 78 p.

2. *Standard IEC 62305-2:2010 Protection against lightning – Part 2: Risk management.* IEC, Geneva, Switzerland, 2010. 87 p.

3. *Standard IEC 62305-3:2010 Protection against lightning – Part 3: Physical damage to structures and life hazards*. IEC, Geneva, Switzerland, 2010. 156 p.
4. Bouquegneau C., Kern A., Rousseau A. Flash density applied to lightning protection standards*. International Conference on Grounding and Earthing & 5th International Conference on Lightning Physics and Effects*. Bonito – Brazil, November, 2012.
5. Available at: https://ghrc.nsstc.nasa.gov/lightning/ (accessed 16 March 2023).
6. Cooray V., Becerra M. Attachment of lightning flashes to grounded structures. *Lightning Protection*, 2010, pp. 165-268. doi: https://doi.org/10.1049/PBPO058E_ch4.
7. Bakar A.H.A., Tan C.K., Abidin A.Z., Khai P.J., Mokhlis H., Illias H.A. Comparative Study on Substation Shielding Due to Direct Lightning Strokes. *Journal of Power and Energy Engineering*, 2014, vol. 2, no. 4, pp. 600-611. doi: https://doi.org/10.4236/jpee.2014.24081.
8. Cooray V., Rakov V., Theethayi N. The lightning striking distance – Revisited. *Journal of Electrostatics*, 2007, vol. 65, no. 5-6, pp. 296-306. doi: https://doi.org/10.1016/j.elstat.2006.09.008.
9. Koliushko D.G., Rudenko S.S., Kiprych S.V. Analysis of the state of the external lightning protection system for operating energy objects. *Electrical Engineering & Electromechanics*, 2020, no. 5, pp. 66-70. doi: https://doi.org/10.20998/2074-272X.2020.5.10.
10. Kern A., Brocke R., Raab V., Hannig M., Rock M., Beierl O., Zischank W. Detailed calculation of interception efficiencies for air-termination systems using the dynamic electro-geometrical model – Practical applications. *2016 33rd International Conference on Lightning Protection (ICLP)*, 2016, pp. 1-6. doi: https://doi.org/10.1109/ICLP.2016.7791518.
11. Tóth Z., Kiss I., Németh, B. (2021). Relation between the material of roof and the risk of lightning caused damage: The rolling sphere method in the use. Electric Power Systems Research, 196, 107286. https://doi.org/10.1016/j.epsr.2021.107286.
12. Leal A.F.R., de Oliveira R.M.S., Lopes N.M., de Lima T.S., Ferreira E.R., Rodrigues N.R.N.M. Lightning Protection Design for Small Riverboats Using the FDTD Method. *Journal of Microwaves, Optoelectronics and Electromagnetic Applications*, 2021, vol. 20, no. 2, pp. 307-319. doi: https://doi.org/10.1590/2179-10742021v20i21074.
13. Guo J., Zhang X., Wang B., Hao X., Zheng S., Xie Y. A three-dimensional direct lightning strike model for lightning protection of the substation. *IET Generation, Transmission & Distribution*, 2021, vol. 15, no. 19, pp. 2760-2772. doi: https://doi.org/10.1049/gtd2.12213.
14. Shostak V., Tyulyukov V. Statistical distributions of current amplitudes and lightning incidence number to structures of various configurations. *2014 International Conference on Lightning Protection (ICLP)*, 2014, pp. 1472-1478. doi: https://doi.org/10.1109/ICLP.2014.6973362.
15. Rakov V.A. et al. CIGRE technical brochure on lightning parameters for engineering applications. *2013 International Symposium on Lightning Protection (XII SIPDA)*, Belo Horizonte, Brazil, 2013, pp. 373-377. doi: https://doi.org/10.1109/SIPDA.2013.6729246.
16. Meppelink J. Statistics of Relevant Parameters of Lightning. *The Lightning Rod as a Danger*, 2023, pp. 143-147. doi: https://doi.org/10.1007/978-3-031-30434-7_15.
17. Rezinkina M.M., Knyazyev V.V., Kravchenko V.I. Computation of the probability of lightning damage to ground objects. *Technical Physics*, 2007, vol. 52, no. 1, pp. 59-64. doi: https://doi.org/10.1134/S1063784207010100.
18. Kniaziev V.V., Melnik S.I. Assessment of probability of lightning direct strike into elements of stationary ground launch complex. *Bulletin of the National Technical University «KhPI» Series: Technique and Electrophysics of High Voltage*, 2018, no. 14 (1290), pp. 76-81.
19. Kniaziev V.V. *Determination of the probability of a lightning strike to the elements of the launch complex using the modified rolling sphere method. Engineering sciences: Development prospects in countries of Europe at the beginning of the third millennium. Collective monograph*. Riga, Baltija Publishing, 2018, vol. 2. 492 p. (pp. 59-92).
20. Dronov V.M., Kniaziev V.V. *Computer program «Calculation of probabilities of lightning protection levels of buildings and structures «Zakhyst-2»*. Patent UA, no. 63631, 2016.
21. Dronov V.M., Kniaziev V.V. *Computer program «Determination of the effective area of the screed and the probability of lightning damage to the elements of the object»*. Patent UA, no. 83877, 2018.

Received 08.11.2022
Accepted 22.02.2023
Published 01.09.2023

V.V. Kniaziev[1], *PhD, Senior Research Scientist,*
[1] Research and Design Institute «Molniya»
of National Technical University «Kharkiv Polytechnic Institute»,
47, Shevchenko Str., Kharkiv, 61013, Ukraine,
e-mail: tc22emc@gmail.com (Corresponding Author)

How to cite this article:
Kniaziev V.V. Determination of the probability of a lightning strike in the elements of the object taking into account the statistical distribution of the current value. *Electrical Engineering & Electromechanics*, 2023, no. 5, pp. 57-62. doi: https://doi.org/10.20998/2074-272X.2023.5.08

UDC 621.311: 537.218 https://doi.org/10.20998/2074-272X.2023.5.09

D.G. Koliushko, S.S. Rudenko, S.O. Tyutyuma, B.V. Vorobiov

Determination of the electric field strength of high-voltage substations

The electric field strength is one of the main factors influencing sensitive microprocessor equipment and personnel on power stations and substations, power lines. Determining its level is an important applied task for ensuring the safe operation of electrical installations. ***The aim*** *is to develop calculation relationships for determining the electric field strength created by the busbar of high-voltage substations in the working areas of personnel. The solution of the problem was based on the use of the method of equivalent charges to determine the strength of the electric field created by the complex busbar of high-voltage substations.* ***Methodology.*** *The development was based on solving the problem of the potential of the electric field of a point charge located in a dielectric half-space for a cylindrical coordinate system. By representing the electrode in the form of a set of point charges and subsequent integration, an expression for calculating the potential is obtained, created by a busbar of arbitrary orientation of finite length in an analytical form. Using the principle of superposition of fields and the definition of the derivative, expressions were obtained for calculating the vertical component of the electric field strength at given heights.* ***Results.*** *Based on the obtained expressions, using Visual Basic, the simulation of the distribution of the electric field strength under a three-phase power line with a voltage of 150 kV was performed. Comparison with the known calculation results obtained on the basis of analytical expressions for infinitely long conductors showed that the obtained expressions have an error of no more than 7%.* ***The scientific novelty*** *lies in the fact that for the first time expressions were obtained for determining the electric field strength created by a system of electrodes of finite length, based on the analytical method for solving differential equations.* ***Practical significance.*** *The proposed technique is implemented as a test module of the LiGro specialized software package, which allows modeling complex busbar systems typical for power stations and substations and power lines. A test calculation was carried out for an operating substation of regional electric networks with a voltage class of 110 kV. By comparing the duration of the calculation of switchgears with a diagonal of about 500 m, it was found that the calculation time in the LiGro complex based on the analytical method is several tens of times less than the calculation based on the finite element method. In addition, a more powerful computer was used for the end element simulation.* References 14, tables 1, figures 5.

Key words: **substation, power line, electric field, method of equivalent charges.**

В електричних станціях та підстанціях, лініях електропередачі напруженість електричного поля є одним з головних факторів впливу на чутливе мікропроцесорне обладнання та персонал. Визначення її рівня є важливою прикладною задачею для забезпечення безпечної експлуатації електроустановок. ***Мета роботи*** *– розробка розрахункових співвідношень для визначення напруженості електричного поля, що створюється ошиновкою високовольтних підстанцій в робочих зонах персоналу. Розв'язання задачі базувалося на використанні методу еквівалентних зарядів для визначення напруженості електричного поля, створюваного складною ошиновкою високовольтних підстанцій.* ***Методика.*** *В основу розробки покладено розв'язання задачі про потенціал електричного поля точкового заряду, розташованого в діелектричному наппівпросторі, для циліндричної системи координат. Шляхом представлення електроду у вигляді множини точкових зарядів та подальшого інтегрування отримано вираз для розрахунку потенціалу, що створений ошиновкою довільної орієнтації кінцевої довжини в аналітичному вигляді. Використовуючи принцип суперпозиції полів і визначення похідної, отримано вирази для розрахунку вертикальної складової напруженості електричного поля на заданих висотах.* ***Результати.*** *На основі отриманих виразів за допомогою Visual Basic виконано моделювання розподілу напруженості електричного поля під трифазною лінією електропередачі напругою 150 кВ. Порівняння з відомими результатами розрахунків, отриманими на основі аналітичних виразів для нескінченно довгих провідників, показало, що отримані вирази мають похибку не більше 7%.* ***Наукова новизна*** *полягає в тому, що вперше отримано вирази для визначення напруженості електричного поля, створюваного системою електродів скінченної довжини, на основі аналітичного методу розв'язування диференціальних рівнянь.* ***Практична значимість.*** *Запропонований спосіб реалізовано у вигляді тестового модулю спеціалізованого програмного комплексу LiGro, що дозволяє виконувати моделювання складних систем ошиновок, характерних для електричних станцій та підстанцій і ліній електропередачі. Виконано тестовий розрахунок для діючої підстанції регіональних електричних мереж класом напруги 110 кВ. Шляхом порівняння тривалості розрахунку розподільчих пристроїв з діагоналлю близько 500 м встановлено, що час розрахунку в комплексі LiGro на основі аналітичного методу в декілька десятків разів менший, ніж розрахунок на основі методу кінцевих елементів. Крім того, для моделювання методом кінцевих елементів використовувався комп'ютер з більш потужними характеристиками.* Бібл. 14, табл. 1, рис. 5.

Ключові слова: **підстанція, лінія електропередачі, електричне поле, метод еквівалентних зарядів.**

Analysis of the problem. Ensuring the resistance of technical objects to the action of powerful electromagnetic fields of natural and artificial origin is an important technical problem, without solving which the reliable and safe use of modern equipment, objects of military equipment and critical infrastructure is impossible.

Distribution devices of electrical stations and substations represent a complex technical system that combines power and measuring equipment of various voltage classes, control and telemechanics devices, including those based on microprocessor technology, cable products and busbars, as well as grounding and lightning protection devices. In such systems, the electric field strength ***E*** is one of the main factors affecting sensitive microprocessor equipment and personnel. Therefore, its permissible value is regulated in a number of normative documents [1–3]. For personnel, this is 5 kV/m for the vertical component of the electric field strength at height of 1.8 m above ground level. If this value is exceeded, the duration of staff stay at the workplace is limited. For example, in electric field with strength of 20 to 25 kV/m, the working time should not exceed 10 minutes, and at 25 kV/m and above, special personal protective equipment should be used. The boundaries of sanitary protection zones for active power transmission lines are determined at the level of 1 kV/m.

Limitations regarding the value of the electric field strength for microprocessor equipment are regulated in the relevant documentation regarding the conditions of its operation.

Determination of the electric field strength level is carried out experimentally [4, 5] and/or by calculation [4–10].

Experimental determination is performed with the help of electric field strength meters, unidirectional or tridirectional. The specified devices when used at power stations and substations should have a wide range of measurements (approximately from 1 to 50 kV/m), not distort the field lines, be insensitive to electromagnetic interference, be resistant to vibration and shocks and be able to work in difficult weather conditions, etc. This leads to a significant complication of the design and an increase in the cost of the specified devices. In addition, measurement in the field is quite time-consuming and does not allow to build detailed plans of strength zones on the territory of switchgear. In addition, there are zones in which it is practically impossible to carry out measurements (the presence of an internal fence, proximity to current-carrying parts, etc.).

In the conditions of targeted strikes by the Russian army on energy facilities of Ukraine and the prompt restoration of critical infrastructure, including by installing new power transmission line supports, the express assessment of field strength and boundaries of sanitary protection zones becomes even more relevant. Operationally, such an assessment can be performed only with the help of calculation methods. Here, it is enough to know the voltage class of the line and its geometric parameters.

The listed factors increase the relevance of the calculation way of determining the electric field strength for both planned and operating electrical stations and substations. As a rule, calculations for electric power facilities with a voltage class of 35–1000 kV are performed using numerical methods, among which the finite volume method has become the most common [9, 10]. By finite we mean a small volume around each grid mesh. In this method, volume integrals that contain expressions with divergence are transformed into surface integrals using the Ostrogradsky formula. Finite difference and finite element methods are also used [4–6]. The application of such methods is quite complicated, requires significant computing resources and is characterized by a long calculation time for large objects, which is explained by the iterative process and the size of the mesh cell. The calculation step should be comparable to the diameter of the busbar, which is tens of millimeters with object sizes up to several hundreds of meters. Thus, with a uniform mesh step, we have a large number of calculation points. Reducing their number is possible thanks to the use of special algorithms for irregular dividing of the computational volume [9, 10], which significantly complicates the modelling of objects with arbitrary orientation of busbars. In addition, in [11] it is stated that these methods are highly dependent on «human experience and trial and error.»

Analytical formulas for determining the electric field strength are given in a number of works, in particular in [6, 8]. They are, as a rule, easier to use, the mathematical expression shows the dependence of the field on all parameters of the line [6], they do not require significant computer resources. Traditionally, in such calculations, the busbar is replaced by a charged axle, and the method of equivalent charges is used to take into account the diameter. However, the main drawback of the existing expressions is that they consider infinitely long conductors (busbars). This leads to the limitation of the use of analytical formulas only for the simplest cases of the location of busbars of power transmission line supports. Here, expressions for determining the equivalent bus radius are usually used to take into account phase splitting. Taking into account that in the distribution devices of electrical stations and substations, the busbar is arbitrarily oriented in space, there are several voltage classes, split phases of different diameters, etc., the use of existing analytical expressions for them is practically impossible. In [4, 11], the implementation of the charge simulation method is proposed, which is actually a combination of numerical and analytical solutions for modelling the field of a substation with a voltage class of 500/220 kV, but in these works it is noted that the given method has similar disadvantages to numerical calculation methods.

Taking into account the perspective of using analytical expressions, their potentially higher accuracy and acceleration of calculation for complex objects of the electric power industry, the solution of the problem of the electric field of an arbitrarily oriented conductor of finite size (electrode) located above the earth's surface is relevant.

The goal of the work is to develop calculation relationships for determining the electric field strength created by the busbar of high-voltage substations in the working areas of the personnel.

Research materials. When using analytical methods to calculate the electric field strength of energy objects, the following assumptions are accepted [9, 10]:

- the electric field of the power frequency is quasi-static, which is explained by the propagation speed of the electromagnetic field in the air of $3 \cdot 10^8$ m/s at frequency of 50 Hz, so the expressions for the instantaneous value of the electric potential or strength will be valid for lines of size << 6000 km;
- busbars are long cylinders, the charge of which is regularly distributed along their axes;
- the voltage on the busbar changes according to the sinusoidal law with constant power frequency;
- the time shift between the busbar voltage phases is 120°;
- the earth's surface is flat, and it is an infinite electrical conductor compared to air and, accordingly, has zero potential;
- the air-ground separation boundary is plane-parallel;
- the influence of buildings and structures of electric stations and substations is not taken into account;
- the relative dielectric permittivity of air is assumed to be $\varepsilon_r = 1$.

Taking into account the above assumptions for solving the problem of the electric field strength of an arbitrarily oriented electrode, consider the electric field of a point charge located above a conductive surface.

The electric field of a point charge has axial symmetry. Therefore, it is advisable to use a curvilinear orthogonal cylindrical coordinate system (r, z, ψ) with an axis perpendicular to the boundary of the half-space with dielectric permittivity ε and passing through the point charge itself (see Fig. 1).

The formulation of the problem under consideration consists of the Laplace equation and additional conditions. The potential does not depend on the coordinate ψ, so the Laplace equation takes the form [12]:

$$\frac{\partial^2\varphi}{\partial r^2}+\frac{1}{r}\frac{\partial\varphi}{\partial r}+\frac{\partial^2\varphi}{\partial z^2}=0\,. \qquad (1)$$

Additional conditions are as follows:

- the condition at the air-ground boundary looks like this:

$$\varphi\big|_{z=0}=0\,; \qquad (2)$$

- when the coordinate z increases, the potential φ goes to zero:

$$\varphi_{\to\infty}=0\,. \qquad (3)$$

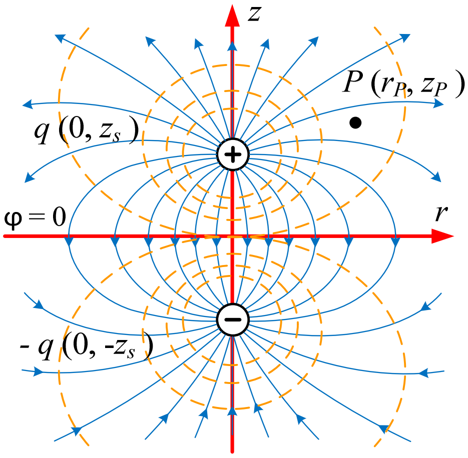

Fig. 1. A point charge located in the dielectric half-space

The solution of such a problem for the observation point $P(r_P, z_P)$ according to the method of mirror images and the principle of superposition is the sum of potentials from an electric dipole [6]:

$$\varphi(r,z)=\frac{q}{4\pi\varepsilon}\left[\frac{1}{\sqrt{{r_P}^2+(z_P-z_s)^2}}-\frac{1}{\sqrt{{r_P}^2+(z_P+z_s)^2}}\right], \qquad (4)$$

where z_s is the coordinate of the point charge along the axis z; ε is the static dielectric permittivity, which is equal to $\varepsilon = \varepsilon_r\varepsilon_0 = 8.8541878176\cdot10^{-12}$ F/m.

We denote the two fractions in the brackets of expression (4) as α_1 and α_2, respectively.

To obtain relationships for calculating the total potential of a system of arbitrary configuration, consider a separated electrode, uniformly charged with length L_i, in the form of a set of point charges located along its axis (Fig. 2). In fact, the electrode is an infinitely thin rod. Here, the linear charge density of such a source, located on the axis of the i-th electrode, has the form:

$$\tau_i=\sum_{l_i=0}^{L_i}q_{si}\Big/L_i\,. \qquad (5)$$

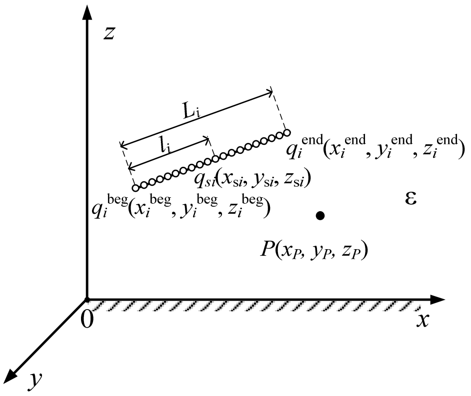

Fig. 2. An electrode in the form of a set of point charges located in a dielectric half-space

When moving from the cylindrical to the Cartesian coordinate system, the distance between the point charge located on the axis of the electrode and the observation point P can be rewritten as:

$$r_i=\sqrt{\left(x_{si}-x_P\right)^2+\left(y_{si}-y_P\right)^2}\,, \qquad (6)$$

where x_P, y_P are the Cartesian coordinates of the observation point P; x_{si}, y_{si}, z_{si} are the Cartesian coordinates of the point charge of the i-th electrode.

In turn, the coordinates of a point charge (Fig. 2) can be given in the form:

$$x_{si}=x_i^{\mathrm{beg}}+\left(x_i^{\mathrm{end}}-x_i^{\mathrm{beg}}\right)\frac{l_i}{L_i}\,,$$
$$y_{si}=y_i^{\mathrm{beg}}+\left(y_i^{\mathrm{end}}-y_i^{\mathrm{beg}}\right)\frac{l_i}{L_i}\,, \qquad (7)$$
$$z_{si}=z_i^{\mathrm{beg}}+\left(z_i^{\mathrm{end}}-z_i^{\mathrm{beg}}\right)\frac{l_i}{L_i}\,,$$

where x_i^{beg}, y_i^{beg}, z_i^{beg} and x_i^{end}, y_i^{end}, z_i^{end} are the Cartesian coordinates of the beginning and end nodes of the i-th electrode, respectively; l_i is the current distance of the point charge from the beginning of the electrode.

Taking into account (6) and (7), the two fractions in expression (4) can be represented in the general form:

$$\alpha_{ki}=\frac{1}{\sqrt{\frac{A_i}{{L_i}^2}l^2+\frac{B_{ki}}{L_i}l_i+C_{ki}}}\,; \qquad (8)$$

where k = 1 or 2 to account for positive or negative charge (Fig. 1)

$$A_i=\left(x_i^{end}-x_i^{beg}\right)^2+\left(y_i^{end}-y_i^{beg}\right)^2+\left(z_i^{beg}-z_i^{end}\right)^2;$$
$$B_{1i}=2\Big[\left(x_i^{beg}-x_p\right)\left(x_i^{end}-x_i^{beg}\right)+\left(y_i^{beg}-y_p\right)\times$$
$$\times\left(y_i^{end}-y_i^{beg}\right)+\left(z_i^{beg}-z_p\right)\left(z_i^{end}-z_i^{beg}\right)\Big];$$
$$C_{1i}=\left(x_i^{beg}-x_p\right)^2+\left(y_i^{beg}-y_p\right)^2+\left(z_i^{beg}-z_p\right)^2;$$
$$B_{2i}=2\Big[\left(x_i^{beg}-x_p\right)\left(x_i^{end}-x_i^{beg}\right)+\left(y_i^{beg}-y_p\right)\times$$
$$\times\left(y_i^{end}-y_i^{beg}\right)+\left(z_i^{beg}+z_p\right)\left(z_i^{end}-z_i^{beg}\right)\Big];$$
$$C_{2i}=\left(x_i^{beg}-x_p\right)^2+\left(y_i^{beg}-y_p\right)^2+\left(z_i^{beg}+z_p\right)^2.$$

When integrating (4) along the electrode and taking into account the transition to the cylindrical coordinate system, we obtain:

$$\varphi_i = \tau_i \frac{1}{4\pi\varepsilon}\left(G_{1i} - G_{2i}\right), \qquad (9)$$

where

$$G_{ki} = \int_0^{L_i} \frac{\mathrm{d}\ell_i}{\sqrt{\frac{A_i}{L_i^2}\ell_i^2 + \frac{B_{ki}}{L_i}\ell_i + C_{ki}}} =$$

$$= \left(\ln\left|\frac{2A_i + B_{ki}}{2\sqrt{A_i}} + \sqrt{A_i + B_{ki} + C_{ki}}\right| - \ln\left|\frac{B_{ki}}{2\sqrt{A_i}} + \sqrt{C_{ki}}\right| \right).$$

With a known value of the voltage on the electrode, we can determine the value of the linear density of the i-th electrode using the principle of «replacing the electrode surface with an equipotential» (method of equivalent charges):

$$\tau_i = \frac{4\pi\varepsilon\varphi_i}{\left(G_{1i} - G_{2i}\right)}. \qquad (10)$$

Here, the observation point P is located on the surface of the electrode in the middle of its length.

The total potential from the system of electrodes (busbars) is determined by the principle of superposition of fields:

$$\varphi = \sum_{i=1}^{Q_{con}} \varphi_i\ , \qquad (11)$$

where Q_{con} is the number of electrodes in busbar system.

The electric field strength is a vector equal to the gradient of the electric field potential with a minus sign. When determining the distribution of the electric field strength, the vertical component of the vector is used to control its impact on the personnel, i.e. the projection of $\boldsymbol{E}$ on the z axis, which is numerically equal to the derivative of the potential along the applicate axis. According to the definition of the derivative, this can be represented as a limit:

$$E_z = \left|\frac{\partial\varphi}{\partial z}\right| = \left|\lim_{\Delta z \to 0} \frac{\Delta\varphi}{\Delta z}\right|. \qquad (12)$$

Thus, having set the calculation step along the applicate axis $\Delta z << z_P$, we can determine the modulus of the vertical component of the electric field strength at the height z_P.

The obtained expressions (9)–(12) allow to calculate the electric field strength of busbar systems when they are replaced by electrodes of arbitrary orientation in space.

To determine the electric field strength, which is created by a three-phase bus system, the equivalent linear charge density of one of the phases is calculated according to (10), and for the other two, it is taken according to the sinusoidal distribution of the instantaneous value of the voltage at a fixed moment in time. For example, for phases B and C it is assumed that $\tau_{\mathrm{B,C}} = \pm 0.5\tau_{\mathrm{A}}$ at the time corresponding to 210°.

On the basis of the obtained expressions (9) – (12) in the MS Excel software product using the Visual Basic application, the busbar of a three-phase power transmission line was modelled with the following parameters: busbar suspension height 10 m, length 1000 m, radius 0.04 m, voltage class 150 kV, interphase distance 6.2 m. The calculation was performed along an axis perpendicular to the busbar at distance of 500 m from the beginning of the span. The analysis was carried out at height of 1 m and 3 m, respectively (see Fig. 3,*a*,*b*).

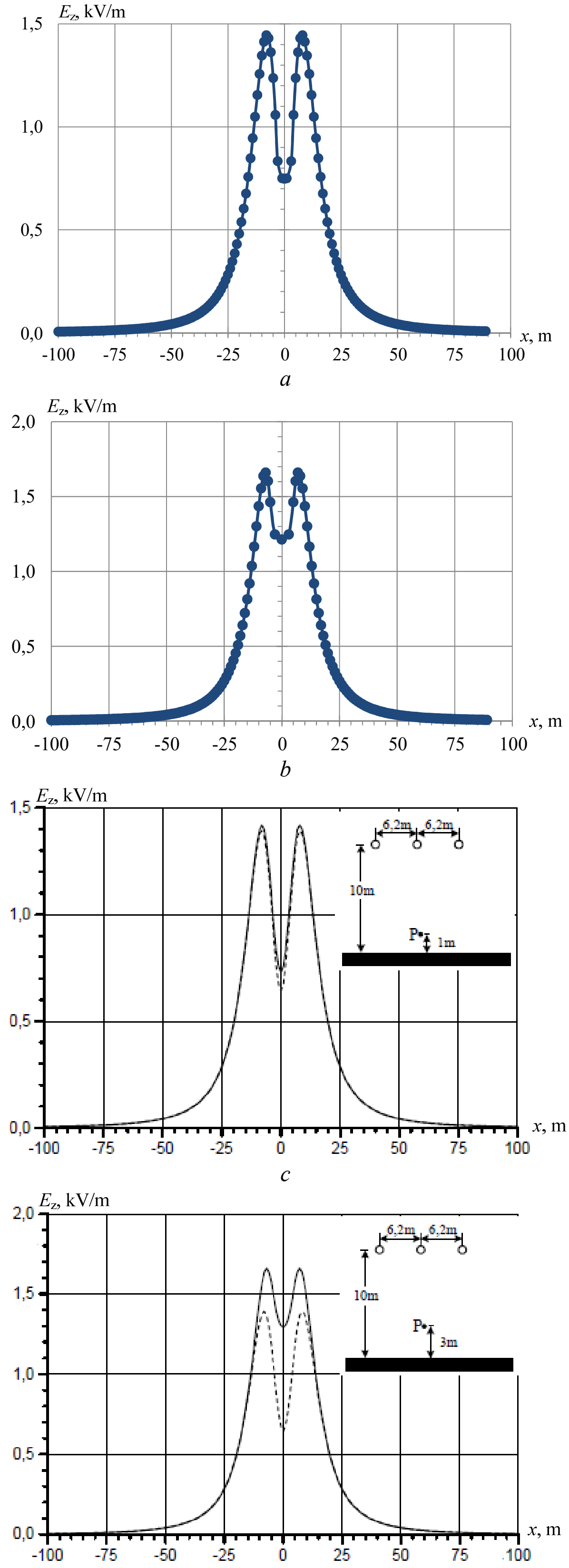

a

b

c

d

Fig. 3. Comparison of the results of calculating the field strength under the busbar of the power transmission line portal according (9)–(12) for height: *a* – 1 m; *b* – 3 m and according to [6] for height: *c* – 1 m; *d* – 3 m

The use of the presented initial data allows to compare the calculation results with the known ones [6], which were obtained for a three-phase line based on analytical expressions for infinitely long conductors (see Fig. 3,*c*,*d*).

Figures 3,*c*,*d* show the curves according to the calculation data [6]: the dashed line is for the approximate expression, and the solid line is for the exact expression. To assess the correspondence of the results obtained by the authors Table 1 summarizes the characteristic values of the vertical component of the electric field strength E_z at the given heights of the analysis z_P and the relative error of the calculation δ.

Table 1

Data for comparative calculation analysis

x, m	E_z, kV/m					
	$z_P = 1$ m			$z_P = 3$ m		
	developed	exact [6]	δ, %	developed	exact [6]	δ, %
0	0,7481132	0,7461	0,3	1,2135346	1,2913	6,0
5	1,2347961	1,1997	2,9	1,4629176	1,5576	6,1
6,2	1,4413401	1,4195	1,5	1,6597963	1,6518	0,5
10	1,3458512	1,3254	1,5	1,4358176	1,4423	0,4
15	0,8472474	0,8584	1,3	0,8140060	0,8733	6,8
20	0,4807888	0,4853	0,9	0,4532538	0,4823	6,0
25	0,2822402	0,2901	2,7	0,2679740	0,2833	5,4
30	0,1756019	0,1778	1,2	0,1684291	0,1785	5,6
40	0,0794274	0,0789	0,7	0,0773403	0,0822	6,0
50	0,0419541	0,0426	1,4	0,0412079	0,0441	6,6

Comparisons with the results obtained by the authors show that the shape of the curves is practically identical, the maximum is observed in all cases under the extreme phases of the busbar at distance of ±6.2 m. The maximum deviation at height of 1 m is 2.9%, and at height of 3 m is 6.8%.

The increase in error when approaching the busbar can be explained by the effect of the geometric size of the conductor (the authors assumed 0.04 m, but it was not specified in [6]). Thus, the validity of the obtained expressions compared to the known calculation results was confirmed.

The proposed calculation method was implemented as a test module for the LiGro software complex [13]. The choice of the specified complex is due to the availability of the necessary palette of modelled objects (busbars, portals, supports, equipment, buildings and communications of arbitrary location and complexity, etc.), as well as 2D and 3D visualization modules. For the convenience of displaying the calculation results, a gradient form of representation is used.

Figure 4 shows fragments of 2D and 3D models of an operating distribution device of the 110/6 kV voltage class of a substation of one of the regional energy companies in the east of Ukraine. The substation plan, heights and geometric parameters of the busbar, which were determined during the diagnosis of the lightning protection system according to the method [14], were used as initial data. The voltage class of each bus system and phasing, set in the parameters of each electrode (busbar) separately, were also taken into account. This allows to take into account all voltage classes that are present on the object.

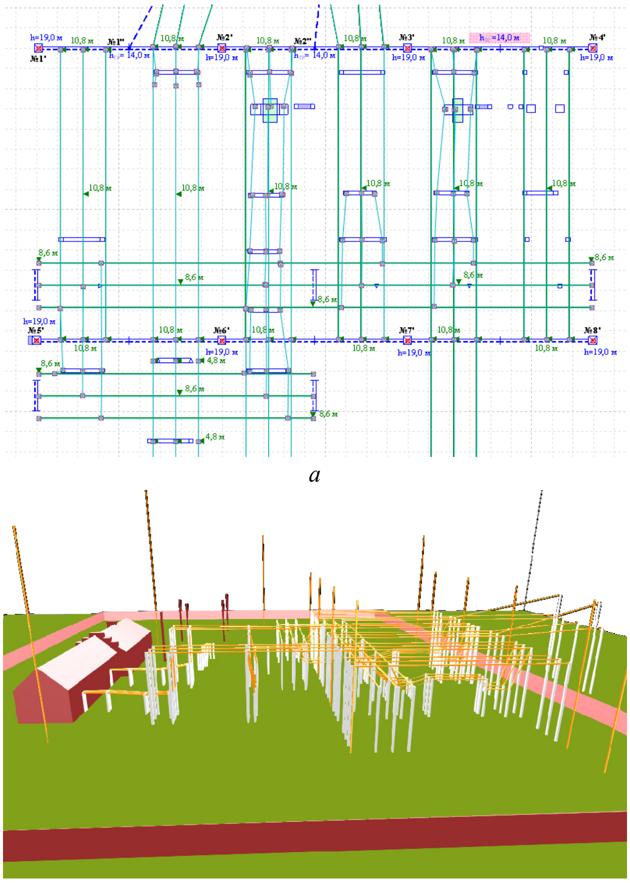

a

b

Fig. 4. Fragments of 2D (*a*) and 3D (*b*) models of a functioning substation of voltage class 110/6 kV in the LiGro complex

The simulation results for an operating distribution device with voltage class of 110/6 kV are shown in Fig. 5. The calculation was carried out at standardized height of 1.8 m, with a mesh with a step of 0.1 m. The calculation did not take into account the sagging of the busbar. But, if necessary, this can be solved by dividing it into parts at the appropriate angle of inclination.

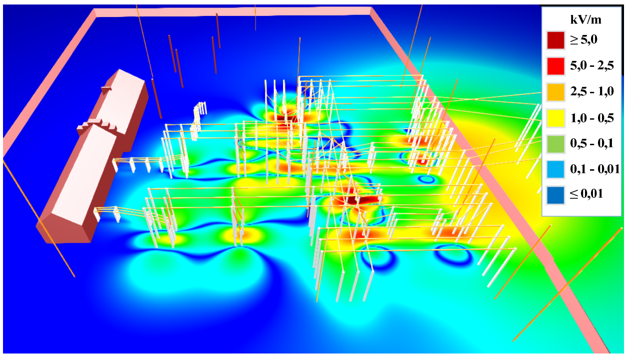

Fig. 5. Distribution of the electric field strength for an operating electric power facility of voltage class of 110/6 kV, obtained in the LiGro software complex

The calculation results show that there are areas at the substation where the field strength exceeds the permissible value of 5 kV/m, and the presence of personnel in these areas should be limited. In addition, it can be noted that the quality of the display of calculation results corresponds to the world level, namely to such software as [4, 5]. Here, in [5], where the simulation was performed on the basis of the finite element method using ANSYS and SolidWorks codes, the calculation time for a substation with voltage class of 1000 kV with a diagonal of approximately 500 m was 7 hours when using a powerful computer with the following parameters: an Intel processor Xeon 8×2.50 GHz and 32 GB RAM. For comparison, the calculation time in the LiGro complex of a similar distribution device with a diagonal of 540 m and voltage class of 750 kV of one of the nuclear power plants of Ukraine with a calculation mesh step of 0.2 m was only 6 minutes when using a computer with significantly worse parameters: an Intel processor Pentium G2020 2×2.90 GHz and 4 GB RAM. Therefore, the model developed by the authors based on the analytical method allows to significantly reduce the time spent and technical requirements for the computer when modeling the electric field strength of complex objects.

Conclusions.

1. On the basis of the method of equivalent charges, for the first time calculation relationships were developed for determining the intensity of the electric field created by the complex busbar of high-voltage substations in the working areas of the personnel.

2. The developed calculation relationships were used to create a computer code that allows to calculate the electric field strength at high-voltage substations and other high-voltage energy facilities taking into account the voltage class of each bus system, and at the design stage of these facilities to determine safe working areas for personnel by electric field.

Conflict of interest. The authors of the article declare that there is no conflict of interest.

REFERENCES

1. *State Standard. NPAOP 40.1-1.01-97 Rules for the safe operation of electrical arrangement.* Kyiv, State Supervision of Occupational Safety and Health, 1997. 97 p. (Ukr)

2. *IEC 62110:2009 – Electric and magnetic field levels generated by AC power systems.* Geneva, IEC, 2009. 103 p.

3. *Regulatory document SOU-N EE 20.179:2008. Calculation of the electric and magnetic fields of power line. Methodology.* Kyiv, Minpalyvenergo of Ukraine Publ., 2016. 37 p. (Ukr).

4. Shaalan E.M., Ghania S.M., Ward S.A. Analysis and measurement of electric field exposure inside 500/220 KV air insulated substation. *Journal of Electrical Engineering*, 2012, vol. 12, no. 2, pp. 77-84.

5. Li N., Yang X., Peng Z. Measurement of Electric Fields Around a 1000-kV UHV Substation. *IEEE Transactions on Power Delivery*, 2013, vol. 28, no. 4, pp. 2356-2362. doi: https://doi.org/10.1109/TPWRD.2013.2269146.

6. Tzinevrakis A.E., Tsanakas D.K., Mimos E.I. Analytical Calculation of the Electric Field Produced by Single-Circuit Power Lines. *IEEE Transactions on Power Delivery*, 2008, vol. 23, no. 3, pp. 1495-1505. doi: https://doi.org/10.1109/TPWRD.2008.916748.

7. Baishya M.J., Kishore N.K., Bhuyan S. Calculation of electric and magnetic field safety limits under UHV AC transmission lines. *2014 Eighteenth National Power Systems Conference (NPSC)*, 2014, pp. 1-6. doi: https://doi.org/10.1109/NPSC.2014.7103794.

8. Patsyuk V.I., Berzan V.P., Ribacova G.A. Mathematical Model of a Three-Phase Electric Line with Split Phases. *Problems of the Regional Energetics*, 2019, no. 1-3(42), pp. 53-67. doi: https://doi.org/10.5281/zenodo.3239218.

9. Rezinkina M.M. Simulation of electric fields in the presence of rods with rounded upper ends. *Technical Physics*, 2015, vol. 60, no. 3, pp. 337-343. doi: https://doi.org/10.1134/S1063784215030238.

10. Rezinkina M.M., Knyazyev V.V., Kravchenko V.I. Computation of the probability of lightning damage to ground objects. *Technical Physics*, 2007, vol. 52, no. 1, pp. 59-64. doi: https://doi.org/10.1134/S1063784207010100.

11. Shaalan E.M., Ghania S.M., Ward S.A. Analysis of electric field inside HV substations using charge simulation method in three dimensional. *2010 Annual Report Conference on Electrical Insulation and Dielectic Phenomena*, 2010, pp. 1-5. doi: https://doi.org/10.1109/CEIDP.2010.5724041.

12. Koliushko D.G., Rudenko S.S., Saliba A.N. Method of integro-differential equations for interpreting the results of vertical electrical sounding of the soil. *Electrical Engineering & Electromechanics*, 2021, no. 5, pp. 67-70. doi: https://doi.org/10.20998/2074-272X.2021.5.09.

13. Koliushko D.G., Rudenko S.S., Istomin O.Ye., Saliba A.N. Simulation of electromagnetic processes in the grounding system with a short circuit in the operating high-voltage substation. *Electrical Engineering & Electromechanics*, 2022, no. 4, pp. 75-80. doi: https://doi.org/10.20998/2074-272X.2022.4.11.

14. Koliushko D.G., Rudenko S.S., Kiprych S.V. Analysis of the state of the external lightning protection system for operating energy objects. *Electrical Engineering & Electromechanics*, 2020, no. 5, pp. 66-70. doi: https://doi.org/10.20998/2074-272X.2020.5.10.

Received 18.11.2022
Accepted 19.01.2023
Published 01.09.2023

D.G. Koliushko[1]*, PhD, Senior Research Scientist,*
S.S. Rudenko[1]*, PhD, Senior Research Scientist,*
S.O. Tyutyuma[1]*, Postgraduate Student,*
B.V. Vorobiov[1]*, PhD,*
[1] National Technical University «Kharkiv Polytechnic Institute»,
2, Kyrpychova Str., Kharkiv, Ukraine, 61002,
e-mail: denys.koliushko@khpi.edu.ua;
serhij_rudenko@ukr.net (Corresponding Author);
agnius.igres@gmail.com;
bohdan.vorobiov@khpi.edu.ua

How to cite this article:
Koliushko D.G., Rudenko S.S., Tyutyuma S.O., Vorobiov B.V. Determination of the electric field strength of high-voltage substations. *Electrical Engineering & Electromechanics*, 2023, no. 5, pp. 63-68. doi: https://doi.org/10.20998/2074-272X.2023.5.09

UDC 621.3.022:621.396.6:533.93 https://doi.org/10.20998/2074-272X.2023.5.10

K.V. Korytchenko, V.F. Bolyukh, S.G. Buriakovskyi,Y.V. Kashansky, O.I. Kocherga

Electromechanical and thermophysical processes in the pulse induction accelerator of plasma formation

Introduction. *Work on the creation and throwing of plasma formations is carried out in the world's leading scientific centers in various ways. The creation of a plasma formation with duration of several milliseconds and its acceleration in an open atmospheric environment to a distance of 0.5-0.6 m was achieved. To create plasma, the energy of the primary discharge circuit is used, followed by the acceleration of the gas-plasma formation with the help of the energy of the secondary circuit. Plasma formation is also obtained due to the electric explosion of a conductor in a rapidly decreasing strong magnetic field, etc. The* ***purpose*** *of the article is a theoretical and experimental study of electromechanical and thermophysical processes in a pulse induction accelerator, which ensures the creation of plasma formation due to thermal ionization as a result of the electric explosion of the conductor and its throwing in the atmospheric environment relative to the inductor.* ***Method.*** *For the analysis of electromechanical and thermophysical processes in the pulse induction accelerator of plasma formation (PIAPF), a mathematical model of the accelerator was developed and implemented in the Comsol Multiphysics software package, in which the armature does not change its shape and aggregate state during operation and takes into account the parameters of the accelerator distributed in space.* ***Results.*** *Calculated electromechanical and thermal characteristics of the accelerator. It is shown that the temperature rise in the aluminum foil armature is significantly nonuniform. The maximum temperature value occurs in the middle part of the foil closer to the outer edge, and this temperature is significantly higher than the boiling point of aluminum.* ***Scientific novelty.*** *Experimental studies of the PIAPF were carried out, in which the armature is made of aluminum and copper foil, and the inductor connected to the high-voltage capacitive energy storage device is made in the form of a flat disk spiral. It was established that during the operation of the PIAPF, the armature goes into a plasma state and moves vertically upwards, turning into a volumetric wad or a pile of small particles that rose to a considerable height relative to the inductor. Experimentally, the characteristic circular circuit of thermal heating of the copper foil of the armature, which is fixed on a glass-textolite sheet, is shown, which indicates a similar nature of plasma formation.* ***Practical value****. The results of experimental studies with an accuracy of up to 15 % coincide with the calculated ones and show the validity of the PIAPF concept, in which, due to the high density of the induced current in the armature, thermal ionization occurs as a result of an electric explosion of the conductor with its transition to the plasma state. And the interaction of the plasma formation with the magnetic field of the inductor leads to the appearance of an electrodynamic force that ensures its movement in the open atmospheric environment.* References 17, figures 9.

Key words: **pulse induction accelerator of plasma formation, mathematical model, electromechanical and thermal processes, experimental studies.**

Вступ. *Роботи по створенню та метанню плазмових утворень різними способами ведуться в провідних наукових центрах світу. Досягнуто формування плазмового утворення тривалістю декілька мілісекунд та його метання у відкритому атмосферному середовищі на відстань 0,5-0,6 м. Для створення плазми використовують енергію первинного розрядного кола з подальшим прискоренням газоплазмового утворення за допомогою енергії вторинного кола. Плазмове утворення отримують і за рахунок електричного вибуху провідника.* ***Метою*** *статті є теоретичне та експериментальне дослідження електромеханічних та теплофізичних процесів в імпульсному індукційному прискорювачі, який забезпечує формування плазмового утворення за рахунок термічної іонізації в результаті електричного вибуху провідника та метання його у атмосферному середовищі відносно індуктора.* ***Методика.*** *Для аналізу електромеханічних та теплофізичних процесів в імпульсному індукційному прискорювачі плазмового утворення (ІІПП) розроблена і реалізована в програмному пакеті Comsol Multiphysics математична модель прискорювача, в якій якір не змінює своєї форми і агрегатного стану в процесі роботи та враховує розподілені у просторі параметри.* ***Результати.*** *Розраховані електромеханічні і теплові характеристики прискорювача. Показано, що перевищення температури в якорі, що виконаний у вигляді алюмінієвої фольги, суттєво нерівномірно. Максимальне значення температури має місце в середній частині фольги ближче до зовнішнього краю, причому ця температура значно перевищує температуру кипіння алюмінію.* ***Наукова новизна.*** *Проведені експериментальні дослідження ІІПП, у якого якір виконаний з алюмінієвої та мідної фольги, а індуктор, що підключається до високовольтного ємнісного накопичувача енергії, виконаний у вигляді плоскої дискової спіралі. В процесі роботи ІІПП якір переходить в плазмовий стан і переміщується вертикально вверх, перетворюючись в об'ємний комок, або на скупчення маленьких частинок, які здіймались на декілька метрів відносно індуктора. Експериментально показано характерний круговий контур термічного нагрівання мідної фольги якоря, яка закріплена на листі склотекстоліту.* ***Практична цінність.*** *Результати експериментальних досліджень з точністю до 15 % співпадають з розрахунковими і показують справедливість концепції ІІПП, в якому за рахунок високої густини індукованого струму в якорі відбувається термічна іонізація в результаті електричного вибуху провідника з переходом його в плазмовий стан. Взаємодія плазмового утворення з магнітним полем індуктора призводить до появи електродинамічної сили, яка забезпечує його переміщення у відкритому атмосферному середовищі на декілька метрів.* Бібл. 17, рис. 9.

Ключові слова: **імпульсний індукційний прискорювач плазмового утворення, математична модель, електромеханічні та теплові процеси, експериментальні дослідження.**

Introduction. Plasma technologies are used in various structural and technological systems and devices, in scientific research, etc. One of the directions of such research is the formation of plasma formations and throwing them at a certain distance from the source of formation. Such work is carried out in the leading scientific centers of the world, primarily in the USA: Princeton Laboratory of Plasma Physics, Los Alamos National Laboratory, University of New Hampshire, Swarthmore Laboratory of Magnetodynamics, etc. [1-4]. The University of Missouri, USA is investigating the acceleration of plasma formation in an open atmospheric environment [5]. The duration of existence of a plasma formation is a few milliseconds, and it moves in the air for a small distance of 0.5-0.6 m.

For the formation of plasma, the energy of the primary discharge circuit is used [6]. The formation of plasma in the form of a ring occurs due to the gas-dynamic process of turbulation of the gas-plasma jet. Acceleration of gas-plasma formation is carried out using the energy of the secondary circuit. The output of thermal plasma from the forechamber is provided by gas-dynamic, not electrodynamic forces.

Plasma formation is also formed due to the electrical explosion of a conductor in a rapidly decreasing magnetic field [7]. The magnetic field is formed due to the current flowing through the plasma, which is formed in the form of a spiral in the wake of the explosion of the conductor. To create conditions for the stability of the ring due to the energy of the magnetic field, it is assumed that the process of returning the energy of the magnetic field to the electric energy of the capacitor charge is interrupted.

In induction plasmatrons, for the formation of a plasma ring, the method of inducing a discharge in a low-pressure gas environment with subsequent increase to atmospheric pressure, or plasma formation in the area near the inductor due to an arc discharge is used [8-10]. Plasmatrons provide induction of eddy current in the plasma formation in atmospheric conditions, but do not solve the problem of magnetic field energy accumulation in the plasma formation.

Analysis of accelerators of plasma formations. A known pulse plasma accelerator is containing electrodes, one of which is made in the form of a copper rod, and the other in the form of a plate. Ablation occurs under the action of an electric discharge between the electrodes in a solid dielectric substance [11]. The accelerator operates under low gas pressure in the accelerator channel. A pulse plasma accelerator is also known, which contains an accelerating channel formed by two electrodes with a Teflon insulator located between them, which is the working substance [12].

These accelerators have low efficiency and specific power, due to the use of only the energy stored by the electric field for acceleration. The effectiveness of these accelerators is limited by the long process of creating the working substance due to the limited speed and nonuniformity of its evaporation.

There is a well-known plasma accelerator, which contains electrodes connected through an ohmic and inductive load to a capacitive energy storage (CES), an end ceramic insulator that separates the electrodes and dielectric checkers installed between the electrodes, made of the material in which the ablation takes place [13]. When a high-voltage pulse is applied to the electrodes, as a result of a surface breakdown, a plasma formation is formed, which short-circuits the electrodes of the accelerator. The working substance that evaporates from the surface of the dielectric checkers is ionized and accelerated under the influence of electromagnetic forces and gas-dynamic pressure. In this accelerator, the efficiency of acceleration is increased due to the use of both electromagnetic forces and gas-dynamic pressure. However, it has a low specific power due to the use of only electrical energy to create electromagnetic and gas-dynamic forces.

There is a known plasma accelerator consists of a cylindrical guide tube, an external hollow cylindrical magnet and a system of thermal ionization of matter to the plasma state [14]. One end of the pipe is in the air environment, and on the other end there is a gas flow formation system using a gas turbine engine. The system of thermal ionization of matter consists of discharge electrodes located inside the guide tube and an induction plasma heater. The electromagnetic coil of the heater, which covers the guide tube, ensures the formation of plasma inside the guide tube. Due to the gas turbine engine, a heated gas flow is formed, which is directed into the cylindrical pipe. Gas heated above 1000 °C is sent to the thermal ionization system, where it is heated by arc discharges to a high temperature (5000-10000 °C). The gas enters the region of the induction heater, where a ring-shaped plasma is formed. Under the action of pulse magnetic fields alternately created by magnets located along the cylindrical guide tube, plasma formation is accelerated.

This device achieves a high specific power due to the combined use of the chemical energy of fuel combustion and the energy of the electromagnetic field. But the well-known accelerator has a too complicated design.

An inductive accelerator is known, which ensures the creation and acceleration of plasma in an air environment [15]. The accelerator consists of a coaxially installed fixed disk inductor excited by CES, and a working substance located opposite the inductor, which during thermal ionization due to the induced current passes into a plasma state with further acceleration along the coaxial axis under the action of electrodynamic forces. This accelerator has a simple design, but the plasma in the form of a ring cannot move a long distance relative to the inductor. Radially directed electrodynamic forces arise in the plasma ring, which «tear» the ring, and thus interrupt the flow path of the induced current.

Thus, the task of creating an accelerator of plasma formation, which ensures its movement in the air medium for a considerable distance, is urgent.

The goal of the article is a theoretical and experimental study of electromechanical and thermophysical processes in a pulse induction accelerator, which ensures the formation of a plasma formation due to thermal ionization as a result of an electric explosion of a conductor and throwing it in the atmospheric environment relative to the inductor.

Mathematical model of the accelerator. The difficulties of calculating the pulse inductive accelerator of plasma formation (PIAPF) are primarily caused by the uncertainty of the plasma formation parameters, which change dynamically. To determine the general characteristics of electromechanical and thermal processes, we will assume that the armature is made solid and does not change its shape and aggregate state during the operation of the accelerator. To implement a mathematical model with spatially distributed parameters, we will use a system of partial differential equations with respect to spatial and temporal variables [16].

The mathematical model of electromagnetic processes in PIAPF, which includes a fixed inductor and a moving conductive armature, is presented in a cylindrical coordinate system in terms of a magnetic vector potential $\vec{A}_i$, which has a φ component.

The differential equations with respect to the φ component of the magnetic vector potential in the region of the inductor Ω_1 give the form:

$$\gamma_1 \frac{\partial A_{1\varphi}}{\partial t} + \frac{1}{\mu_0} \frac{\partial^2 A_{1\varphi}}{\partial z^2} + \frac{1}{\mu_0} \frac{\partial}{\partial r} \left(\frac{1}{r} \cdot \frac{\partial (r A_{1\varphi})}{\partial r} \right) = -\frac{i_1(t) \cdot N_1}{S_1} k_{1s}, \quad (1)$$

in the region of solid conductive armature Ω_2:

$$\begin{gathered} \gamma_2 \frac{\partial A_{2\varphi}}{\partial t} + \frac{1}{\mu_0} \frac{\partial^2 A_{2\varphi}}{\partial z^2} + \frac{1}{\mu_0} \frac{\partial}{\partial r} \left(\frac{1}{r} \cdot \frac{\partial (r A_{2\varphi})}{\partial r} \right) - \\ - v_{z2}(t) \cdot \frac{\gamma_2}{\mu_0} \cdot \frac{\partial A_{2\varphi}}{\partial z} = 0 \end{gathered}, \quad (2)$$

in the region of air environment Ω_0:

$$\frac{1}{\mu_0} \frac{\partial^2 A_{0\varphi}}{\partial z^2} + \frac{1}{\mu_0} \frac{\partial}{\partial r} \left(\frac{1}{r} \cdot \frac{\partial (r A_{0\varphi})}{\partial r} \right) = 0, \quad (3)$$

where $j_1(t)$ is the tangential component of the current density in the inductor; $i_1(t)$ is the instantaneous value of the current in the inductor; γ_1, γ_2 is the specific conductivity of the inductor and armature, respectively; μ_0 is the magnetic constant; $v_{z2}(t)$ is the speed of the armature; N_1 is the number of turns of the inductor; S_1 is the cross-sectional area of the inductor; k_{1s} is the inductor filling factor.

Differential equations (1) – (3) are supplemented by the corresponding boundary and initial conditions:

$$\begin{gathered} \frac{1}{\mu_0} \mathrm{rot} A_1 \cdot n = -\frac{1}{\mu_0} \mathrm{rot} A_2 \cdot n; \\ \mathrm{rot} A_1 \cdot n = -\mathrm{rot} A_2 \cdot n; \\ A_{1\varphi}(0) = A_{2\varphi}(0) = 0, \end{gathered} \quad (4)$$

where A_i is the magnetic vector potential of the magnetic field of the i-th region; n is the unit normal vector.

The axial component of the force acting on the accelerator armature is determined using the corresponding component of the Maxwell tension tensor T:

$$f_z = \oint_S 2\pi r T_z \mathrm{d}s = \frac{1}{\mu_0} \oint_S 2\pi r (B_r \cdot B_z) \mathrm{d}s, \quad (5)$$

where B_r, B_z are the radial and axial component of the magnetic flux density.

The electrical state of the accelerator can be described by equations:

$$2\pi \frac{N_1}{S_1} \int_{S_1} \frac{\mathrm{d} r A_{1\varphi}}{\mathrm{d}t} \mathrm{d}r \mathrm{d}z + (L_0 + L_1) \frac{\mathrm{d} i_1}{\mathrm{d}t} + i_1 (R_0 + R_1) + u_C = 0, \quad (6)$$

$$2\pi \frac{1}{S_2} \int_{S_2} \frac{\mathrm{d} r A_{2\varphi}}{\mathrm{d}t} \mathrm{d}r \mathrm{d}z + L_2 \frac{\mathrm{d} i_2}{\mathrm{d}t} + i_2 R_2 = 0, \quad (7)$$

where L_0, R_0 are the inductance and active resistance of the excitation circuit, respectively; R_1, R_2 are the active resistances of the inductor and armature, respectively; L_1, L_2 are the inductances of the inductor and the armature, respectively; i_2 is the instantaneous value of the current in the armature; S_2 is the cross-sectional area of the armature; u_C is the CES voltage, which is supplemented by the appropriate initial conditions.

Thermal processes in the PIAPF are described using the equation:

$$\begin{gathered} c_k(T) \cdot \gamma_k \frac{\partial T_k}{\partial t} = \\ = \frac{\partial}{\partial r} \left(\lambda_k(T) \frac{\partial T_k}{\partial r} \right) + \frac{1}{r} \lambda_k(T) \frac{\partial T_k}{\partial r} + \frac{\partial}{\partial z} \left(\lambda_k(T) \frac{\partial T_k}{\partial z} \right) + \\ + j_k^2(t) \cdot \rho_k(T), \end{gathered} \quad (8)$$

where $c_k(T)$ is the average specific heat capacity of the k-th active element (inductor and armature); γ_k is the average material density of the k-th active element; $j_k(t)$ is the current density of the k-th active element; $\lambda_k(T)$ is the thermal conductivity of the k-th active element; $\rho_k(T)$ is the resistivity of the k-th active element; T_k is the temperature distribution in space and time of the k-th active element.

On the cooled surfaces of the active elements, the system of equations (8) is supplemented by boundary conditions of the third kind, which takes into account convective and radiative heat exchange, and on the axis of symmetry by boundary conditions of the second kind.

The mathematical model of the PIAPF with nonuniform distribution of currents in the inductor and armature is implemented in the *Comsol Multiphysics* software package using the Finite Element Method when taking into account all relationships between physical processes [17]. Here, data is exchanged between processes, calculation regions are allocated for each physical problem, provided that the mesh division is consistent for all problems. Modeling is performed in the following sequence:

- physics modules («Magnetic fields», «Electrical circuit», «Heat transfer in solid», «Fluid structure interaction») are selected, which implement the corresponding tasks, dimensions (2D), model type (time-dependent) and calculation methods;
- the geometry of the accelerator is formed and the calculation regions for the selected physical problems are determined;
- output data are set in the form of constant values and functions that describe the relationship between parameters, for example, the dependence of specific resistance on temperature;
- initial and boundary conditions of the considered physical problems are set;

- discretization of calculation reguions is carried out taking into account the geometric model of the electrodynamic accelerator;
- methods of solving the considered problems MUMPS, PARDISO are chosen and numerical calculations are carried out.

The calculation area of the model was a cylinder with radius whose value was more than 5 times greater than the radius of the farthest element of the accelerator in the radial direction from the *z* axis. The height of the calculated cylinder was more than 10 times higher than the largest height of the accelerator elements. This made it possible to achieve the required accuracy with acceptable calculation time, considering the calculation boundary to be conditionally infinite.

The model used the «Free triangular» mesh with «Extra fine» element sizes (the maximum meshelement size for remote areas of the environment was 5 mm, and for the accelerator, the mesh element size was chosen in the interval from (0.001 to 1 mm)). Relative displacement of elements of the accelerator was determined by the use of Automatic remeshing (criterion mod1.fsi.minqual>0.2). Spatial discretization consists in dividing a limited area into separate piecewise continuous subareas. The set of such elements is defined as a mesh or triangulation, which is a model of the calculation area. Moreover, for each of the physical modules («Magnetic fields», «Electrical circuit», «Heat transfer in solid»), the interpolation of the solution for individual finite elements, determined by quadratic or cubic discretization, was used. The main variables are approximated by nodal values multiplied by base vector that is required for interpolation within the element. An implicit finite-difference scheme of the fifth order is used for time approximation.

Electromechanical and thermal processes of the accelerator. Consider the PIAPF, in which the fixed inductor is made in the form of a flat spiral made of steel, and the armature is made in the form of a disk-shaped aluminum foil, located coaxially with respect to the inductor. PIAPF parameters are as follows: **CES**: voltage U_0 = 25 kV, capacity C_0 = 360 μF; **inductor**: number of turns N_1 = 7, inner diameter D_{in} = 10 mm, outer diameter D_{ex} = 600 mm, cross-sectional area of the turn $S_1 = 5\times25 =$ $= 125$ mm^2; **armature**: thickness h_2 = 8 μm; outer diameter D_{ex} = 600 mm, distance from the inductor z_0 = 0.5 mm; **excitation circuit**: L_0 = 1.5 μH, R_0 = 50 mΩ.

Figure 1 presents the calculated characteristics of the PIAPF, namely, the change in the CES voltage u_C, the current density in the inductor j_1 and in the armature j_2 (*a*), the current density in the armature distributed along its radius at the moment of maximum current (*b*).

There is a non-simultaneous increase in the maximum values of the currents in the inductor and the armature. The armature current reaches its maximum value after about 0.15 ms, while the inductor current reaches its maximum value after about 0.75 ms. Moreover, the density of the induced current in the armature is nonuniform across the cross-section in the radial direction: in the middle part, closer to the outer edge, it reaches a maximum value of j_2 = 118 kA/mm^2, and on the outer edge it decreases to j_2 = 76 kA/mm^2.

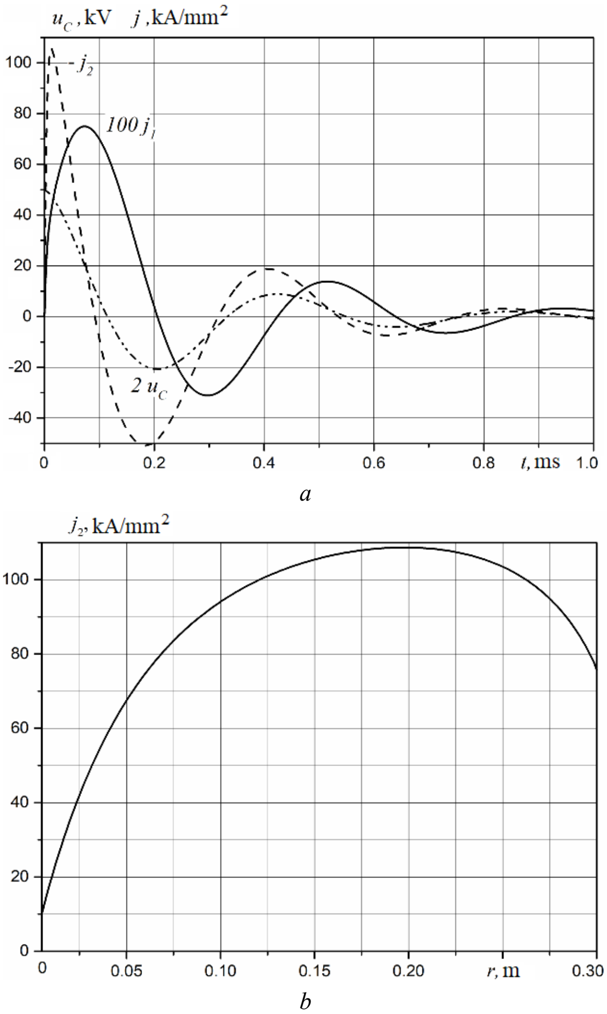

a

b

Fig. 1. Calculated characteristics of the PIAPF: *a* – change in the CES voltage and current density in the inductor and armature; *b* – current density distribution in the armature at the moment of maximum induced current

Figure 2 shows the electrodynamic force f_{z2}, the speed v_z and the displacement h_z of the armature. The maximum value of the electrodynamic force of repulsion reaches about f_{z2} = 185 kN. But due to the phase shift between the currents in the inductor and the armature in the interval of 0.9 – 2.1 ms, the electrodynamic force of attraction acts on the armature, which is much smaller than the force of repulsion. As a result of this nature of the force, the speed of the armature reaches a maximum value of approx. v_z = 113 m/s at 0.08 ms, after which the speed decreases to 66 m/s at 0.2 ms after the start of the work process with a slight increase later.

Figure 3 shows the change and radial distribution at the moment of the maximum current of exceeding the temperature of the armature θ_2. The change in θ_2 over time is determined by the nature of the change in the current density in the armature j_2. The temperature rise increases to a value of about θ_2 = 4200 °C at the moment of 0.6 ms from the start of the work process. After that, there is a slight decrease to θ_2 = 4000 °C with a gradual increase to θ_2 = 6300 °C and higher after 0.25 ms.

But the temperature excess is distributed over the cross-section of the armature (aluminum foil) in the radial direction significantly nonuniformly. In the center of the foil $\theta_2 = 0$. The maximum value of $\theta_2 = 7900$ °C occurs in the middle part of the armature closer to the outer edge. Note that the boiling point of aluminum is 2519 °C, and that of copper is 2580 °C.

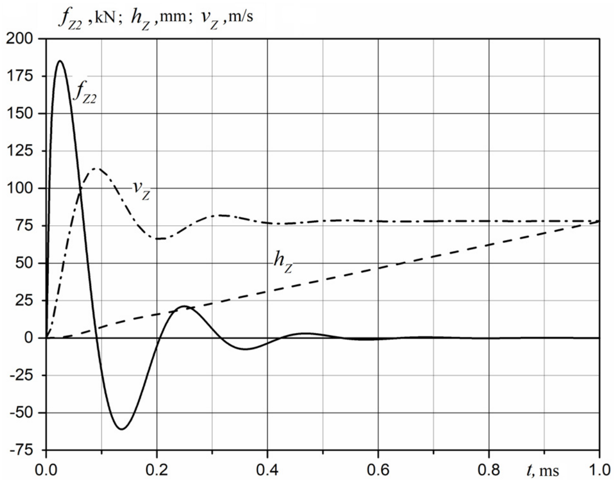

Fig. 2. Electrodynamic force f_{z2}, speed v_z and displacement h_z of the armature in PIAPF

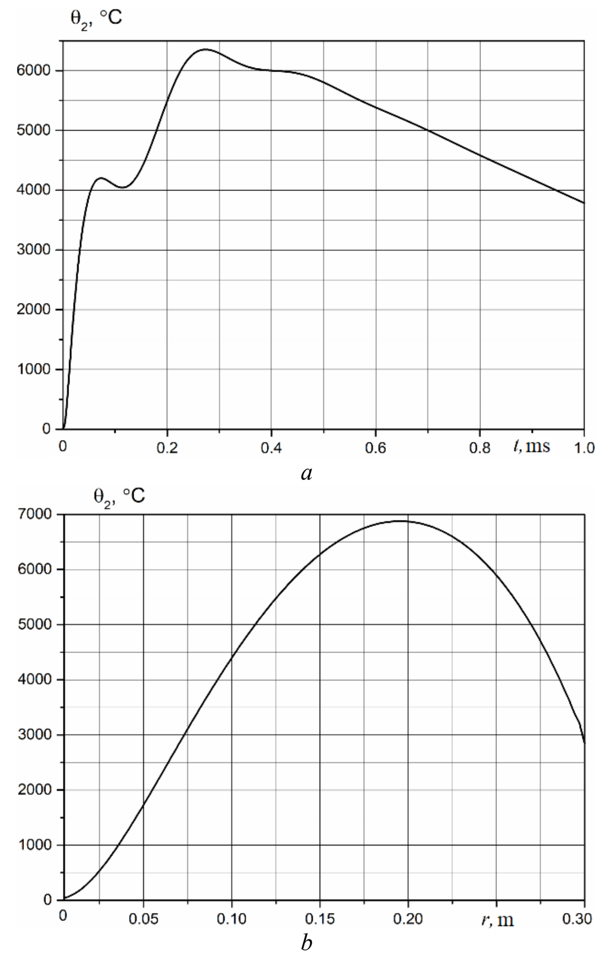

a

b

Fig. 3. Armature temperature rise: change in temperature rise over time (*a*), radial distribution of temperature rise at the moment of maximum current (*b*)

In order to validate the mathematical and computer models, the energy balance of the PIAPF was checked. Figure 4 presents: W_C – CES energy; W_{floss} – heat losses in the armature; W_i – heat losses in the inductor; W_{mag} – magnetic field energy; W_{Sr} – heat losses on the limiting resistor and lead wires; W_{Sind} – magnetic energy on underwater wires; W_{kin} – kinetic energy. Since the energy balance is fulfilled, this indicates the reliability of the obtained results.

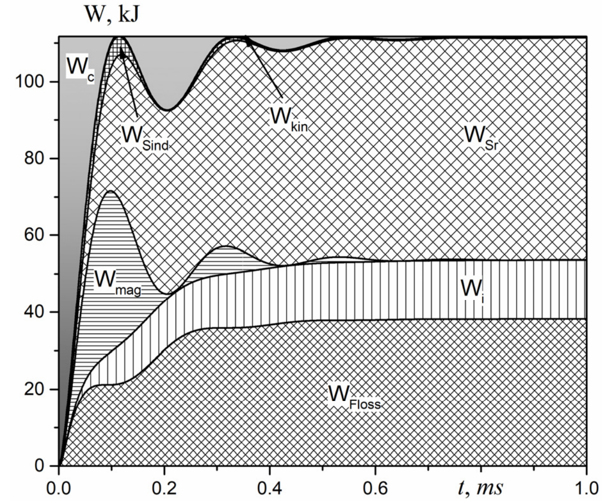

Fig. 4. Distribution of energy in the PIAPF

During the work process, the magnetic energy W_{mag} and the CES energy W_C have an oscillatory-damping character, and they change almost in antiphase. All other energy components in the accelerator grow to different levels, going to a certain constant value. As follows from the results of the calculation, the main part of the CES energy is transformed into thermal energy in the active elements and elements of the PIAPF excitation circuit.

Experimental studies of PIAPF. Experimental studies of the PIAPF of plasma formation were conducted on the basis of the Research and Design Institute «Molniya» using the methodology presented in [16]. The experimental setup includes the CES of the GITM-10/350 current generator, which consists of 120 parallel-connected IK503Y4 type capacitors, each of which has capacity of 3 μF. The middle output of each capacitor is connected to the common bus through 4 TVO-60 resistors connected in parallel with resistance of 24 Ohms. Switching of CES is carried out through a high-voltage arrester.

Parameters of the experimental setup: the total capacity of the CES –360 μF, the maximum voltage of the CES – 50 kV, the measured active resistance of the inductor – 9 mΩ, the total resistance of the excitation circuit – 50 mΩ, the inductance of the inductor – 15 mH.

Experimental studies of the PIAPF with armature of various shapes and materials, made of conductive foil, were carried out. During the research, the inductor was horizontally attached to the insulating base, and an armature was installed on top of it through the insulating plate. This design of the accelerator ensured vertical movement of the armature under the action of electrodynamic forces.

The inductor was made in the form of a flat disc spiral made of steel with outer diameter of 600 mm. A gap is made between turns of the spiral, which ensures the impossibility of inter-turn electrical breakdown. The turns of the spiral are attached to the insulating plate with the help of steel screws (Fig. 5). The cross-section of the spiral turn was 5×25= 125 mm^2. Two variants of the inductor were used in the experiments. In the first version

(7 turns), the inner turn of the inductor was placed in the center and the inductance of the inductor L_1 = 12 μH. In the second version, the two inner turns of the inductor were removed and the diameter of the inner hole was 230 mm.


a *b*

Fig. 5. External view of the PIAPF inductor: the first version (*a*), the second version (*b*)

Figure 6 shows the results of the operation of the PIAPF, in which the armature is made as an aluminum foil with thickness of 18 μm in the form of a disc with outer diameter D_{ex} = 600 mm (Fig. 6,*a*), and the inductor of the first variant is connected to the CES with voltage U_0 = 20 kV. After the tests, the disk armature is aluminum foil compressed into a volumetric wad (Fig. 6,*b*). During the operation of the accelerator, the armature enters the plasma state and moves vertically upwards for several meters (in Fig. 6,*c*,*d*, the armature is shown by a straight line).

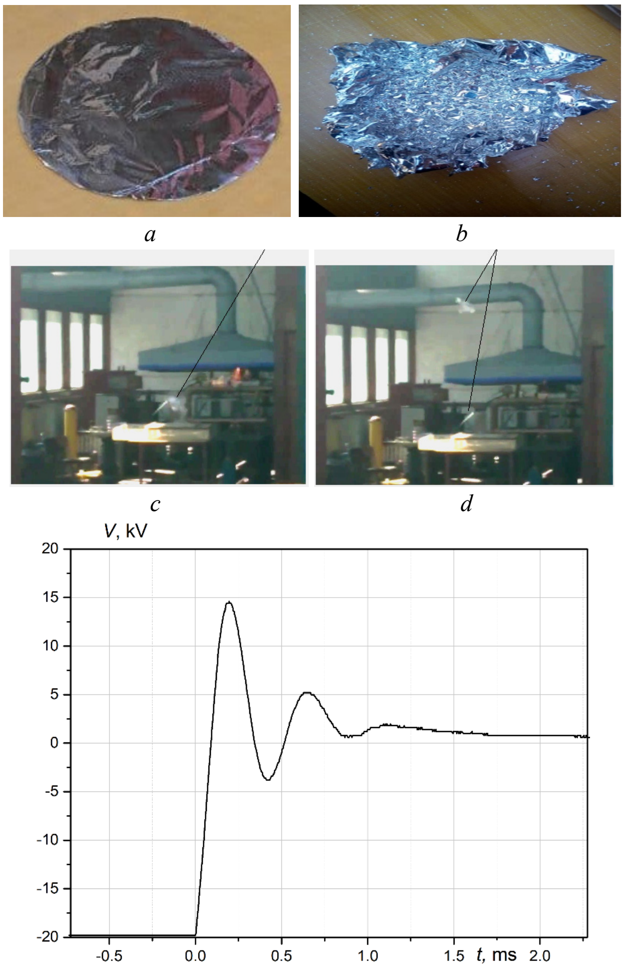

a *b*

c *d*

e

Fig. 6. Disk armature before (*a*) and after (*b*) tests, the position of the armature at the initial (*c*) and next (*d*) moments of operation and the oscillogram of the CES voltage (*e*) of the PIAPF

Figure 7 shows the results of the PIAPF operation, in which the armature is made in the form of a torus of aluminum foil with thickness of 10 μm, and the inductor of the second variant is connected to the CES with voltage U_0 = 23 kV. The average diameter of the torus is 300 mm (Fig. 7,*a*). When the accelerator was working, the toroidal armature, after transitioning into the plasma state, turned into a cluster of small particles that rose to a considerable height relative to the inductor (Fig. 7,*b*). The transformation of the armature, made of thinner foil than in the previous experiment, into a cluster of small particles can be explained both by the action of electrodynamic forces in the armature and by nonuniform thermal damage to its individual sections.

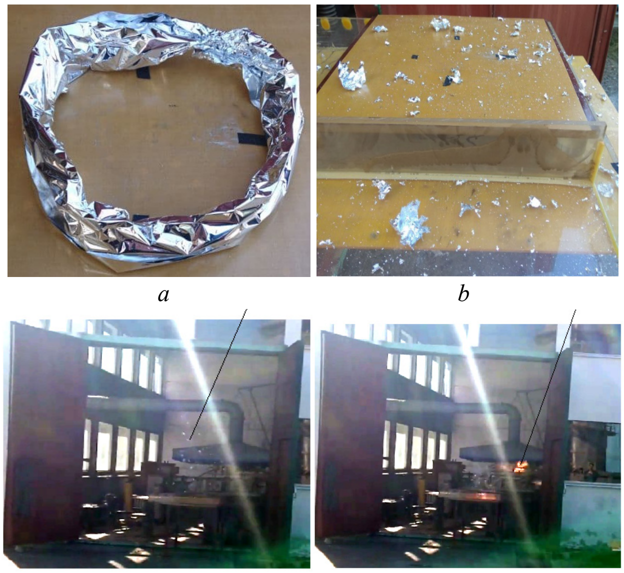
a *b*

c *d*

Fig. 7. Toroidal armature before (*a*) and after (*b*) tests; position of the armature at the initial (*c*) and next (*d*) moments of the PIAPF operation

Figure 8 shows the results of the PIAPF operation, in which the inductor of the second variant is excited at voltage U_0 = 20 kV, and the armature is made of copper foil, 9 mm thick, which is fixed on a sheet of fiberglass with dimensions of 900×900×1 mm. Since the fiberglass sheet was curved, an insulating support with a load was used to press it evenly to the inductor (Fig. 8,*a*).

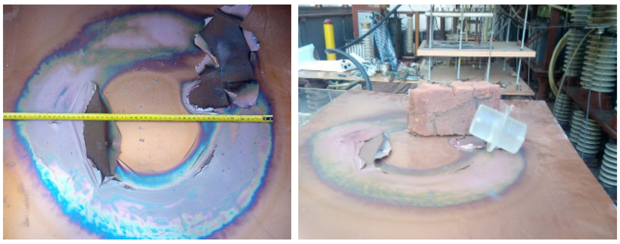
a *b*

Fig. 8. Armature made of copper foil, which is fixed on a sheet from fiberglass, after PIAPF tests

After the operation of the accelerator, an area of thermal combustion (Fig. 8,*b*) appeared in the place where the glass-textolite sheet was pressed against the copper foil, the particles of which flew up. Here, the characteristic circular contour of the heating of the copper foil is clearly visible, which indicates the similar nature of the induced current in the armature. Since the melting temperature of copper is higher than that of aluminum, thermal ionization of the copper foil did not occur even in the zone of induced current flow. In other areas, thermal heating of the foil is practically absent.

When using a more compact inductor (outer diameter 280 mm, coil width 9.4 mm, distance between coils 5 mm) on CES with higher voltage U_0 = 35 kV and with smaller capacity C_0 = 18.5 μF (total resistance of the excitation circuit R_0 = 0.1 Ω, total inductance of the excitation circuit L_0 = 1.5 μH) a plasma formation is formed, which moves relative to the inductor. Figure 9 shows an oscillogram of the current in the inductor, the external view of the inductor and the plasma formation that has moved away from the inductor. The armature is made of copper foil, 9 mm thick, which is fixed on a fiberglass sheet with dimensions of 900×900×1 mm.

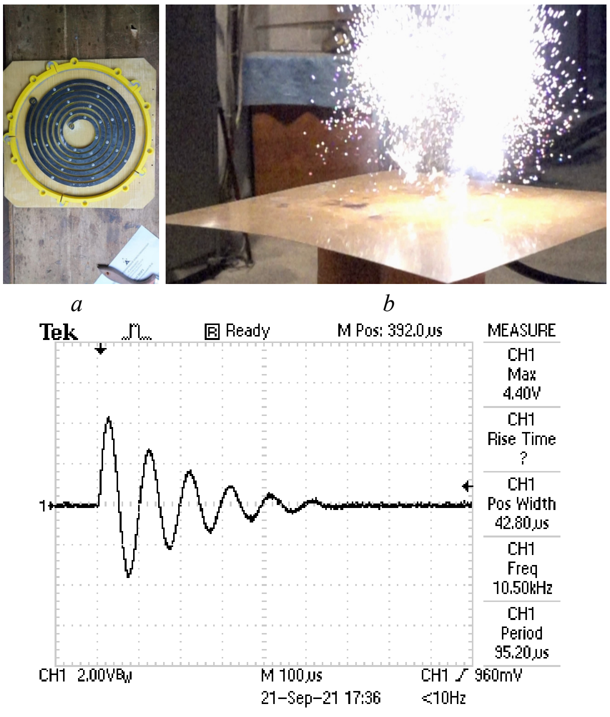
a b

c

Fig. 9. External view of the inductor (*a*), the plasma formation (*b*) of the accelerator, and the oscillogram of the inductor current (*c*)

The oscillogram of the inductor current has an oscillatory-damping character with amplitude of the first half-wave of 51.6 kA. In Fig. 9,*b*, it can be seen that the plasma formation under the action of electrodynamic forces detaches from the sheet of copper foil and moves several meters vertically upwards.

Thus, if the CES voltage does not exceed certain values, then the induced current in the armature is relatively small and during the heating process does not form a thermally ionized plasma formation of a certain part of the copper foil. And with an increase in the CES voltage, there is an increase in the induced current in the armature, which carries out thermal ionization of the corresponding part of the armature with the transition into a plasma formation, which, under the action of electrodynamic forces, moves vertically upwards for several meters.

The results of experimental studies, namely, the shape, voltage and current in the inductor coincide with the calculated ones with accuracy of up to 15 %, which indicates the reliability of the mathematical model of the accelerator.

Thus, experimental and theoretical studies show the validity of the concept of a pulse induction accelerator, in which, due to the high density of the induced current in the armature made of electrically conductive foil, thermal ionization occurs as a result of an electric explosion of the conductor with its transition into a plasma state. The interaction of this plasma formation with the magnetic field of the inductor leads to the appearance of the electrodynamic force, which ensures its movement in the open atmospheric environment by several meters relative to the stationary inductor.

Conclusions.

1. Work on the creation and throwing of plasma formations is relevant and is carried out in leading scientific centers of the world using gas-dynamic and electromagnetic forces.
2. A mathematical model of a pulse induction accelerator was developed and implemented in the Comsol Multiphysics software package, in which the armature does not change its shape and aggregate state during operation. The mathematical model, which takes into account the parameters of the accelerator distributed in space, uses a system of partial differential equations with respect to spatial and temporal variables.
3. Electromechanical and thermal characteristics of the accelerator have been calculated. It is shown that the temperature rise in the aluminum foil armature is significantly nonuniform. The maximum temperature value occurs in the middle part of the foil closer to the outer edge, and this temperature significantly exceeds the boiling point of aluminum.
4. Experimental research was carried out on an accelerator in which the armature is made of aluminum and copper foil, and the inductor connected to the high-voltage CES is made of steel in the form of a flat disk spiral. It was established that during the operation of the accelerator, the armature enters a plasma state and moves vertically upwards for several meters, turning into a volumetric wad or a cluster of small particles that rose to a considerable height relative to the inductor.
5. The characteristic circular contour of the thermal heating of the copper foil of the armature, which is fixed on a glass-textolite sheet, is experimentally shown, which indicates a similar nature of plasma formation.

Conflict of interest. The authors of the article declare that there is no conflict of interest.

REFERENCES

1. Myers C.E., Belova E.V., Brown M.R., Gray T., Cothran C.D., Schaffer M.J. Three-dimensional magnetohydrodynamics simulations of counter-helicity spheromak merging in the Swarthmore Spheromak Experiment. *Physics of Plasmas*, 2011, vol. 18, no. 11, pp. 112512-112530. doi: https://doi.org/10.1063/1.3660533.

2. Gray T., Lukin V.S., Brown M.R., Cothran C.D. Three-dimensional reconnection and relaxation of merging spheromak plasmas. Physics of Plasmas, 2010, vol. 17, no. 10, pp. 102106-102114. doi: https://doi.org/10.1063/1.3492726.

3. Ji H., Daughton W. Phase diagram for magnetic reconnection in heliophysical, astrophysical, and laboratory plasmas. *Physics of Plasmas*, 2011, vol. 18, no. 11, pp. 111207-111217. doi: https://doi.org/10.1063/1.3647505.

4. Baalrud S.D., Bhattacharjee A., Huang Y.-M., Germaschewski K. Hall magnetohydrodynamic reconnection in the plasmoid unstable regime. *Physics of Plasmas*, 2011, vol. 18, no. 9, pp. 092108-092116. doi: https://doi.org/10.1063/1.3633473.

5. Sebastian Anthony. *Open-air plasma device could revolutionize energy generation, US Navy's weaponry*. Available: https://www.extremetech.com/defense/153630-open-air-plasma-device-could-revolutionize-energy-generation-us-navys-weaponry (accessed 10.05.2022).

6. Curry R.D. *Systems and Methods to Generate a Self-Confined High Density Air Plasma*. Patent US WO2012173864. 2012. Available: https://patentscope.wipo.int/search/en/detail.jsf?docId=WO2012173864. (accessed 10.01.2023).

7. Takahashi K. Helicon-type radiofrequency plasma thrusters and magnetic plasma nozzles. *Reviews of Modern Plasma Physics*, 2019, vol. 3, no. 1, art. no. 3. doi: https://doi.org/10.1007/s41614-019-0024-2.

8. Shumeiko A.I., Telekh V.D., Mayorova V.I. Development of a novel wave plasma propulsion module with six-directional thrust vectoring capability. *Acta Astronautica*, 2022, vol. 191, pp. 431-437. doi: https://doi.org/10.1016/j.actaastro.2021.11.028.

9. Guo J. Induction plasma synthesis of nanomaterials. *Plasma Science and Technology – Progress in Physical States and Chemical Reactions*. Rijeka, InTech, 2016. pp. 3-30. doi: https://doi.org/10.5772/62549.

10. Rudikov A.I., Antropov N.N., Popov G.A. Pulsed plasma thruster of the erosion type for a geostationary artificial Earth satellite. *Acta Astronautica*, 1995, vol. 35, no. 9–11, pp. 585-590. doi: https://doi.org/10.1016/0094-5765(95)00025-U.

11. Spanjers G., McFall K., Gulczinski III F., Spores R. Investigation of propellant inefficiencies in a pulsed plasma thruster. *32nd Joint Propulsion Conference and Exhibit*, 1996. doi: https://doi.org/10.2514/6.1996-2723.

12. Takahashi K. Magnetic nozzle radiofrequency plasma thruster approaching twenty percent thruster efficiency. *Scientific Reports*, 2021, vol. 11, no. 1, art. no. 2768. doi: https://doi.org/10.1038/s41598-021-82471-2.

13. Di Canto G. *Plasma propulsion system and method*. Patent US WO2016151609. 2016. Available: https://patentscope.wipo.int/search/en/detail.jsf?docId=WO2016151609&_cid=P10-LL70BV-97870-1. (accessed 10.01.2023).

14. Polzin K.A., Choueiri E.Y. Performance optimization criteria for pulsed inductive plasma acceleration. *IEEE Transactions on Plasma Science*, 2006, vol. 34, no. 3, pp. 945-953. doi: https://doi.org/10.1109/TPS.2006.875732.

15. Korytchenko K.V., Bolyukh V.F., Rezinkin O.L., Burjakovskij S.G., Mesenko O.P. Axial coil accelerator of plasma ring in the atmospheric pressure air. *Problems of Atomic Science and Technology*, 2019, vol. 119, no. 1, pp. 120-123.

16. Bolyukh V.F., Kocherga A.I. Efficiency and Practical Implementation of the Double Armature Linear Pulse Electromechanical Accelerator. *2021 IEEE 2nd KhPI Week on Advanced Technology (KhPIWeek)*, 2021, pp. 153-158. doi: https://doi.org/10.1109/KhPIWeek53812.2021.9570065.

17. Bolyukh V.F., Schukin I.S. Excitation with a series of pulses of a linear pulse electrodynamic type converter operating in power and high-speed modes. *Electrical Engineering & Electromechanics*, 2020, no. 4, pp. 3-11. doi: https://doi.org/10.20998/2074-272X.2020.4.01.

Received 08.01.2023
Accepted 15.03.2023
Published 01.09.2023

K.V. Korytchenko[1], *Doctor of Technical Science, Professor,*
V.F. Bolyukh[1], *Doctor of Technical Science, Professor,*
S.G. Buriakovskyi[2], *Doctor of Technical Science, Professor,*
Y.V. Kashansky[1],
O.I. Kocherga[1], *PhD,*
[1] National Technical University «Kharkiv Polytechnic Institute»,
2, Kyrpychova Str., Kharkiv, 61002, Ukraine,
e-mail: korytchenko_kv@ukr.net;
vfbolyukh@gmail.com (Corresponding Author);
yurii.kashanskyi@khpi.edu.ua;
kocherga.oleksandr07@gmail.com
[2] Research and Design Institute «Molniya»
of National Technical University «Kharkiv Polytechnic Institute»,
47, Shevchenko Str., Kharkiv, 61013, Ukraine,
e-mail: sergbyr@i.ua

How to cite this article:

Korytchenko K.V., Bolyukh V.F., Buriakovskyi S.G., Kashansky Y.V., Kocherga O.I. Electromechanical and thermophysical processes in the pulse induction accelerator of plasma formation. *Electrical Engineering & Electromechanics*, 2023, no. 5, pp. 69-76. doi: https://doi.org/10.20998/2074-272X.2023.5.10

UDC 621.318: 539.3 https://doi.org/10.20998/2074-272X.2023.5.11

D.V. Lavinsky, Yu.I. Zaitsev

Computational analysis method of the electromagnetic field propagation and deformation of conductive bodies

Introduction. *The electromagnetic field is an integral attribute of the operation of many technical and technological systems. The action of an electromagnetic field leads to deformation, a change in temperature, a change in the physical properties of the materials.* ***Problem.*** *High-intensity electromagnetic fields can cause such a strong deformation of conductive bodies that it can lead to irreversible shape change or destruction. This fact is used in a class of technological operations: electromagnetic forming. Here, both the workpiece and the equipment are subjected to intense force action. As a result, equipment elements may become inoperable.* ***Goal.*** *Creation of a computational analysis method of the electromagnetic field propagation in systems of conductive bodies and subsequent analysis of deformation. Application of this method to the study of processes in electromagnetic forming systems in order to determine rational operational parameters that provide the result of a technological operation.* ***Methodology.*** *A variational formulation of the problems of an electromagnetic field propagation and deformation of conductive bodies systems is used. Numerical modeling and analysis are performed using the finite element method.* ***Results.*** *In a general form, a system of resolving equations for the values of the vector magnetic potential and displacements is obtained. The influence of the electromagnetic field is taken into account by introducing electromagnetic forces. The results of calculations for a technological system designed for electromagnetic forming of curved thin-walled workpieces are presented.* ***Originality.*** *For the first time, a method of computational analysis is presented, which involves modeling within the framework of one design scheme both the process of electromagnetic field propagation and the process of deformation.* ***Practical significance.*** *The proposed method of computational analysis can be used for various technological systems of electromagnetic forming in order to determine the rational parameters that ensure both the operability of the equipment and the purpose of the technological operation - the necessary shaping of the workpiece.* References 18, table 1, figures 3.

Key words: **computational analysis, electromagnetic field, electromagnetic forming, deformation, finite element method.**

Вступ. *Електромагнітне поле є невід'ємним атрибутом роботи багатьох технічних і технологічних систем. Дія електромагнітного поля призводить до деформації, зміни температури, зміни фізичних властивостей матеріалів.* ***Проблема.*** *Електромагнітні поля високої інтенсивності можуть викликати настільки сильну деформацію провідних тіл, що це може призвести до незворотної зміни форми або руйнування. Цей факт використовується в класі технологічних операцій: електромагнітна обробка. Тут як заготовка, так і обладнання піддаються інтенсивній силовій дії. В результаті елементи обладнання можуть виходити з ладу.* ***Мета.*** *Створення методу розрахункового аналізу поширення електромагнітного поля в системах провідних тіл і подальшого аналізу деформування. Застосування цього методу для дослідження процесів в системах електромагнітної обробки з метою визначення раціональних робочих параметрів, що забезпечують результат технологічної операції.* ***Методологія.*** *Використано варіаційну постановку задач про поширення електромагнітного поля та деформування систем провідних тіл. Чисельне моделювання та аналіз виконано методом скінченних елементів.* ***Результати.*** *У загальному вигляді отримано систему визначальних рівнянь для значень векторного магнітного потенціалу та переміщень. Вплив електромагнітного поля враховується введенням електромагнітних сил. Наведено результати розрахунків для технологічної системи електромагнітної обробки вигнутих тонкостінних заготовок.* ***Оригінальність.*** *Вперше представлено метод розрахункового аналізу, який передбачає моделювання в рамках єдиної розрахункової схеми як процесу поширення електромагнітного поля, так і процесу деформування.* ***Практичне значення.*** *Запропонований метод розрахункового аналізу може бути використаний для різних технологічних систем електромагнітного формування з метою визначення раціональних параметрів, що забезпечують як працездатність обладнання, так і мету технологічної операції – необхідне формоутворення заготовки.* Бібл. 18, табл. 1, рис. 3.

Ключові слова: **розрахунковий аналіз, електромагнітне поле, електромагнітна обробка, деформування, метод скінченних елементів.**

Introduction. A large number of technical and technological facilities are exploited under conditions of intense electromagnetic fields (EM-fields). Technologies that use EM-fields cause a variety of power, thermal effects on materials, influence on magnetic properties, and so on. The most important is the power effect that occurs when the EM-field acts on the conductive body and causes its motion or deformation. The above-stated facts indicate the necessity of using the computational methods analysis of EM-field propagation and deformation process of technological devices equipment elements of the electromagnetic forming (EMF) at the design and proofing stage. Thus, the scientific and applied problem, which consists in the creation of new computational methods for evaluating the EM-fields effect on elastic-plastic deformation of workpieces and equipment, taking into account the association of EM-field propagation and deformation processes, as well as computational investigations of the EM-field distribution and deformation processes under the conditions of specific technological operations is relevant, which determines the direction of this article.

The creation of computational methods for the analysis of any processes is based on an appropriate theoretical basis. Theoretical fundamentals describing models of continuum mechanics, which take into account the effect of the coupled fields of different physical nature (including electromagnetic) presents in classical works of Maugin, Nowacki, Eringen and others [1-4]. Within the framework of these models, the influence of an external EM-field on the thermomechanical state of the body is taken into account by introducing electromagnetic forces into the equilibrium equations. The presented model is based on Maxwell's equations, describing the nature of the electromagnetic field in vacuum and in moving deformed body, in accordance with its electromagnetic properties. For tasks in which the main objective is the analysis of the structural strength can be used the theory of magnetoelasticity. Fundamentals of the theory of magnetoelasticity with consideration of the coupling effects EM-field and mechanical stresses and strains in a moving conductive body (in the general case, the body is polarized or magnetized), were founded by Knopoff [5].

Force influence is used in the class of technological operations, called EMF. The technological equipment of EMF is deformed together with the workpieces under the influence of EM-field, which can lead to a reduction in durability and inoperability.

Modeling of forming and stamping workpieces processes dedicated [6, 7], in which, using the finite element method (FEM), highlights the solutions features of the coupled problems of magneto-thermo-elastic with regard to high-strain-rate deformation. The current state of issues related to the classification of EMF technological operations and descriptions of the corresponding equipment is comprehensively presented in review articles [8, 9]. It should be noted that non-traditional directions of the EMF are currently being developed. The basic questions of some modern trends in the development of EMF technologies are presented in articles [10-12].

The development of technological equipment for any EMF operation requires scrupulous computational studies. For example, works [13, 14] are devoted to these issues. An analysis of modern sources of information allows us to conclude that the most effective calculation tool in this case is the FEM. FEM allows in this case, within the framework of a single design scheme, to analyze the distribution of the main components of both the EM-field and the stress-strain state (SSS).

The goal of the paper is the theoretical substantiation and creation of a computational analysis method of the EM-field propagation and the process of conductive bodies deformation.

Mathematical formulation of the calculation analysis problem. For real technical and technological systems, which have a rather complex geometry and the deformation process is characterized by nonlinearities of various nature the solution process should be based on the use of appropriate numerical methods. FEM at the current stage of the computational mechanics development is the most suitable for solving the problems of the deformable body mechanics. Also, FEM has proven itself well for solving problems of various physical nature fields determine, including electromagnetic and thermal.

The construction of the FEM algorithm is based on weak formulations of the corresponding initial boundary value problems and is reduced to finding the stationary values of the corresponding functionals. Functionals can be obtained in various ways, for example, provided that the original differential equation is the Euler-Ostrogradsky equation for a certain functional, or the functional is constructed according to some general physical principle.

Certain difficulties arise when taking into account the nonlinearity of the process and the procedure of using functionals requires linearization of the original problem in one way or another, most often, an iterative process is built in which the original nonlinear problem is presented as a series of linearized problems.

The complete system of differential equations of the EM-field propagation initial-boundary problem and deformation of conductive bodies systems is presented in the articles [15, 16].

To construct functionals that correspond to the initial-boundary problem of EM-field propagation, we will consider the vector magnetic $\vec{A}$ and scalar electric φ potentials:

$$\vec{B} = \nabla \times \vec{A}; \quad \nabla \cdot \vec{A} = 0; \quad \vec{E} = -\frac{\partial \vec{A}}{\partial t} - \nabla \varphi , \tag{1}$$

here $\vec{B}$ is the magnetic induction vector; $\vec{E}$ is the vector of electric field intensity.

Initial and boundary conditions are formulated for vector magnetic and scalar electric potentials:

$$\vec{A}(0) = 0; \varphi(0) = 0. \tag{2}$$

$$\vec{A}\Big|_{\infty} = 0; \ \varphi\Big|_{\infty} = 0. \tag{3}$$

$$\begin{aligned} &\left.\frac{\partial \varphi_i}{\partial x_i}\right|_{\Gamma} = -E_{\Gamma i}, \quad i = 1,2,3; \\ &\left.\left(\frac{\partial A_i}{\partial x_j} - \frac{\partial A_j}{\partial x_i}\right)\right|_{\Gamma} = B_{\Gamma k}, \quad i \neq j \neq k = 1,2,3. \end{aligned} \tag{4}$$

Boundary conditions (3) are applied when the body is considered together with the surrounding environment and model the attenuation of the EM-field at a distance. In the case when the EM-field components are specified at some boundary of the body, then (in the quasi-stationary case) the boundary conditions (4) are applied. Here, the symbol Γ means that the corresponding quantity belongs to the boundary of the body.

In the case of elastic deformation of the conductive bodies system, the solution is sought from the condition of minimum total energy E_{TOT}:

$$\delta E_{TOT} = 0, \quad E_{TOT} = U + W , \tag{5}$$

where U is the energy of elastic deformation; W is the EM-field energy. The energy of elastic deformation is determined as follows:

$$\begin{aligned} &U = \frac{1}{2}\int_V \hat{\varepsilon} \cdot\cdot {}^{(4)}\hat{C} \cdot\cdot \hat{\varepsilon} dV - \int_S \vec{p} \cdot \vec{u} dS; \\ &{}^{(4)}\hat{C} = -\frac{\nu E}{(1+\nu)(1-2\nu)} \hat{I} \otimes \hat{I} + \\ &+ \frac{E}{2(1+\nu)}\left(e_k \otimes \hat{I} \otimes e^k + e_i \otimes e_k \otimes e^i \otimes e^k\right), \end{aligned} \tag{6}$$

where $\hat{\varepsilon}$ is the tensor of deformations; $\vec{p}$ is the vector of surface mechanical loads; $\vec{u}$ is the vector of displacements; ν is the Poisson's ratio; E is the Young's modulus; $\hat{I}$ is the unit tensor; V is the body volume; S is the body surface on which mechanical loads and displacements are known.

The EM-field energy is generally defined as follows:

$$W = \int_V \left(\int_0^B \vec{H} d\vec{B} \right) dV + \int_V \left(\int_0^D \vec{E} d\vec{D} \right) dV, \tag{7}$$

where $\vec{H}$ is the vector of magnetic field intensity; $\vec{D}$ is the induction vector of electric field.

In the case of a linear relationship between the vectors that characterize the EM-field (or in the case of a linearized problem), the expression for the EM-field energy is simplified to the form:

$$\begin{aligned} &W = \frac{1}{2}\int_V \vec{H} \cdot \vec{B} dV + \frac{1}{2}\int_V \vec{E} \cdot \vec{D} dV = \\ &= \frac{1}{2}\int_V \frac{1}{\mu_c} \left(\vec{B}\right)^2 dV + \frac{1}{2}\int_V \varepsilon_c \left(\vec{E}\right)^2 dV, \end{aligned}$$

where μ_c and ε_c are the magnetic and electrical permeability of the material.

Let's carry out the substitution through the potentials and get the following expression:

$$W=\int\limits_V\left(\frac{1}{2\mu_c}\left|\vec{\nabla}\times\vec{A}\right|^2-\vec{j}\times\vec{A}\right)dV+ \\ +\int\limits_V\left(\frac{\varepsilon_c}{2}\left|\vec{\nabla}\varphi\right|^2-\rho_e\varphi\right)dV. \tag{8}$$

Formula (8) takes into account the possibility of EM-field sources – currents $\vec{j}$ and electric charges ρ_e distributed over the volume.

If we use formal mathematical approaches, then in the variational equation (5) we have three independent variables – scalar electric potential, vector magnetic potential and displacement, therefore the equality of zero of the total energy variation leads to three equalities:

$$\delta E_{TOT}=0\Rightarrow\begin{cases}\dfrac{\partial E_{TOT}}{\partial\varphi}=0;\\ \dfrac{\partial E_{TOT}}{\partial\vec{A}}=0;\\ \dfrac{\partial E_{TOT}}{\partial\vec{u}}=0.\end{cases} \tag{9}$$

If we present the expressions for the elastic deformation energy and the EM-field energy in matrix-vector form:

$$U=\frac{1}{2}\int\limits_V\{u\}^{\mathrm{T}}[K]\{u\}dV-\int\limits_S\{p\}\{u\}dS; \tag{10}$$

$$W=\frac{1}{2}\int\limits_V\{A\}^{\mathrm{T}}[M]\{A\}dV-\int\limits_V\{J\}\{A\}dV+ \\ +\frac{1}{2}\int\limits_V\{\varphi\}^{\mathrm{T}}[\Sigma]\{\varphi\}dV-\int\limits_V\{\rho_e\}\{\varphi\}dV, \tag{11}$$

where $[K]$ is the stiffness matrix; $[M]$ is the «magnetic» matrix; $[\Sigma]$ is the «dielectric» matrix; $\{u\}$, $\{p\}$, $\{A\}$, $\{\varphi\}$, $\{J\}$, $\{\rho_e\}$ are the column vectors of displacements, surface distributed forces, vector magnetic potential, electric potential, specified current densities and electric charge.

Then condition (9) leads to such a system of algebraic equations:

$$\begin{cases}[\Sigma]\{\varphi\}+[\Sigma_m]\{A\}+[\Sigma_k]\{u\}=\{\rho_e\};\\ [M]\{A\}+[M_e]\{\varphi\}+[M_k]\{u\}=\{J\};\\ [K]\{u\}+[K_\varphi]\{\varphi\}+[K_m]\{A\}=\{p\},\end{cases} \tag{12}$$

the additional matrices that arose after the variation are defined as follows:

$$[\Sigma_m]=\frac{1}{2}\{A\}^{\mathrm{T}}\frac{\partial[M]}{\partial\{\varphi\}},\quad[\Sigma_k]=\frac{1}{2}\{u\}^{\mathrm{T}}\frac{\partial[K]}{\partial\{\varphi\}},$$

$$[M_e]=\frac{1}{2}\{\varphi\}^{\mathrm{T}}\frac{\partial[\Sigma]}{\partial A};$$

$$[M_k]=\frac{1}{2}\{u\}^{\mathrm{T}}\frac{\partial[K]}{\partial\{A\}},\quad[K_\varphi]=\frac{1}{2}\{\varphi\}^{\mathrm{T}}\frac{\partial[\Sigma]}{\partial u},$$

$$[K_m]=\frac{1}{2}\{A\}^{\mathrm{T}}\frac{\partial[M]}{\partial u},$$

where the matrices $[\Sigma_m]$, $[M_e]$ characterize the changes in the magnetic field due to the presence of an electric one, and vice versa, the matrices $[\Sigma_k]$, $[M_k]$ characterize the changes in the electric and magnetic fields due to deformation (i.e, piezo effects). When considering traditional structural materials, such changes are either absent or insignificant and these components can be neglected.

In order to find out the nature of the second and third components from the third equation, we will use the principle of virtual work, with the help of which we will determine the forces by which the EM-field acts on a conductive body. At the same time, we believe that the EM-field energy is completely spent on body deformation. In the general case of dependence between EM-field vectors, we obtain the following expression:

$$\vec{f}_{\mathrm{em}}=-\frac{\partial W}{\partial\vec{u}}=-\frac{\partial}{\partial\vec{u}}\left(\int\limits_V\left(\int\limits_0^B\vec{H}\mathrm{d}\vec{B}\right)\mathrm{d}V\right)- \\ -\frac{\partial}{\partial\vec{u}}\left(\int\limits_V\left(\int\limits_0^B\vec{E}\mathrm{d}\vec{D}\right)\mathrm{d}V\right)=-\int\limits_V\vec{H}\frac{\partial\vec{B}}{\partial\vec{u}}\mathrm{d}V- \\ -\int\limits_V\left(\int\limits_0^B\frac{\partial\vec{H}}{\partial\vec{u}}\mathrm{d}\vec{B}\right)\mathrm{d}V-\int\limits_V\vec{E}\frac{\partial\vec{D}}{\partial\vec{u}}\mathrm{d}V- \\ -\int\limits_V\left(\int\limits_0^B\frac{\partial\vec{E}}{\partial\vec{u}}\mathrm{d}\vec{D}\right)\mathrm{d}V. \tag{13}$$

In the case of considering a linear relationship between the vectors characterizing the EM-field distribution, we obtain the following expression for electromagnetic forces:

$$\{f_{\mathrm{em}}\}=-\frac{\partial W}{\partial\{u\}}=-\frac{\partial}{\partial\{u\}}\left(\frac{1}{2}\{A\}^{\mathrm{T}}[M]\{A\}\right)- \\ -\frac{\partial}{\partial\{u\}}\left(\frac{1}{2}\{\varphi\}^{\mathrm{T}}[\Sigma]\{\varphi\}\right)= \\ =-\frac{1}{2}\{A\}^{\mathrm{T}}\frac{\partial[M]}{\partial\{u\}}\{A\}-\frac{1}{2}\{\varphi\}^{\mathrm{T}}\frac{\partial[\Sigma]}{\partial\{u\}}\{\varphi\}= \\ =-[K_m]\{A\}-[K_\varphi]\{\varphi\}. \tag{14}$$

So, we see that the expression for electromagnetic forces is exactly the same as the sum of the second and third components of (12), i.e. in conditions of a conductive body elastic deformation under the action of EM-field; its influence is limited to electromagnetic forces distributed over the volume of the body. Elastic deformation, in turn, for the selected model does not affect the distribution of EM-field, therefore the analysis of the distribution of EM-field and the analysis of SSS taking into account electromagnetic forces in the case of quasi-stationary approximation can be carried out separately.

The first and second equations in the system (12) become independent (based on the results of their solution, we obtain the EM-field distribution), and on this basis, it is possible to solve the third equation taking into account the electromagnetic forces (12) for the purpose of SSS analysis. Thus, the system of defining equations of the problem takes the form:

$$\begin{cases}[\Sigma]\{\varphi\}=\{\rho_e\};\\ [M]\{A\}=\{J\};\\ [K]\{u\}=\{p\}+\{f_{em}\},\end{cases} \qquad (15)$$

$$\{f_{em}\}=-\frac{1}{2}\{A\}^{\mathrm{T}}\frac{\partial[M]}{\partial u}\{A\}-\frac{1}{2}\{\varphi\}^{\mathrm{T}}\frac{\partial[\Sigma]}{\partial u}\{\varphi\}.$$

In the resulting equations (15), electromagnetic forces are a consequence of the both magnetic and electrostatic fields' action; however, it is known that the force effect of an electrostatic field is many times smaller than that of a magnetic field. Based on this, the contribution of the electrostatic field can be neglected for the analysis of systems deformation that takes place in technologies based on strong magnetic fields. Moreover, in the quasi-stationary setting, the electrostatic field does not affect the magnetic field (independence of the first and second equations in (13)).

So, to analyze the deformation of conductive bodies systems under the action of large magnetic fields in the quasi-stationary approximation, the defining system of equations takes the form:

$$\begin{cases}[M]\{A\}=\{J\};\\ [K]\{u\}=\{p\}+\{f_{em}\},\end{cases} \qquad (16)$$

$$\{f_{em}\}=-\frac{1}{2}\{A\}^{\mathrm{T}}\frac{\partial[M]}{\partial u}\{A\}.$$

Calculation example. Let us consider the application of the proposed approach to the analysis of EM-field distribution and subsequent deformation for the case of EMF of thin-walled curved workpieces. In many cases, curved thin-walled metal workpieces are the basis for the manufacture of structural elements for various purposes.

Usually, the necessary curved structural elements are manufactured in two stages: in the first stage, they reach the required general (overall) dimensions and shape, in the second stage they achieve the required quality directly in the corner zone.

Part of the EMF technological operations is aimed at creating conditions for the occurrence of residual deformations in curved thin-walled metal workpieces directly in the bending zone. This group of technological operations was named technological operations of «filling corners». This term is known from the field of «traditional» pressure metal processing, and, in practice, it means the reduction of rounding radii to acceptable values in the bending zones of thin-walled workpieces. From the point of view of the technological operation conditions, it is necessary to exert the maximum force around the corner.

In works [17, 18], it is proposed to use an inductor with two turns, which have one common current line directed along the bend, to «fill the corners» on thin-walled curved workpieces, each of the turns is a plane that makes an angle of up to 15° with the wall of the workpiece.

Consider the results of EM-field calculations and deformation analysis for the design diagram shown in Fig. 1.

An electric current evenly distributed over the cross-section of the current conductor turns was considered as a source of EM-field. The magnitude of the non-zero component of the current density vector varied over time according to the law:

$$j(t)=j_m e^{-\delta\omega t}\sin(2\pi\nu t), \qquad (17)$$

where $j_m=\dfrac{4I_m}{\pi d^2}$ is the current density amplitude; I_m = 40 kA is the amplitude of the current in the pulse; ν = 2 kHz is the current frequency in the pulse; $\omega = 2\pi\nu$ is the cyclic frequency; δ = 0.3 is the attenuation coefficient; d is the diameter of the coil of the current conductor.

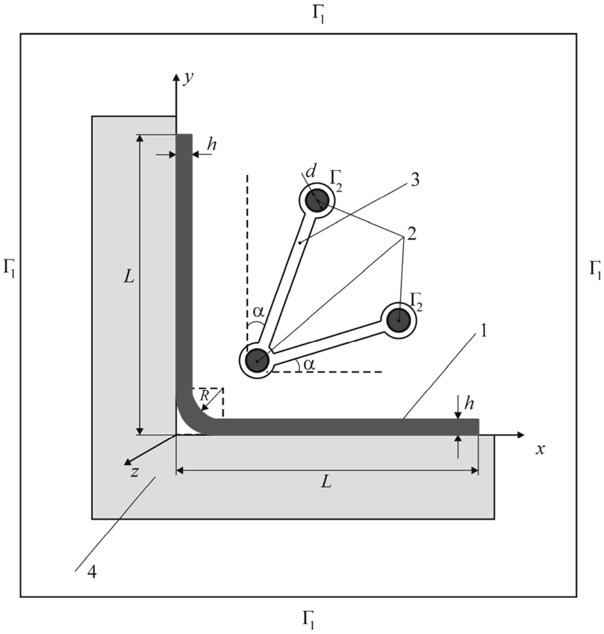

Fig. 1. Design diagram of a curved workpiece together with a two-turn inductor and a dielectric mold: 1 – workpiece; 2 – coils of the current conductor of the inductor; 3 – inductor insulation; 4 – dielectric mold

The solution was performed for zero initial conditions for one current pulse, in the time range from 0 to 3 ms, which guaranteed complete decay of the current in the pulse.

During calculations, the following values of geometric dimensions were considered: d = 10 mm, L = 100 mm, h = 2 mm, α = 15°. Finite element modeling was carried out using three nodal finite elements with a linear approximation of the corresponding (z) component of the vector magnetic potential and displacements (Fig. 2).

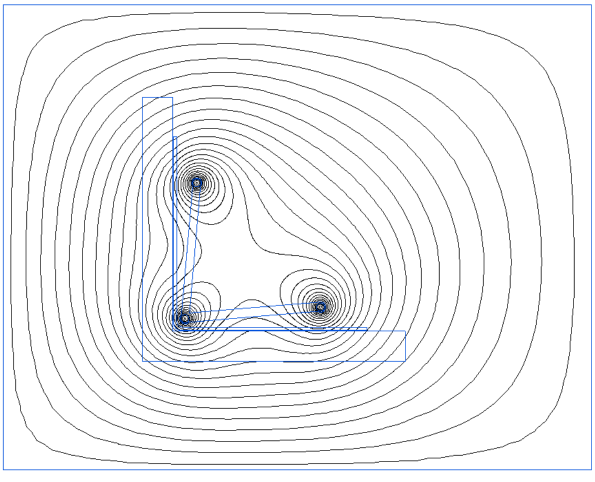

Fig. 2. Permanent lines of vector magnetic potential

The physical and mechanical parameters of the system elements, which were used in all subsequent calculations, are given in Table 1 (where σ_y is the yield strength of the material, σ_B^+ is the tensile strength limit, σ_B^- is the compressive strength limit.)

Table 1

Physic-mechanical parameters of system elements

	Current conductor, copper	Workpiece, aluminum alloy	Insulation, kaprolon	Dielectric mold, fiberglass
μ_r	1	1	1	1
γ, $(\Omega\cdot m)^{-1}$	$7\cdot10^7$	$4.6\cdot10^7$	0	0
E, GPa	120	71	2.5	200
ν	0.33	0.29	0,3	0.27
σ_y, MPa	380	190	–	–
σ_B^+, MPa	–	–	70	100
σ_B^-, MPa	–	–	90	120

For the considered value of the current in the inductor, the maximum value of the stress intensity in the workpiece, which is observed on the workpiece surface, is 227 MPa (Fig. 3), which is greater than the yield strength of the aluminum alloy, thus it can be stated that from the point of view of the plastic deformations possibility in the workpiece, the technological operation is efficient.

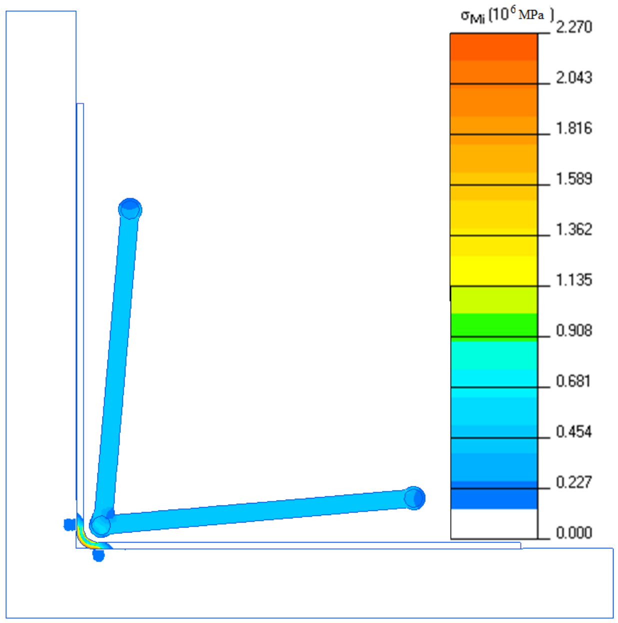

Fig. 3. Distribution of stress intensity

Note that the maximum values of normal stresses also occur on the workpiece surface. The largest displacement values are observed in the middle part of the workpiece rounding, i.e. directly opposite the current conductor of the inductor. Their maximum value is 5.4 mm, that is, under the operating conditions considered, the initial rounding of the workpiece is reduced by approximately 50 %. Note that the maximum intensity of stress in the current conductor of the inductor is approximately 60 MPa, which does not exceed the yield strength of the material, the maximum value of the equivalent stress according to Mohr's criterion in the insulation of the inductor is 52 MPa, which also does not exceed the limit of the tensile strength of the material. So, it can be concluded that in this case the inductor remains operational.

Conclusions. The prerequisites are considered and the necessity of creating computational methods for analyzing the propagation of an electromagnetic field and the further process of technological systems elements deformation of electromagnetic forming is substantiated.

To create an appropriate method of computational analysis, the main variational relations based on the principle of minimum total energy of the system are given. For a correct and convenient description of the electromagnetic field propagation processes, the concepts of scalar electric and vector magnetic potentials are introduced. Formulas for the energy of the electromagnetic field and the energy of elastic deformation are presented. For the case of elastic deformation of conductive bodies subjected to the action of an electromagnetic field, a system of resolving algebraic equations for the values of the vector magnetic potential and displacements is obtained in general form. The influence of the electromagnetic field is taken into account by introducing electromagnetic forces, the expression for which is also obtained.

As an illustration of the computational analysis proposed method application, the computational analyzing of a technological system for electromagnetic forming of thin-walled curved workpieces is considered.

The further development of this work consists in extending the proposed method of computational analysis to the cases of various nature nonlinearities and carrying out calculations for complex technological systems of electromagnetic forming.

Conflict of interest. The authors of the article declare that there is no conflict of interest.

REFERENCES

1. Maugin C.A. Electromagnetic internal variables in electromagnetic continua. *Archives of Mechanics*, 1981, vol. 33, no. 1, pp. 927-936.

2. Nowacki W. *Efekty Elektromagnetyczne w Stałych Ciałach Odkształcalnych*. Państwowe Wydawnictwo Naukowe, Warsaw, 1983. (Pol).

3. Eringen A.C., Maugin G.A. *Electrodynamics of continua I: foundations and solid media*. Springer Science & Business Media, 2012.

4. Maugin G.A. *Continuum mechanics of electromagnetic solids*. Elsevier, 2013.

5. Knopoff L. The interaction between elastic wave motions and a magnetic field in electrical conductors. *Journal of Geophysical Research*, 1955, vol. 60, no. 4, pp. 441-456. doi: https://doi.org/10.1029/JZ060i004p00441.

6. Kleiner M., Beerwald C., Homberg W. Analysis of process parameters and forming mechanisms within the electromagnetic forming process. *CIRP annals*, 2005, vol. 54, no. 1, pp. 225-228. doi: https://doi.org/10.1016/S0007-8506(07)60089-4.

7. Mamalis A.G., Manolakos D.E., Kladas A.G., Koumoutsos A.K. Electromagnetic Forming Tools and Processing Conditions: Numerical Simulation. *Materials and Manufacturing Processes*, 2006, vol. 21, no. 4, pp. 411-423. doi: https://doi.org/10.1080/10426910500411785.

8. Psyk V., Risch D., Kinsey B.L., Tekkayaa A.E., Kleiner M. Electromagnetic forming – a review. *Journal of Materials Processing Technology*, 2011, vol. 211, no. 5, pp. 787-829. doi: https://doi.org/10.1016/j.jmatprotec.2010.12.012.

9. Gayakwad D., Dargar M.K., Sharma P.K., Purohit R., Rana R.S. A Review on Electromagnetic Forming Process. *Procedia*

Materials Science, 2014, vol. 6, pp. 520-527. doi: https://doi.org/10.1016/j.mspro.2014.07.066.

10. Batygin Yu.V., Chaplygin E.A., Shinderuk S.A., Strelnikova V.A. The main inventions for technologies of the magnetic pulsed attraction of the sheet metals. A brief review. *Electrical Engineering & Electromechanics*, 2018, no. 3, pp. 43-52. doi: https://doi.org/10.20998/2074-272X.2018.3.06.

11. Batygin Yu., Barbashova M., Sabokar O. *Electromagnetic Metal Forming for Advanced Processing Technologies*. Cham, Springer International Publ. AG., 2018. 93 p. doi: https://doi.org/10.1007/978-3-319-74570-1.

12. Batygin Y.V., Chaplygin E.A. Vortical currents in flat metallic sheet. *Electrical Engineering & Electromechanics*, 2006, no. 5, pp. 54-59. (Rus).

13. Unger J., Stiemer M., Schwarze M., Svendsen B., Blum H., Reese S. Strategies for 3D simulation of electromagnetic forming processes. *Journal of Materials Processing Technology*, 2008, vol. 199, no. 1-3, pp. 341-362. doi: https://doi.org/10.1016/j.jmatprotec.2007.08.028.

14. Stiemer M., Unger J., Svendsen B., Blum H. An arbitrary Lagrangian Eulerian approach to the three-dimensional simulation of electromagnetic forming. *Computer Methods in Applied Mechanics and Engineering*, 2009, vol. 198, no. 17-20, pp. 1535-1547. doi: https://doi.org/10.1016/j.cma.2009.01.014.

15. Altenbach H., Konkin V., Lavinsky D., Morachkovsky O., Naumenko K. Verformungsanalyse elektrisch leitender metallischer Bauteile bei Magnetimpulsbearbeitung. *Forschung im Ingenieurwesen*, 2018, vol. 82, no. 4, pp. 371-377. (Ger). doi: https://doi.org/10.1007/s10010-018-0285-x.

16. Lavinskii D.V., Morachkovskii O. K. Elastoplastic Deformation of Bodies Interacting Through Contact Under the Action of Pulsed Electromagnetic Field. *Strength of Materials*, 2016, vol. 48, no. 6, pp. 760-767. doi: https://doi.org/10.1007/s11223-017-9822-3.

17. Batygin Y.V., Golovashchenko S.F., Gnatov A.V., Smirnov D.O. Magnetic field and pressures excited by four pairwise coplanar solenoids in the cavity of a rectangular tube. *Electrical Engineering & Electromechanics*, 2010, no. 2, pp. 46-49. (Rus).

18. Batygin Y.V., Serikov G.S. Magnetic field and pressures excited by a single-turn inductor in a corner bend of a sheet worpiece. *Electrical Engineering & Electromechanics,* 2006, no. 6, pp. 66-70. (Rus).

Received 19.11.2022
Accepted 27.01.2023
Published 01.09.2023

D.V. Lavinsky[1], *Doctor of Technical Science, Associate Professor,*
Yu.I. Zaitsev[1], *Candidate of Technical Science, Professor,*
[1] National Technical University «Kharkiv Polytechnic Institute»,
2, Kyrpychova Str., Kharkiv, Ukraine, 61002,
e-mail: Denys.Lavinskiy@khpi.edu.ua (Corresponding Author);
yurii.zaitsev@khpi.edu.ua

How to cite this article:
Lavinsky D.V., Zaitsev Yu.I. Computational analysis method of the electromagnetic field propagation and deformation of conductive bodies. *Electrical Engineering & Electromechanics*, 2023, no. 5, pp. 77-82. doi: https://doi.org/10.20998/2074-272X.2023.5.11

UDC 621.314 https://doi.org/10.20998/2074-272X.2023.5.12

J.P. Desai

Transmission line planning using global best artificial bee colony method

***Introduction**. Network expansion, substation planning, generating expansion planning, and load forecasting are all aspects of modern power system planning. The **aim** of this work is to solve network planning considering both future demand and all equality and inequality constraints. The transmission network design problem for the 6-bus system is considered and addressed using the Global Best Artificial Bee Colony (GABC) method in this research. The program is written in the Matrix Laboratory in MATLAB environment using the proposed methodology. **Novelty** of the work consist in considering the behavior of bees to find food source in most optimized way in nature with feature of user based accuracy selection and speed of execution selection on any scale of the system to solve Transmission Lines Expansion Problem (TLEP). The proposed method is implemented on nonlinear mathematical function and TLEP function. When demand grows, the program output optimally distributes new links between new generation buses and old buses, determines the overall minimum cost of those links, and determines if those linkages should meet power system limits. **Originality** of the proposed method is that it eliminated the need of load shedding while planning the future demand with GABC method. **Results** are validated using load flow analysis in electrical transient analyzer program, demonstrating that artificial intelligence approaches are accurate and particularly effective in non-linear transmission network planning challenges. **Practical value** of the program is that it can use to execute cost oriented complex transmission planning decision.* References 15, table 4, figures 3.

Key words: **artificial intelligence, artificial bee colony, transmission line network planning, load flow analysis.**

***Вступ**. Розширення мережі, планування підстанцій, планування розширення виробництва та прогнозування навантаження - все це аспекти планування сучасної енергосистеми. **Мета** цієї роботи полягає в тому, щоб вирішити мережеве планування з урахуванням як майбутнього попиту, так і всіх обмежень рівності та нерівності. У цьому дослідженні проблема проектування мережі передачі для системи з шістьма шинами розглядається і вирішується з використанням методу Global Best Artificial Bee Colony (GABC). Програма написана у Matrix Laboratory у середовищі MATLAB за запропонованою методикою. **Новизна** роботи полягає у розгляді поведінки бджіл для пошуку джерела їжі найбільш оптимальним способом у природі з можливістю вибору користувачем точності та вибору швидкості виконання у будь-якому масштабі системи для вирішення проблеми розширення ліній електропередачі (TLEP). Пропонований метод реалізований на нелінійній математичній функції та функції TLEP. Коли попит зростає, вихідні дані програми оптимально розподіляють нові з'єднання між шинами нового покоління та старими шинами, визначають загальну мінімальну вартість цих з'єднань та визначають, чи ці з'єднання повинні відповідати обмеженням енергосистеми. **Оригінальність** запропонованого методу полягає в тому, що він усунув необхідність скидання навантаження під час планування майбутнього попиту методом GABC. **Результати** підтверджуються за допомогою аналізу потоку навантаження у програмі аналізу перехідних процесів, демонструючи, що підходи штучного інтелекту точні та особливо ефективні під час вирішення завдань планування нелінійної мережі передачі. **Практична цінність** програми полягає в тому, що вона може бути використана для виконання економічно орієнтованого комплексного рішення щодо планування передачі.* Бібл. 15, табл. 4, рис. 3.

Ключові слова: **штучний інтелект, штучна бджолина родина, планування мережі ЛЕП, аналіз потоку навантаження.**

Introduction. Electrical power system is a very ancient system that has transitioned from serving a small local load with a local generator to serving a big system load with a massive power system grid over many years. It is now one of the most powerful real-time operating systems. The artificial intelligence algorithm is extremely beneficial for power system expansion and protection. Power system expansion includes planning from 1 to 10 years from now [1].

Static planning entails making decisions from the current year to the next 5 years. One way is to analyze the system for each year separately, regardless of subsequent years. The study described above is known as static planning [2].

The Artificial Bee Colony (ABC) approach is based on actual bees obtaining nectar in the field and sharing information about the food sources with bees in the hive [3]. Power management optimization problem has been solved in [4], which support the use of metaheuristic approach for multi constrained cost optimization problem. The whale optimization is used in [5] to solve dynamic economic emission dispatch problem for the efficient operation of generators in a power network. The cost involved in establishment of new transmission line links is high due to rising real estate price and right of way issues [6]. The problem of rising real estate price and right of way issues necessitates the solution to deal the planning in cost optimized way with maintaining technical standard of the grid.

Load uncertainty is major concern of existing transformation of bidirectional power grid due to unknown photovoltaic generation behind meter by distribution company [7]. Generally Monte-Carlo method is conventionally used for such load uncertainty based Transmission Lines Expansion Problem (TLEP). However, Monte-Carlo method required considerable amount of time to solve the problem. The location of the bus where the capacity shortage is happened is found using linear programming method [8]. Once the bus has been selected than next step is to estimate how many number of links to be required between old bus to new bus and what should be its cost of planning. The later problem is considered in this work using heuristic approach. ABC method has one of the limitations that it is poor at poor at exploitation [9, 10]. In order to improve the exploitation the proposed method used Global Best Artificial Bee Colony (GABC), which focus more on global best solution. Active power and reactive power mismatch result in to a power system stability problem [11, 12]. So, the TLEP problem is solve in this research by considering all equality and inequality constraint.

The goal of this paper is as follows:

- fast programming computation oriented Global Best Artificial Bee Colony based Transmission Lines Expansion Problem algorithm using MATLAB;
- efficient method for validation result of algorithm using Electrical Transient Analyzer Program to insure inaccuracy of software and filter it by manual intervention if needed;
- minimization of Transmission Lines Expansion Problem cost considering equality and inequality constraint.

The paper starts with introduction, where problem statement and need of solution is described with recent literature survey. The next section is focused on behavioral studies and mathematical formulation of problem. GABC based proposed algorithm is explained in the middle of the paper. In the end of the paper results of MATLAB program and Electrical Transient Analyzer Program (ETAP) analysis is described. Finally, conclusion section ends the paper.

Global Best Artificial Bee Colony Method.

A. Classification of bees:

1) *The employed bee*: It works in the field and stays close to the food source, gathering and memorizing information about the local food supply.

2) *The bystander bee*: It attempts to obtain information about food sources from employed bees who come or stay in the hive to gather nectar. As a result, they are seeking for work.

3) *The scout bee*: As the name implies, they are in charge of finding new sources of nectar nourishment.

B. Behavior of the bees. The GABC model's main components include employed bees, spectator bees (or unemployed bees), food sources, and dance places. Working bees are dancing and selecting food sources in a multidimensional search area based on their previous experience. When the search is completed, the information exchange procedure will begin with the bystander bee that are staying and waiting in a hive. The waggle dance may be used to share information. By performing the art of dance to observer bees, employed bees may exchange information such as path, distance to patches of flowers, and superiority of food sources [13]. A waggle dance performance in the hive provides information about the angle between the sun's location and the track of food sources. The initial time interval of the waggle dance represents the distance. The length of time they do the same waggle dance up to reflects the distance of the food sources from their current position. If the waggle dance interval is 1 s, the bee must travel 1 km to reach the food source from the hive. Importantly, alkenes secreted from the stomachs of employed bees communicate the quality of the food supply [14].

The shake dancers are dancing in response to the sun's shifting path. As a result, bees that perform the waggle dance are left at food sources without mistake. The likelihood may be calculated analytically using (1), the information provided by the working bee:

$$p = \left(\frac{0.9\cdot f_p}{\max(f)+0.1}\right), \tag{1}$$

where p is the probability of food; f_p is the fitness value of the answer number p, which is directly relative to the nectar amount of the food source in the position number p.

Using (1), the unemployed bee now causes a shift in the location. It uses this to compute the nectar amount of the novel source [3]:

$$X'_{ab} = X_{ab} + \phi_{ab}\left(X_{ab} - X_{fb}\right), \tag{2}$$

where $a \in \{1, 2 \ldots n\}$ and $b \in \{1, 2 \ldots D\}$ are the arbitrarily chosen indexes. Although «f» variable is chosen at random, it must be distinct from «a» variable, and «D» represents the number of parameters to be optimized. «ab» is merely an arbitrary integer between 0 and 1. «ab» is in charge of the production of neighborhood food supplies.

If the new source nectar food amount is more than the previous one, observers remember this new position; otherwise, they recall the prior one, which was previously determined. In other words, when the choice operation between old and new food sources is accessible, the hungry selection approach is performed. If the rejected source is X_{ab}, where, b = 1, 2 … D. The scout uses equation to discover a new food source X_{ab} using (3):

$$X_{ab} = X_{b\min} + rand(0,1)\cdot\left(X_{b\max} - X_{b\min}\right), \tag{3}$$

where $X_{b\min}$, $X_{b\max}$ are the minimum and maximum restrictions of the constraint to be optimized.

To balance exploration and exploitation procedures, the GABC method combines the working bee's search with the observer bee's search and the observer bee's search with the scout bee's search [3].

C. Program development for graver's 6 bus system. The test system is used to design and simulate the proposed GABC-based transmission line planning algorithm is depicted in Fig. 1 based on graver's test system [15].

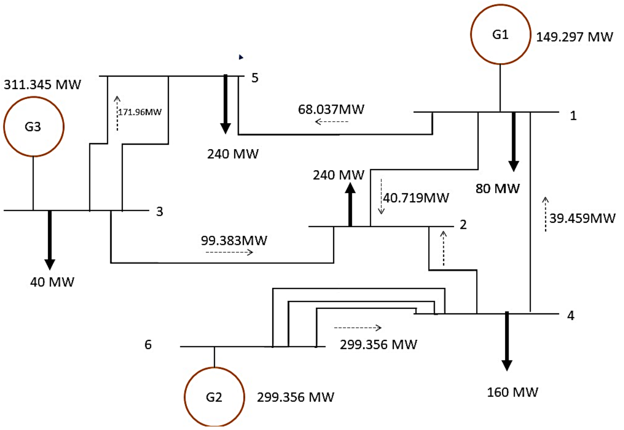

Fig. 1. Graver's 6 bus test system

The system contains 3 sources and 5 loads, each with 10 lines. The planning need is to link lines from the new generation bus 6 to the older buses 1 to 5 (Fig. 1). The objective function of transmission network expansion planning is to minimize the cost of investment through optimum value of line connection from existing bus to new bus. Minimize

$$C^k_{it} = \sum_{i,k,c}\left(CO_{ik}\cdot n_{ik}\right), \tag{4}$$

Subjected to

$$f_{ik} = P_{Gi} - P_{Di}, \tag{5}$$

$$f_{ik} - \left|\beta_{ik}\cdot\left(n^e_{ik}+n^n_{ik}\right)\cdot\left(\alpha^e_i+\alpha^n_k\right)\right| = 0, \tag{6}$$

$$\left|f_{ik}\right| \le \left(n^e_{ik}+n^n_{ik}\right)\cdot f^{\max}_{ik}, \tag{7}$$

$$P^{\max}_{Gi} \le P_{Gi} \le P^{\min}_{Gi}, \tag{8}$$

$$Q^{\max}_{Gi} \le Q_{Gi} \le Q^{\min}_{Gi}, \tag{9}$$

$$0 \le n^n_{ik} \le n^{\max}_{ik}, \tag{10}$$

where C^k_{it} is the total cost of investment in Indian rupees at new bus k; CO_{ik} is the construction cost of one transmission line per km at i-k bus; n_{ik} is the number of circuits added at each right of way; f_{ik} is the power flow between line i to k; $f^{\max}_{ik}$ is the maximum value of thermal reach of the line; P_{Gi}, Q_{Gi} are real and reactive power generation at i bus; $P^{\max}_{Gi}$, $P^{\min}_{Gi}$ are the maximum and minimum possible real power generation at i bus; $Q^{\max}_{Gi}$, $Q^{\min}_{Gi}$ are the maximum and minimum possible reactive power generation at i bus; n^n_{ik}, $n^{\max}_{ik}$ are the number of existing line and maximum possible line to be added; β_{ik} is the susceptance value between i and k bus.

Proposed algorithm. Figure 2 depicts the suggested algorithm's flowchart, which employs (1) – (3) to compute an optimum link from new bus 6 to the current system's old buses.

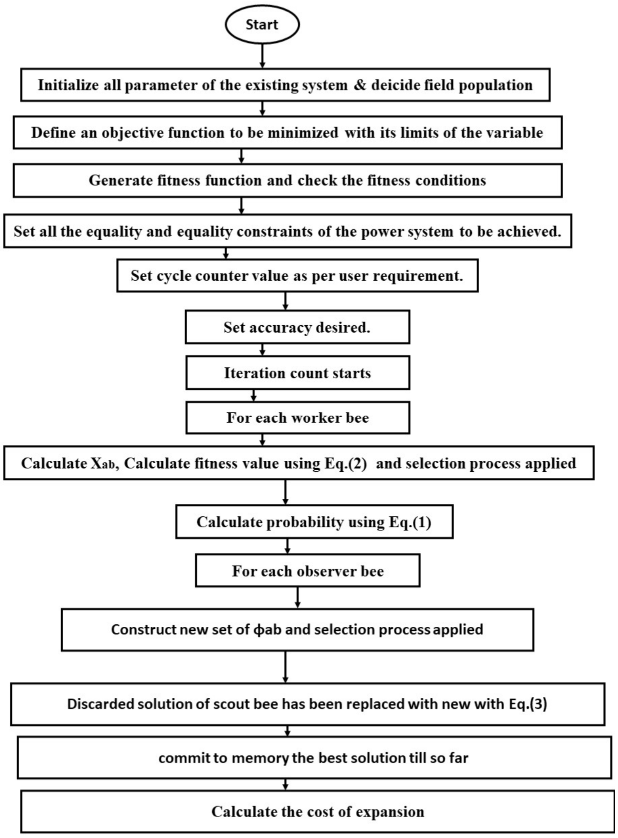

Fig. 2. Flowchart of proposed algorithm

Initially proposed program asked system data from users. It also gives option of desired speed by selecting number of iteration and desired accuracy. GABC is program such way that it improves the global minimum after each iteration. Once the global minimum achieve considering all the constrained from (5)–(10). The algorithm calculates the minimized cost using (4) once n_{ik} is calculated.

Prior to developing the TNP software for the 6-bus system. It is necessary to use a fundamental mathematical function with a known value to evaluate the accuracy of the developed programmed [12].

Consider an example equation with a known minimum solution and constrained of it. Initially, program was ran for 2000 colonies and 1000 iterations for the function below, minimize,

$$f(x) = x^2. \tag{11}$$

Subject to,

$$-1 \le x \le 1. \tag{12}$$

For function of (11) and constrained of (12), the minimum is known as x = 0 and program achieves the same results, which is shown in Table 1.

Table 1

Accuracy of developed program

Function $f(x)$: $x^2 = 0$, where $-1 \le x \le 1$		
Function is to be minimize	Actual minima	Program give the minima
	0	$2.3762\cdot 10^{-4}$

Results of program of TNP of 6-bus system. The 6-bus data is input to program (Fig. 1). The line power constraints are taken into account. Table 2 displays the results, which suggests that from bus 6 to 1, one line and from bus 6 to bus 2, two lines are recommended as per program. It also suggests 2 lines from bus 6 to bus 5 in order to get optimized cost. It is obvious that as the number of iterations increases, the accuracy falls, meaning that the more you iterate, the better the accuracy. It is also critical to recognize that the outcome includes more of the no colony [10].

Table 2

Final program results

From new generation bus	To old bus	Optimal line is to be connected
6	1	$1.2085 \approx 1$
6	2	2
6	3	0
6	4	0
6	5	2
6	6	0
Total new cost of planning will be added is	$R_s = 6.2501\cdot 10^7$ (approx.)	

Load flow results. Figure 3 shows that the newly built system based on program results is valid with power flow analysis.

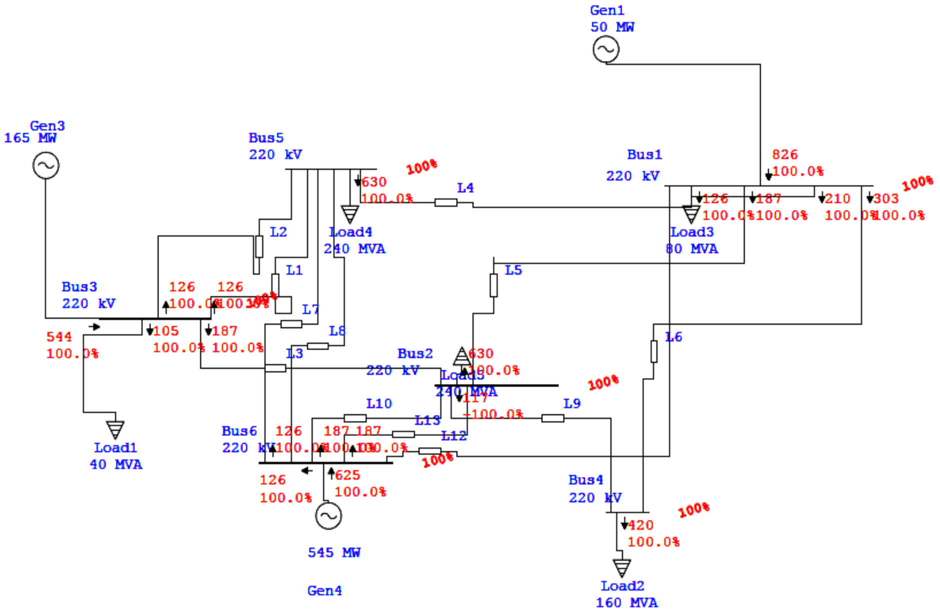

Fig. 3. Power flow results of 6-bus systems after planning

Bus voltages are within the limit. Following plans according to program, no buses are in a critical condition. Load flow also ensures that power flow from the lines is limited and that all inequality and equality restrictions are met after planning using the load flow summary presented in Table 3. The overall mismatch is 0, indicating that limitations have been met and load flow has been successful.

Table 3
Summary of total generation, loading and demand of load flow analysis

Bus	MW	MVAr	MVA	Power factor, %
Swing bus	760	0.08	760	100 lagging
Generators	0	0.109	0.109	0 lagging
Total demand	760	760	760	100 lagging
Total mismatch = 0 MW				

Comparison with other PSO methods In this section, the comparison of the proposed GABC based method is compared with ABC method for same problem. Table 4 shows the comparison in terms of computation time consumed, accuracy, exploration of new line, exploitation of achieve results and minimized cost achieve through ABC and GABC.

Table 4
GABC compare with ABC for TLEP problem solution

Parameters	Conventional ABC	GABC
Computational time, s	1	0.8
Accuracy	Less accurate	More accurate
Exploration of results	Good	Good
Exploitation	Poor	Improved
Minimized cost	10.5 % cost more than GABC	10.5 % less cost than ABC

Conclusions. When the system's issues are nonlinear and depend on more than one parameter, artificial intelligence approaches come in handy. The planning problem taken in this work can be handled using the Global Best Artificial Bee Colony approach, and load flow results in decision-making can be done with less effort under load uncertainty. The adoption of program and load flow analysis can improve power engineering capability, save planning time, and increase planning accuracy. The nonlinear issue of transmission line planning is not only addressed, but can also be tested and implemented in a real power system using a combined method of artificial intelligence and load flow analysis.

Conflict of interest. The author declares no conflict of interest.

REFERENCES

1. Desai J.P. Analysis of Power Swings and Blackouts. 2021 *IEEE Congreso Estudiantil de Electrónica y Electricidad (INGELECTRA)*, 2021, pp. 1-6. doi: https://doi.org/10.1109/INGELECTRA54297.2021.9748070.

2. Seifi H., Sepasian M.S. *Electric Power System Planning: Issues, Algorithms and Solutions*. Springer Science & Business Media, 2011.

3. Rathore C., Roy R. Load uncertainty based transmission network expansion planning. *2013 3rd International Conference on Electric Power and Energy Conversion Systems*, 2013, pp. 1-6. doi: https://doi.org/10.1109/EPECS.2013.6713034.

4. Mahdad B., Srairi K. Interactive artificial ecosystem algorithm for solving power management optimizations. *Electrical Engineering & Electromechanics*, 2022, no. 6, pp. 53-66. doi: https://doi.org/10.20998/2074-272X.2022.6.09.

5. Mehdi M.F., Ahmad A., Ul Haq S.S., Saqib M., Ullah M.F. Dynamic economic emission dispatch using whale optimization algorithm for multi-objective function. *Electrical Engineering & Electromechanics*, 2021, no. 2, pp. 64-69. doi: https://doi.org/10.20998/2074-272X.2021.2.09.

6. Desai J.P. Three-Terminal Transmission Line Protection By Considering Effect of Infeed Current. *Journal of The Institution of Engineers (India): Series B*, 2022, vol. 103, no. 6, pp. 2165-2175. doi: https://doi.org/10.1007/s40031-022-00795-7.

7. Razavi S.E., Arefi A., Ledwich G., Nourbakhsh G., Smith D.B., Minakshi M. From Load to Net Energy Forecasting: Short-Term Residential Forecasting for the Blend of Load and PV Behind the Meter. *IEEE Access*, 2020, vol. 8, pp. 224343-224353. doi: https://doi.org/10.1109/ACCESS.2020.3044307.

8. Garver L. Transmission Network Estimation Using Linear Programming. *IEEE Transactions on Power Apparatus and Systems*, 1970, vol. PAS-89, no. 7, pp. 1688-1697. doi: https://doi.org/10.1109/TPAS.1970.292825.

9. Gao W., Liu S., Huang L. A global best artificial bee colony algorithm for global optimization. Journal of Computational and *Applied Mathematics*, 2012, vol. 236, no. 11, pp. 2741-2753. doi: https://doi.org/10.1016/j.cam.2012.01.013.

10. Saif U., Guan Z., Zhang L., Mirza J., Lei Y. Hybrid Pareto artificial bee colony algorithm for assembly line balancing with task time variations. *International Journal of Computer Integrated Manufacturing*, 2017, vol. 30, no. 2-3, pp. 255-270. doi: https://doi.org/10.1080/0951192X.2016.1145802.

11. Desai J., Makwana V. Power Swing Blocking Algorithm based on Real and Reactive Power Transient Stability. *Electric Power Components and Systems*, 2020, vol. 48, no. 16-17, pp. 1673-1683. doi: https://doi.org/10.1080/15325008.2021.1906794.

12. Desai J.P., Makwana V.H. A novel out of step relaying algorithm based on wavelet transform and a deep learning machine model. *Protection and Control of Modern Power Systems*, 2021, vol. 6, no. 1, art. no. 40. doi: https://doi.org/10.1186/s41601-021-00221-y.

13. Aoyang H., Shengqi Z., Xuehui J., Zhisheng Z. Short-term Load Forecasting Model Based on RBF Neural Network Optimized by Artificial Bee Colony Algorithm. *2021 IEEE 2nd International Conference on Big Data, Artificial Intelligence and Internet of Things Engineering (ICBAIE)*, 2021, pp. 486-489. doi: https://doi.org/10.1109/ICBAIE52039.2021.9390043.

14. Bozogullarindan E., Bozogullarindan C., Ozturk C. Transfer Learning in Artificial Bee Colony Programming. *2020 Innovations in Intelligent Systems and Applications Conference (ASYU)*, 2020, pp. 1-7. doi: https://doi.org/10.1109/ASYU50717.2020.9259801.

15. Mínguez R., García-Bertrand R., Arroyo J.M. Adaptive Robust Transmission Network Expansion Planning using Structural Reliability and Decomposition Techniques. *Computational Engineering, Finance, and Science*, 2015, 12 p. doi: https://doi.org/10.48550/arXiv.1501.06613.

Received 16.11.2022
Accepted 20.01.2023
Published 01.09.2023

Jigneshkumar P. Desai[1]*, PhD, Assistant Professor,*
[1] Electrical Engineering Department,
U.V. Patel College of Engineering, Ganpat University, India,
e-mail: Jpd.fetr@gmail.com (Corresponding Author)

How to cite this article:
Desai J.P. Transmission line planning using global best artificial bee colony method. *Electrical Engineering & Electromechanics*, 2023, no. 5, pp. 83-86. doi: https://doi.org/10.20998/2074-272X.2023.5.12

UDC 621.3.013:621.311 https://doi.org/10.20998/2074-272X.2023.5.13

V.Yu. Rozov, D.Ye. Pelevin, K.D. Kundius

Simulation of the magnetic field in residential buildings with built-in substations based on a two-phase multi-dipole model of a three-phase current conductor

Problem. *Substations 10(6)/0.4 kV built into residential buildings create a magnetic field with magnetic flux density of more than 10 μT in nearby residential premises, which is a danger to the health of the population and makes the study of this magnetic field relevant for the development of methods for its protection. The main source of the substations external magnetic field is their low-voltage current conductor, the contribution of which to the total level of the magnetic field is more than 90 %. Multi-dipole mathematical models, which have a clear physical interpretation, are a promising method of modeling the substations magnetic field, which is important for the further development of methods of population protection. The* ***purpose*** *of the work is to modify the well-known multi-dipole model for calculation based on it with a limited error of the external magnetic field of current conductors of built-in substations that are close to residential buildings at a distance of up to one meter.* ***Methodology.*** *A modified two-phase multi-dipole mathematical model of the main source of the external magnetic field of substation – its three-phase low-voltage current conductors – is proposed, which, unlike the existing model, is based on a two- you to halve the distance to the area of calculation without increasing the error.* ***Verification****. An experimental verification of the modified two-phase multi-dipole model of the magnetic field of a three-phase 100 kVA transformer substation on its full-scale physical model was carried out, and the results of the experiment were presented, confirming the coincidence of the calculation and the experiment with a spread of no more than 7 %.* References 37, tables 1, figures 10.

Key words: **built-in substation, residential building, current conductor, external magnetic field, multi-dipole mode**.

Вбудовані у житлові будинки трансформаторні підстанції (ТП) 10(6)/0,4 кВ створюють у сусідніх житлових приміщеннях магнітне поле з індукцією більш 10 мкТл, що складає небезпеку для здоров'я населення і робить актуальним дослідження цього магнітного поля для розробки методів від його захисту. Основним джерелом зовнішнього магнітного поля ТП є їх низьковольтні струмопроводи, вклад яких в загальний рівень магнітного поля складає більш 90 %. Перспективним методом моделювання магнітного поля ТП є мультидипольні математичні моделі, що мають чітку фізичну інтерпретацію, важливу для подальшої розробки методів захисту населення. Метою роботи є модифікація відомої мультидипольної моделі для розрахунку на її основі з обмеженою похибкою зовнішнього магнітного поля струмопроводів вбудованих трансформаторних підстанцій, що наближені до житлових приміщень на відстань до одного метра. Запропоновано модифіковану двофазну мультидипольну математичну модель основного джерела зовнішнього магнітного поля трансформаторної підстанції – його трифазного низьковольтного струмопроводу, яка на відміну від існуючої моделі ґрунтується на двофазній дипольній моделі трифазного електричного кола і дозволяє вдвічі наблизити розрахункову область без збільшення похибки. Здійснено експериментальну перевірку модифікованої двофазної мультидипольної моделі магнітного поля трифазного струмопроводу ТП 100 кВА на його повномасштабній фізичній моделі та наведені результати експерименту, що підтверджують співпадіння розрахунку і експерименту із розкидом не більш 7 %. Бібл. 37. табл. 1, рис. 10.

Ключові слова: **вбудована трансформаторна підстанція, житлове приміщення, струмопровід, зовнішнє магнітне поле, мультидипольна модель.**

Introduction. One of the main sources of magnetic field (MF) of power frequency, which pose a danger to the population, are transformer substations (TSs) 10(6)/0.4 kV (Fig. 1) built into residential buildings, which have power from 100 to 1260 kVA, and the study of MFs of which is receiving more and more attention in the world [1-26].

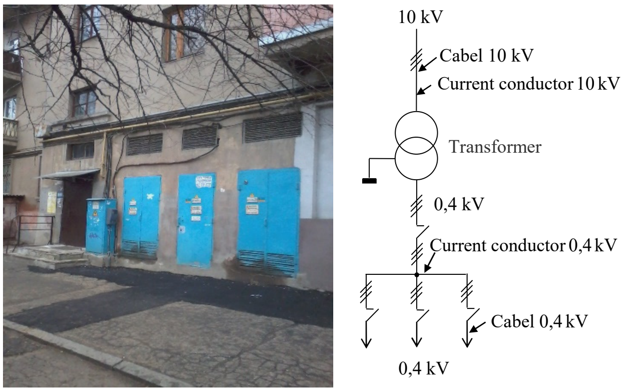

a *b*

Fig. 1. Built-in TS10/0.4 kV (*a*) and its simplified electrical circuit (*b*)

The magnetic flux density created by built-in TSs with power of 100 to 1260 kVA in neighboring residential premises located at a distance of 1-2 m above the TS can exceed 10 μT, which is confirmed as foreign (Fig. 2) [2, 3, 5, 21, 25, 26], as well as domestic (Fig. 3) studies [27]. This is more than an order of magnitude higher than the maximum permissible level of the magnetic flux density (0.5 μT) adopted in Ukraine [28], which requires its reduction. Therefore, the problem of modeling the MF of built-in TSs to determine their real level is relevant for the further development of means of its calculation and shielding on this basis [1, 4-15, 18, 27-31].

Justification of the topic of the article. As shown by the results of research by European scientists [2, 4, 6, 9], as well as research by authors [27], the main source of TSs MF is a low-voltage current conductor of 0.4 kV (Fig. 1,*b*), the external magnetic field (EMF) of which at a distance of 2 m is more than 90 % of the total TS's MF (Fig. 4). Therefore, for engineering calculations, the EMF of built-in TSs can be replaced by the EMF of their low-voltage current conductors.

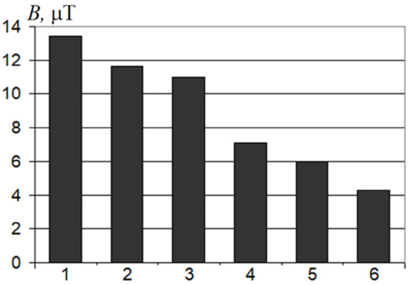

Fig. 2. Experimentally determined MFs in residential premises of buildings with built-in TSs of power of up to 1000 kVA in Europe (1 – Finland [21], 2 – Serbia [2], 3 – Hungary [3], 4 – Spain [25], 5 – Sweden [5], 6 – Switzerland [26])

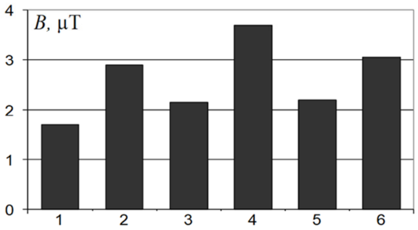

Fig. 3. Experimentally determined MFs in residential premises of houses with built-in TSs in the city of Kharkiv (1 – 360 kVA, 2 – 440 kVA, 3 – 630 kVA, 4 – 715 kVA, 5 – 565 kVA, 6 – 640 kVA)

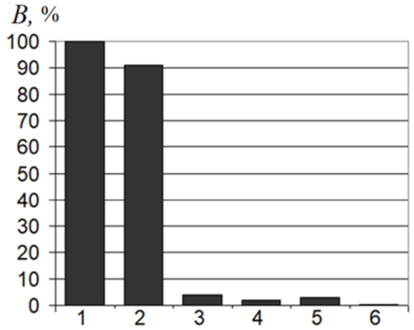

Fig. 4. The influence of individual sources of the TS's MF on the general level of the EMF at a distance of 2 m of them (1 – the total TS's MF; 2 – the MF of the low-voltage current conductor; 3 – the MF of the transformer; 4 – the MF of the low-voltage cable; 5 – the MF of the high-voltage current conductor; 6 – the MF of the high-voltage cable)

Three-phase current conductors of built-in TSs 10/04 kV 100 – 1260 kVA have straight sections located in horizontal (vertical) planes and are made of rigid aluminum (copper) busbars [28] with an interphase distance of up to 0.3 m.

A feature of the location of built-in TSs is the small distance between the surface of their current conductors and neighboring residential premises, which is from 1 to 2 m.

It is expedient to perform the modeling of the MF of the current conductors of the built-in TSs on the basis of the multi-dipole model (1) [27]. This model was developed to calculate the MF of power transmission lines (PTLs) [32]. It is suitable for modeling the three-dimensional MF of current conductors of any shape and has a clear physical interpretation, which simplifies the development of means of MF reduction based on it.

The multi-dipole model (1) is built on the basis of a system of dipole sources of the MF, which are characterized by magnetic moments $\vec{m}_i$ located in the geometric centers of independent rectangular microcircuits $d_i \times a$ with interphase current $\dot{I}_{AB}, \dot{I}_{BC}, \dot{I}_{CA}$ and areas $\vec{S}_{AB}, \vec{S}_{BC}, \vec{S}_{CA}$ into which all circuits of the interphase current of the current conductor are conventionally divided with length a:

$$\dot{\vec{H}}(P) = -\sum_{l=1}^{G}\sum_{\alpha=1}^{3}\sum_{c}\sum_{i=1}^{N}\nabla\left[\frac{\left(\dot{\vec{m}}_{l\alpha ci},\vec{R}_{l\alpha ci}\right)}{4\pi R^{3}_{l\alpha ci}}\right]; \qquad (1)$$

$$\dot{\vec{m}}_{l\alpha ci} = \dot{I}_{l\alpha}\cdot\vec{S}_{l\alpha ci} = I_{l\alpha}\cdot e^{-j\varphi_{\alpha}}\cdot a\cdot d_{l\alpha ci}\cdot\vec{n}_{l\alpha ci},$$

where N is the number of microcircuits in each PTL circuit; $\vec{S}_i$ is the area vector of the i-th microcircuit; $\vec{n}_i$ is the unit vector normal to S_i; $\vec{R}_i$ is the radius vector from the geometric center of the i-th microcircuit to the observation point P; c are the parts of the PTL under investigation; α is the number of phases of the PTL; G is the number of split wires of each phase; $d_{l\alpha ci}$ is the current distance between the wires of different phases.

The error when using the multi-dipole model (1) also, like the dipole model [33], depends on the ratio of the maximum geometric size L of the object (microcircuit) and the distance R from its surface to the area of application, and is less than 10 % at $R/L \geq 3$. Therefore, for a guaranteed limitation of the error of model (1) at the level of 10 %, where $L = d_{\max}$, the following conditions must be met:

$$R \geq 3d_{\max} \text{ at } a_i \leq 2d\,, \qquad (2)$$

where $d_{\max}$ is the maximum interphase distance between the current conductors of the phases in the case of their location on the plane.

However, the use of the multi-dipole model (1) for the simulation of the TS's EMF has limitations. For example, this model with typical values of d = 0.3 m, $d_{\max}$ = 0.6 m allows to perform the calculation of the TS's EMF only at distances $R \geq 1.8$ m, since the interphase distance between the extreme phases, which determines the area S_{CA}, is $2d$ (Fig. 5,a). But the minimum value of R for built-in TSs is about 1 m, which limits the application of this model.

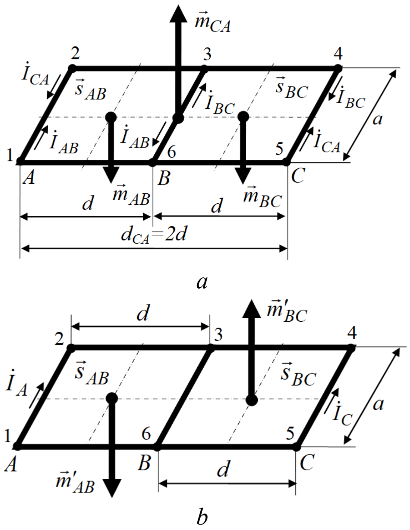

Fig. 5. Multi-dipole representation of an elementary three-phase circuit as a source of the MF: a) – traditional three-phase model; b) – two-phase model

Thus, the well-known multi-dipole model (1), which was developed for PTLs, needs modification to expand the scope of its application to built-in TSs with their typical minimum distances (from 1 m) from current conductors to residential premises.

The goal of the work is to modify the well-known multi-dipole model for calculation based on it with a limited error of the external magnetic field of current conductors of built-in transformer substations that are close to residential premises at a distance of up to 1 m.

A modified multi-dipole model of the current conductor of the built-in TS. When building a modified multi-dipole model of the TS's EMF, we believe that the walls of the TS, as well as the walls of buildings, practically do not shield the MF at frequency of 50 Hz [34, 35], and we accept the following assumptions:

- the premises of TS (except active elements of TS) and residential buildings do not have conductive and ferromagnetic elements and sources of MF;
- the currents of the current conductors are represented in the form of current filaments;
- the TS's MF is potential;
- all rectilinear parts of TS current conductors are flat and located either in a horizontal or in a vertical plane;
- the voltage of the TS power supply network is symmetrical and sinusoidal.

Let's transform the known multi-dipole model (1) for use on the TS, isolating the MF created by its interphase circuits with current:

$$\dot{\vec{B}}_S(P) = -\mu_0 \sum_{l=1}^{K}\sum_{i=1}^{N}\left[\nabla\left[\frac{\left(\dot{\vec{m}}_{ABli},\vec{R}_{ABli}\right)}{4\pi R_{ABli}^3}\right] + \nabla\left[\frac{\left(\dot{\vec{m}}_{BCli},\vec{R}_{BCli}\right)}{4\pi R_{BCli}^3}\right] + \nabla\left[\frac{\left(\dot{\vec{m}}_{CAli},\vec{R}_{CAli}\right)}{4\pi R_{CAli}^3}\right]\right] \qquad (3)$$

$\dot{\vec{m}}_{ABli} = \dot{I}_{ABli}\cdot\vec{S}_{ABli}$, $\dot{\vec{m}}_{BCli} = \dot{I}_{BCli}\cdot\vec{S}_{BCli}$, $\dot{\vec{m}}_{CAli} = \dot{I}_{CAli}\cdot\vec{S}_{CAli}$.

The condition for using model (3), which limits its error to 10 %, is relationship (2), which is not fulfilled at R = 1 m, since $d_{\max}$ = 0.6 m for it.

We will modify the known model (3). For this, we will use the two-phase model of the MF of the three-phase electric circuit (Fig. 5,*b*) proposed in [36], which is equivalent to the known three-phase model (Fig. 5,*a*) in terms of the space-time structure of the MF, but has half the maximum interphase distance. According to [36], the MF of an elementary three-phase current conductor with symmetry of the supply network voltages can be represented as a superposition of the MFs from 2 magnetic moments $\dot{\vec{m}}'_{AB}$, $\dot{\vec{m}}'_{BC}$, instead of three ones:

$$\dot{\vec{H}}(P) = -\nabla\frac{\left(\dot{\vec{m}}'_{AB},\vec{R}_{AB}\right)}{4\pi R_{AB}^3} - \nabla\frac{\left(\dot{\vec{m}}'_{BC},\vec{R}_{BC}\right)}{4\pi R_{BC}^3}, \qquad (4)$$

$$\dot{\vec{m}}'_{AB} = \dot{I}_A\vec{s}_{AB}, \quad \dot{\vec{m}}'_{BC} = -\dot{I}_C\vec{s}_{BC}.$$

Here, the maximum overall size of the elementary microcircuit decreases from 2*d* (Fig. 5,*a*) to *d* (Fig. 5,*b*), which makes it possible to halve the distance to the area of application of the model – from 6*d* to 3*d* (up to 0.9 m at *d* = 0.3 m).

Then, on the basis of (4), we will obtain a modified two-phase multi-dipole mathematical model of the MF of the three-phase TS current conductor, consisting of *K* rectilinear circuits, which have *N* two-phase microcircuits:

$$\dot{\vec{B}}_S(P) = -\mu_0 \sum_{l=1}^{K}\sum_{i=1}^{N}\left[\nabla\left[\frac{\left(\dot{\vec{m}}_{ABli},\vec{R}_{ABli}\right)}{4\pi R_{ABli}^3}\right] + \nabla\left[\frac{\left(\dot{\vec{m}}_{BCli},\vec{R}_{BCli}\right)}{4\pi R_{BCli}^3}\right]\right], \qquad (5)$$

$$\dot{\vec{m}}_{ABli} = \dot{I}_{Ali}\cdot\vec{S}_{ABli} = \dot{I}_{Ali}\cdot a_i\cdot d_l\cdot\vec{n}_{li},$$

$$\dot{\vec{m}}_{BCli} = -\dot{I}_{Cli}\cdot\vec{S}_{BCli} = -\dot{I}_{Cli}\cdot a_i\cdot d_l\cdot\vec{n}_{li},$$

where *l* is the number of the rectilinear circuit of the TS (*l* = 1,…, *K*); *N* is the number of elementary microcircuits in the rectilinear contour *l*.

The condition for using model (5) with a limited error of 10 % is

$$R \ge 3d \text{ at } a_i \ge d;\ d_{\max} = d. \qquad (6)$$

Figure 6,*b* presents a diagram of the distribution of magnetic moments of a low-voltage current conductor of a TS 100 kVA (Fig. 6,*a*) when implementing the proposed modified two-phase multi-dipole model (5).

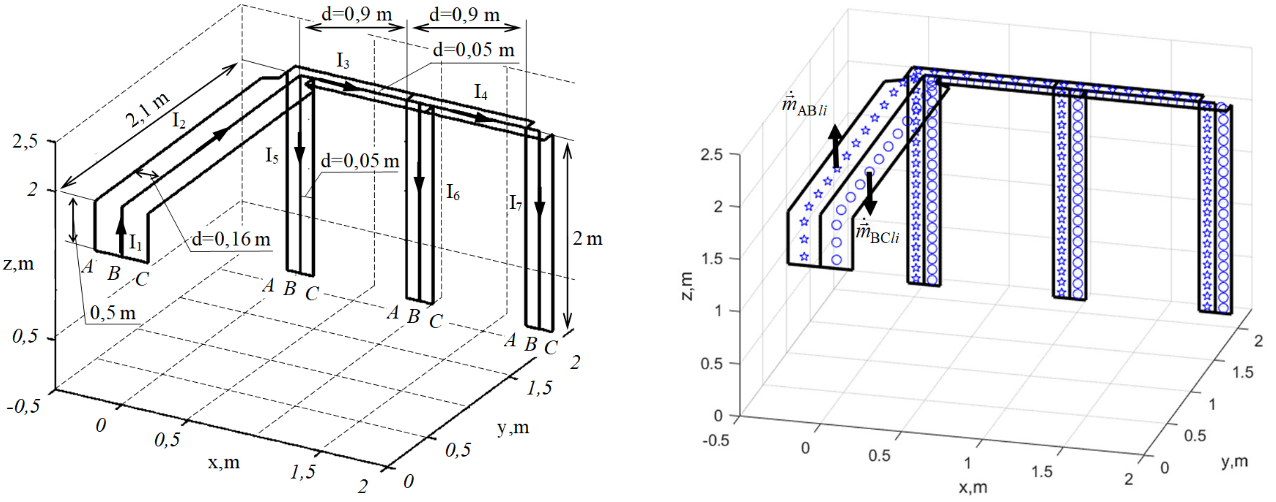

a *b*

Fig. 6. Low-voltage current conductor of the TS 10/0,4 kV, 100 kVA (I_n = 150 A (0.4 кВ); $I_1 = I_2 = I_n$; $I_3 = 2/3I_n$; $I_4 = I_5 = I_6 = I_7 = 1/3I_n$) (*a*) and the distribution of magnetic moments of microcircuits when using the two-phase multi-dipole mathematical model of the MF (*b*)

Thus, the modified two-phase multi-dipole mathematical model of the TS's MF proposed by the authors (5) allows to zoom in twice as close the calculation area due to the reduction of the minimum overall size of its microcircuit – from double the interphase distance 2*d* to the interphase distance *d*, which makes it possible to model the EMF for all built-in TSs at distances from 1 m to their current conductors. In addition, the modified model (5) allows to reduce the volume of calculations due to the corresponding decrease in the number of magnetic moments in comparison with the known model (3).

Verification of the modified multi-dipole model of the TS current conductor. We perform experimental verification of the proposed model of the TS's EMF (5) on the basis of a comparison of the results of the calculation of the EMF magnetic flux density of the 100 kVA TS current conductor (Fig. 6) and the measurements of the magnetic flux density of a full-scale laboratory model of this current conductor (Fig. 9).

The results of calculating the magnetic flux density of the current conductor in the horizontal plane, located at a height of 1.85 m above the current conductor of the TS (at a height of 0.5 m above the floor of the premise), were performed in accordance with (5) on the basis of the original computer code of the authors in the MATLAB software package and presented in Fig. 7,*a* and Fig. 8.

Experimental studies of the TS's EMF were performed on a full-scale laboratory model of the TS 100 kVA (Fig. 9) with nominal current of 150 A, where a low-voltage current conductor is a source of the MF (Fig. 6,*b*).

The layout of the current conductor (Fig. 9) is made of wooden rails and a PVC wire with a cross-section of 30 mm^2 and is mounted on the working site of the magnetic measuring stand of the unique magnetodynamic complex of the IPMach of the National Academy of Sciences of Ukraine [37]. The laboratory installation (Fig. 10) includes a layout of the current conductor (Fig. 9), which is fed through an induction regulator of the IR 59/32 type with the ability to adjust the three-phase current in the range of 0-220 A. Measurements of the current values of the magnetic flux density were performed at the nodes of the coordinate mesh with a step 0.25 m by EMF-828, Magnetoscop 1.069 type magnetometers on a control plane 1.85 m away from the current conductor.

To simplify measurements, the TS layout (Fig. 9) is placed on its side. Here, the measurements were performed on a vertical plane 1.85 m away from the current conductor, which is similar to the conditions of the performed calculation.

The results of the measurements are presented in Fig. 7,*b* and Table 1. A comparison of the calculation results with the experimental results shows that the calculated value of the magnetic flux density of the TS's EMF with a spread of less than 7 % coincides with the experimental results. This confirms the correctness of the modified two-phase multi-dipole model of the TS's EMF proposed by the authors and the assumptions made above.

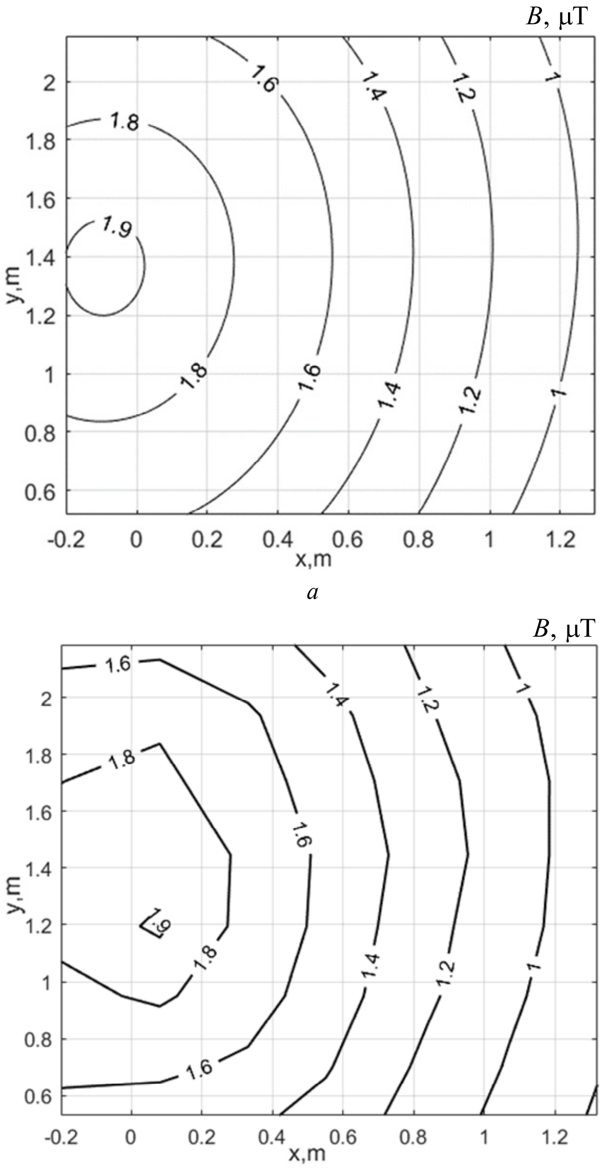

a

b

Fig. 7. Distribution of the EMF of the TS 100 kVA in the horizontal plane above the TS at a height of 1.85 m at nominal load: *a* – calculation; *b* – experiment

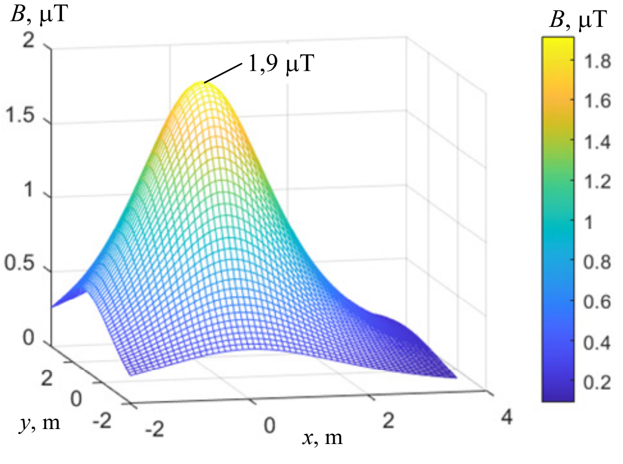

Fig. 8. Calculated values of the distribution of the EMF of the low-voltage current conductor of the TS 100 kVA at a height of 1.85 m above the current conductor at nominal load

Fig. 9. Full-scale laboratory layout of a low-voltage current conductor of the TS 10/0.4 kV, 100 kVA on the magnetic measuring stand

Table 1

Results of comparison of calculation and measurements of the EMF of the TS 100 kVA

x, m	y, m	Calculation B, μT	Experiment B, μT	Error, %
–0,1	0,33	1,622	1,526	5,92
0,43	0,75	1,506	1,443	4,22
0,94	1,25	1,159	1,098	5,25
1,42	1,74	0,821	0,779	5,14
0,18	0,5	1,698	1,640	3,43
0,65	1	1,445	1,418	1,91
1,17	1,51	1,038	0,984	5,21
–0,1	0,33	1,822	1,757	3,57
0,94	1,25	1,289	1,230	4,58
0,18	0,5	1,869	1,914	2,43
0,65	1	1,586	1,546	2,51
–0,1	0,33	1,900	1,863	1,93
0,43	0,75	1,766	1,785	1,04
0,94	1,25	1,349	1,302	3,47
1,42	1,74	0,946	0,886	6,31
0,18	0,5	1,848	1,847	0,04
0,65	1	1,579	1,524	3,49
–0,1	0,33	1,773	1,700	4,16
0,43	0,75	1,666	1,625	2,45
0,94	1,25	1,291	1,214	5,97
1,42	1,74	0,920	0,876	4,78
0,18	0,5	1,628	1,556	4,40
0,65	1	1,417	1,345	5,08
1,17	1,51	1,047	0,990	5,39

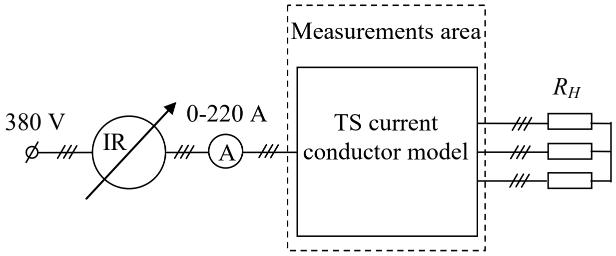

Fig. 10. Diagram of the laboratory installation for the study of the EMF of the layout of the TS 100 kVA current conductor

Thus, a modified two-phase multi-dipole mathematical model (5) was proposed for calculating the EMF of the TS current conductors and its experimental verification was performed on a full-scale laboratory model of a 100 kVA TS low-voltage current conductor. A comparison of the calculation and experimental results confirms the correctness of the proposed modified mathematical model and the calculation relations based on it.

It is promising to use the proposed modified two-phase multi-dipole mathematical model for calculating the MF of curvilinear (flexible) current conductors.

Conclusions.

1. It has been confirmed that the main source of the MF of built-in TSs is their low-voltage current conductor, the contribution of which to the total level of the magnetic field at a distance of 2 m is more than 90 %, which allows engineering calculations to ignore other sources of the TS's MF.

2. On the basis of the analysis of the results of research by foreign authors, as well as own research of the MF in residential buildings with built-in TSs in Ukraine, it is shown that the magnetic flux density level of built-in TSs with power of 100-1260 kVA, located in residential premises above the TSs, is from 1.5 to 13 μT, which significantly exceeds the maximum permissible level adopted in Ukraine (0.5 μT), constitutes a danger to the health of the population and confirms the urgency of reducing the TS's MF.

3. A modified two-phase multi-dipole mathematical model of the external MF is proposed for the main source of the magnetic field of the TS – its three-phase current conductor, which is based on the two-phase dipole model of a three-phase electric circuit and, compared with the known multi-dipole model, allows to approximate the calculation area twice without increasing the error and ensure the calculation of the external MF from the built-in TS in all residential premises of the building, including those located at a distance of one meter from the TS.

4. An experimental test of the modified two-phase multi-dipole model of the three-phase current conductor was carried out on a full-scale physical model of the TS 100 kVA current conductor, performed on the magnetic measuring stand of the unique magnetodynamic complex of the IPMach of the National Academy of Sciences of Ukraine, which confirmed the coincidence of the calculation and experimental results with a spread of less than 7 %.

5. The use of the proposed two-phase multi-dipole model of the three-phase current conductor of built-in TSs will allow the calculation of the MFs based on it to be extended to all neighboring residential premises, including those close to a distance of up to 1 m, which will contribute to solving the problem of protecting the population from the negative effects of the power frequency magnetic field.

Conflict of interest. The authors of the article declare that there is no conflict of interest.

REFERENCES

1. Leung S.W., Chan K.H., Fung L.C. Investigation of power frequency magnetic field radiation in typical high-rise building.

European Transactions on Electrical Power, 2011, vol. 21, no. 5, pp. 1711-1718. doi: https://doi.org/10.1002/etep.517.

2. Grbic M., Canova A., Giaccone L. Magnetic field in an apartment located above 10/0.4 kV substation: levels and mitigation techniques. *CIRED – Open Access Proceedings Journal*, 2017, no. 1, pp. 752-756. doi: https://doi.org/10.1049/oap-cired.2017.1230.

3. Thuroczy G., Janossy G., Nagy N., Bakos J., Szabo J., Mezei G. Exposure to 50 Hz magnetic field in apartment buildings with built-in transformer stations in Hungary. *Radiation Protection Dosimetry*, 2008, vol. 131, no. 4, pp. 469-473. doi: https://doi.org/10.1093/rpd/ncn199.

4. Geri A., Veca G. M. Power-frequency magnetic field calculation around an indoor transformer substation. *WIT Transactions on Modelling and Simulation*, 2005, vol. 39, pp. 695-704. doi: https://doi.org/10.2495/BE050641.

5. Salinas E., Aspemyr L., Daalder J., Hamnerius Y., Luomi J. Power Frequency Magnetic Fields from In-house Secondary Substations. *CIRED'99, 15th Conference on Electricity Distribution, Technical Reports*, session 2. 1999, pp. 161-164.

6. Burnett J., Du Yaping P. Mitigation of extremely low frequency magnetic fields from electrical installations in high-rise buildings. *Building and Environment*, 2002, vol. 37, no. 8-9. pp. 769-775. doi: https://doi.org/10.1016/S0360-1323(02)00043-4.

7. Bravo-Rodriguez J., Del-Pino-Lopez J., Cruz-Romero P.A Survey on optimization techniques applied to magnetic field mitigation in power systems. *Energies*, 2019, vol. 12, no. 7, art. no. 1332. doi: https://doi.org/10.3390/en12071332.

8. Alotto P., Guarnieri M., Moro F., Turri R. Mitigation of residential magnetic fields generated by MV/LV substations. *42nd International Universities Power Engineering Conference*. Brighton, UK, 2007, pp. 832-836. doi: https://doi.org/10.1109/UPEC.2007.4469057.

9. Buccella C., Feliziani M., Prudenzi A. Active shielding design for a MV/LV distribution transformer substation. *2002 3rd International Symposium on Electromagnetic Compatibility*. Beijing, China, 2002, pp. 350-353. doi: https://doi.org/10.1109/ELMAGC.2002.1177442.

10. Canova A., Giaccone L. Real-time optimization of active loops for the magnetic field minimization. *International Journal of Applied Electromagnetics and Mechanics*, 2018, vol. 56, no. S1, pp. 97-106. doi: https://doi.org/10.3233/JAE-172286.

11. Del-Pino-Lopez J.C., Giaccone L., Canova A., Cruz-Romero P. Ga-based active loop optimization for magnetic field mitigation of MV/LV substations. *IEEE Latin America Transactions*, 2014, vol. 12, no. 6, pp. 1055-1061. doi: https://doi.org/10.1109/TLA.2014.6894000.

12. Del-Pino-Lopez J., Giaccone L., Canova A., Cruz-Romero P. Design of active loops for magnetic field mitigation in MV/LV substation surroundings. *Electric Power Systems Research*, 2015, vol. 119. pp. 337-344. doi: https://doi.org/10.1016/j.epsr.2014.10.019.

13. Garzia F., Geri A. Active shielding design in full 3D space of indoor MV/LV substations using genetic algorithm optimization. *IEEE Symposium on Electromagnetic Compatibility*. Boston, MA, USA, 2003, vol. 1. pp. 197-202. doi: https://doi.org/10.1109/ISEMC.2003.1236591.

14. Garzia F., Geri A. Reduction of magnetic pollution in urban areas by an active field cancellation. *WIT Transactions on Ecology and the Environment*, 2004, vol. 72, pp. 569-579. doi: https://doi.org/10.2495/SC040561.

15. Celozzi S., Garzia F. Active shielding for power-frequency magnetic field reduction using genetic algorithms optimization. *IEE Proceedings – Science, Measurement and Technology*, 2004, vol. 151, no. 1, pp. 2-7. doi: https://doi.org/10.1049/ip-smt:20040002.

16. Shenkman A., Sonkin N., Kamensky V. Active protection from electromagnetic field hazards of a high voltage power line. *HAIT Journal of Science and Engineering*, 2005, vol. 2, no. 2, pp. 254-265.

17. Celozzi S. Active compensation and partial shields for the power- frequency magnetic field reduction. *2002 IEEE International Symposium on Electromagnetic Compatibility*, Minneapolis. MN, USA, 2002, vol. 1, pp. 222-226. doi: https://doi.org/10.1109/isemc.2002.1032478.

18. Canova A., del-Pino-Lopez J.C., Giaccone L., Manca M. Active Shielding System for ELF Magnetic Fields. *IEEE Transactions on Magnetics*. March 2015, vol. 51, no. 3, pp. 1-4. doi: https://doi.org/10.1109/tmag.2014.2354515.

19. Szabo J., Janossy G., Thuroczy G. Survey of residential 50 Hz EMF exposure from transformer stations. *Bioelectromagnetics*, 2007, vol. 28, no. 1, pp. 48-52. doi: https://doi.org/10.1002/bem.20264.

20. Ilonen K., Markkanen A., Mezei G., Juutilainen J. Indoor transformer stations as predictors of residential ELF magnetic field exposure. *Bioelectromagnetics*, 2008, vol. 29, no. 3, pp. 213-218. doi: https://doi.org/10.1002/bem.20385.

21. Okokon E. O., Roivainen P., Kheifets L., Mezei G., Juutilainen J.. Indoor transformer stations and ELF magnetic field exposure: use of transformer structural characteristics to improve exposure assessment. *Journal of Exposure Science & Environmental Epidemiology*, 2014, vol. 24, no. 1, pp. 100-104. doi: https://doi.org/10.1038/jes.2013.54.

22. Grbic M., Canova A., Giaccone L. Levels of magnetic field in an apartment near 110/35 kV substation and proposal of mitigation techniques. *Mediterranean Conference on Power Generation, Transmission, Distribution and Energy Conversion*. Belgrade, 2016, pp. 1-8. doi: https://doi.org/10.1049/cp.2016.1025.

23. Rahman N.A., Rashid N.A., Mahadi W.N., Rasol Z. Magnetic Field Exposure Assessment of Electric Power Substation in High Rise Building. *Journal of Applied Sciences*, 2011, vol. 11, pp. 953-961. doi: https://doi.org/10.3923/jas.2011.953.961.

24. Izagirre J., Del Rio L., Gilbert I.P., Rodriguez-Seco J.E., Güemes J.A., Iralagoitia A.M. Application of a new IEC magnetic field assessment methodology to promote transformer substation sustainable development. *IEEE 2011 EnergyTech*. Cleveland, OH, USA, 2011, pp. 1-6. doi: https://doi.org/10.1109/EnergyTech.2011.5948529.

25. Navarro-Camba E.A., Segura-García J., Gomez-Perretta C. Exposure to 50 Hz Magnetic Fields in Homes and Areas Surrounding Urban Transformer Stations in Silla (Spain): Environmental Impact Assessment. *Sustainability,* 2018, vol. 10, no. 8, art. no. 2641. doi: https://doi.org/10.3390/su10082641.

26. Röösli M., Jenni D., Kheifets L., Mezei G. Extremely low frequency magnetic field measurements in buildings with transformer stations in Switzerland. *Science of the Total Environment*, 2011, vol. 409, no. 18, pp. 3364-3369. doi: https://doi.org/10.1016/j.scitotenv.2011.05.041.

27. Rozov V.Y., Pelevin D.Y., Pielievina K.D. External magnetic field of urban transformer substations and methods of its normalization. *Electrical Engineering & Electromechanics*, 2017, no. 5, pp. 60-66. doi: https://doi.org/10.20998/2074-272X.2017.5.10.

28. *Electrical installation regulations*. Kharkiv, Fort Publ., 2017. 760 p. (Ukr).

29. Kuznetsov. B.I., Nikitina T.B., Bovdui I.V. Method of adjustment of three-circuit system of active shielding of magnetic field in multi-storey buildings from overhead power lines with wires triangular arrangement. *Electrical Engineering & Electromechanics*, 2022, no. 1, pp. 21-28. doi: https://doi.org/10.20998/2074-272X.2022.1.03.

30. Kuznetsov. B.I., Nikitina T.B., Bovdui I.V. Comparison of the effectiveness of thriple-loop and double-loop systems of active shielding of a magnetic field in a multi-storey old buildings *Electrical Engineering & Electromechanics*, 2022, no. 3, pp. 21-27. doi: https://doi.org/10.20998/2074-272X.2022.3.04.

31. Kuznetsov. B.I., Nikitina T.B., Bovdui I.V. Synthesis of an effective system of active shielding of the magnetic field of a power transmission line with a horizontal arrangement of wires using a single compensation winding. *Electrical Engineering & Electromechanics*, 2022, no. 6, p. 15-21. doi: https://doi.org/10.20998/2074-272X.2022.6.03.
32. Rozov V.Yu., Reutskyi S.Yu., Pelevin D.Ye., Pyliugina O.Yu. The magnetic field of power transmission lines and the methods of its mitigation to a safe level. *Technical Electrodynamics*, 2013, no. 2, pp. 3-9. (Rus).
33. Rozov V.Yu. *External magnetic fields of power electrical equipment and methods for reducing them*. Kyiv, the Institute of Electrodynamics Publ., 1995, no. 772, 42 p. (Rus).
34. Pelevin D.Y. Screening magnetic fields of the power frequency by the walls of houses. *Electrical Engineering & Electromechanics*, 2015, no. 4, pp. 53-55. (Rus). doi: https://doi.org/10.20998/2074-272X.2015.4.10.
35. Rozov V.Yu., Grinchenko V.S., Pelevin D.Ye., Chunikhin K.V. Simulation of electromagnetic field in residential buildings located near overhead lines. *Technical Electrodynamics*, 2016, no. 3, pp. 6-8. (Rus).
36. Rozov V.Yu., Pelevin D.Ye. The dipole model of magnetic field of three-phase electric circuit. *Technical Electrodynamics*, 2012. no. 4. pp. 3-7. (Rus).
37. Baranov M.I., Rozov V.Y., Sokol Y.I. To the 100th anniversary of the national academy of sciences of Ukraine – the cradle of domestic science and technology. *Electrical Engineering & Electromechanics*, 2018, no. 5, pp. 3-11. doi: https://doi.org/10.20998/2074-272X.2018.5.01.

Received 18.01.2023
Accepted 25.03.2023
Published 01.09.2023

V.Yu. Rozov[1], *Doctor of Technical Science, Professor,*
Corresponding member of NAS of Ukraine,
D.Ye. Pelevin[1], *PhD, Senior Researcher,*
K.D. Kundius[1], *Leader Engineer, Post Graduate Student,*
[1] Anatolii Pidhornyi Institute of Mechanical Engineering Problems of the National Academy of Sciences of Ukraine,
2/10, Pozharskogo Str., Kharkiv, 61046, Ukraine,
e-mail: vyurozov@gmail.com;
pelevindmitro@ukr.net (Corresponding Author);
kundiuckateryna@ukr.net

How to cite this article:
Rozov V.Yu., Pelevin D.Ye., Kundius K.D. Simulation of the magnetic field in residential buildings with built-in substations based on a two-phase multi-dipole model of a three-phase current conductor. *Electrical Engineering & Electromechanics*, 2023, no. 5, pp. 87-93. doi: https://doi.org/10.20998/2074-272X.2023.5.13

Матеріали приймаються за адресою:
Кафедра "Електричні апарати", НТУ "ХПІ", вул. Кирпичева, 2, м. Харків, 61002, Україна
Електронні варіанти матеріалів по e-mail: a.m.grechko@gmail.com

Довідки за телефонами: +38 067 359 46 96 Гречко Олександр Михайлович

Передплатний індекс: 01216